Orientation Tomography in Liquid Crystals & Shearmetry in Hydrovoltaic Systems by Spectroscopy of Polarized Luminescence of LaPO4 : Eu Nanorods

Lilian Magermans

INSTITUT POLYTECHNIQUE DE PARIS

NNT : 2024IPPAX088

Thèse de doctorat

Orientation Tomography in Liquid Crystals & Shearmetry in Hydrovoltaic Systems by Spectroscopy of Polarized Luminescence of $LaPO_4$:Eu Nanorods

Thèse de doctorat de l'Institut Polytechnique de Paris
préparée à École Polytechnique

Ecole doctorale n°626 Ecole doctorale de l'Institut Polytechnique de Paris (ED IP Paris)
Spécialité de doctorat: Physique de la matière condensée

Thèse présentée et soutenue à Palaiseau, le 30 Octobre 2024, par

Lilian Magermans

Composition du Jury :

Emmanuelle Lacaze Directrice de recherche, Sorbonne Université	Présidente
Ben Erné Associate professor, Utrecht University	Rapporteur
François Marquier Professor, Ecole Normale Supérieure Paris-Saclay	Rapporteur
Jan Lagerwall Professor, University of Luxembourg	Examinateur
Seok Woo Lee Associate professor, Nanyang Technological University	Examinateur
Thierry Gacoin Directeur de recherche, CNRS-École Polytechnique, IP Paris	Directeur de thèse
Jongwook Kim Professeur assistant, École Polytechnique, IP Paris	Co-directeur de thèse

Acknowledgements

Firstly, I would like to sincerely thank the jury members for taking the time to review my work and participating in my PhD defense. I highly appreciated the scientific discussion and the useful comments shared.

I would like to express my gratitude for my thesis directors **Thierry Gacoin** and **Jongwook Kim**, who helped me become the scientist I am today. From the beginning, they always respected my opinions and created a safe environment for rigorous scientific discussions. Specifically, I thank Thierry for his curiosity and enthusiasm for science, which initially convinced to do my masters and PhD at École Polytechnique. I thank Jongwook for all the experimental skills he taught me, from synthesis to optics, and the many impromptu scientific discussions we had in his office. I am also grateful for his guidance in shaping my professional carreer. Most of all, I thank them both for always believing in me.

I would also like to thank our collaborators. **Seok Woo Lee** for giving me the opportunity to work on such an interesting topic and for welcoming me into his group when I visited Singapore. It was a pleasure to work together and I learned a lot from the discussions we had regarding the experimental results. **Timothy Atherton** for providing the numerical simulations of the liquid crystal structures and for making time for me to visit his lab at Tufts. **Gabriel Amselem** for his help regarding the microfluidics experiments and **Fouad Maroun** for the many discussions we had regarding the electrochemical systems and experimental results.

Next, I'd like to thank all the previous and current members of the nanorod team at PMC who I've had the pleasure to work with. **Jeongmo** and **Zijun**, who provided me with valuable training and laid much of the groundwork needed for my work. I especially appreciate their continued involvement and support even after they left the group. **Qilin** for the many scientific and personal discussions, and **Zhengyu** for his help developing the theoretical frameworks. Finally, I thank **Marcello** for his great questions, positive attitude and enthusiasm. I have no doubt he will do a great job continuing the work.

I also need to thank my colleagues at PMC who made my days in the lab so enjoyable. My office mate **Didier**, who always made an effort to interact with me even when we initially had a language barrier. **Rabei** for his help with chemistry experiments, but above all for his infectious positive attitude and for reinvigorating my passion for tennis. **Clément** for always stopping by my office for a chat, **Simon** for his interest in my work and his welcoming spirit, **Khalid** for his endless jokes and **Alistair** for all the pleasant conversations we shared over lunch. **Eric** and **Sandrine** for their friendliness and help with the TEM and XRD measurements. **Anne-Marie** for her efforts helping PhD students, as well as **Anne-Chantal, François** and **Tomas** for their thoughtful involvement in the end of thesis workgroup. Finally, I want to thank **Joël** and **Edgar** for organizing the PMC football team and motivating me to play despite my lack of experience.

I also thank all my fellow PhD students for sharing this experience with me and making sure I never felt alone. **Camille, Hannes** and **Rafaela,** who I am grateful to be able to call my close friends and who I shared many great moments with, both in- and outside the lab. **Gyeongjun** for his humor and creating a nice environment in our office, **Samy** for his thoughtfulness and caring nature, **Randy** for his big smile and funny jokes, **Tram** for her kindness and compassion and **Edgar** for his positivity and efforts to create a close-knit PhD community. I also want to thank everyone who came to play tennis with me after work, including **Changhyun, Adrien, Leonard** and **Raouf**. Finally, a special thank you to **Jisoo**, whose bubbly persona and empathy made every day a better one. I am truly grateful for being able to have closely shared this experience with her. My PhD wouldn't have been the same without her and I will miss our daily interactions in the lab.

Finally, I would like to thank my family and friends for always being there for me. My parents and brothers, who supported me in so many different ways. My aunt, uncle and cousins who always showed interest in my work and travelled to Paris for my defense. I also thank my close friends **Jen** and **Anthony** who followed my defense online from the US and have continuously been my greatest cheerleaders. Finally, I want to thank my partner **Claude-Alban** for his undying support and for always believing in me. Beyond his emotional support, I am grateful for the many scientific discussions we had and for him always taking the time to give feedback on my work. I look forward to continuing to grow together.

Preface

After completing my bachelor's degree in mechanical engineering, I realized that I preferred working on fundamental science and thus chose to continue my studies in physics and material science. In particular, I was fascinated (and still am) by the study of nanoscopic objects and processes, which are invisible by the naked eye. The Condensed Matter Physics (PMC) laboratory has a long history of working with a variety of luminescent nanocrystals and their applications for the fundamental study of phenomena at the nano- and microscale, making it a perfect fit for my research interests. I therefore joined PMC, first as a master's student and afterwards to pursue my PhD, and have spent the last five years working with europium doped lanthanum phosphate ($LaPO_4$:Eu) nanorods for their applications as orientation probes.

Before the start of my PhD, our group had already developed proof-of-concepts for spectroscopic orientation analysis using the polarized luminescence originating from lanthanide dopants, both on the single particle level and in particle ensembles. Moreover, an innovative approach for measuring shear stresses in microfluidic systems using these luminescent nanorods had been developed. However, some limitations remained and during my master's internship I realized that the existing methodology didn't always give accurate and reproducible results. During my PhD, I therefore first worked on improving the orientation analysis methodology as well as the experimental setup required for the spectroscopic measurements.

In order to verify the accuracy of the methodology, I wanted to perform tomographic orientation mapping inside a system with a well-known structure. For this, I planned to use the liquid crystal (LC) assemblies naturally formed by suspensions of $LaPO_4$:Eu nanorods. However, when preparing the LC suspensions, I observed not only the formation of well-known structures, but also the appearance of complex structures resembling a periodic flower-like pattern. In fact, our group had previously observed these "flowers" but only in one sample, which had deteriorated over time, making it difficult to reproduce. Fascinated by their unexpected appearance, I decided to dedicate part of my thesis work on the study of the structure and evolution of these LC assemblies.

I personally believe that developing sustainable, renewable energy sources will be one of the main challenges of this century. I therefore wanted to apply our group's shearmetry technique to aid the development of such technologies. In this context, we started a collaboration with a research group at the Nanyang Technological University (NTU), which had developed a novel type of hydrovoltaic system based on the shear flow induced sweeping of ions adsorbed to capacitive electrodes. Although they successfully demonstrated that their system could harvest kinetic energy from flows, the mechanism was not yet understood. In my PhD, I therefore aimed to study the electrochemical response in relation to the interfacial shear stresses at the electrode surface, by performing *in situ* shearmetry using the luminescent

nanorods. These studies can hopefully be used to improve the efficiency of the system and to produce fundamental insights relevant to the broader hydrovoltaic research community.

Contents

1 Europium doped $LaPO_4$ nanorods and their applications for orientation probing

1.1 Europium doped $LaPO_4$ nanorods

1.1.1 Self-assemblies and alignment of anisotropic $LaPO_4$ nanocrystals

In our group, we have a long history of working with anisotropic $LaPO_4$ nanocrystals, which exhibit interesting optical properties, such as strong birefringence when collectively aligned, arising from the combined effects of shape- and crystallographic anisotropy[1]. The anisotropic growth rate along the c-axis of the crystal allows the synthesis of large aspect ratio nanorods by straightforward hydrothermal methods[2,3]. This highly anisotropic shape allows them to be easily aligned, both in spontaneous self-assemblies and by application of external forces. Stable colloidal suspensions of such nanorods can be achieved without any surface modification in acidic conditions, under which the surface of the nanorods is positively charged, stabilizing the colloidal suspension through electrostatic repulsion. Suspensions of such nanorods act as a colloidal liquid crystal (LC) which should be able to form highly aligned phases for a sufficiently high volume fraction Φ. However, increasing Φ above ~1% causes the particles to aggregate breaking the colloidal stability[2]. To overcome this, the colloidal stability can be further enhanced by either changing the solvent or by surface functionalization.

Redispersion of the nanorods in ethylene glycol (EG) contributes to the colloidal stability through an enhanced complexation of glycol groups on the surface of $LaPO_4$ and creates stable colloidal suspension even for high Φ(up to ~6%)[2]. As expected, we start to see the appearance of aligned LC phases when increasing Φ, as illustrated in **Figure 1.1**. $LaPO_4$ suspensions have been observed in an isotropic phase (complete lack of order) andtwo types of LC phases; the nematic phase (orientational order but no long range positional order) and the hexagonal columnar phase (orientational and positional order). The transition between these phases is governed by the competing effects of orientational entropy and the translational entropy of the excluded volume as described by Onsager's theory[4]. As Φ increases, it becomes more energetically favorable to form dense, ordered domains. At intermediate volume fractions nematic droplets called tactoids appear within the isotropic phase as seen in **Figure 1.1b**. At slightly higher Φ, the nematic phase dominates and anti-tactoids of the isotropic phase may be present (**Figure 1.1c**). The formation of such tactoids and anti-tactoids is very typical and has been reported for both colloidal and molecular nematic LC mesophases[5–7].

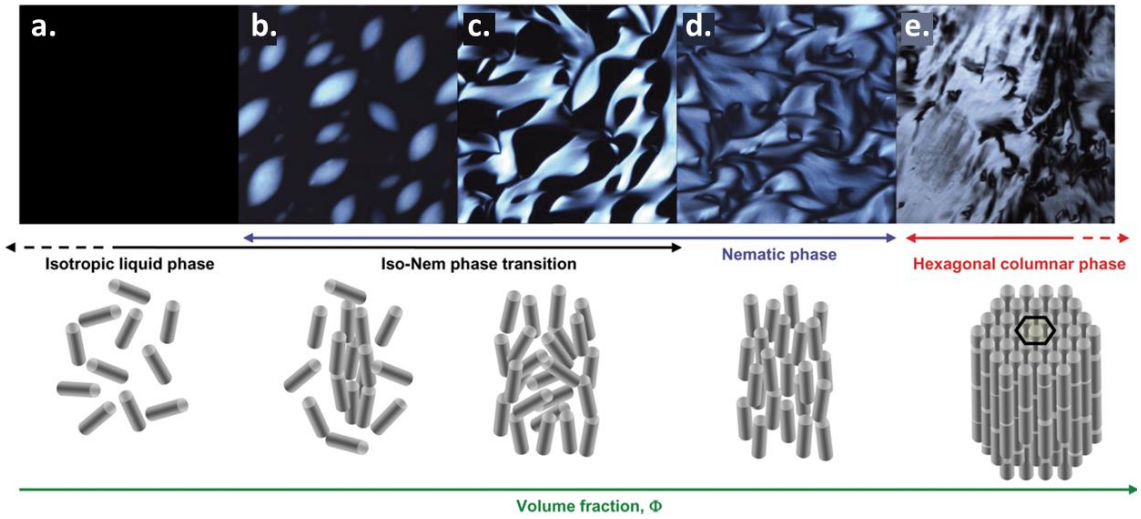

Figure 1.1 Liquid crystal phases of $LaPO_4$ suspensions observed between crossed polarizers and their schematic representation for increasing volume fractions. **a)** isotropic phase **b)** nematic tactoid droplets surrounded by isotropic phase **c)** combination of nematic and isotropic phase including anti-tactoids **d)** nematic phase **e)** hexagonal columnar phase. Figure from J-W. Kim *et al.* (2012)[2].

Interestingly, we found that if a droplet of the biphasic LC is confined between two rigid walls, new structures may appear (**Figure 1.2**). Depending on the surface chemistry and geometry of the confinement cell the final stable structure may resemble fingerprint patterns (**Figure 1.2b**) or even a novel complex flower-like structure (**Figure 1.2c**). Fingerprint-like structures are often observed in chiral or layered (smectic) LCs[8,9], but there is no indication that the $LaPO_4$ based colloidal LC is chiral or smectic in nature, suggesting its internal structure may be significantly different. Moreover, the flower structure presenting brightly birefringent streaks radiating from the center with four-fold symmetry (**Figure 1.2c**), has never been reported to our knowledge.

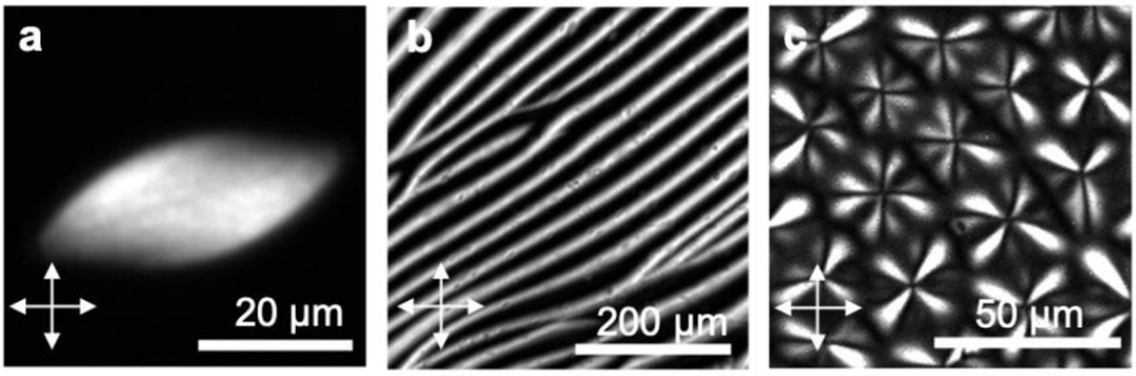

Figure 1.2 Different liquid crystalline structures of $LaPO_4$:Eu suspensions when confined between rigid walls. **a)** nematic tactoid droplet **b)** fingerprint-like nematic domains **c)** flower-shaped nematic domains Figure from PhD thesis of Jeongmo Kim[10].

Another way to stabilize the colloidal suspensions of $LaPO_4$ nanorods is by functionalization of the nanorod surface with zwitterionic polymers, allowing similarly high volume fractions and the associated LC behavior[11]. Aqueous suspensions of such functionalized nanorods are stable over a wide range of pH and salt concentration. The nanorods remain stable even in physiological media and were shown to be biocompatible, opening up the possibility to use them to probe biological systems[11].

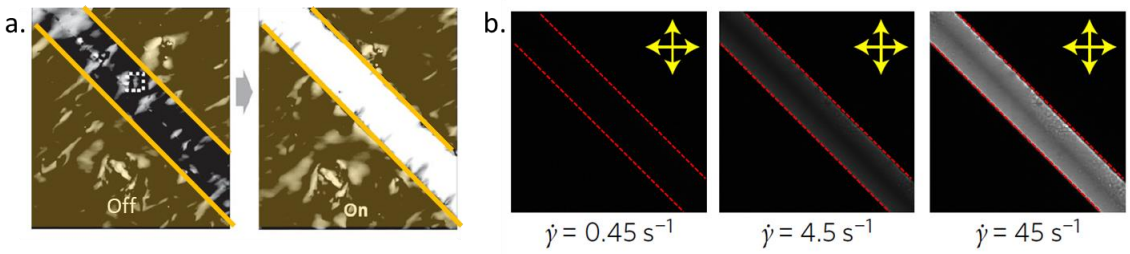

Figure 1.3 Active alignment of $LaPO_4$ nanorod suspensions indicated by bright birefringence observed through PLM. **a)** LC domain aligned by application of an electric field formed in the gap between two parallel electrodes (indicated in yellow). **b)** Collective alignment by hydrodynamic shear forces under flow through a rectangular microfluidic channel (walls indicated in red) increasing with the average shear rate $\dot{\gamma}$. Figures from references[2,12].

Besides the spontaneous alignment of the nanorods in LC systems, their high shape anisotropy also allows the colloidal nanorods to be easily oriented by external forces. When applying an alternating electric field, the nanorods will collectively align parallel to the field lines due to interactions with electric dipolesApplying an alternating electric field to a suspension generates a collective alignment of the nanorods, inducing a bright birefringence, seen under crossed polarizers, as shown in **Figure 1.3a**[2,13]. Similarly, when a suspension of the nanorods flows through a microfluidic channel, the hydrodynamic shear forces cause the rods to collectively align with the streamlines and the so-called flow birefringence appears (**Figure 1.3b**). The degree of alignment depends on the relative strength of the shear stress versus Brownian motion. Hence, the rods align more as the shear stress is increased as seen in **Figure 1.3b**.

Developing a robust method to quantify the three-dimensional (3D) orientation in such nanoparticle assemblies is of high interest for both spontaneously and actively aligned systems. It would allow us to characterize the internal structure of the complex LC domains, such as the flower pattern in **Figure 1.2**. Moreover, by calibrating the relationship between orientation behavior and the alignment forces, the nanoparticles could be used as sensors in unknown systems. In the case of nanorods in microfluidic systems, the shear stresses could be monitored *in situ*, as will be discussed in **section 1.3**[12]. To address this need for 3D orientation measurements, we dope our nanoparticles with the trivalent europium ion and use the resulting photoluminescence to retrieve their orientation, as will be discussed in the next sections.

1.1.2 Europium (III) photoluminescence

Photoluminescence (PL) occurs when an electron is excited to a higher energy level through photon absorption and then transitions back to a lower level through a radiative energy transfer, creating an emitted photon. The electronic configuration of the Eu^{3+} ion is [Xe] $4f^6$, resulting in 3003 degenerate energy configurations across the seven 4f-orbitals. Interactions between electrons (interelectronic repulsion) and between the nucleus and the magnetic dipole of the moving electron (spin-orbit coupling) cause these degeneracies to be (partially) lifted into various J-levels (**Figure 1.4**a). Each of those levels are denoted by the term $^{2S+1}L_J$, where $2S+1$ is the total spin multiplicity with S as the total spin quantum number, L the total orbital angular momentum and J the total angular momentum of the free electrons. As an example, J-level $^7F_2$ corresponds to 6 unpaired electrons (S = 3) with a total orbital momentum number of 3 (F for L=3), distributed such that J=2. Moreover, when the ion is placed within a (crystalline) host material, the surrounding crystal-field further lifts the degeneracies into different sublevels (known as Stark levels), illustrated in **Figure 1.4**a.

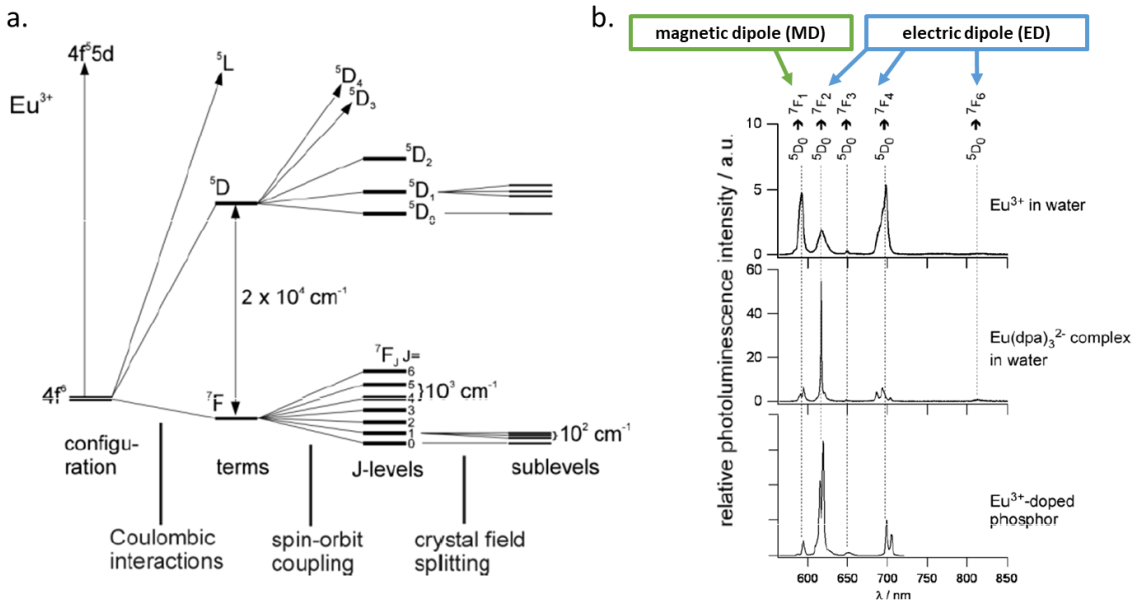

Figure 1.4 a) Energy level splitting of Eu^{3+} ion caused by various interactions. **b)** Emission spectra of Eu^{3+} in different environments. Figures adapted from reference[14].

The typical absorption spectrum of lanthanides consists of a broad charge transfer band (CTB) and several sharp peaks associated to 4f-4f transitions. Energy transitions within of the CTB are between the valence band of a host ion to the incompletely filled 4f-shell of the Eu^{3+} ion. This results in a broad absorption band as the energy required for the transfer is highly dependent on the distance between the two ions, making it sensitive to lattice distortions[15]. In contrast, the 4f orbitals are well shielded from the environment which results in narrow absorption peaks, with the $^7F_0$-$^5L_6$ typically being the most intense[16]. Electrons excited to

the $^5L_6$ state will fall back to the ^5D states through radiationless deactivation, which makes the emission from these levels to the ground states independent on the polarization of the absorbed photon.

In inorganic crystals, emission can be observed from several ^5D states and the most intense luminescence emission is generated by transitions from the $^5D_0$ to the various sublevels of ^7F[16]. Due to the effective screening by the 5s and 5p electrons, the J-levels are not impacted by the chemical environment of the ion, which results in emission peaks centered around the same wavelength no matter the environment (**Figure 1.4**b) [14]. Each transition is associated to either a magnetic dipole (MD) or electric dipole (ED), as indicated in **Figure 1.4**b. Within these energy levels not all transitions are allowed, as they need to meet various selection rules. MD transitions are always allowed as dictated by the Laporte selection rule, but ED transition can only occur through the vibrionic coupling and crystal field of the matrix as induced ED transitions[16]. This means that the intensity from MD transitions is mostly independent on the environment, whereas the relative intensity of ED transitions may vary strongly between host materials. Transitions $^5D_0$-$^7F_0$ and $^5D_0$-$^7F_3$ are forbidden by ΔJ selection rule of Judd-Ofelt theory and thus do not generate significant luminescence.

As the Stark levels are dominated by the crystal field splitting, putting the ion in a different environment changes the amount and relative intensity of subpeaks for each transition. Additionally, the magnetic and electric dipoles of an anisotropic host lattice can cause transitions to occur only in specific directions, giving rise to linearly polarized luminescence directly linked to the orientation of the dipole[16]. The choice of host material is therefore extremely important for spectroscopic applications.

1.1.3 Polarized photoluminescence of $LaPO_4$:Eu^{3+}

Lanthanum phosphate ($LaPO_4$) provides an excellent host for lanthanide ions due to its high quantum efficiency[17]. For $LaPO_4$:Eu^{3+}, the most intense absorption in the 4f-manifold is due to the characteristic $^7F_0$-$^5L_6$ transition and photoluminescence measurements are therefore performed using an excitation source at its associated wavelength ($\lambda \sim 394\ nm$)[18]. $LaPO_4$ nanocrystals may appear in the rhabdophane (hexagonal) or monazite (monoclinic) crystal phase depending on the synthesis parameters (**Figure 1.5a-b**). The corresponding site symmetries of La^{3+}, and therefore Eu^{3+}, are D_2 and C_1 respectively, resulting in different polarized emission spectra (**Figure 1.5c-d**). Due to the difference in the experienced crystal field of the Eu^{3+} ion, the number of subpeaks and their intensity vary between the two phases. The number of subpeaks can theoretically be predicted by group theory, but in practice the real number of subpeaks may differ due to lattice defects[18,19].

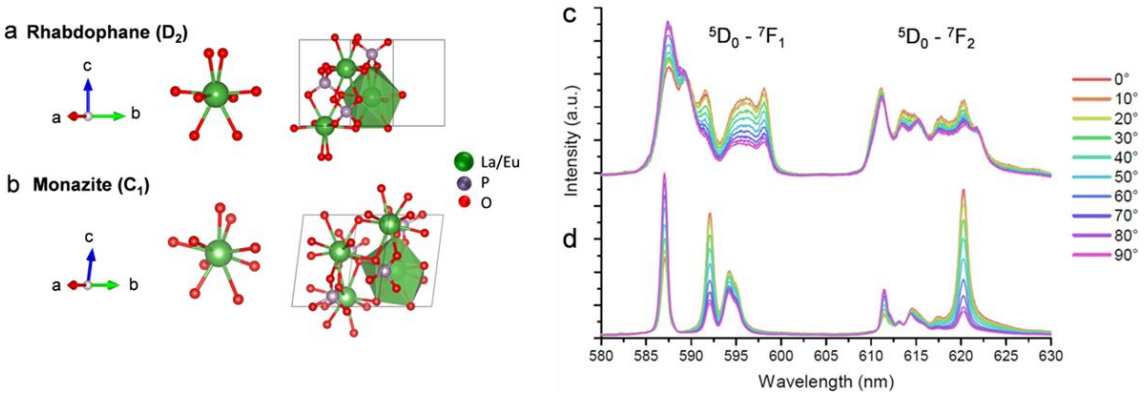

Figure 1.5 Illustration of the crystal structures of $LaPO_4$ in **a)** the hexagonal rhabdophane phase and **b)** monoclinic monazite phase. **c-d)** Normalized polarized emission spectra taken at 77K of thin films of aligned **c)** rhabdophane and **d)** monazite phase $LaPO_4$:Eu nanorods. From reference Chaudan *et al.* (2018)[18].

Additionally, each subpeak should have a certain polarization configuration, either parallel (π) or perpendicular (σ) to the c-axis of the crystal lattice. In reality, the observed peaks are always a mixture of the two which is quantified by the degree of polarization (DOP). This mixing of polarization configurations can be attributed to lattice distortions affecting the crystal field and seems to be stronger in rhabdophane than monazite. The monazite phase is therefore preferable for spectroscopic applications as it provides narrow, highly polarized peaks. Initial studies also showed an enhanced emission intensity compared to rhabdophane[18]. The first demonstration of monazite phase $LaPO_4$:Eu was achieved by a high temperature post-synthesis thermal treatment[18]. However, this approach makes it impossible to retrieve colloidal suspensions. Recently, a new colloidal synthesis approach was developed in our group, making it possible to synthesize monazite phase nanorod suspensions with excellent colloidal stability[3]. This is done by microwave synthesis with excess phosphate precursor invoking a rapid phase transition from rhabdophane to monazite phase[3]. Due to this advancement, we can now also address orientation sensing applications with monazite $LaPO_4$:Eu nanoprobes.

Summary of chapter 1.1

Suspension of highly anisotropic $LaPO_4$ nanorods spontaneously form aligned liquid crystalline (LC) phases at sufficiently high volume fractions and can be actively aligned through the application of an electric field or under shear flow. Mapping the orientation of the nanorod assemblies would allow to probe the shear stresses in microfluidic systems and to characterize novel streak- and flower-like LC structures.

To address this need for orientation sensing, we dope the $LaPO_4$ nanocrystals with europium, which provides highly polarized photoluminescence (PL) with narrow emission peaks linked to the orientation of the crystal's c-axis. Next, we will discuss how spectroscopic measurements of the PL allow to perform tomographic orientation mapping.

1.2 Three-dimensional orientation tomography in nanoparticle assemblies

Measuring the in-plane orientation of assemblies of anisotropic nanoparticles/molecules, such as LCs, is relatively straightforward and can usually be achieved through standard polarized light microscopy (PLM)[20]. Optical anisotropy is observed as birefringence between crossed polarizers. Measuring the intensity variation as the polarizers or sample is rotated allows to find the collective azimuthal orientation ϕ. The intensity should follow a sinusoidal dependency where the maximum intensity corresponds to a +/-45° angle between the orientation of the nanoparticles and the polarizer. An additional measurement with a first-order retardation plate is required to distinguish the mirror angles associated with the sinusoidal function. Birefringence measurements can also be used to measure the degree of order in nanoparticle ensembles under certain conditions. This approach is widely used to characterize liquid crystal defects and has also been used to measure shear stresses of viscoelastic media[21–23]. However, birefringence cannot be used to determine the out-of-plane angle, making it impossible to capture the true 3D orientation. Additionally, as PLM collects the light throughout the depth of the sample, it is not suited for reconstruction of 3D structures.

Alternatively, small-angle X-ray scattering (SAXS) can provide a more quantitative characterization of assemblies but has a limited spatial resolution. Electron microscopy methods have also been used in some cases[24,25], but are usually destructive and require the sample to be stabilized and can therefore not be used on dynamic samples. Non-destructive tomographic imaging of the 3D orientation is therefore a real challenge.

Instead, the optical anisotropy of the particle can be enhanced by adding a luminescence source. This can provide a more intense signal and combined with confocal microscopy opens up the possibility to perform

tomographic imaging. If the probe is oriented parallel to the observation plane, its 2D orientation ϕ can be simply found by collecting the luminescence intensity for different analyzer angles. For linearly polarized light, the intensity will follow a sinusoidal relationship with the angle of the analyzer, shown as a dumbbell-shaped polar diagram in **Figure 1.6a**. The axis of this measured dumbbell is directly linked to the orientation of the emission dipole and thus the orientation of the luminescent probe. However, determining the 3D orientation including the out-of-plane angle of the emission dipole is more challenging. This is because the emission measured in a single direction captures only the projected polar diagram which is influenced by both its azimuthal (ϕ) and polar angle (θ).

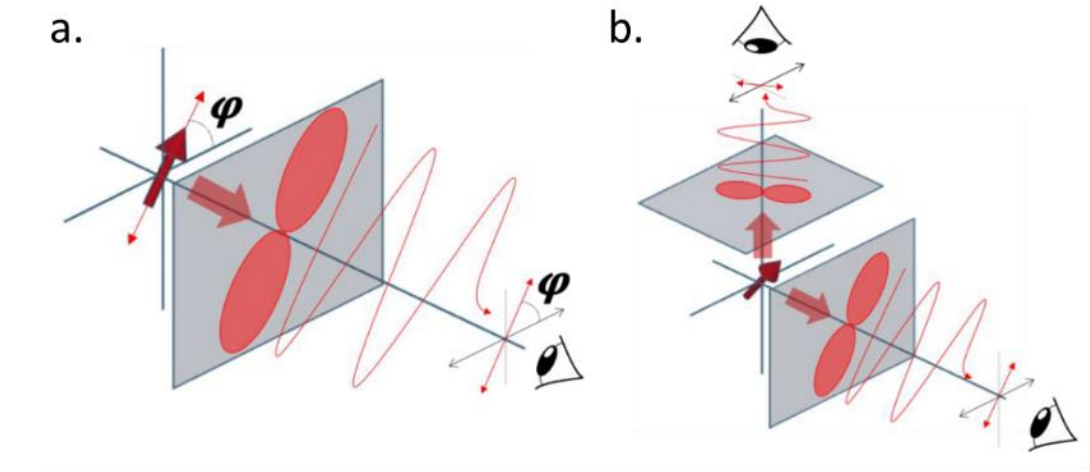

Figure 1.6 Schematic illustration of the emission dipoles and their corresponding polar diagrams projected on the observation plane(s). **a)** A single electric dipole laying in the observation plane. Its 2D orientation can be determined from single polar diagram. **b)** A single electric dipole with arbitrary 3D orientation. Its orientation can be determined from the projections of the polar diagram on two different observation planes. Figures adapted from J-M Kim *et al.* (2021)[26].

Stereoscopic imaging

One way to address this challenge is by either viewing or exciting the dipole from different directions through stereoscopic methods, as illustrated in **Figure 1.6b**. For single objects, a common example is back focal plane imaging utilizing a large NA objective to collect luminescence from a continuous range of viewing angles. The orientation of the emission dipole can then be determined by analyzing the defocused pattern formed on the back focal plane[27–29]. This method is convenient as it can be performed on conventional microscopes and has been demonstrated for organic dyes, plasmonic nanoparticles and semiconductor quantum rods[30–32]. However, such a technique is unsuitable for dense assemblies of nano-objects which generate a complex optical environment, making it impossible to generate an accurate numerical model required for the pattern analysis.

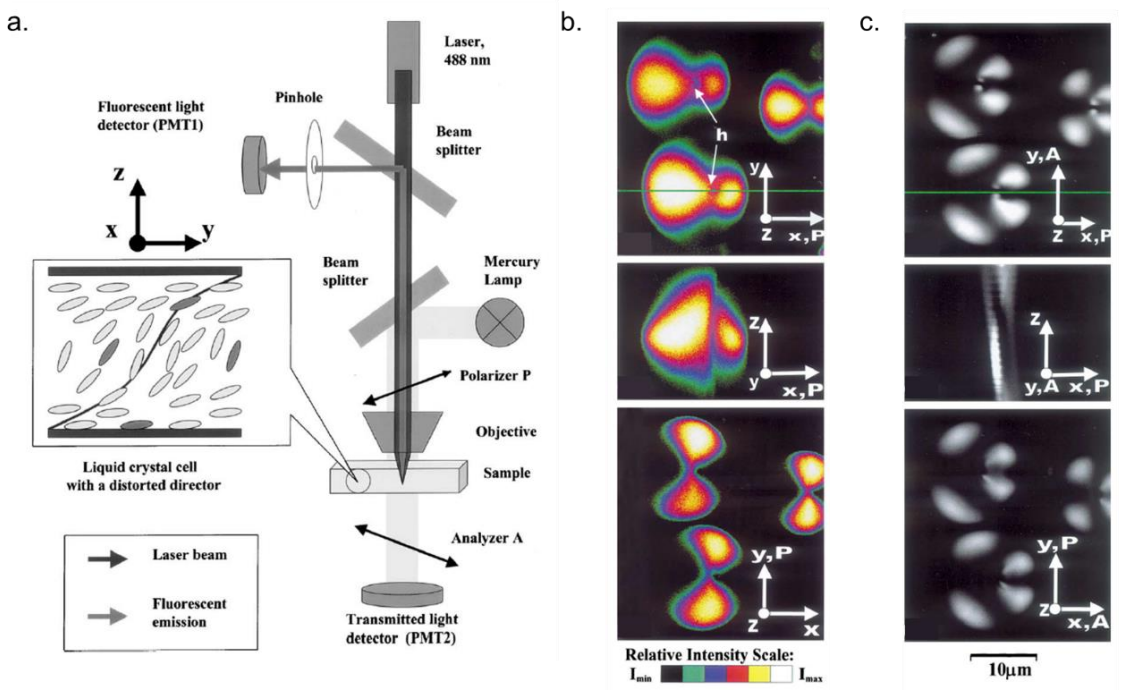

Figure 1.7 a) Fluorescence confocal polarizing microscopy (FCPM) experimental setup **b-c)** images of focal conic domains (FCD) obtained using **b)** FCPM and **c)** PM. Figures from Smalyukh *et al.* (2001)[33].

Smalyukh *et al.* proposed another approach using fluorescence confocal polarizing microscopy (FCPM) (**Figure 1.7**)[33]. They use a fluorescent dye whose absorption depends on the polarization of the excitation source, such that it is maximum when the collective orientation, known as the director, is parallel to the polarizer P and minimum when they are orthogonal. This dye is added to a LC assembly and using the FCPM setup (**Figure 1.7**) the fluorescence intensity is collected over many optical slices, which allows to reconstruct intensity maps both for the observation plane and the cross sections as seen in **Figure 1.7b**. By analyzing the relative intensity changes, the director orientation can be approximated. Although this technique provides more information than classical polarization microscopy (PM) imaging (**Figure 1.7c**), it cannot provide a precise, quantitative 3D orientation. Moreover, the intrinsic nature of dyes (i.e. FRET, photo-bleaching) as well as their potential impact on the liquid crystal behavior pose a major limitation.

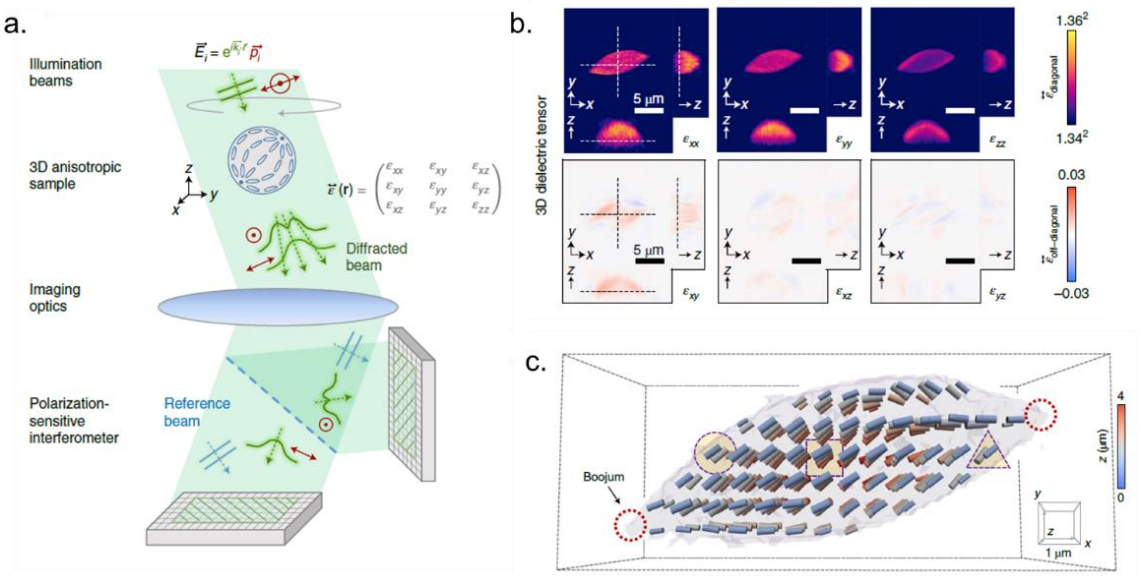

Figure 1.8 Dielectric tensor tomography (DDT) demonstrated in nematic tactoids. **a)** Schematic illustration of the experimental setup used for holographic imaging. **b)** Dielectric tensor calculated by solving the vectorial wave equation from the measured vectorial field. **c)** Reconstructed 3D director. Figures from Shin *et al.* (2022)[34].

Recently, Shin *et al.* demonstrated dielectric tensor tomography (DTT) which allows to reconstruct the internal structures of nematic LC from holographic images[34]. This can also be considered a stereoscopic method, but instead of imaging a luminescence dipole, they use the anisotropic dielectric tensor. The sample is illuminated by illumination beams with various angles and polarization states. The vectorial fields scattered from the sample are then measured holographically, as illustrated in **Figure 1.8a**. The vectoral field measurements are then used to inversely solve the vectorial wave equation and reconstruct the 3D dielectric tensor distributions. **Figure 1.8b** shows a demonstration of the calculated 3D dielectric tensor distributions for a nematic tactoid. Diagonalization of the dielectric tensor allows to find the 3D orientation distribution, as depicted in **Figure 1.8c**. The 3D structures of nematic tactoids and their non-equilibrium dynamics, such as their merging, were experimentally observed for the first time using this technique. However, this approach requires a complex optical setup and thorough theoretical framework.

Spectroscopic imaging

Instead of stereoscopic imaging, we propose another spectroscopic approach. If the luminescence has multiple degenerate dipoles (linked to the same energy transition) whose orientation are not identical with respect to the object, the 3D orientation can be found by simultaneously imaging those dipoles as illustrated in **Figure 1.9**. Such a spectroscopic approach only requires a single viewing angle and excitation beam, eliminating the need for complex image processing and/or numerical models. Moreover, using a lanthanide's luminescence with its distinct emission peaks, allows the spectroscopic approach to be based on relative intensity fluctuations, which reduces avoids sensitivities to blinking and background noise.

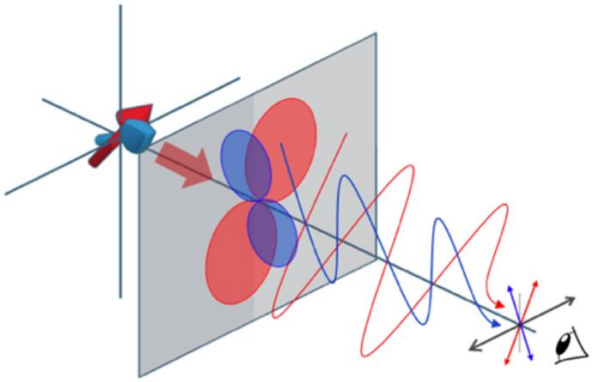

Figure 1.9 Spectroscopic imaging. An electric dipole (red) and magnetic dipole (blue) with a given angle between them. The orientation of the coupled dipoles can be determined from the corresponding polar diagrams as projected onto a single viewing plane. Figures adapted from J-M Kim *et al.* (2021)[26].

In our group, we have developed such a spectroscopic technique utilizing the polarized PL originating from the interactions with magnetic- and electric dipoles associated to the anisotropic crystal, as illustrated in **Figure 1.10a-b**. The polarized emission of a single nanoparticle can be described by three components; the radial components π and σ corresponding to the emission polarized parallel and perpendicular to the axis of the rod, and the unpolarized axial component α. Due to the coupling with the electric field component of the emission, the α component is identical to σ for ED transitions and identical to π for MD transitions (**Figure 1.10a-b**). Spectra obtained in aligned nanorod suspensions shown in **Figure 1.10c-d** confirm that this is indeed the case both for $NaYF_4:Eu^{3+}$ and $LaPO_4:Eu^{3+}$ nanocrystals.

These relationships between the intensity of I_π, I_σ and I_α are the key to the orientation analysis, as it allows to express the measured PL of an unknown system as the sum of the projection of each component on the measurement axis. With the reference spectra $I_\pi(\lambda)$ and $I_\sigma(\lambda)$ collected from a well-aligned reference sample the orientation of the particle(s) can then be determined either through spectral fitting or a ratiometric approach[12,26]. An in-depth summary of all our previous work on such orientation measurements and its limitations will be discussed in **chapter 2.1.1.**

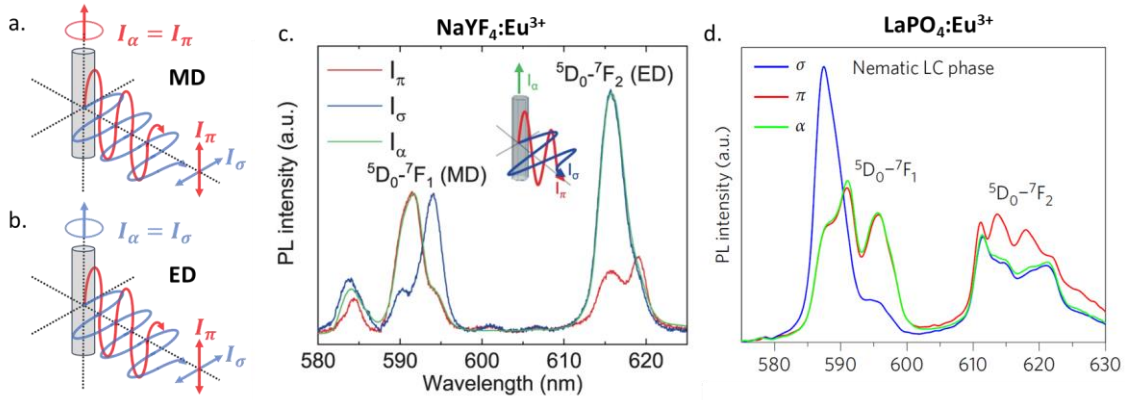

Figure 1.10 Polarized emission of europium doped nanorods. **a-b)** Schematic illustration of the emission components for magnetic dipole (MD) and electric dipole (ED) transitions. **c-d)** Polarized photoluminescence spectra associated to the π, σ and α components of $NaYF_4:Eu^{3+}$ and $LaPO_4:Eu^{3+}$ nanorods respectively. Figures from J-M Kim *et al*. (2021) and J-W Kim *et al.* (2017)[12,26].

Li *et al.* recently demonstrated a similar spectroscopic approach using single $NaYF_4$:Eu nanorods[35]. They consider the MD $^5D_0$-$^7F_1$ transition and measure the integrated intensity of each subpeak by fitting the sum of Lorentzian profiles. The orientation is then derived from the measured linear degree of polarization (LDOP) which can be obtained in two ways; using the Poincaré sphere (PS) or by polarization fitting (PF). The method based on the PS requires 6 measurements at distinct angles in order to calculate the Stokes parameters and the PF method is essentially based on fitting the dumbbell shape formed by measurements with the analyzer rotating from 0° to 360°. This method requires large amount of spectroscopic measurements to determine the orientation of a single crystal, making it impossible to image dynamic systems. Moreover, the Lorentzian fitting of each subpeaks can only be performed on emission spectra with well-defined, separated subpeaks, which is not always the case for lanthanide doped nanocrystals. Finally, the theoretical methodology is not adaptable to the analysis of the collective orientation of such nanoparticles, and can therefore not be used to perform 3D orientation tomography in assemblies.

In contrast, the approach developed by our group only requires a single measurement to find the 3D orientation of a single rare-earth doped nanocrystal and doesn't require any spectral fitting[12,26]. We have previously demonstrated this technique not only on single nanocrystals but also in a variety of systems consisting of collectively aligned particles[10,12,26,36–38]. This PhD work focuses on performing 3D orientation tomography in the diverse $LaPO_4$ assembly structures overcoming the previously encountered major limitations in the theoretical methodology as well as the experimental optical setup.

Summary of chapter 1.2

Quantitative tomography of the 3D orientation within nanoparticle assemblies, such as liquid crystals, remains challenging. Standard techniques like polarized light microscopy (PLM) only capture 2D orientation, whereas SAXS and electron microscopy approaches suffer from limited spatial resolution or result in the destruction of the sample. Optical imaging of the 3D orientation can be achieved by viewing the anisotropic probe, e.g. an emission dipole or dielectric tensor, from various viewing angles or using multiple excitation/illumination beams. Such *stereoscopic* approaches require complex optical configurations and image analysis algorithms. Instead, we have developed a *spectroscopic* approach simultaneously imaging multiple emission dipoles, inherent to lanthanide PL, from the same viewing angle. By expressing the polarized PL as a function of reference spectra obtained from highly aligned samples, the orientation of nanoparticle(s) can be retrieved.

1.3 Shearmetry using $LaPO_4$:Eu nanoprobes

One main application of orientation tomography explored by our group is its application for *in situ* shear monitoring[12]. The development of such an *in situ* shear probing technique is of interest for a variety of research fields, as shear stresses are known to play an important role in biomechanical and hydrovoltaic processes, as will be discussed later on.

Currently, the most common technique for measuring the shear rate in microfluidic systems are particle imaging velocimetry (PIV) and particle tracking velocimetry (PTV) in which individual tracer particles are imaged to deduce the velocity profile[39]. **Figure 1.11** shows an example of fluorescent tracer particles in a cylindrical channel and the velocity profile obtained through PIV. In PIV a large amount of small particles is captured and the velocity distribution is obtained from the image frames using cross-correlation algorithms[40], whereas in PTV larger individual particles are tracked frame by frame[41]. Such techniques cannot directly measure the shear rate, but rather it is obtained by differentiating the discrete velocity profile, which worsens measurement errors. Additionally, close to the walls, the particles move slowest which may cause the sensitivity and accuracy to be reduced. This is particularly troublesome, as for many processes it's exactly those interfacial shear stresses which play an important role.

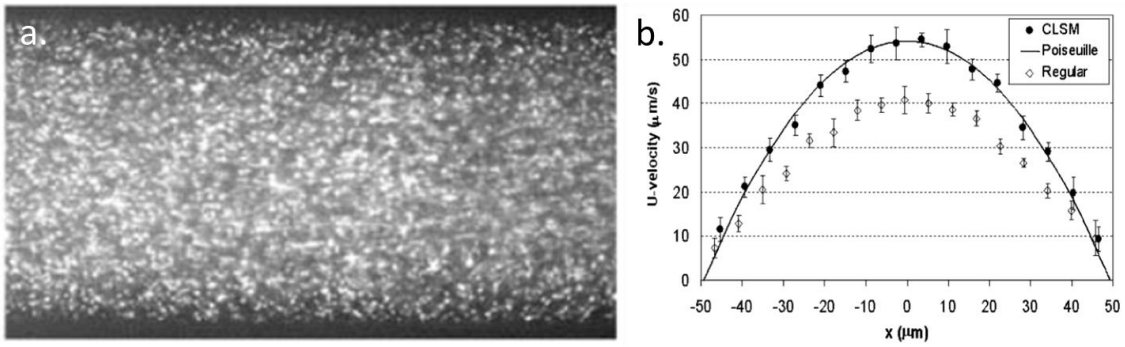

Figure 1.11 Micro-PIV using confocal laser scanning microscopy (CLSM) **a)** Example image of fluorescent tracer particles at the middle plane of a cylindrical channel **b)** Measured velocity profile across the channel. The open diamonds are based on images with a conventional microscope (not shown here). Figures from Park *et al.* (2004)[42].

One solution is to perform PIV using evanescent wave imaging and nanoparticle tracers, which allows shear measurement within several hundred nanometers from the substrate[43]. However, due to the exponential decay of the intensity of evanescent waves, this technique cannot be used to map the shear throughout a larger area or volume. Moreover, a large downside to all velocimetry techniques is that it requires the collection of a large number of image frames, making the post-treatment and analysis time consuming and difficult. This makes it especially challenging to make time-resolved, instantaneous shear measurements.

Our group has developed an alternative approach, using luminescent anisotropic nanoparticles as shear probes, which allows for tomographic mapping across the whole channel with the highest sensitivity and accuracy near the walls[12,38]. When the $LaPO_4$:Eu suspension is flowing through a microfluidic channel the nanorods will align according to the competing effects of the hydrodynamic forces and rotational diffusion, as illustrated in **Figure 1.12a**[44]. Comparing the spectra collected in the center and near the wall of the channel shows the different degree of alignment due to the difference in shear forces (**Figure 1.12b**). Near the center, there are no strong shear forces and the spectra collected with orthogonal polarizers are nearly identical, indicating an isotropic configuration dominated by rotational diffusion. In contrast, the spectra near the walls are strongly polarized, indicating collective alignment.

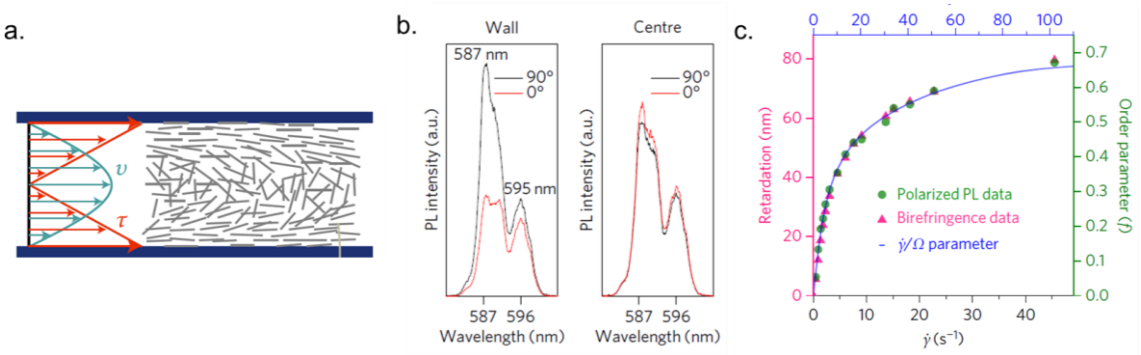

Figure 1.12 a) Schematic illustration of the collective alignment of nanorods under flow due to the shear stress τ **b)** Polarized PL measured with the analyzer oriented at 0° and 90° with respect to the flow direction close to the wall and near the center of the channel. **c)** The orientation factor f obtained through spectral analysis as a function of the shear rate $\dot{\gamma}$. The blue line is a theoretical fit based on the stress-optical law and acts as the calibration curve. Figures adapted from J-W Kim et al. (2017)[12].

The degree of collective alignment is quantified by the orientation factor (also known as order parameter) f and can be directly measured through the spectral analysis of the PL originating from the Eu^{3+} ion. In fact, there is a direct relationship between the shear rate $\dot{\gamma}$ and f governed by the stress-optical law, which will be discussed in detail in **chapter 4.1.1**[23,44]. This relationship $f(\dot{\gamma})$ can be experimentally established through PL measurements of f for controlled values of $\dot{\gamma}$ (**Figure 1.12c**). Once this $f(\dot{\gamma})$ calibration curve is established, the shear can be tomographically mapped using a scanning confocal microscope in systems for unknown flow conditions.

Applications of shearmetry

Shear stresses are known to play an important role in biomechanical processes on the cellular level, such as wound healing, cell deformation and adhesion[45–47]. Additionally, some types of cells actively produce shear to move (e.g. sperm cells) or to move their surrounding medium (e.g. cilia cells)[48,49]. Over the last few years, our group has made significant advances in the application of this technique for the study of such biological systems. We showed that the functionalized nanorods remain well dispersed in physiological media and do not interfere with cell function[11]. Recently, we demonstrated the shear tomography around living epithelial cancer cells cultured to the bottom of a microfluidic channel (see

Figure 1.13)[38]. Although not the focus of this work, the shear measurements were performed using the experimental setup and improved methodology developed as part of this PhD thesis.

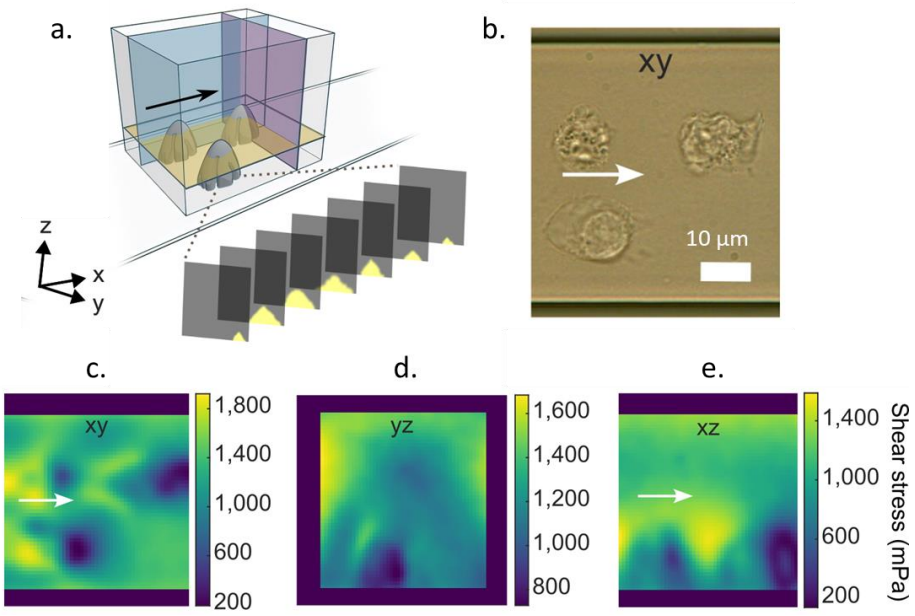

Figure 1.13 a) Schematic illustration of the microfluidic channel with cultured cancer cells attached to the bottom substrate. The images show cross-sectional slices of a single cell obtained by thresholding the PL intensity. **b)** Optical microscopy image of the three cells in the microfluidic channel **c-e)** Shear stress maps for the xy, yz, and xz planes (indicated in a)) based on the orientation factor maps obtained through the improved methodology described in **chapter 2**. Figures are adapted from Z. Wang *et al.* (2024)[38].

Beyond its application in biomedical research, we can envision the application of the shearmetry technique to different research fields where flow shear plays an important role.

Summary of chapter 1.3

Shear stresses play an important role in many processes, but obtaining *in situ* measurements challenging. The conventional approach relies on tracking the movement of tracer particles in order to deduce the velocity profile, from which the shear rate is derived. However, this requires large amounts of images and has a decreased accuracy close to solid interfaces. Our group developed an alternative approach which enables direct measurement of the shear by monitoring the orientation behavior of nanorods through spectral analysis of their polarized PL.

1.4 Hydrovoltaics based on ion sweeping on a capacitive electrode

As part of this PhD thesis, we also explored the impact of shear stresses on the electric double layer (EDL) formed at the interface of a capacitive electrode. When electrolyte flows over such a charged capacitive electrode, ions in its EDL are swept away due to the interfacial shear stress. If this ion sweeping occurs at

only one electrode of a circuit, it induces potential bias and can thus generate electric current[50]. This hydrovoltaic phenomenon enables us to harvest various types of kinetic energy on different scales (e.g. microbiological dynamics, human motions, ocean tide) and convert to useful electric energy sources.

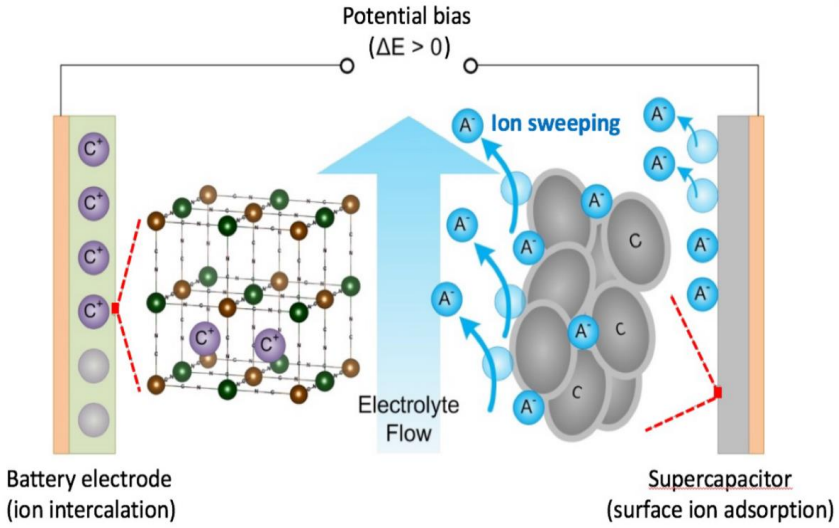

Figure 1.14 Concept of energy harvesting by selective ion sweeping. Schematic illustration of the hybrid cell made of a battery electrode where cations are incorporated inside the crystal lattice and a supercapacitor electrode with anions adsorbed to the surface. Applying a flow of electrolyte to the electrodes' surfaces only sweeps away the adsorbed ions, creating a potential bias between the two electrodes. Based on the demonstration by I.D. Jung *et al* (2022)[50].

The proof-of-concept of kinetic energy harvesting based on selective ion sweeping was developed at the Lee's Nano Energy Laboratory at Nanyang Technological University (NTU)[50]. They demonstrated this using a hybrid cell containing a copper hexacyanoferrate (CuHCFe) battery type electrode and activated carbon supercapacitor electrode, illustrated in **Figure 1.14**. When the two electrodes are put into contact, anions adsorb to the capacitive electrode and cations are incorporated inside the matrix of the battery electrode in order to compensate for the electrochemical potential difference. When the electrolyte is flowed across the electrodes, only ions in the EDL formed on the supercapacitor electrode will be swept away, as the ions hosted within the battery electrode are not affected by the flow, and a potential bias is established which can be used to generate a current.

Although successfully shown to convert mechanical energy to electrical energy, the fundamental ion sweeping mechanism is not yet understood. Initial studies showed a linear relationship between the flow rate and the amount of charges removed by the flow[50], but quantitative evaluation of the shear at the electrode interface was not possible. We started a collaboration with this research group at NTU to use our developed method using photoluminescent nanorods to probe the shear close to the electrode interface during ion sweeping. By understanding the role of shear on the ion sweeping behavior, we can optimize the device design and increase the overall energy harvesting efficiency.

Summary of chapter 1.4

As a possible application of the shearmetry technique previously discussed, we investigate the role of flow shear on the EDL formed on capacitive electrodes. This is done in collaboration with a research team at the Nanyang Technological University (NTU), which have previously demonstrated a kinetic energy harvesting system based on the flow induced ion sweeping from the EDL. We aim to characterize the electrochemical response of the cell as a function of the interfacial shear stress at the capacitive electrode surface, which can help design more efficient devices.

1.5 Thesis objectives and overview

This thesis is focused on the use of luminescent $LaPO_4$:Eu nanocrystals and the tomographic imaging of their collective orientation for the application in two main systems: LC assemblies and shear flows. In this section, the main challenges and objectives addressed will be outlined, followed by an overview of the manuscript.

Methodology for orientation tomography

Although we have previously performed our spectroscopic orientation analysis approach in a variety of nanoparticle systems, the methodology required an assumption on the out-of-plane orientation for collections of nanoparticles. This made it impossible to perform 3D orientation tomography in complex LC structures and limited the applicability of the shearmetry technique. The first main objective of this thesis is therefore to develop the spectroscopic orientation measurements to be applicable to nanoparticle assemblies with arbitrary orientation. We also found that subtle changes in the reference spectra could significantly impact the results of the orientation analysis. We should therefor develop a way to evaluate the quality of the reference spectra, guaranteeing reproducible results.

Additionally, the confocal micro-spectroscopy setup used for tomographic imaging suffered from a suboptimal spatial resolution and distortions in the polarization of the collected PL emission. Another objective of this thesis was therefore to improve the optical setup and make it possible to perform high resolution tomographic orientation mapping.

Study of evolution of 3D LC structures

We previously discovered the formation of novel streak- and flower-like structures in biphasic LC samples confined between two rigid walls. A first attempt at characterizing their structure was made by the previous PhD student Jeongmo Kim, but due to the limitations in the methodology, this could not correctly reconstruct the 3D orientation. Here, we aim to use the improved methodology to finally characterize the full 3D structure throughout the evolution of the confined LC system.

In order to understand the mechanisms responsible for the formation and stability of these structures, we also attempt to model the free energy of the LC system. In order to create an accurate model, some material specific parameters (like the elastic constants and surface tension) should be known. In this work, we therefore try to first retrieve the material parameters by studying the established structure of nematic tactoids and use the results to model the complex linear-streak and flower structures.

Shearmetry and its application for the characterization of selective ion sweeping

Recently, we found that the nanorod suspensions used for shearmetry exhibit slight shear thinning behavior. Previously, we assumed the suspensions were Newtonian when performing the calibration experiments linking the shear rate to the orientation factor. To improve the accuracy of our technique, we should develop a calibration protocol incorporating the rheological properties of the suspensions.

Here, we apply the developed shearmetry technique to investigate the role of flow shear on the sweeping of ions in the EDL of a capacitive electrode for the application of kinetic energy harvesting. However, in order to be able to perform the shear measurements, we first had to redesign the previously demonstrated kinetic energy harvesting device to be compatible with the optical microscopy setup. To do so, we aim to reproduce the selective ion sweeping effect in microfluidic channels with incorporated electrodes. Additionally, we wanted to explore the possibility of selective ion sweeping in a system with two capacitive electrodes by designing the channel in such a way that only one of them is experiencing strong flow shear. The final two goals of this project were therefore to 1) development of a microfluidic selective ion sweeping device and 2) perform shear measurements close to the electrode interface.

Chapter 2 provides the methodology of 3D orientation measurements based on polarization resolved spectroscopy of lanthanides. A thorough overview of our previous work on the characterization of the orientation of europium doped nanoparticles is given. The initial experimental setup for polarization resolved confocal microscopy is discussed to outline the challenges to overcome. The further development of this setup and its final achieved performance are detailed. The PL of the two phases of $LaPO_4:Eu^{3+}$ and the procedure for obtaining the reference spectra from highly aligned samples is discussed. The theoretical methodology and associated limitations for orientation measurements are detailed. Different spectral analysis methods, based on spectral fitting and ratiometry, are compared. Orientation tomography is demonstrated in LC structures and for flowing suspension in microfluidic channels.

Chapter 3 focusses on the 3D tomography in LC assemblies. A background on the physics of (colloidal) liquid crystals and topological defects is given. The LC behavior and variety of observed structures of the colloidal $LaPO_4$ suspensions are detailed. PLM studies of nematic tactoids are performed to characterize the balance between the elastic and interfacial energies of the colloidal LC. Then, the polarized luminescence-based methodology is used to tomographically reconstruct the 3D structures of the nematic domains and the isotropic-nematic interface. Using the demonstrated techniques, the morphogenesis of the confined biphasic LC from typical tactoid into the unexpected streak- and flower-like structures is studied. Combining the observations with theoretical LC defect theories, a formation mechanism resulting in the flower structure is proposed.

Chapter 4 explores the role of shear stresses on selective ion sweeping for kinetic energy harvesting applications. The theoretical background for *in situ* shearmetry and improved methodology including the rheological properties of the nanorod suspension is discussed. The state-of-the art of flow based kinetic energy harvesting is discussed. The concept of selective ion-sweeping and the approach for miniaturizing the system are outlined. The design of microfluidic channels exhibiting large anisotropy in shear stresses is performed using numerical models and validated using the nanorod shear probes. Electrochemical characterization is performed both in fabricated microfluidic devices and in a beaker cell with macroscopic electrodes.

2 Three-dimensional orientation tomography of lanthanide doped nanocrystals through polarization-resolved micro-spectroscopy

2.1 Introduction on experimental methodology for orientation analysis

In this section, an overview of the previous work of our group regarding the orientation analysis of different types of europium doped nanorods will be given, so that it can serve as a reference point for the work completed as part of this thesis. Additionally, the experimental setup for polarization resolved micro-spectroscopy and its performance before the start of the PhD will be discussed.

2.1.1 Previous work on orientation analysis of europium doped nanorods

During his PhD, Jeongmo Kim used $NaYF_4$:Eu nanocrystals to demonstrate that their polarized PL can be used to retrieve the 3D orientation of a single nanoparticle[10,26]. $NaYF_4$ is a common host material for lanthanide doping and is widely studied for its application in nano-thermometry and as an up-conversion probe[51–53]. Additionally, it can be synthesized to be a micrometer in length, which is an order of magnitude larger than the $LaPO_4$ nanocrystals. This allows the rods to be visible by the optical microscope, enabling a direct evaluation of the accuracy of orientation obtained through spectral analysis.

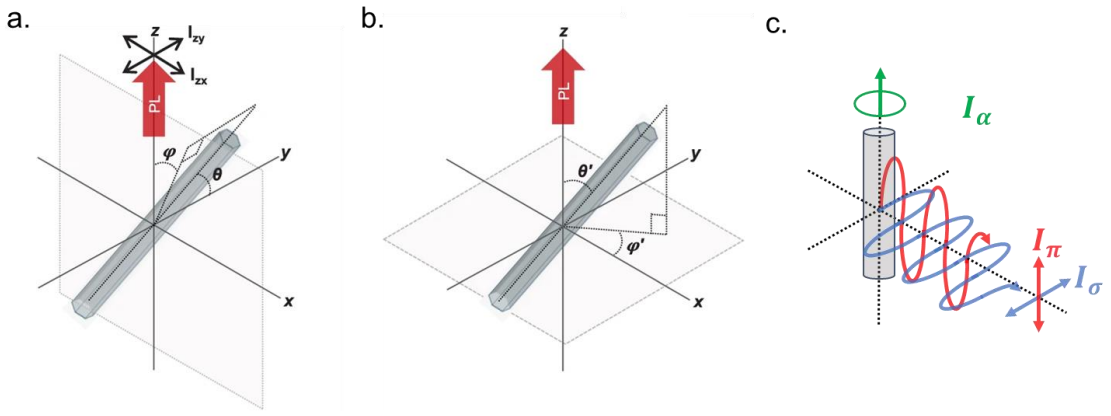

Figure 2.1 Illustration of the orientation of a single nanorod in different coordinate systems, such that (θ, ϕ) and (θ', ϕ') represent the polar and azimuthal angle with respect to the **a)** y-axis and **b)** z-axis respectively. The PL propagates along the z-axis and I_{zy} and I_{zx} are the spectra collected with the analyzer parallel to the y- and x-axis respectively. Figures from J-M. Kim et al. (2021)[26]. **c)** Schematic illustration of the two radial emission components I_π (polarized parallel to the rod axis), I_σ (polarized perpendicular to the rod axis) and the isotropic axial emission I_α.

For a single nanorod, the emission spectra measured at orthogonal polarizer axes can be expressed as a projection of the reference spectra onto the polarizer axis such that:

$$I_{zx}(\lambda) = I_{\pi}(\lambda) \cdot \sin^2\theta \cdot \sin^2\phi + I_{\sigma}(\lambda) \cdot \cos^2\theta + I_{\alpha}(\lambda) \cdot \sin^2\theta \cdot \cos^2\phi \quad \textbf{2.1}$$

$$I_{zy}(\lambda) = I_{\pi}(\lambda) \cdot \cos^2\theta + I_{\sigma}(\lambda) \cdot \sin^2\theta \cdot \sin^2\phi + I_{\alpha}(\lambda) \cdot \sin^2\theta \cdot \cos^2\phi \quad \textbf{2.2}$$

where I_{zx} and I_{zy} are the emission spectra measured with the analyzer parallel to the x and y-axis respectively and θ, ϕ are the polar and azimuthal angles with respect to the y-axis, as illustrated in **Figure** 2.1**a**. Moreover, we can use the relationships of I_{π}, I_{σ} and I_{α} (**Figure 2.1c**),

$$I_{\alpha,MD}(\lambda) = I_{\pi,MD}(\lambda) \quad \textbf{2.3}$$

$$I_{\alpha,ED}(\lambda) = I_{\sigma,ED}(\lambda) \quad \textbf{2.4}$$

to rewrite **equations 2.1**-**2.2** for a MD transition

$$I_{zx,MD}(\lambda) = I_{\pi,MD}(\lambda) \cdot \sin^2\theta + I_{\sigma,MD}(\lambda) \cdot \cos^2\theta \quad \textbf{2.5}$$

$$I_{zy,MD}(\lambda) = I_{\pi,MD}(\lambda) \cdot (\cos^2\theta \cdot \sin^2\phi + \cos^2\phi) + I_{\sigma,MD}(\lambda) \cdot \sin^2\theta \cdot \sin^2\phi \quad \textbf{2.6}$$

and for an ED transition,

$$I_{zx,ED}(\lambda) = I_{\pi,ED}(\lambda) \cdot \sin^2\theta \cdot \sin^2\phi + I_{\sigma,ED}(\lambda) \cdot (\cos^2\theta \cdot \sin^2\phi + \cos^2\phi) \quad \textbf{2.7}$$

$$I_{zy,ED}(\lambda) = I_{\pi,ED}(\lambda) \cdot \cos^2\theta + I_{\sigma,ED}(\lambda) \cdot \sin^2\theta \quad \textbf{2.8}$$

The choice of the coordinate system (θ, ϕ) generates expressions of $I_{zx,MD}$ and $I_{zy,ED}$ which only depend on a single angle (θ), which is useful for the orientation analysis. The reference I_{π} and I_{σ} spectra can be obtained from a highly aligned sample, in this case by aligning a colloidal suspension in an electric field, and are shown in **Figure 1.10c**. Using the previous equations and the reference, the 3D orientation of the nanocrystal can be found by two approaches; spectral fitting or area under the curve (AUC) ratiometry. The first method retrieves the values of $\cos^2\theta$ and $\sin^2\phi$ by performing a curve fit on the measured spectrum using the I_{π} and I_{σ} as inputs. First, $\cos^2\theta$ is found evaluating either $I_{zx,MD}$ or $I_{zy,ED}$ (**equations 2.5**,**2.8**), as those spectra are independent on the ϕ angle. Using the found $\cos^2\theta$, spectral fitting of $I_{zx,ED}$ or $I_{zy,MD}$ is then performed to find $\sin^2\phi$. **Figure 2.2** shows an example of the spectral fitting of a single nanorod using either the I_{zx} or I_{zy} spectrum.

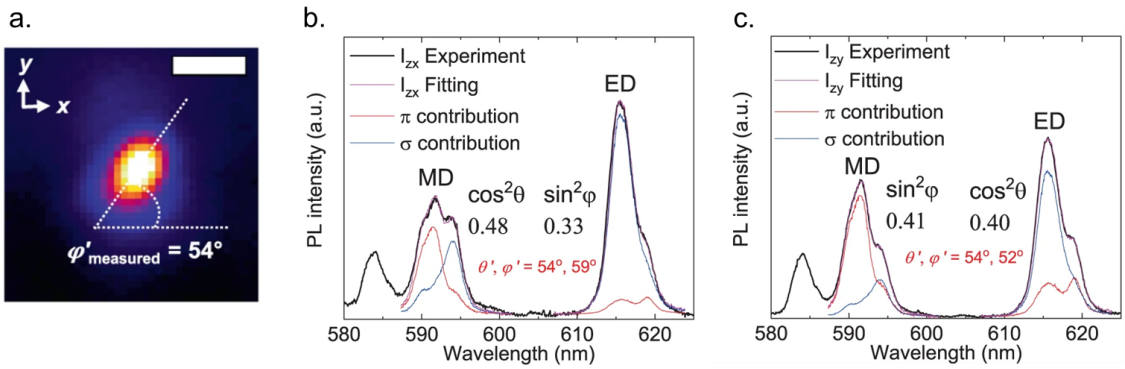

Figure 2.2 a) Image of the PL intensity of a single $NaYF_4$:Eu nanorod used to measure its azimuthal orientation. Scale bar is 1µm. **b-c)** Spectral fitting is performed to find $\cos^2\theta$ and $\sin^2\phi$ using the **b)** I_{zx} and **c)** I_{zy} spectra. Figures from J-M. Kim *et al.* (2021)[26].

In the second approach, instead of using the full spectra as the reference, the integrated intensity for each subpeak of I_π and I_σ (illustrated in **Figure 2.3**) are used as reference values. To find the orientation of an unknown nanorod, we use the ratio between the AUC of two subpeaks for each transition, such that $k = \frac{I_{D1}}{I_{D2}}$ where D1 and D2 refer to two peaks from the same dipole transition. Using the reference values and definitions for k allows to directly formulate an expression for $\cos^2\theta$ and $\sin^2\phi$, for a MD transition,

$$\cos^2\theta = \frac{k_{zx,MD}\cdot I_{\pi,MD2} - I_{\pi,MD1}}{k_{zx,MD}\cdot\left(I_{\pi,MD2} - I_{\sigma,MD2}\right) - \left(I_{\pi,MD1} - I_{\sigma,MD1}\right)} \quad \textbf{2.9}$$

$$\sin^2\phi = \frac{k_{zy,MD}\cdot I_{\pi,MD2} - I_{\pi,MD1}}{(1-\cos^2\theta)\cdot\left(\left(I_{\sigma,MD1} - I_{\pi,MD1}\right) - k_{zy,MD}\cdot\left(I_{\sigma,MD2} - I_{\pi,MD2}\right)\right)} \quad \textbf{2.10}$$

and for an ED transition,

$$\cos^2\theta = \frac{k_{zy,ED}\cdot I_{\sigma,ED2} - I_{\sigma,ED1}}{k_{zy,ED}\cdot\left(I_{\sigma,ED2} - I_{\pi,ED2}\right) - \left(I_{\sigma,ED1} - I_{\pi,ED1}\right)} \quad \textbf{2.11}$$

$$\sin^2\phi = \frac{k_{zx,ED}\cdot I_{\sigma,ED2} - I_{\sigma,ED1}}{(1-\cos^2\theta)\cdot\left(\left(I_{\pi,ED1} - I_{\sigma,ED1}\right) - k_{zx,ED}\cdot\left(I_{\pi,ED2} - I_{\sigma,ED2}\right)\right)} \quad \textbf{2.12}$$

where $k_{zx,D} = \frac{I_{zx,D1}}{I_{zx,D2}}$ and $k_{zy,D} = \frac{I_{zy,D1}}{I_{zy,D2}}$ (with $D = MD\ or\ ED$). By picking two subpeaks which have opposite polarization behavior, the sensitivity to the orientation is enhanced as the DOPs of k are higher than those of the individual peaks. Moreover, considering the relative intensity makes the measurement independent on global intensity fluctuations. **Figure 2.3** shows $\cos^2\theta$ and $\sin^2\phi$ as calculated by the AUC ratiometry approach for the same particle as **Figure 2.2a**.

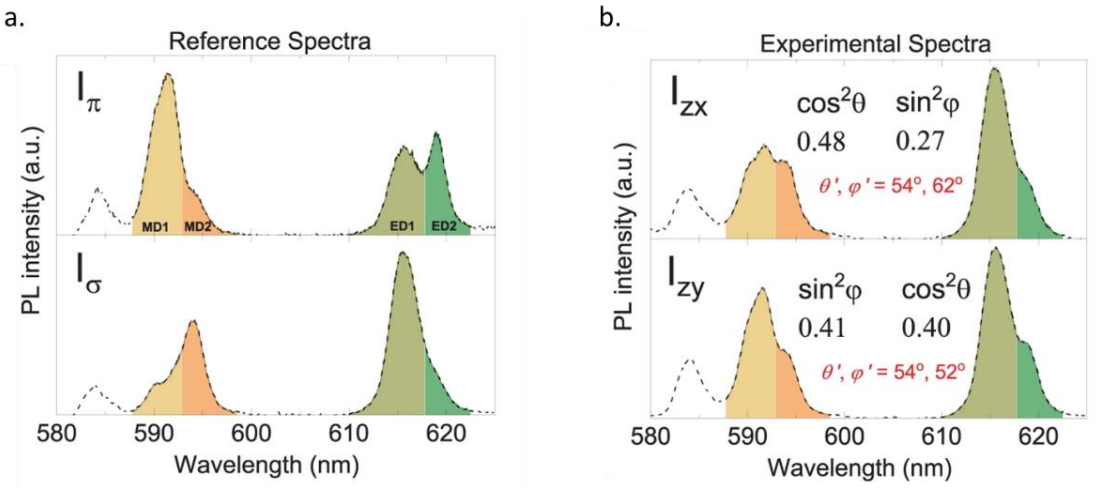

Figure 2.3 Orientation analysis based on area under the curve (AUC) ratiometry. Each colored region corresponds to the AUC under a single subpeak. **a)** Reference spectra I_π and I_σ. **b)** Measured I_{zx} and I_{zy} spectra for the nanorod shown in **Figure 2.2a** and the values of $cos^2\,\theta$ and $sin^2\,\phi$ calculated using **equations 2.9-2.12**. Figures from J-M. Kim *et al.* (2021)[26].

Using either the spectral fitting or AUC ratiometry approach, the values of $\cos^2\theta$ and $\sin^2\phi$ of the particle can therefore be determined by evaluation of a single spectrum, considering both an ED and MD transition. To convert to a more intuitive coordinate system which describes the polar and azimuthal angle with respect to the observation plane (θ', ϕ'), the following transformations can be used

$$\theta' = \cos^{-1}(\sin\theta \cdot \cos\phi) \qquad \textbf{2.13}$$

$$\phi' = \sin^{-1}\left(\frac{\cos\theta}{\sqrt{1-\sin^2\theta\cdot\cos^2\phi}}\right) \qquad \textbf{2.14}$$

Due to the dependency on the trigonometric functions, θ' and ϕ' are indistinguishable from $-\theta'$ and $-\phi'$. Discrimination of the mirror angle of θ' would require a measurement from another viewing angle, requiring a much more complex optical setup and was therefore not explored. However, the mirror angle of ϕ' can be eliminated by collecting the PL spectrum for a third analyzer axis. A measurement with the analyzer in between the x- and y-axis ($I_{z45°}$) was therefore used. The k-values of each measurement (k_{zx},k_{zy} and $k_{z45°}$) are compared to the reference (k_π and k_σ) to find the sign of ϕ'. A thorough discussion of the evaluation of the mirror angle is covered in **section 2.4.3**.

To evaluate the accuracy of the approach, the found azimuthal angle is compared by the one measured using the PL intensity image (**Figure 2.2a**). Considering more than 30 measurements of randomly oriented, isolated rods, the absolute error on ϕ' was found to be 4.6° using the spectral fitting approach and 4.8° using AUC ratiometry. The absolute error on θ' could not be determined, as there is no way to verify it using the PL intensity image. The spectral fitting approach provides more consistent results when comparing the results for I_{zx} and I_{zy} or when using either ED or MD dipoles only. The best accuracy is

therefore expected with the spectral fitting approach. However, the advantage of considering only AUC values is that the experiment can be performed without a spectrometer by directly measuring the intensity of each subpeak using bandpass filters and a detector.

Order parameter in an assembly of vertically aligned rods

Using the same type of $NaYF_4$:Eu nanorods, Jeongmo Kim also developed a methodology for measuring the order parameter in an assembly of vertically aligned rods[10,36]. For a collection of particles, its orientation is expressed by the average orientation, the director $\vec{n}$, and the order parameter S. The order parameter describes the local degree of orientation and is 1 when all particles are perfectly aligned along $\vec{n}$ and is 0 when there is no collective orientation at all. The order parameter of the assembly is defined by the angle between individual rods and $\vec{n}$, called θ_s, such that

$$S = \frac{3 \cdot \langle \cos^2 \theta_s \rangle - 1}{2} \qquad \textbf{2.15}$$

where $\langle \cos^2 \theta_s \rangle$ describes the average over many rods. In the case where $\vec{n}$ is defined as perpendicular to the surface the ensemble is said to be homeotropic. The associated homeotropic order parameter S_{homeo} varies from -1/2 (degenerate planar alignment) to 1 (perfect homeotropic alignment), as illustrated in **Figure 2.4**.

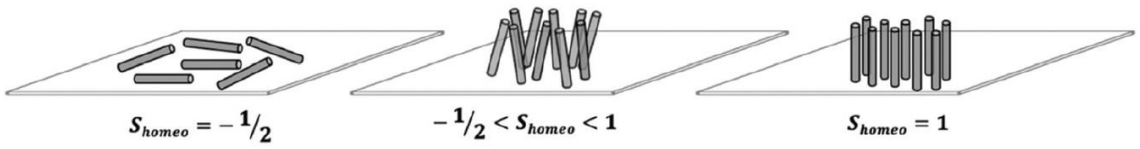

Figure 2.4 Schematic illustration of collections of nanorods with different homeotropic order parameter S_{homeo}. Figure from J-M. Kim *et al.* (2021)[36].

In this case, it makes sense to define the previous expressions for the PL measurements in terms of the orientation with respect to the observation plane normal, θ', ϕ' as defined in **Figure 2.1b**, such that for a single particle

$$I_{zx}(\lambda) = I_\pi(\lambda) \cdot \sin^2 \theta' \cdot \cos^2 \phi' + I_\sigma(\lambda) \cdot \sin^2 \theta' \cdot \sin^2 \phi' + I_\alpha(\lambda) \cdot \cos^2 \theta' \qquad \textbf{2.16}$$

$$I_{zy}(\lambda) = I_\pi(\lambda) \cdot \sin^2 \theta' \cdot \sin^2 \phi' + I_\sigma(\lambda) \cdot \sin^2 \theta' \cdot \cos^2 \phi' + I_\alpha(\lambda) \cdot \cos^2 \theta' \qquad \textbf{2.17}$$

The sum of the two orthogonal polarizations I_{zx} and I_{zy} corresponds to the PL collected without the presence of any analyzer I_z and can be expressed as

$$I_z(\lambda) = I_{zx}(\lambda) + I_{zy}(\lambda) = \big(I_\pi(\lambda) + I_\sigma(\lambda)\big) \cdot \sin^2 \theta' + 2 \cdot I_\alpha(\lambda) \cdot \cos^2 \theta' \qquad \textbf{2.18}$$

By summing the two spectra together, we eliminate the ϕ' dependency, and are left with a single unknown value, namely θ'. When dealing with an ensemble of nanorods instead of a single one, the same

equations apply but we need to consider the average orientation of all particles within the focal volume during the time of the measurement. **Equation 2.18** can thus be adapted by replacing $\cos^2\theta'$ with $\langle\cos^2\theta'\rangle$. Combining **equations 2.18 and 2.15** therefor allows to express I_z in terms of S_{homeo} such that

$$\frac{3}{2}I_z(\lambda) = (1 - S_{homeo}) \cdot I_{\pi+\sigma}(\lambda) + (1 + 2 \cdot S_{homeo}) \cdot I_\alpha(\lambda) \qquad \textbf{2.19}$$

Where $I_{\pi+\sigma}(\lambda)$ is the sum of the reference spectra $I_\pi(\lambda)$ and $I_\sigma(\lambda)$. S_{homeo} can therefore be determined by collecting a single PL measurement without any analyzer and applying a spectral fit using the reference spectra and **equation 2.19**.

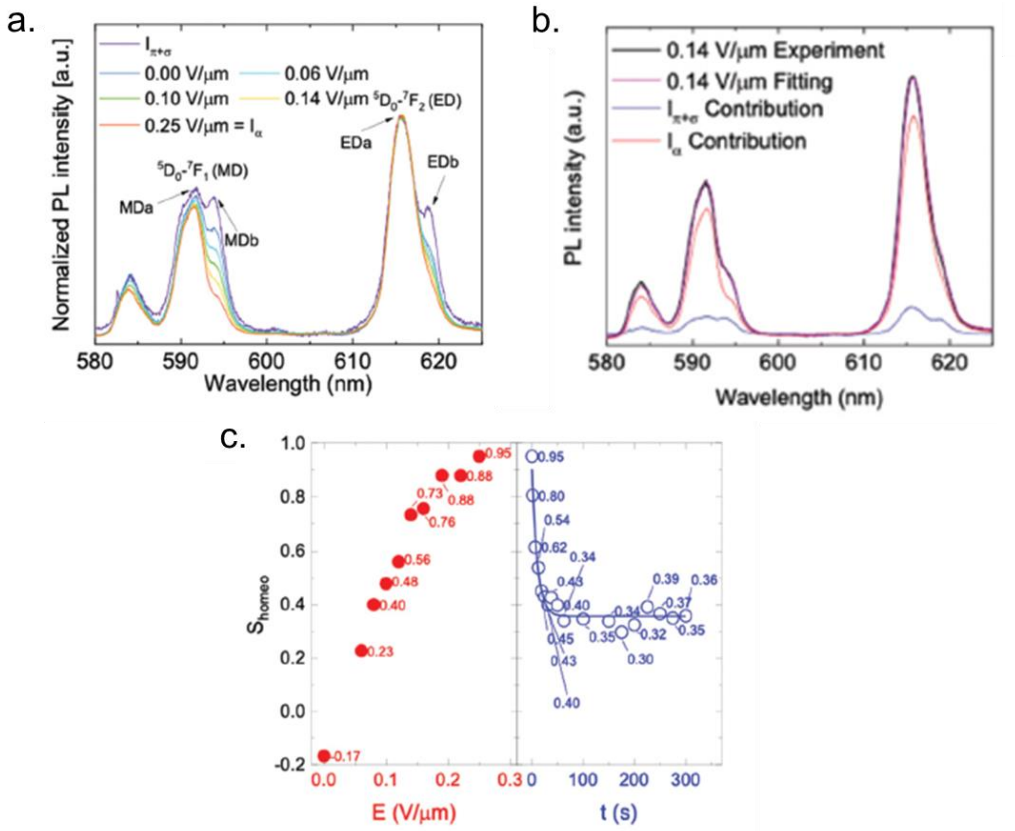

Figure 2.5 Measurements of S_{homeo} for different electric field strengths. **a)** Measured emission spectra I_z for electric field strength from 0-0.25 V/µm. The purple spectrum corresponds to $I_{\pi+\sigma}$. **b)** Example of the spectral fitting to find S_{homeo}. **c)** Plot of the calculated S_{homeo} against the electric field strength (red) and the relaxation time (blue) after turning off the field once the alignment saturated. Figures from J-M. Kim *et al.* (2021)[36].

To demonstrate this approach, colloidal suspensions of $NaYF_4$:Eu nanorods were aligned using an electric field. **Figure 2.5a** shows the measured emission I_z for different electric field strengths. The value of S_{homeo} is found for each measurement by spectral fitting of the weighted sums of $I_{\pi+\sigma}$ and I_α, as illustrated in **Figure 2.5b**. As the electric field gets stronger, S_{homeo} increases and I_z becomes closer to I_α (**Figure 2.5c**). Once the field is turned off, the nanorod suspension relaxes back to a random orientation

distribution due to diffusion. This approach successfully demonstrates the observation of orientation dynamics, which play an important role in self-assemblies. Moreover, as this approach does not require polarized measurements, it can be easily performed using standard fluorescence microscopy.

Orientation of an ensemble with unknown planar director

The first demonstration of orientation measurements of an ensemble of nanoparticles was done in a microfluidic system, where the nanoparticles collectively align due to the hydrodynamic shear forces (as discussed in **chapter 1.3**)[12,37]. Whereas the previous system was defined by a homeotropic $\vec{n}$, in this case $\vec{n}$ is assumed to be fully planar. This implies that $\theta' = 90°$ and means that ϕ is equivalent to ϕ' (based on the definition in **Figure 2.1**). Of course, this assumption is only applicable considering the middle xy-plane of the microfluidic channel due to the symmetry of the vertical shear profile. In **chapter 2.4.5** a methodology for $\theta' \neq 90°$ will be developed.

Under the planar assumption, both S and the azimuthal angle of the director ϕ are unknown and can be found using the PL. In principle, this could be done by a spectral fitting or AUC ratiometry as was demonstrated for the single nanocrystal and vertically aligned assemblies. However, when the initial demonstration of the technique was done, it was not yet possible to automatically collect the emission spectra in a tomographic manner. Instead, the emission associated to the MD and ED transitions were separated using bandpass filters and individually collected on detectors. All the analysis was thus done based on the total integrated intensity of the two transitions.

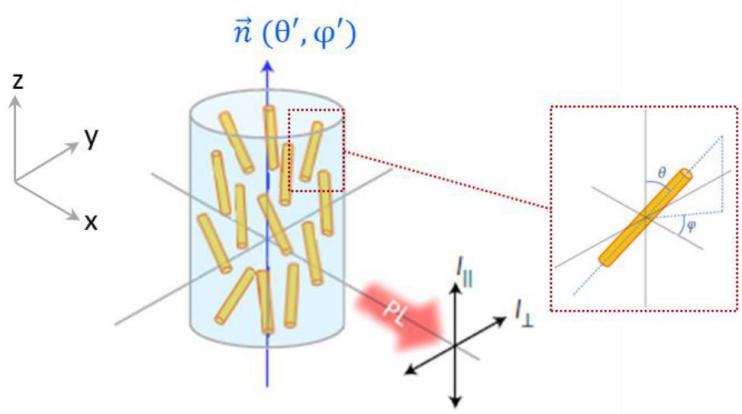

Figure 2.6 Schematic illustration of the orientation of the director and the orientation of a single nanorod in the ensemble which has polar and azimuthal angles (θ_s, ϕ_s) with respect to $\vec{n}$. Figure from the PhD thesis of Elodie Chaudan[37].

We first need to adapt the previous equations to express the PL of a collection of rods with an unknown director $\vec{n}$. In this case, the spectra polarized parallel and perpendicular to the director $\vec{n}$ are averages of all the contributions from different nanorods, each of which has an orientation with respect to the director (θ_s, ϕ_s) as illustrated in **Figure 2.6**:

$$I_{\parallel} = \langle I_{\pi} \cdot \cos^2\theta_s + I_{\sigma} \cdot \sin^2\theta_s \cdot \sin^2\phi_s + I_{\alpha} \cdot \sin^2\theta_s \cdot \cos^2\phi_s \rangle \quad \textbf{2.20}$$

$$I_{\perp} = \langle I_{\pi} \cdot \sin^2\theta_s \cdot \sin^2\phi_s + I_{\sigma} \cdot \cos^2\theta_s + I_{\alpha} \cdot \sin^2\theta_s \cdot \cos^2\phi_s \rangle \quad \textbf{2.21}$$

Where $\langle \ \ \rangle$ indicates the average over many nanorods. Using **equations 2.3**-**2.4** and considering cylindrical symmetry such that $\langle \cos^2\phi_s \rangle = \langle \sin^2\phi_s \rangle = \frac{1}{2}$:

For MD transitions,

$$I_{\parallel,MD} = \frac{I_{\pi,MD}}{2} \cdot (1 + \langle \cos^2\theta_s \rangle) + \frac{I_{\sigma,MD}}{2} \cdot (1 - \langle \cos^2\theta_s \rangle) \quad \textbf{2.22}$$

$$I_{\perp,MD} = I_{\pi,MD} \cdot (1 - \langle \cos^2\theta_s \rangle) \ + I_{\sigma,MD} \cdot \langle \cos^2\theta_s \rangle \quad \textbf{2.23}$$

For ED transitions,

$$I_{\parallel,ED} = I_{\pi,ED} \cdot \langle \cos^2\theta_s \rangle + I_{\sigma,ED} \cdot (1 - \langle \cos^2\theta_s \rangle) \quad \textbf{2.24}$$

$$I_{\perp,ED} = \frac{I_{\pi,ED}}{2} \cdot (1 - \langle \cos^2\theta_s \rangle) + \frac{I_{\sigma,ED}}{2} \cdot (1 + \langle \cos^2\theta_s \rangle) \quad \textbf{2.25}$$

To express the measured PL for a given polarizer axis, we adapt the equations previously described for a single nanorod, but replace I_{π} with $I_{\parallel}$ and I_{σ} with $I_{\perp}$ respectively. Using the assumption that the director is perfectly in-plane (meaning $\theta' = 90°$), the emission measured can be expressed as contributions of the projections of $I_{\parallel}$ and $I_{\perp}$ onto the measurement axis such that for both MD and ED transitions:

$$I_{zx} = I_{\parallel} \cdot \cos^2\phi' + \ I_{\perp} \cdot \sin^2\phi' \quad \textbf{2.26}$$

$$I_{zx} = I_{\parallel} \cdot \sin^2\phi' + \ I_{\perp} \cdot \cos^2\phi' \quad \textbf{2.27}$$

$$I_{z45°} = \frac{I_{\parallel} + I_{\perp}}{2} + \sin 2\phi' \cdot \frac{I_{\parallel} - I_{\perp}}{2} \quad \textbf{2.28}$$

I_{z45} can therefore be expressed in terms of I_{zx}, I_{zy} such that:

$$\tan 2\theta' = \frac{2I_{z45} - I_{zx} - I_{zy}}{I_{zx} - I_{zy}} \quad \textbf{2.29}$$

Considering that the domain of ϕ' is $\left[-\frac{\pi}{2}, \frac{\pi}{2}\right]$, we can formulate the following solution

$$\phi' = \frac{1}{2}\left(\tan^{-1}\Sigma - \frac{\pi}{2} \cdot \frac{\Sigma}{|\Sigma|} \cdot \left(\frac{\Gamma}{|\Gamma|} + 1\right)\right) \quad \textbf{2.30}$$

Where,

$$\Sigma = \frac{2 \cdot I_{z45} - I_{zx} - I_{zy}}{I_{zx} - I_{zy}}\ , \qquad \Gamma = I_{zx} - I_{zy}$$

Evaluating the total PL intensity for the three polarizer angles therefore allows to solve for ϕ'. To demonstrate the technique, a suspension of $LaPO_4$:Eu nanorods is flowed through a microfluidic channel

with a hemicylindrical constriction. **Figure 2.7a** shows the total intensity at the middle height in such a channel measured at I_{zx}, I_{z45} and I_{zy} respectively. Using these intensity values and **equation 2.30**, ϕ' was calculated and is represented by the arrows in **Figure 2.7b**. Using the found ϕ' value, the expressions for I_{zx} and I_{zy} (**equations 2.26**-**2.27**) were then used to find $I_{\parallel}$ and $I_{\perp}$. Finally, the values of $\langle \cos^2 \theta_s \rangle$ and S were determined using the more strongly polarized MD transition and the expressions for $I_{\parallel,MD}$ and $I_{\perp,MD}$ (**equations 2.22**-**2.24**). This resulted in the order parameter map seen in **Figure 2.7b**.

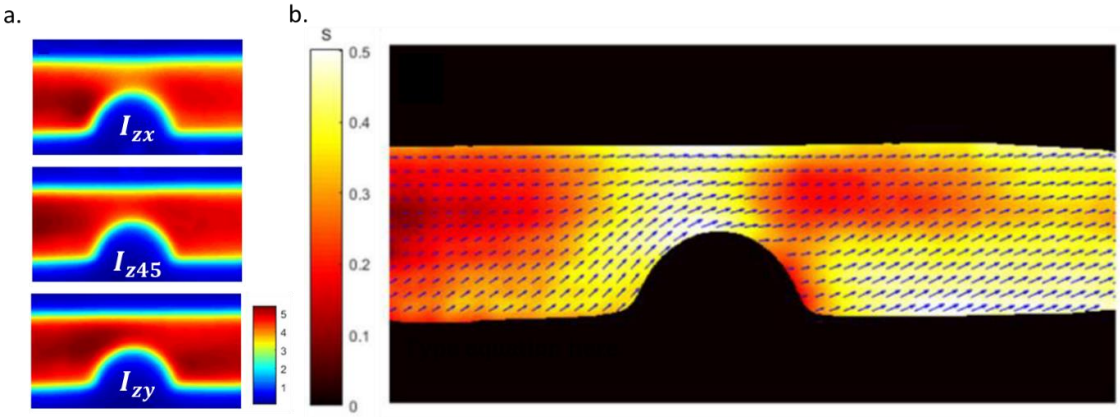

Figure 2.7 a) PL intensity maps of the MD transition selected using bandpass filters, for three different analyzer angles. **b)** Calculated profile of S. The calculated $\vec{n}$ is represented by the orientation and S by the size of the arrows. Figures from PhD thesis of Elodie Chaudan[37].

As discussed in **chapter 1.3**, the shear rate $\dot{\gamma}$ can be retrieved from the map of S using the stress-optical law. This initial demonstration of shear tomography was the start of a whole new research direction in our group. We explore the shearmetry technique to study both biological and electrochemical systems and continuously improve both the nanoprobe suspension, experimental configuration and theoretical methodology. At the start of my PhD, shear tomography had been realized using AUC ratiometry of collected spectra (by using bandpass filters). A technical goal of my PhD was therefore set to develop the experimental and computational methodologies based on spectral fitting, also considering a more general case of non-planar $\vec{n}$.

Orientation of an ensemble with fully unknown director

The previous orientation analysis demonstrated for collections of nanorods relied on the assumption that $\vec{n}$ was either homeotropic or planar, leaving only one degree of freedom. However, in complex systems, such as the liquid crystalline flower structure discussed in **chapter 1.1.1**, this is not appropriate. Without making any assumptions on either the orientation of $\vec{n}$ or the value of S, the following expressions were formulated for the measured PL[12],

$$I_{zx}(\lambda) = I_{\parallel}(\lambda) \cdot \sin^2 \theta' \cdot \sin^2 \phi' + I_{\perp}(\lambda) \cdot (\cos^2 \theta' \cdot \sin^2 \phi' + \cos^2 \phi') \qquad \textbf{2.31}$$

$$I_{zy}(\lambda) = I_{\parallel}(\lambda) \cdot \cos^2\theta' + I_{\perp}(\lambda) \cdot \sin^2\theta' \qquad \textbf{2.32}$$

However, it was incorrectly assumed that these equations were applicable to both MD and ED transitions. In reality, we need separate expressions for the MD and ED transitions, similar to the single particle equations. **Equations 2.31**-**2.32** are only accurate for ED transitions or when $\vec{n}$ is planar.

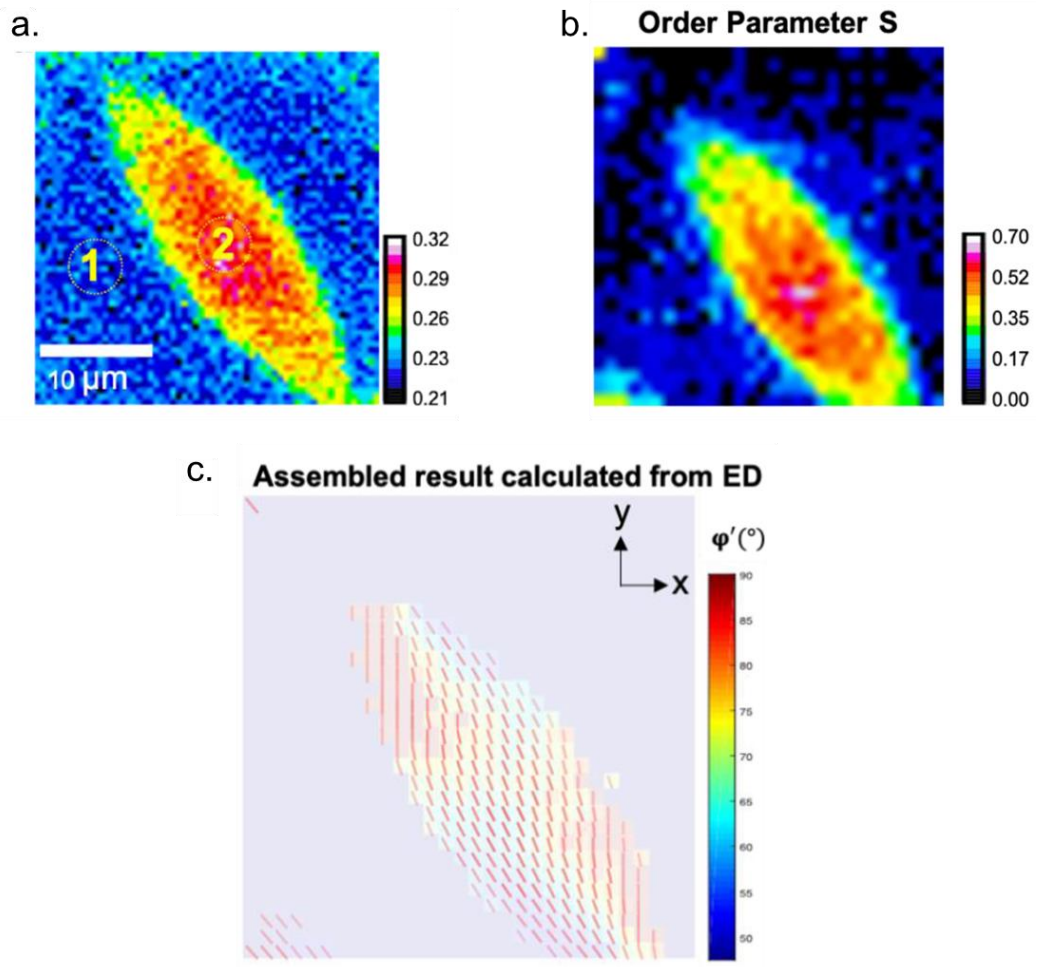

Figure 2.8 Orientation tomography in a nematic tactoid. **a)** PL Intensity **b)** order parameter S **c)** director $\vec{n}$ indicated by the red arrows and ϕ'indicated by color. Figures from PhD thesis of Jeongmo Kim[10].

Nonetheless, a first demonstration of the orientation analysis was made in a liquid crystal (LC) assembly of $LaPO_4$:Eu nanorods[10]. In such a LC, domains of collective alignment appear spontaneously when the volume fraction is high enough[2]. An example of this is the formation of highly aligned, rugby ball shaped droplets called *tactoids*. Due to the increased nanorod density in the aligned domain, such tactoids can be clearly observed by mapping the PL intensity (**Figure 2.8a**). As $\vec{n}$ is expected to be close to planar near the center plane of the tactoid, the orientation could be correctly reconstructed. **Figure 2.8b-c** shows the resulting S and $\vec{n}(\theta', \phi')$ as calculated by AUC ratiometry. The order parameter is highest near the center

of the tactoid and the director profile follows the contours of the droplet, which is consistent with previous reports[54,55].

However, as $\vec{n}$ is expected to follow the 3D interface of the tactoid, it is not planar throughout. Moreover, initial experiments suggest that the streak and flower like structures (discussed in **chapter 1.1.1**) exhibit a mostly homeotropic $\vec{n}$. This means that the methodology at its current state, based on **equations 2.31**-**2.32**, cannot be used to successfully reconstruct the 3D orientation in such LC systems. A major objective of my thesis was therefore to develop the appropriate equations and methodology to address 3D orientation in systems with a fully unknown $\vec{n}$.

2.1.2 Polarization resolved confocal fluorescence microscopy

The previously discussed orientation measurements of single particles as well as the tomographic orientation mapping were achieved through polarization resolved fluorescence microscopy. Although the above-demonstrated methodologies were originally developed by our group, the published experimental works on the tomographic imaging were achieved by using scanning confocal microscopes owned by collaborator groups. This was because, at the time, the performance of our own confocal setup was not yet adequate. In this section, the state of the optical setup at PMC before the start of my PhD will be discussed in order to identify the challenges to overcome.

Confocal fluorescence microscopy is a widely used technique as it provides non-destructive imaging with high spatial resolution. Although most well-known for its applications in biological research, such as the imaging of (sub)cellular systems and neuronal processes[56–58], it is used across other disciplines. For example, it can be used to study material properties of nano-objects[59,60] and electronic transport phenomena in semiconductors[61,62]. Coupled with lanthanide doped nanoprobes, the technique can be used for tracking 3D orientation dynamics[26], local temperature sensing[51] and shearmetry in microfluidics[12,38].

In a confocal microscope, the lateral resolution is achieved by focusing the excitation laser into a small focal volume and the axial resolution by optical slicing of the emission beam using a pinhole[63]. Images are generated by scanning the excitation laser across the sample, which can be done by moving the sample holding stage (stage scanning) or the beam itself (beam scanning)[63]. However, high resolution tomographic imaging of lanthanides cannot be achieved using commercial/conventional confocal microscopy due to large difference in excitation and emission wavelength (200-300 nm) and long lifetimes (~10^{-3} s) of their luminescence. The resolution, particularly in the axial direction, would be suboptimal as the chromic aberration of the objective causes a difference in focal planes of the excitation and emission. Secondly, the typical built-in mirror scanning mechanism takes less than 50µs for each pixel in the image, which is faster than the lifetime of lanthanide luminescence. Indeed, initial measurements performed in

our group using the commercial confocal microscope equipped with a beam scanning mechanism resulted in a very poor axial resolution (~9 µm) and low signal intensity[37]. This is why the tomographic imaging in the microfluidic channel in **Figure 2.7b** could only be created by averaging over 32 consecutive measurements followed by image smoothing[37]. To address these issues the microscopy setup had to be adapted.

Figure 2.9 shows a schematic overview of the experimental setup before the start of my PhD thesis. The excitation laser (λ_{exc} = 394nm) is collimated by a collimator and slightly defocused using a beam expander to match its focal plane to that of the PL emission (λ_{em} ~500−700 nm). The excitation beam is then reflected to the objective by a dichroic mirror and right-angle prism mirror.

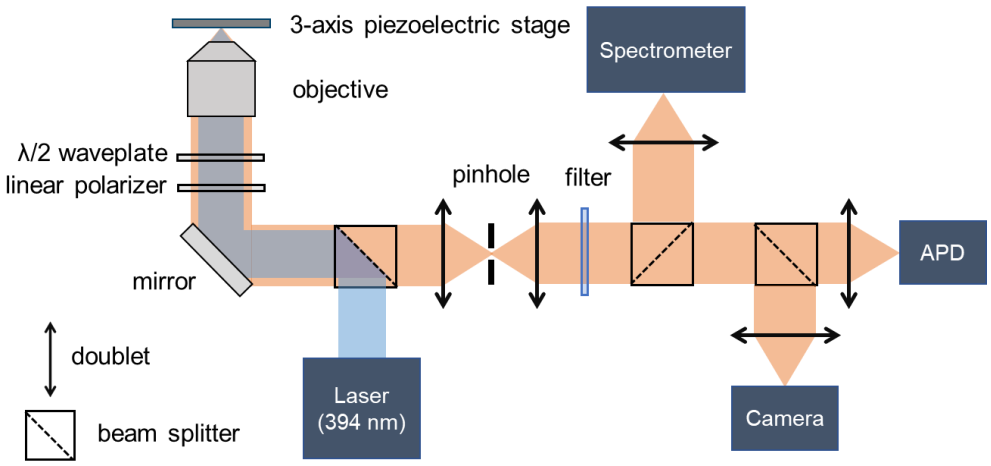

Figure 2.9 Schematic illustration of the confocal microscopy setup in July 2021.

The objective focusses the excitation beam and collects the emission. The polarization state was selected by rotating a λ/2 waveplate in front of a linear polarizer placed between the metal mirror and objective. The emission is reflected by the metal mirror and transmitted through the dichroic mirror and focused onto a pinhole of 15µm. A beam splitter is used such that 50% of the beam is reflected to the spectrometer and the other 50% is transmitted. The linear polarizer is aligned such that the emission beam is always s-polarized which avoids distortion due to the optical anisotropic of the grating of the spectrometer. The transmitted light is again split using a beamsplitter and focused on an avalanche photodiode (APD) for PL intensity measurements and onto a camera to image the pinhole position. Finally, the setup uses a three-axis piezoelectric stage to scan the PL and generate intensity images.

Theoretical versus experimental spatial resolution

The spatial resolution can be defined by the Rayleigh criterion, which states that two focused light spots can be resolved when the principal diffraction maximum of the first spot aligns with the first minimum of the second spot[64]. Based on this, the theoretical resolution can be found using the following expressions[65]:

$$Lateral\ resolution = \frac{0.51\lambda_{exc}}{NA} \quad \textbf{2.33}$$

$$Axial\ resolution = \frac{0.88\lambda_{exc}}{n - \sqrt{n^2 - NA^2}} \quad \textbf{2.34}$$

where λ_{exc} is the excitation wavelength, n is the refractive index of the immersion medium and NA is the numerical aperture of the objective. To optimize the spatial resolution, a large numerical aperture is required. The experimental setup uses a 60x oil immersion objective (n=1.51) with NA=1.49, corresponding to a theoretical lateral resolution of ~0.14 µm and axial resolution of ~0.3 µm. It should be noted that the theoretical resolution is not affected by the pinhole size due to the assumption that the light originates from a single emitter. In reality, the experimental resolution (especially axially) is highly impacted by the size of the pinhole, as this reduces the emission collected from outside the focal volume. The choice of pinhole size should be small enough to guarantee a good axial resolution and large enough to retain most of the luminescence intensity.

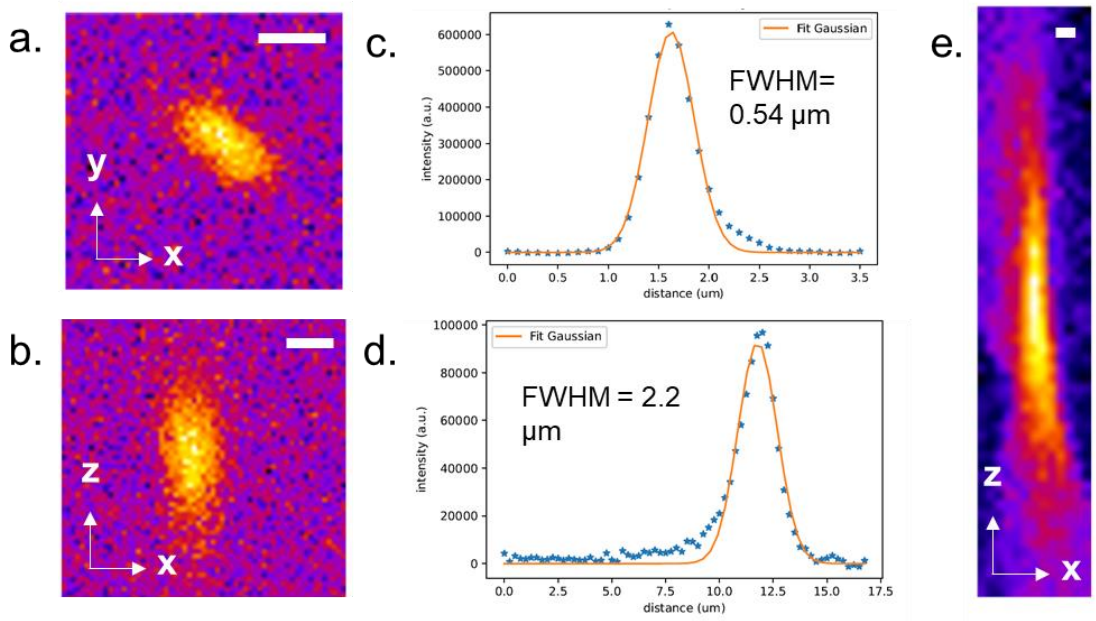

Figure 2.10 Resolution measurements using a single $NaYF_4$:Eu nanocrystal. **a-b)** APD images of the PL intensity using a 15 µm pinhole for the xy and xz plane respectively. **c-d)** corresponding PSFs as scanned across the diameter of the nanorod. **e)** PL intensity collected without the pinhole. Scale bars all 1µm. Figures from M2 internship report.

In order to evaluate the spatial resolution of the confocal microscopy setup, the PL emission of a single $NaYF_4$:Eu nanocrystal is mapped using the piezoelectric stage and APD (**Figure 2.10**). Images of similar nanorods taken and the intensity profile measured across their diameter using both experimental setups are shown in **Figure 2.10a-d**. Assuming that the diameter of the rod is smaller than the resolution, this profile indicates the one-dimensional point spread function (PSF). The resolution can then be

approximated as the full width half maximum (FWHM) found by fitting a Gaussian function[65]. The optimal lateral resolution was found to be ~0.5 µm and the axial resolution ~2.2 µm respectively.

The fact that the axial resolution is more than four times as high as the lateral resolution indicates a poor alignment of the optical setup, as we expect a factor of two difference. In fact, its axial resolution was extremely poor (~14 µm) when the pinhole was removed, as is seen in **Figure 2.10e**. This indicates insufficient correction of the chromatic aberration, causing a significant difference in the position of the focal plane of emission and excitation.

In addition, we observed a large decrease in signal-to-noise ratio when placing the 15 µm pinhole. We also took APD images of the PL intensity using a 300 µm and 50 µm pinhole (see annex **Figure 5.29a-b)**. Placing the 300 µm pinhole does not affect the lateral resolution (with respect to no pinhole inserted), but almost halves the axial resolution to 7.7 µm. For the 50 µm pinhole >80% of the signal intensity is maintained, (see **Figure 5.29c**), and the axial resolution was found similar to that with the 15 µm pinhole (2.2 µm). However, the lateral resolution worsened to 0.9 µm. In practice, the signal intensity was too low with the smallest pinhole to make spectral measurements at a reasonable exposure time for tomographic imaging, so only the 50 µm pinhole could be used for orientation experiments. This meant the final resolution of the optical setup was 0.9 µm by 2.2 µm.

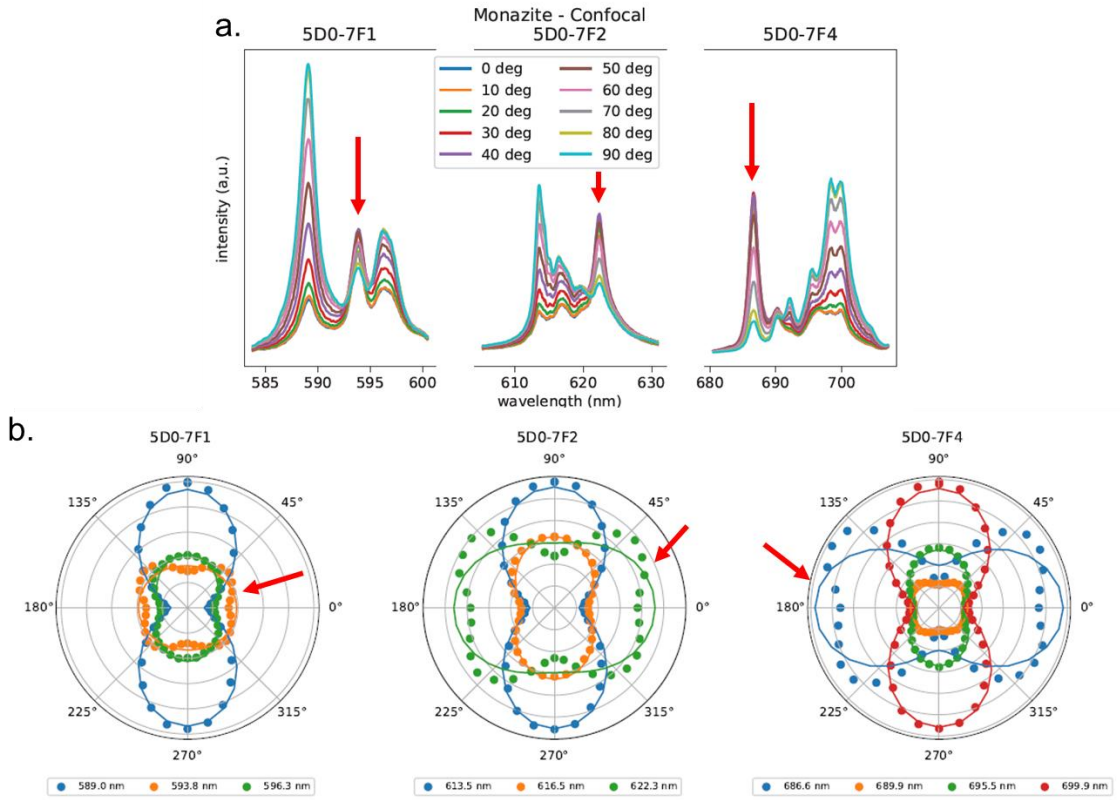

Figure 2.11 a) Polarized emission spectra of monazite phase $LaPO_4$:Eu nanorods collected in a planar nematic LC. **b)** Polar diagrams of the intensity for the main peaks of the emission spectra. Most peaks follow a dipolar model, but peaks indicated with the red arrows display a butterfly-shaped dependency on the analyzer angle.

Polarization

Another challenge in the design of the confocal microscopy setup is the ability to maintain the polarization state throughout the whole optical path of the emission. In the original setup at PMC, the polarization was selected by a linear polarizer right after the microscope objective. Using this configuration, we observed that some of the subpeaks of the monazite PL didn't follow the typical linear polarization model. As illustrated in **Figure 2.11**, the polar diagrams of the emission peaks indicated with the red arrows were butterfly-shaped, instead of the expected dumbbell shape. All peaks displaying this behavior correspond to the π polarization component of the PL.

However, the amount of distortion seemed to strongly depend on the absolute orientation of the nanorods with respect to the laboratory frame. Measurements taken using a regular microscope with low NA objectives also did not produce such butterfly-shaped polar diagrams. This suggests that it is not (purely) caused by the sample itself, but is created/enhanced by the optics of the confocal microscope.

Summary of chapter 2.1

Our group has previously demonstrated orientation measurements of single nanocrystals, as well as ensembles with a homeotropic or planar alignment through spectral analysis of polarized luminescence origination from the Eu^{3+} ion. This can be achieved either by spectral fitting or area under the curve (AUC) ratiometry, utilizing reference spectra obtained in an aligned sample. However, the spectral fitting approach has not been demonstrated in nanorod assemblies and the developed methodologies were not applicable for arbitrary out-of-plane orientations.

Polarization resolved confocal micro- spectroscopy allows us to perform tomographic orientation measurements. However, at the start of my PhD, our optical setup had a suboptimal spatial resolution of 0.9 µm by 2.2 µm and caused distortions in the polarization state of the collected PL emission.

2.2 Polarization resolved confocal micro-spectroscopy

One of the main goals during my PhD was to improve our confocal microscopy setup in order to be able to perform high resolution tomographic orientation measurements. Specifically, the goal was to achieve a submicron axial resolution, retain more than half of the signal intensity when placing the pinhole and to minimize distortion of the polarization state of the emission collected.

2.2.1 Improved confocal microscopy setup

Figure 2.12 shows the final optical configuration used for most measurements shown in this work. The setup was continuously improved over the course of the first 2 years of my PhD, and the main important changes will be detailed here.

The excitation source is a monochromatic laser ($\lambda_{exc} = 394$ nm), which corresponds to the narrow absorption peak of the $^7F_0$-$^5L_6$ transition of Eu^{3+} ions[12]. To improve the quality of the focused beam spot, several modifications were made to the initial configuration of the excitation beam path. First, a dichroic mirror with higher surface flatness was used, which resulted in a more symmetric laser spot with visible diffraction rings. Secondly, we replaced the commercial beam expander by two doublets of different focal lengths (f=5 cm and f=10 cm). The difference in focal lengths was chosen to enlarge the size of the excitation beam such that it more closely matched the size of the large objective aperture (11 mm). Additionally, the first doublet is mounted on an adjustable z-axis mount, which allows to precisely defocus the excitation beam. This defocusing is used to correct the achromatic aberration associated to the large difference in excitation and emission wavelength, as will be discussed in **section 2.2.2**.

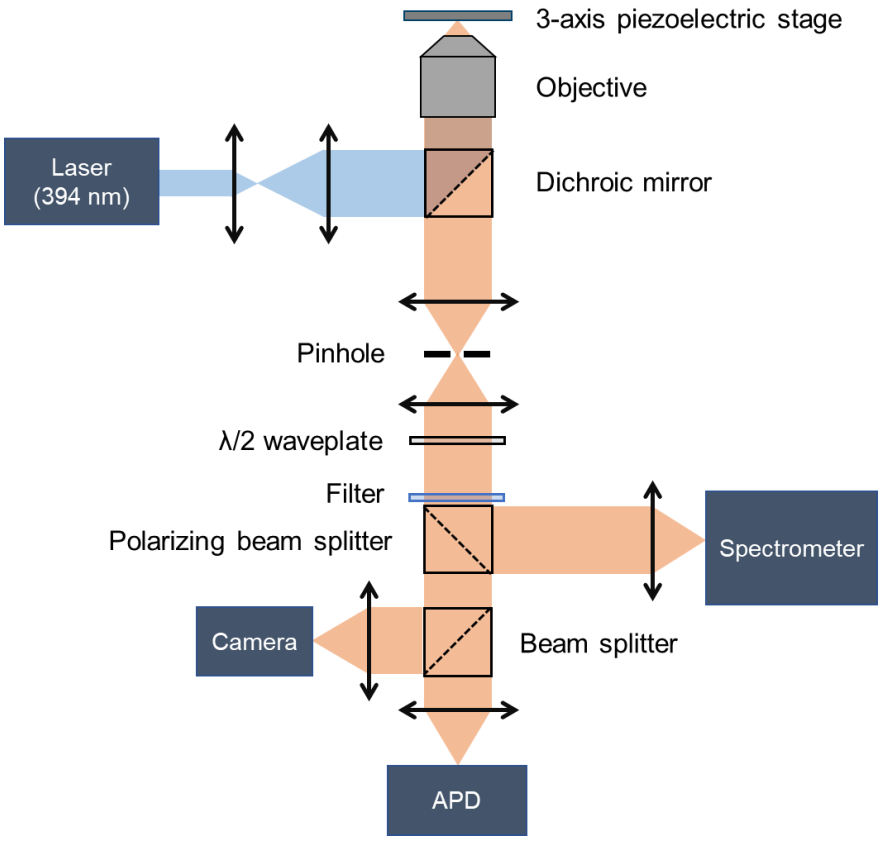

Figure 2.12 Schematic representation of the optimized polarization resolved confocal micro-spectroscopy setup.

The excitation laser is focused on the sample and the emission is collected by a 60x oil immersion objective with NA=1.49. Previously, focusing the emission beam on the pinhole was very challenging, as it was done by adjusting the z-position of a doublet outside of the microscope body. To simplify the setup, we decided to change the configuration such that the emission beam could exit through one of the viewing ports. In this way, we could use the built-in tube lens (f=20cm) to focus the emission beam onto the pinhole. This also allowed us to use the built-in prism mirror to reflect the emission, instead of the metal mirror which we suspected to be the cause of the polarization distortion.

The pinhole is mounted on a 3-axis adjustable mount so that its position could be accurately adjusted. To pick the correct pinhole size, we need to consider the size of the Airy disk (the diffraction pattern) which would be seen at the pinhole position. For the emission wavelength of ~ 650 nm and a 60x magnification the radius of the Airy disk $R_{Airy} \sim 16$ µm[66]. For conventional microscopy systems, the pinhole size is typically matched to 0.7-1 times R_{Airy} as this can provide a high resolution without cutting too much of the signal intensity[63]. For our system, this corresponds to a pinhole diameter of 22-32 µm. We experimented with a pinhole of 25 µm, but found that it cut too much of the signal intensity and therefore chose to use a 50 µm pinhole diameter instead.

After the pinhole, the beam is collimated by a doublet with f = 15 cm. The collimated beam then passes through a λ/2 waveplate to rotate its polarization axis. The waveplate is mounted on a motorized rotating mount and placed right before a polarizing beam splitter in order to select the polarization state. Selecting the polarization state near the end of the optical path minimizes distortions to the linear polarization state. Additionally, a long pass filter (>560 nm) is placed before the polarizing beam splitter in order to block the reflection of the excitation laser. The s-polarized light is reflected towards the spectrometer and the p-polarized light is transmitted towards the APD and a camera. The spectrometer is equipped with a 500 g/mm grating which has a large spread, allowing to simultaneously observe all transitions between 570-720 nm. The APD can be used with the piezoelectric stage to rapidly scan the sample and reconstruct PL intensity maps. The camera allows to simultaneously image the pinhole and sample, which helps the alignment procedure.

A piezoelectric stage with 3-axes is used to scan across the sample for tomographic imaging. A commercial software (Inscoper) is used to synchronize the piezoelectric stage, waveplate orientation, APD and spectrometer, which allows to automate the data acquisition.

2.2.2 Alignment procedure and performance

The key to achieving a good spatial resolution is the correction of the chromatic aberration of the excitation and emission light. According to the specification sheet of the 60x oil immersion objective (Nikon Plan Apo 1.40 OFN24 DICN2) it can be used as an achromatic objective in the window of 405-656nm for confocal microscopy. With $\lambda_{exc} = 394$ nm and an emission range of λ_{em} =500∼700 nm, we can therefore not assume that the objective can fully correct the chromatic aberration on its own. Instead, we manually adjust the collimation of the excitation laser. This alignment procedure is done using a $NaYF_4$:Eu nanocrystal which is large enough to observe on the camera and whose emission is similar to that of $LaPO_4$:Eu.

During the alignment procedure, the position of the first doublet in the telescope lens is moved in controlled, incremental steps which changes the focus of the excitation laser. **Figure 2.13a** shows how the PSF changes as the doublet is moved incrementally. The center of the PSF moves up (away from the substrate) as the doublet is moved with 0.5 mm increments away from the second doublet, causing the excitation beam to be increasingly divergent as it enters the objective. Consequently, the size of the bright spot in the center of the PSF increases and the contrast decreases slightly. However, it is difficult to evaluate the quality of the alignment purely based on the 2D shape of the PSF. Instead, after each adjustment, the resolution is quantified by evaluation of the full width half maximum (FWHM) of the one-dimensional (1D) PSF across the center of the nanorod.

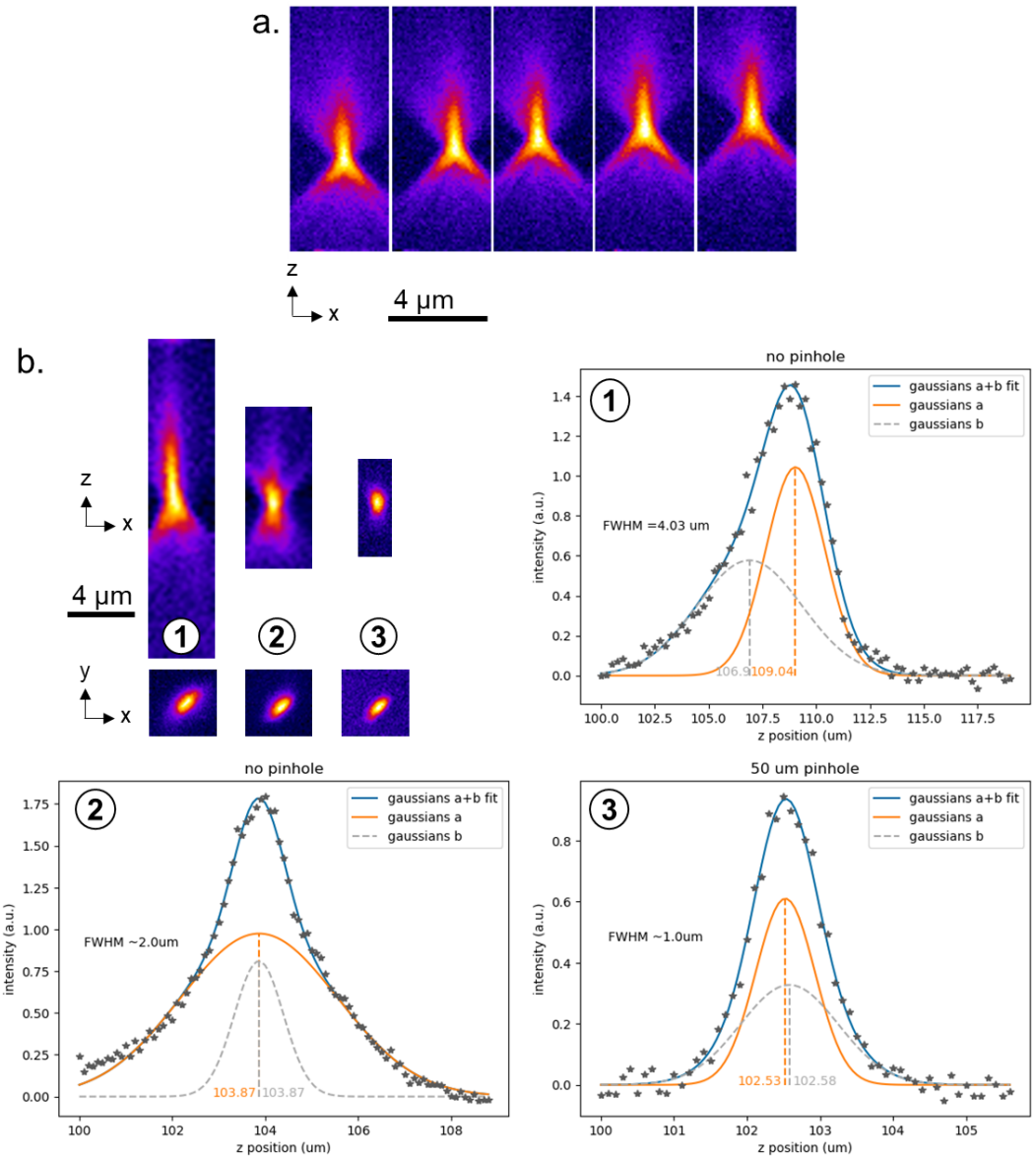

Figure 2.13 Resolution improvement during alignment procedure. **a)** PL intensity images of the PSF of a single $NaYF_4$:Eu nanorod at different points in the alignment procedure. Between each image (from left to right) the first doublet in the telescope lens is moved 0.5 mm away from the second lens. **b)** PL intensity images and corresponding resolution measurements by evaluating the 1D PSF through the center of the nanorod for different stages of the alignment procedure. PSF are fit using a sum of two Gaussian functions. 1: Without any correction 2: After correcting the excitation focus 3: With a 50 µm pinhole inserted.

Figure 2.13b shows PL images of a single $NaYF_4$:Eu nanorod taken with the APD at different stages of the alignment procedure and the corresponding plots of the 1D PSF. The images and graph labeled with the number 1 correspond to the initial alignment before correcting the excitation focus. In this case the PSF is highly asymmetric, with the z-resolution being more than 4 µm (which is more than four times the lateral resolution). Moreover, the 1D PSF taken by plotting the intensity along the z-direction through the center of the particle cannot be fit with a single Gaussian function. Instead, it seems to be a combination of two Gaussians, one which corresponds to the excitation and one corresponding to the emission. By

continuous adjustments and resolution measurements, the optimal position of the focusing doublet can be determined (number 2 in **Figure 2.13b**). When there is a good match of focal planes, the two Gaussians fitting the 1D PSF have the same center position as is seen in **Figure 2.13b**. This proper alignment of the excitation laser reduces the z-resolution to around 2 µm. To further improve the resolution, a pinhole is introduced to ensure only the emission from a thin optical slice at the focal plane is collected. The position of the pinhole is adjusted to maximize the signal intensity collected on the spectrometer, which results in an axial resolution of 1 µm (number 3 in **Figure 2.13b**).

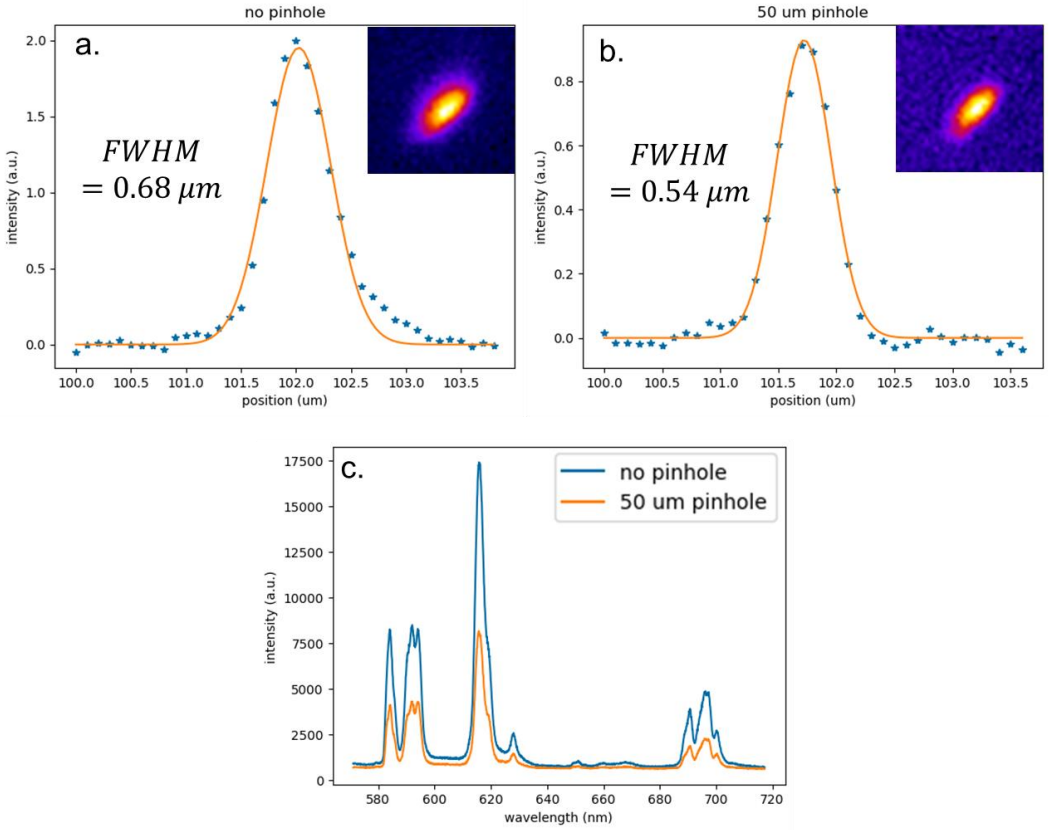

Figure 2.14 Lateral resolution and intensity. **a-b)** 1D PSF across the center of the $NaYF_4$:Eu nanorod and their corresponding FWHM without and with a 50 µm pinhole respectively. Inset images of the PL intensity are 4 µm by 4 µm. **c)** PL emission spectra measured at the center of the nanorod. Placing the pinhole results in an intensity loss of ~50%.

Placing the pinhole also improves the lateral resolution from 0.68 µm to 0.54 µm (**Figure 2.14a-b**). However, from the APD images, we see that the contrast is slightly decreased as the pinhole is introduced and the intensity of the measured spectrum using the spectrometer drops by around 50% (**Figure 2.14c**). Some intensity loss is expected, due to elimination of the emission from outside the optical slice, but such a large decrease in intensity may be explained by an incorrect z-position of the pinhole, as this remains difficult to align. It might therefore be possible to improve the resolution further by continuing to improve

the experimental setup and alignment. Nonetheless, the contrast and total signal intensity is drastically improved compared to the initial configuration shown in **Figure 2.10**.

Calibration of waveplate orientation

To determine the orientation of the waveplate (attached to a rotating mount) with respect to the laboratory frame we can use the polarized luminescence behavior of the $NaYF_4:Eu^{3+}$ nanorod which was also used to align the excitation beam and measure the resolution. **Figure 2.15a-b** shows a PL image of a single nanorod and its polarized emission. When plotting the k-values, the ratio of the first and second subpeak (highlighted in blue), of the $^5D_0$-$^7F_1$ (MD) and $^5D_0$-$^7F_4$ (ED) transitions, we find they form two orthogonal dumbbell shapes (**Figure 2.15c**). We know that the long axis of the dumbbell of the MD transition should be aligned with the rod axis[26]. More specifically, the polarized emission measured at a given analyzer angle θ follows the typical dipolar model

$$I(\theta) = I_\sigma \cdot \sin^2\theta + I_\pi \cdot \cos^2\theta \qquad \textbf{2.35}$$

By curve fitting the dumbbell shape, we find $\theta = 56°$ for this specific rod. From the APD image, we find that the rod is orientated at 5-10° with respect of the x-axis. Considering that rotating a λ/2 waveplate 1° is equivalent to rotating a linear analyzer by 2°, the waveplate is parallel to the x-axis when the rotating mount is at 23-25.5°. To improve the calibration, it is better to repeat the measurement on a few different single particles. From this, we estimate that the waveplate calibration introduces a systematic error around 5° on the orientation measurements. This error is mostly due to the uncertainty from determining the rod orientation based on the PL image (**Figure 2.15a**), rather than the instrumental error of the rotating mount. The calibration could be improved by using a macroscopic polarization standard.

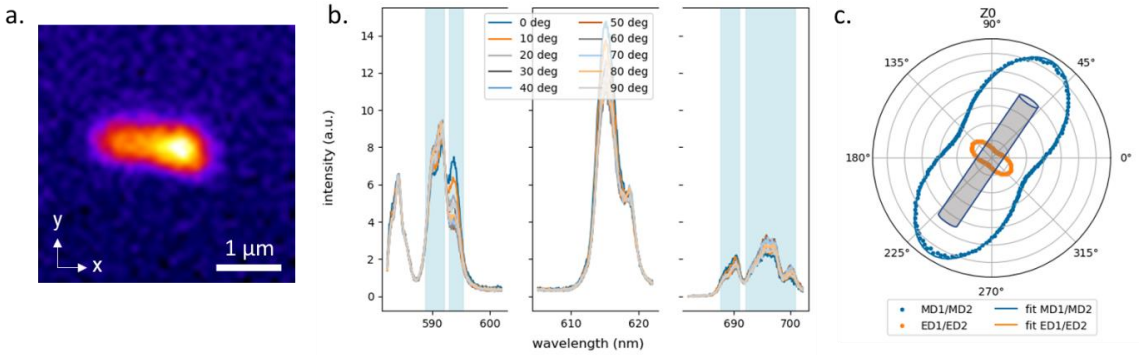

Figure 2.15 Calibration of waveplate. **a)** APD image of the luminescence of a single $NaYF_4$:Eu nanorod. **b)** Emission spectra collected for different analyzer angles. The highlighted blue regions indicate the regions where the integrated intensity is calculated for MD1, MD2, ED1 and ED2 respectively. **c)** Polar diagram of the ratio between the first and second subpeak for the MD and ED transitions.

Polarization

To check if the optical setup distorts the polarization state in any way, we measure the polarized PL in a well aligned and fully isotropic reference sample. First, we verify the polarized emission of monazite phase $LaPO_4$:Eu in a planar nematic LC domain (**Figure 2.16a**). For a highly aligned planar sample, the intensity follows the dipolar model described by **equation 2.35**. Considering the angle dependency of the integrated intensities (indicated by the highlighted regions) we see that the oppositely polarized subpeaks always form orthogonal dumbbell shapes in the polar diagrams (**Figure 2.16b**). We do not see any wavelength dependency on the polarization, as the orientation of the orthogonal dumbbells are the same (< 1.5° deviation) for all three transitions.

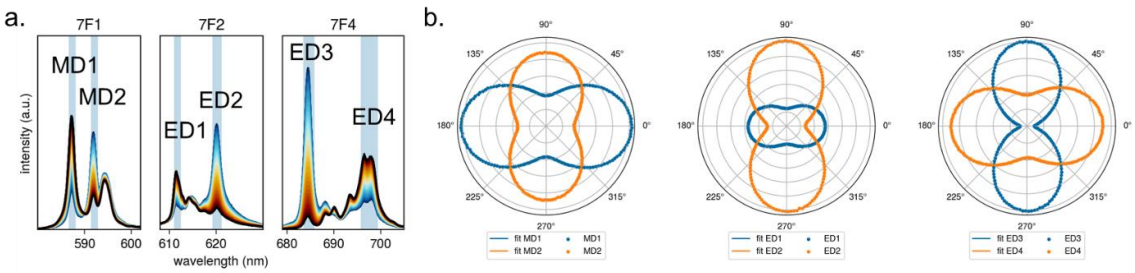

Figure 2.16 a) Polarized emission spectra of monazite phase $LaPO_4$:Eu nanorods collected in a planar nematic LC aligned by an electric field. **b)** Polar diagrams of the integrated intensity of the peaks highlighted in the emission spectra. All peaks perfectly fit the dipolar model (**equation 2.35**).

As was discussed in section **2.1.2**, we previously found that the subpeaks associated to the π configuration of the monazite spectrum didn't follow the typical linear dipole model when plotting their intensity against the analyzer angle (**Figure 2.11**). After eliminating the metal mirror from the setup, all subpeaks perfectly fit the dipolar model as seen in **Figure 2.16b**. The metal mirror used previously must have had a polarization-specific reflectance, which coupled with the linear polarizer, caused the distortion in the polarization state. However, it is not yet clear why this distortion only affected the π polarized subpeaks.

We then consider the isotropic spectra measured using the new setup. The isotropic spectrum is obtained from the isotropic phase of the LC suspension which was diluted to minimize any interparticle interactions or self-alignment. A perfectly isotropic spectrum should have circular k-diagrams, but in this case, they are slightly elliptical, as seen by the inset in **Figure 2.17a**. Repeating the measurement at different positions (**Figure 5.30**) or in a more diluted sample always gives a similar elliptical shape. Adding a coverslip or sealing the isotropic phase in a confinement cell does not significantly alter the measured spectra either. The long axis of the MD k-diagram always corresponds to the y-axis of the stage, suggesting that the anisotropic shape is an artefact of the optics rather than the sample itself. One explanation is the potential difference in the reflectance of the prism mirror for s- and p-polarized light. This effect be clearly

observed when considering the magnitude of the baseline (annex, **Figure 5.31**). However, it is unclear why this would impact the k-diagrams, as the taking the ratio of two peaks should largely compensate overall intensity fluctuations.

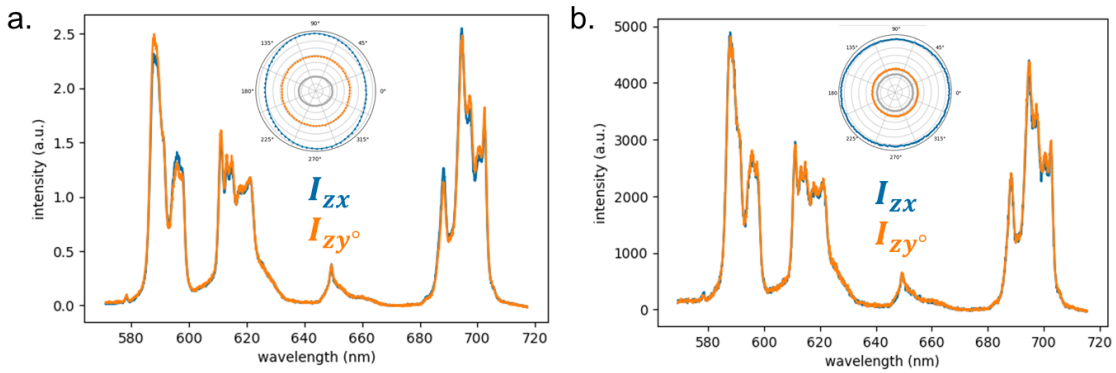

Figure 2.17 Isotropic emission collected from rhabdophane phase $LaPO_4$:Eu colloidal suspensions. **a-b**) emission spectra obtained when the polarizer is parallel to the x- and y-axis and as an inset the polar diagram of the k-values (ratio between two major peaks), for **a)** diluted isotropic droplet and **b)** the isotropic phase in a phase separated sealed cell, with a nematic phase spanning the bottom substrate surface. Additional polar diagrams at different depths in each sample can be found in annex **Figure 5.30**.

Interestingly, when measuring the spectra in the isotropic phase of a biphasic confined sample the k-diagrams become significantly more circular (**Figure 2.17b**). Similarly, the k-diagrams collected in a homeotropic sample shows a similar (close to) circular shape. In such samples, a nematic layer of 10-30 µm thickness fills the bottom of the cell, and the isotropic cell fills the rest of the space up to the coverslip on top. Due to the difference in density there may be a small difference in effective refractive index between the nematic and isotropic phase. This may cause reflection or refraction at the isotropic-nematic interface, affecting the collected emission when probing the isotropic phase. Additionally, if the refractive index of the nematic is closer to the refractive index of the glass coverslip, there may be less interfacial phenomena than for the dilute isotropic phase.

Summary of chapter 2.2

The confocal microscopy setup is improved. To obtain a good axial resolution, it is crucial to correct the chromatic aberration and use a pinhole. After alignment, the final spatial resolution is 0.5 µm by 1 µm which is half that of the initial configuration. We lose ~50% of the signal intensity when inserting the pinhole, which suggests a suboptimal pinhole position and further improvement to the resolution should be feasible.

After replacing the metal mirror with a prism mirror, the emission peaks of monazite perfectly match the dipolar model. Using an isotropic nanorod suspension, we observe a slightly ellipsoidal angular dependency of the ratio between oppositely polarized peaks whose axes match the x,y axes of the optics. In the case where a nematic phase spans the glass interface, the polar diagrams of isotropic and homeotropic arrangements only show minor ellipticity which may be linked to a slight difference in reflectance of s- and p-polarized light.

2.3 Polarized photoluminescence of $LaPO_4$:Eu polymorphs

In order to interpret the alignment behavior of $LaPO_4$:Eu nanorod suspensions and how the alignment impact their collective emission, it is important to first characterize them. In this section, the elaboration of both rhabdophane and monazite phase $LaPO_4$:Eu nanocrystals will be detailed. Their polarized emission spectra will be compared, with a focus on the $^5D_0$-$^7F_4$ transition which was not covered by the initial studies[18]. Finally, the procedure for obtaining the reference spectra needed for orientation measurements will be discussed.

2.3.1 Elaboration of $LaPO_4$:Eu nanorod suspensions

Suspension of $LaPO_4$:Eu nanorods in ethylene glycol (EG) were prepared according to the protocols in the **annex 5.1**. $LaPO_4$:Eu nanorods were prepared in the rhabdophane and monazite phase for 5% and 20% europium doping, as increasing the doping label was shown to increase the PL intensity which should allow for faster spectroscopic measurements. However, the highly doped monazite nanorods aggregated and didn't form stable colloidal suspensions, as discussed in **annex 5.1**.

Particle size distribution

To obtain the size statistics of the synthesize nanocrystals and verify the crystallinity, TEM imaging was performed. From the high resolution TEM images in **Figure 2.18a-b**, we can discern an excellent crystallinity of the hexagonal and monoclinic lattices respectively. TEM imaging was used to characterize the particle size distribution and representative images of each sample can be found in the annex **Figure 5.34**. **Figure 2.18c** shows the distributions for the length l, width w and aspect ratio AR for each sample of interest. We find a similar size for both rhabdophane and monazite with a 5% europium doping, but

the 20% doped rhabdophane nanorods are slightly smaller. As the width is comparable throughout, this also means that the aspect ratio of the 20% doped sample is lower.

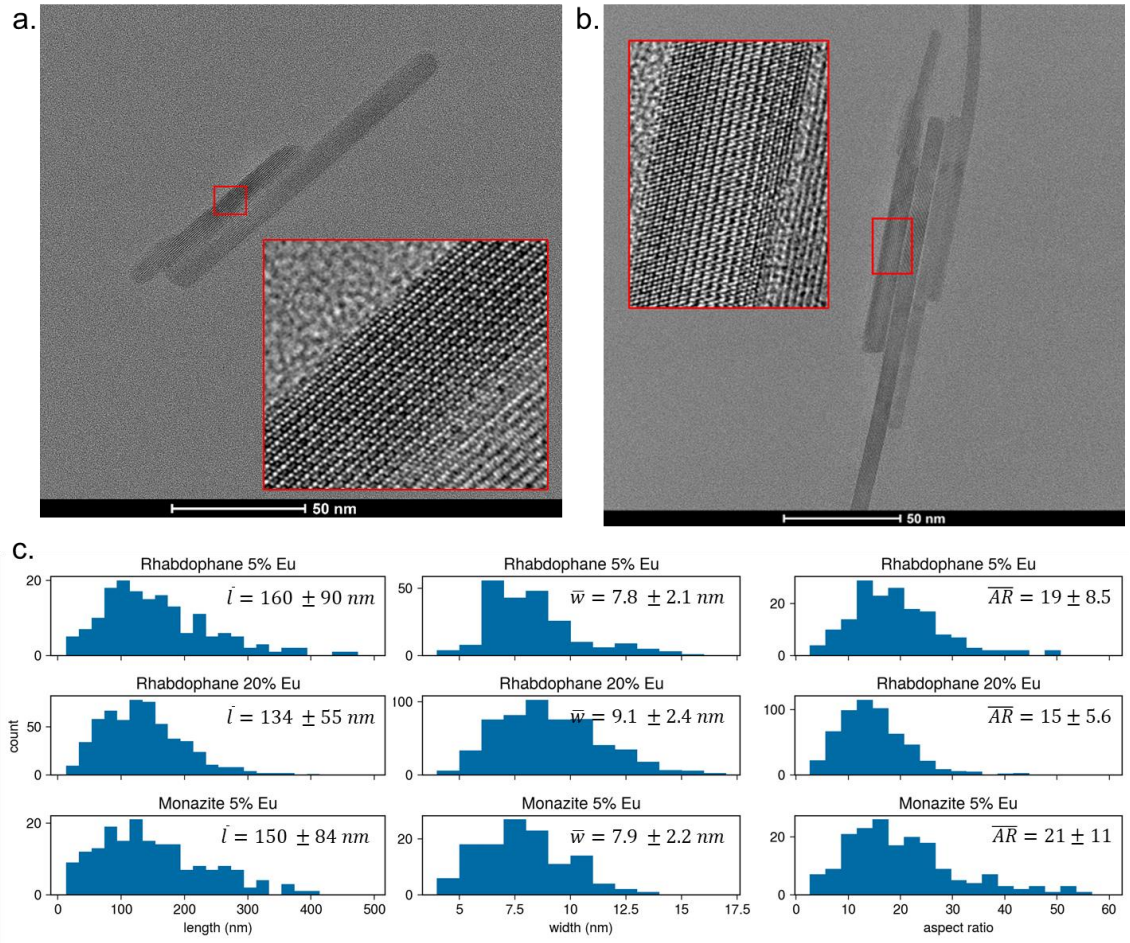

Figure 2.18 High resolution TEM images of synthesized $LaPO_4$:Eu nanorods showing the crystal structure in the **a)** rhabdophane phase, **b)** monazite phase. **c)** size statistics and the average and standard deviation of the length l, width w and aspect ratio AR obtained by TEM imaging.

Finally, we see that all samples are rather polydisperse, with a standard deviation of l on the order of 40-60% of the mean. As the photoluminescence of lanthanides depends on the crystal structure rather than the overall morphology of the host material, this should not impact the optical properties. However, the polydispersity and the aggregation state will affect the rheological behavior of the suspension[67] and has been shown to affect the relaxation time in samples initially aligned under electric fields[68]. Quantifying the impact of polydispersity and particle size on the $LaPO_4$ suspensions is an ongoing work within our group.

2.3.2 Polarized photoluminescence of rhabdophane and monazite $LaPO_4$:Eu

Figure 2.19 shows the polarized emission spectra for horizontally aligned assemblies of the synthesized rhabdophane and monazite nanocrystals, measured at room temperature using the confocal microscopy

setup. In addition to the previously characterized $^5D_0$-$^7F_1$ and $^5D_0$-$^7F_2$ transitions[18], we can now also collect the emission of the $^5D_0$-$^7F_3$ and $^5D_0$-$^7F_4$ transitions through the use of a spectrometer grating with larger spread. The $^5D_0$-$^7F_3$ transition, which is forbidden by the Judd-Offelt theory, only produces a weak emission. It is more pronounced for the rhabdophane phase, which indicates a stronger perturbation of the crystal-field which may be attributed to the higher amount of defects[16]. The $^5D_0$-$^7F_4$ transition creates very strongly polarized emission with well-defined subpeaks, for both phases. This makes it appealing to use as the ED transition for orientation analysis as it provides an alternative to the weakly polarized $^5D_0$-$^7F_2$ transition.

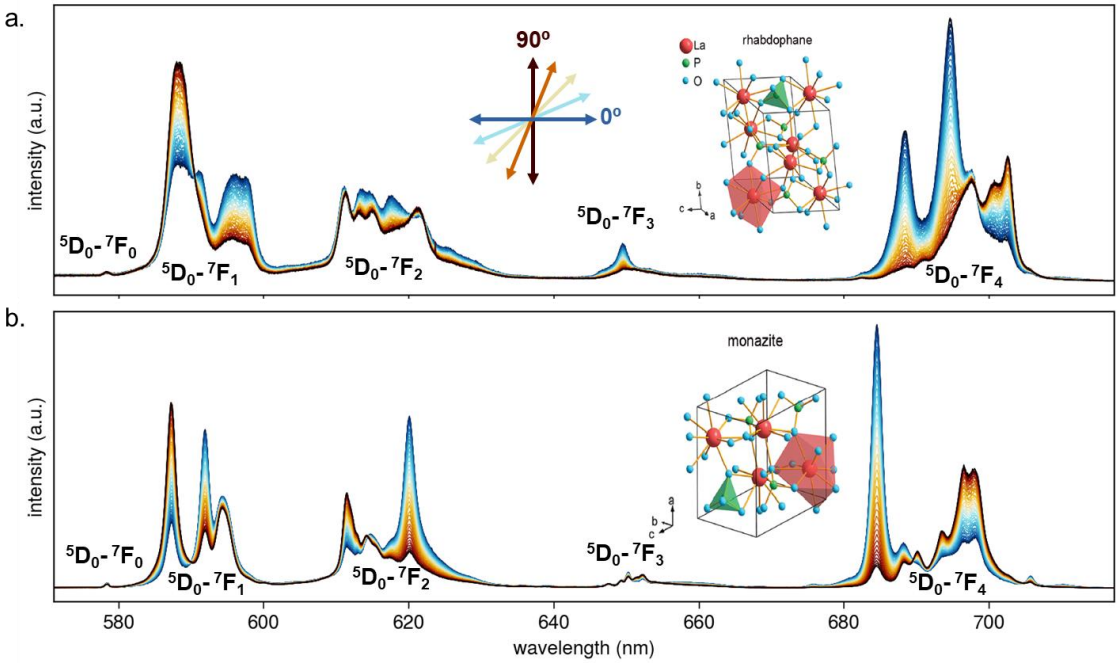

Figure 2.19 Polarized emission spectra of nematic $LaPO_4$:Eu nanorod suspensions aligned using electric field as a function of the analyzer angle with respect to the collective orientation of the rods, for the **a)** rhabdophane phase, **b)** monazite phase. Measurements are performed at room temperature using the confocal microscopy setup with NA=1.49.

From the emission spectra collected in a planar sample, we can extract the I_π and I_σ spectra which correspond to the analyzer parallel and perpendicular to the rod axis respectively. For the ratiometric orientation analysis we consider the integrated intensity of two subpeaks for each transition. **Figure 2.20** indicates the regions associated to the most strongly polarized emission peaks and their associated polar diagrams. For the final peak, two subpeaks are considered together as they are difficult to separate. We can see that all subpeaks fit well with the dipolar model (**equation 2.35**) from the associated dumbbell shape.

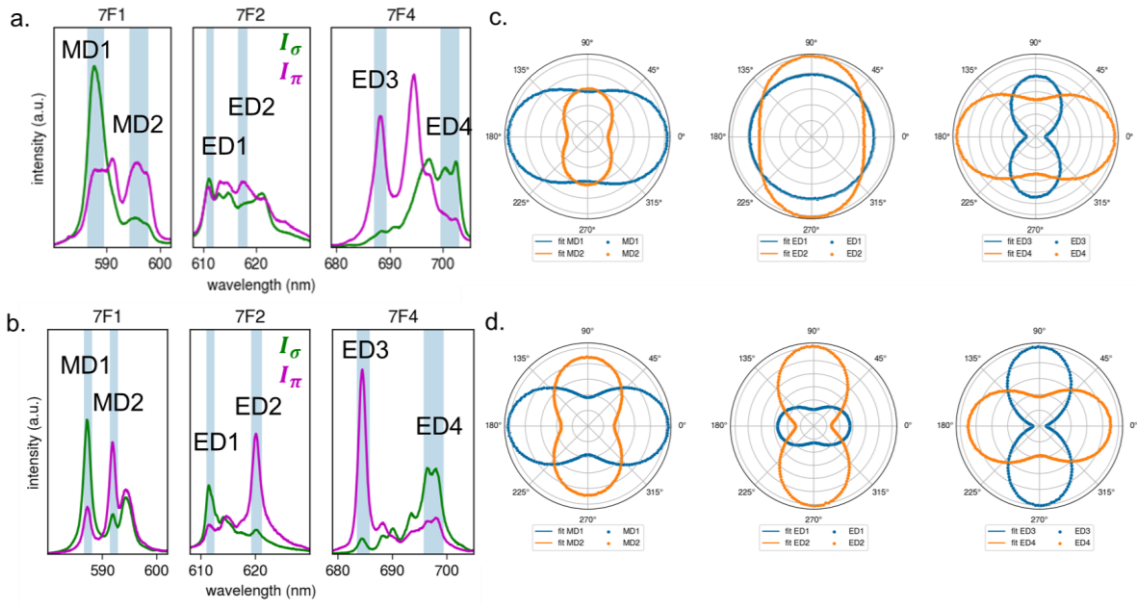

Figure 2.20 a-b) Emission components I_π and I_σ corresponding to the analyzer parallel and perpendicular to the rod axis respectively for **a)** rhabdophane and **b)** monazite. **c-d)** Polar diagrams of the integrated intensity of the highlighted regions of the emission spectra for **c)** rhabdophane and **d)** monazite.

The degree of polarization (DOP) is defined according to the relative contribution of each component for a specific emission peak such that

$$DOP = \frac{I_\pi - I_\sigma}{I_\pi + I_\sigma} \qquad \textbf{2.36}$$

In theory, if the magnetic and electric dipoles align perfectly with the crystallographic axes, each emission peak will be perfectly polarized according their ED and MD interactions and have a DOP of +/- 1. In reality, each peak consists of a mixture of the two contributions and has a partial degree of polarization, due to lattice distortions and imperfections which can easily perturb the local crystal field[18]. **Table 1** documents the DOP for each of the peaks highlighted in **Figure 2.20a-b**.

Table 1 Typical DOP for each peak of rhabdophane (R) and monazite (M) for NA = 1.49

		MD1	MD2	ED1	ED2	ED3	ED4
R	**λ (nm)**	586.3-589.5	594.4-598.0	610.8-612.1	616.6-618.4	687.1-689.4	699.5-703.1
	DOP	-0.29	0.44	-0.05	0.23	0.71	-0.39
M	**λ (nm)**	586.7-588.1	591.3-592.8	611.0-612.4	619.2-621.2	683.5-685.8	695.8-699.4
	DOP	-0.47	0.45	-0.37	0.64	0.85	-0.42

It should be noted that the measured DOP is not only affected by the emitter itself, but also by the NA of the objective used, as an increase in NA results in a decrease of the DOP[10]. A tradeoff therefore exists

between the spatial resolution of imaging (dominated by NA) and the angular resolution of orientation analysis (dominated by DOP). Nonetheless, even with our high NA (1.49) objective, many peaks are still strongly polarized.

For the application of spectroscopic orientation measurements, it is favorable to enhance the DOP as much as possible, as this would increase the measurement sensitivity. Based on DOP alone, we can therefore expect that monazite will generally be a better candidate for orientation analysis. Additionally, when rhabdophane is considered, only the $^5D_0$-$^7F_4$ transition provides sufficiently high DOP peaks to perform orientation analysis for an ED.

2.3.3 Reference spectra measurement

Obtaining the reference spectra $I_\pi(\lambda)$ and $I_\sigma(\lambda)$ is the key to all types of spectroscopic orientation measurements discussed in this work. In principle, they can be experimentally obtained from any well-aligned, planar reference sample such as dense liquid crystal assembly, suspensions aligned using an electric field or thin films. To do so, the reference sample is mounted on the microscopy set up and spectra are collected while varying the analyzer angle by 2-degree increments (corresponding to a 1-degree rotation of the waveplate) over the full 360 degree range. This allows us to construct the polar diagrams which help determine the precise azimuthal orientation ϕ of the director $\vec{n}$, which is needed to identify the I_π and I_σ spectra. This procedure is fully automated by a Python script, which makes it possible to treat large amounts of measurements.

Automatic selection of the reference spectra

A Python script was written to be able to treat large amounts of measurements and automatically extract the spectra corresponding to the π and σ configuration and computes the DOP for each peak. First a constant baseline is subtracted as illustrated in **Figure 2.21a-b**. The baseline was previously calculated by averaging the PL intensity in a small window unaffected by the Eu^{3+} emission. However, due to the broad shoulders of the emission peaks (particularly for rhabdophane) such regions are difficult to identify and instead a baseline algorithm is used which considers the whole spectrum.

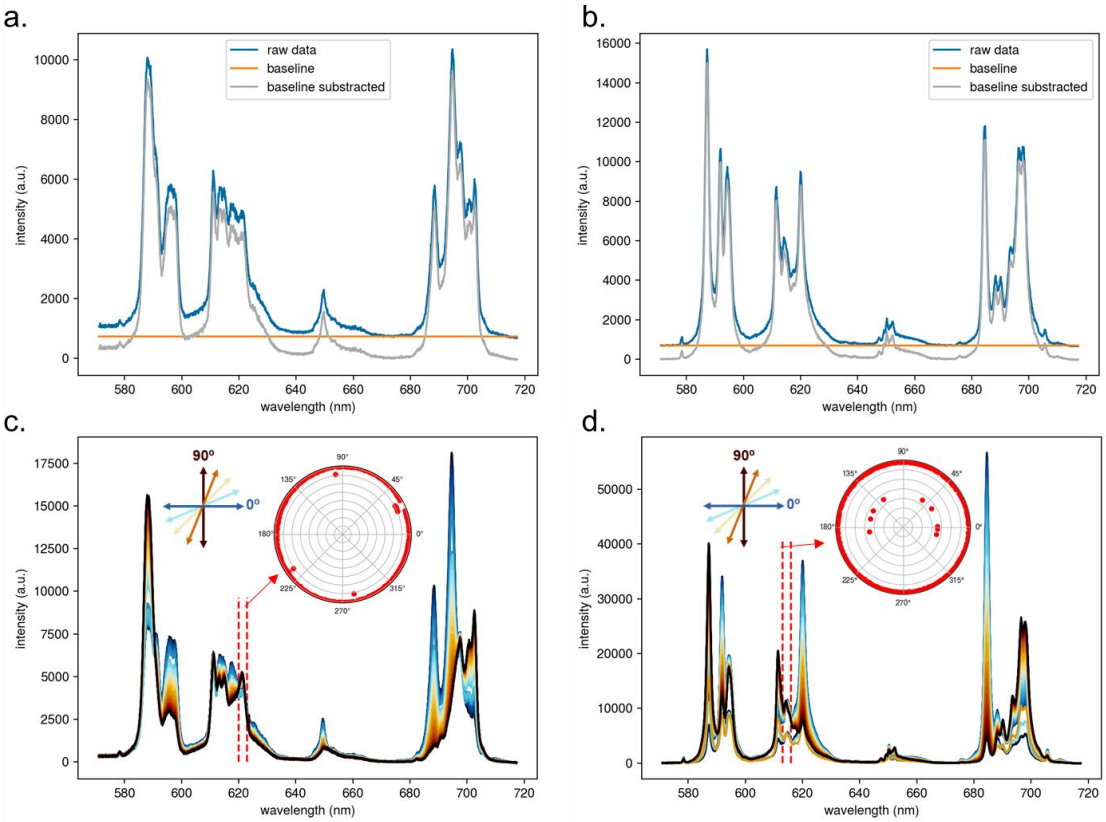

Figure 2.21 a-b) Baseline subtraction and normalization of measured spectra. **c-d)** Baseline subtracted spectra for various analyzer angles. Inset shows the integrated intensity of an unpolarized emission peak indicated by the red dashed-lines.

Unfortunately, due to an issue in the operating software of our microscope, the total exposure time seems not to be constant for all measurements. A normalization to correct for this inconsistency was done based on the integrated intensity of the final subpeak of the $^{0}D_{5}$-$^{7}F_{2}$ transition for rhabdophane and the second subpeak for monazite (**Figure 2.21c-d**). The inset in **Figure 2.21c-d** shows that these peaks are close to perfectly unpolarized and illustrates the acquisition bug which causes some seemingly random points to have reduced intensity. **Figure 2.22a** shows an example of the measured spectra after normalization, displaying a continuous change in spectra as the analyzer is turned.

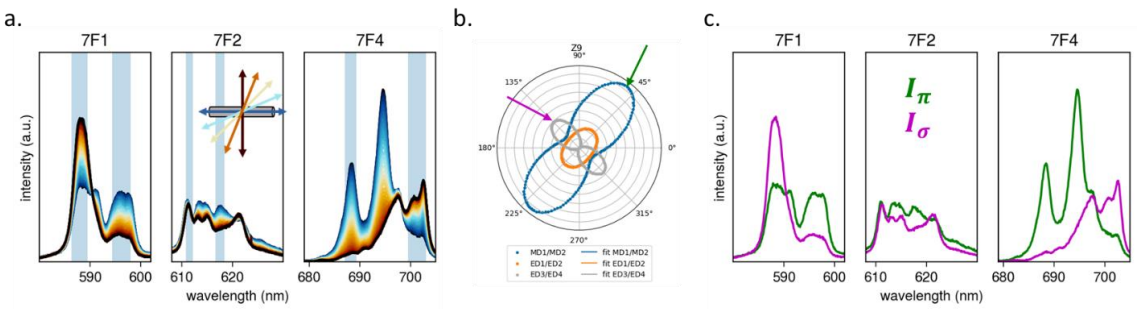

Figure 2.22 Example reference spectra measurement. In nematic LC sandwiched between glass substrates with a gap of 60 µm. **a)** Polarized emission measured near the middle of the LC. **b)** k-diagram constructed from the ratio between peaks indicated in a). **c)** I_π and I_σ as indicated by the arrows on the k-diagram

Next, the measurements corresponding to the π and σ configuration are selected by evaluating the k-values. The k-value signifies the ratio between the integrated intensity of the first and second subpeak for each transition as indicated by the blue regions in **Figure 2.22a**. By dividing the two intensities any effect from global intensity fluctuations is negated and the anisotropy of the dumbbell shapes are enhanced, making it easier to distinguish the orientation. The k-values for each transition are computed and plotted against the analyzer angle as seen in **Figure 2.22b**. The datapoints for each transition are fit using the expression

$$k(\theta) = \frac{A \cdot \cos^2\theta - \alpha + B \cdot \sin^2\theta - \alpha}{C \cdot \cos^2\theta - \beta + D \cdot \sin^2\theta - \beta} \qquad \textbf{2.37}$$

where θ is the analyzer angle with respect to the x-axis. From this curve fit we can extract the DOP for each subpeak using **equation 2.36**, as the A, B, C and D values correspond to integrated intensity of I_σ and I_π for the first and second subpeak respectively. As an example, for the MD ($^5D_0$-$^7F_1$) transition in **Figure 2.22**, $A = I_{\sigma 1} = 106$, $B = I_{\pi 1} = 58.8$, $C = I_{\sigma 2} = 25.1$ and $D = I_{\pi 2} = 65.7$, which gives a DOP of -0.29 for the first subpeak and 0.45 for the second subpeak. The α and β values in **equation 2.37** correspond to orientation of the axis of the linear polarization of each subpeak. For the dataset shown in **Figure 2.22**, $\alpha = 52.7°$ and $\beta = 51.6°$, which suggests that $\vec{n}$ is oriented at roughly $52°$. I_π can then be extracted from the measurement taken with the analyzer at $52°$ and I_σ is taken as the measurement with the analyzer at 142° (**Figure 2.22c**).

Because this process is fully automated, such measurements can be easily repeated at different positions and different depths in the sample. This can give a first indication about the quality of the sample, as uniform k-value distributions throughout the depth of the sample indicate long range order suggesting a high degree of alignment, an example of this can be found in the annex **Figure 5.35**.

Comparison of types of reference samples

The quality of the reference spectra highly depends on the sample used to collect it. In order to collect the pure I_π and I_σ spectra, we must avoid any contribution of the axial propagation I_α on the

measurement. To do so, the prepared nanorod sample must have a fully planar alignment and a perfect order parameter. In practice, this is extremely challenging, but different sample preparations may be considered. In this section, reference samples using the nematic LC phase under different conditions and thin films will be compared.

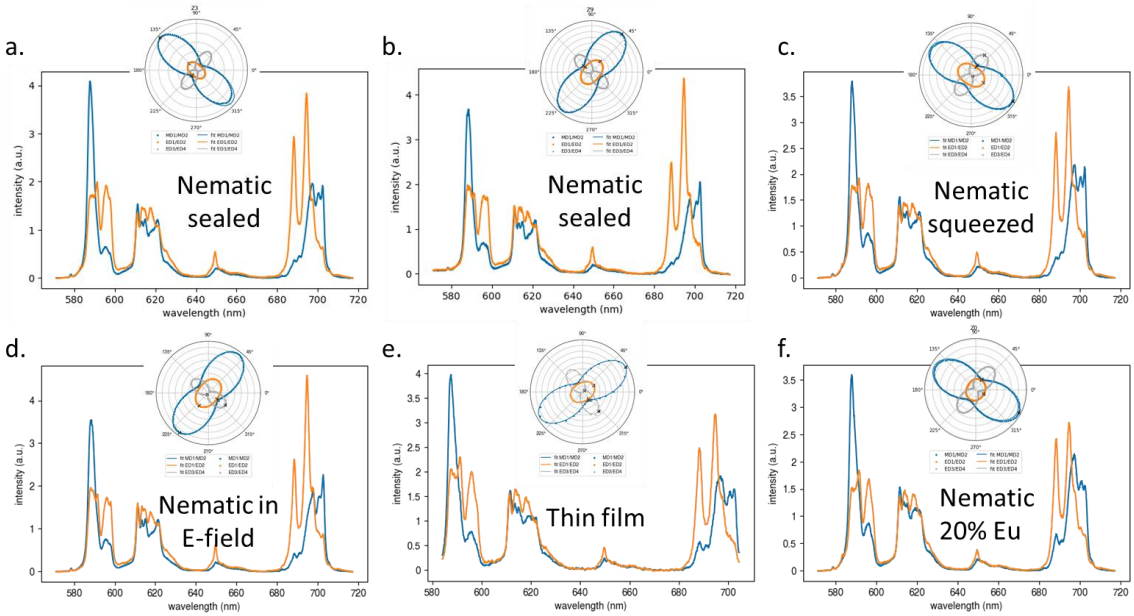

Figure 2.23 Obtained reference spectra I_π (orange) and I_σ (blue) and corresponding k-diagrams from various rhabdophane $LaPO_4$:Eu samples. **a-b)** Nematic LC sandwiched between untreated glass coverslips with at 60 µm gap and sealed with UV glue to prevent evaporation. **c)** Nematic LC squeezed between glass coverslips. **d)** Nematic LC aligned under electric field. **e)** Thin film **f)** Nematic squeezed between untreated coverslips and sealed with UV glue. Doping percentage is 20% instead of 5% for all the others.

First, a droplet of the nematic phase of prepared LC sample can be sandwiched between two well-cleaned glass coverslips. Any dirt or scratches should be avoided, as this might induce a non-planar alignment. The coverslips can be compressed for a few hours to try to force a planar alignment or a spacer can be used to give the LC space to settle on its own. The first row in **Figure 2.23** shows the k-diagrams and corresponding I_π (orange) and I_σ (blue) spectra obtained in such samples. The spectra corresponding to the nematic within the spacer cell typically show a higher DOP than the squeezed samples (seen from the narrower dumbbells in the k-diagram), insinuating a higher order parameter. Squeezing the nematic may cause the local density of rods to decrease or a lack of uniformity in the applied pressure might induce some out of plane alignment, which could result in a lower perceived order parameter.

Additionally, an electric field can be applied to help align the nematic phase. For this, we use a glass microscope slide on which two parallel ITO electrodes have been deposited. A droplet of the nematic LC is deposited on the slide such that the electrodes and gap are covered. Then an alternating field of 90V at 250 kHz is applied which aligns the rods along the field. The PL emission is then collected near the center

of the gap, where the electric field is assumed to be planar. The resulting reference spectra and k-diagram are quite comparable to those obtained in the nematic droplets without electric fields (**Figure 2.23d**). Although aligning the nematic using the electric field doesn't seem to improve the order parameter (the DOP is similar to the squeezed sample), it may help to ensure a fully planar alignment.

Another approach is to use a thin film, rather than a thick nematic, which may provide a more planar alignment. Previous SEM studies showed that the order parameter in such samples was close to unity. The preparation of the nanoparticle thin film used to obtain the reference in **Figure 2.23e** was done prior by a colleague, using the reported protocol[69]. The nanoparticles were thus originating from a different synthesis batch, which may affect the PL emission as the fine crystal structure and number of defects may be different. Nonetheless, the k-diagram obtained from such a sample is quite similar to those taking in the nematic LC (**Figure 2.23a**). Interestingly, the DOP does not seem to be enhanced for the thin film which suggests that its order parameter is comparable to that of the nematic LC.

Finally, to illustrate the impact of the doping percentage on the fine emission spectra, a nematic sample of 20% doped $LaPO_4$:Eu nanorods is used. From the reference spectra obtained, there is no obvious difference with the 5% doped samples. Carefully comparing the spectra in **Figure 2.23a** and **Figure 2.23f** shows that the 20% doped sample may have slightly less well defined, sharp peaks, as seen in the final peak of the $^5D_0$-$^7F_1$ transition.

Even from the same exact synthesis, the fine line sphape of the measured reference spectra can vary slightly depending on the local alignment in the sample. If we consider for example the spectra obtained at two different positions in the same exact LC sample (**Figure 2.23a-b**), we can see that the first subpeak in the $^5D_0$-$^7F_1$ transition looks much flatter for the first one than the second one. The k-diagram also seems slightly more elongated for the first measurement. This could be due to slight variations in the local (out-of-plane) orientation or order parameter.

Additionally, the relative intensities of the $^5D_0$-$^7F_1$ and $^5D_0$-$^7F_4$ transitions can vary quite a lot between measurements. We didn't find a clear relationship between this relative intensity difference and the director orientation or the depth in the sample. For the spectroscopic applications it doesn't pose a problem because each transition is evaluated independently, either by considering the ratio of the two subpeaks or by having independent scaling factors for the spectral fitting.

Evaluation of the quality of reference spectra

The slight changes in spectral shape between the different reference spectra have a direct impact on the results of the orientation analysis. In particular, we found that the absolute value of the calculated order parameter and polar angle could vary significantly when using different I_π and I_σ spectra. To address this, we needed a way to evaluate the quality of the reference spectra, such that the orientation measurements

could be performed in a reproducible manner. Initially, we thought DOP might be a good value of merit, but we found that even datasets with similar DOPs didn't always results in the same calculated orientation.

A quantitative method using an additional measurement in an isotropic sample was developed to validate the quality of the obtained reference spectra. The reference spectra can be evaluated either by simulating the isotropic spectrum and comparing it to the measured one or by calculating the order parameter of the measured isotropic spectrum. Both approaches give a clear value of quantitative value of merit, allowing rapid comparison of large amounts of measurements.

The isotropic reference is obtained in a sealed, phase separated LC samples (**Figure 2.17d**). For the first approach, the isotropic spectrum can be simulated using the following expressions for MD and ED transitions respectively

$$I_{iso,MD}(\lambda) = 2 \cdot I_{\pi,MD}(\lambda) + I_{\sigma,MD}(\lambda) \quad \textbf{2.38}$$

$$I_{iso,ED}(\lambda) = I_{\pi,ED}(\lambda) + 2 \cdot I_{\sigma,ED}(\lambda) \quad \textbf{2.39}$$

Figure x shows a comparison of the measured isotropic spectrum (in red) and the simulated isotropic spectrum (in blue) using the reference spectra shown in **Figure 2.24**. To quantitatively compare the measured and simulated spectra, the mean squared error is computed for each transition. From this, the first measurement taken of the nematic droplet in the spaced cell seems to provide the best match, which has the lowest mean squared error (**Figure 2.24a**). The thin film reference performs very poorly, but this may also be due to the optical setup at the time, as it is the only dataset performed on a previous iteration of the microscopy configuration.

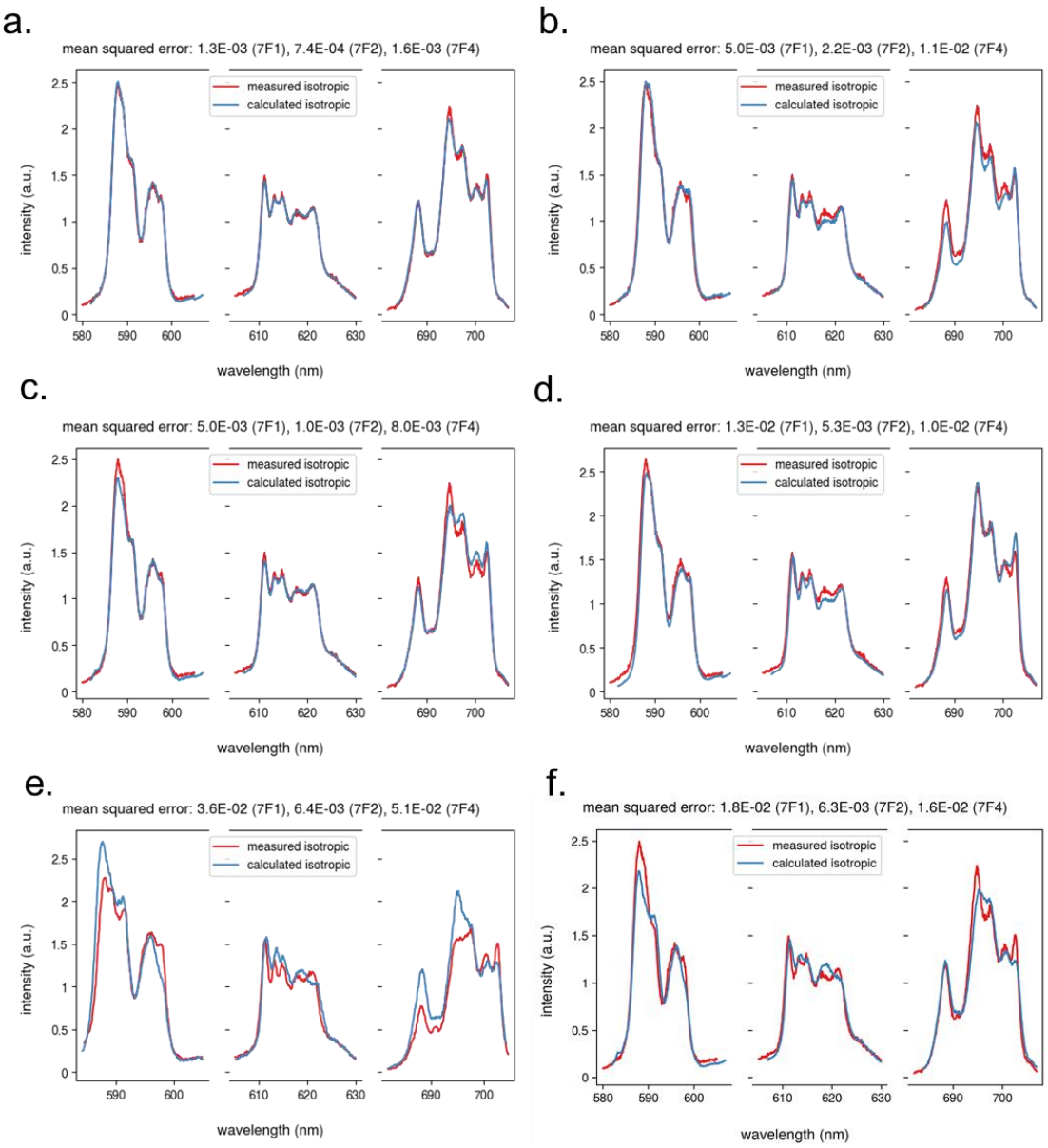

Figure 2.24 Comparison of the measured isotropic spectrum in a diluted sample (from **Figure 2.17b)** and the simulated isotropic spectrum based on the reference spectra. **a-f)** match the samples of **Figure 2.23**

It should be noted that samples with a low DOP can still provide a simulated isotropic spectrum which is very close to the measured one. However, for low DOP samples it is likely that the measured reference spectra contain a significant contribution from the α component. This would distort the measured orientation and it is therefore better to evaluate the reference in a different way.

In the second approach, the quality of the reference spectra is evaluated by computing the order parameter and comparing it to the expected value. For a diluted isotropic suspension, there should be no collective order and the (homeotropic) order parameter should therefore be 0. The homeotropic order parameter S_{homeo} can be found by curve fitting the measured isotropic spectrum using I_π and I_σ as

inputs. To consider the intensity fluctuations of the transitions, the fits include a constant scaling factor such that

$$I_{z,MD}(\lambda) = constant * \left((1 - S_{homeo}) \cdot I_{\pi,MD+\sigma,MD}(\lambda) + (1 + 2 \cdot S_{homeo}) \cdot I_{\alpha,MD}(\lambda)\right) \quad \textbf{2.40}$$

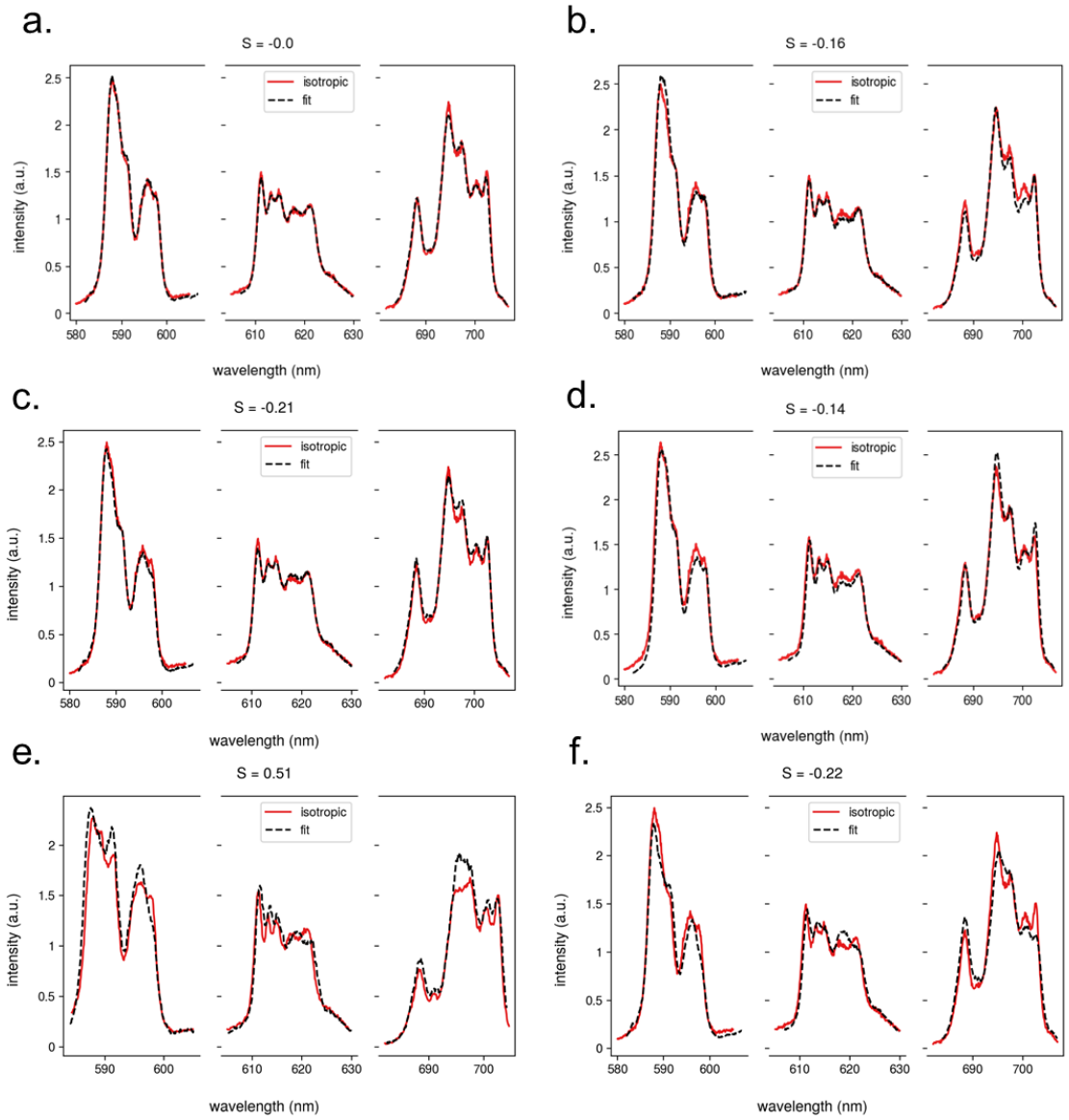

Figure 2.25 Homeotropic order parameter calculated by curve fit of the measured isotropic spectrum using the reference spectra from **Figure 2.17d. a-f)** match the samples of **Figure 2.23**

As discussed prior, I_α is identical to I_π for MD transitions and to I_σ for ED transitions. **Figure 2.25** shows the results of the spectral fitting. Remarkably, the calculated order parameter value varies significantly depending on the reference. Considering **Figure 2.25a,c** we see that although the spectral shape of I_π and I_σ looked very similar (**Figure 2.23a,c**), $S_{homeo} = 0.0$ for one and $S_{homeo} = -0.21$ for the other. This difference can be attributed to the decreased DOP as seen from the k-diagrams (insets **Figure 2.23a,c**).

Notably, we see that the simulated isotropic spectrum and the spectral fitting based on the 20% doped sample doesn't provide a good match for the isotropic spectrum measured in the 5% doped sample (**Figure 2.25f**). The increased doping rate creates distortions in the lattice parameter and inevitably increases the number of defects, impacting the fine emission spectrum. It is also possible that slight differences in synthesis conditions may affect the emission spectra in a similar manner. It is therefore best to use the same sample for obtaining the reference spectra as the one used for orientation measurements.

Amongst the samples shown here, only one of them finds the correct value of S_{homeo} and can thus be used for the orientation analysis. It should be noted that many other reference spectra were obtained from various nematic samples which also had a similar DOP and passed the quality evaluation of $S_{homeo} \approx 0$. However, finding such reference spectra may require many measurements at different positions or in different samples. In order to easily identify a good reference amongst many measurements, the code automatically calculates S_{homeo} when selecting the reference spectra from the polar diagram.

Wavelength dependency of the polarization angle

Initially, when we checked the polarization behavior of the microscopy setup using a monazite sample, we didn't find any wavelength dependency on the polarization state (discussed in **section 2.2.2**). However, throughout the many reference measurements performed, we found that this was not always the case. **Figure 2.26a-b** shows the polarized emission and the integrated peak intensities while rotating the analyzer. By fitting each polar diagram with the expression

$$I(\theta) = I_\sigma \cdot sin^2(\theta - \alpha) + I_\pi \cdot cos^2(\theta - \alpha) \qquad \textbf{2.41}$$

the orientation of each dumbbell (the angle α) can be found. Plotting the change in α as a function of the change in the wavelength reveals a linear relationship (**Figure 2.26c**). Due to the low DOP for the peaks for the $^5D_0$-$^7F_2$ transition there is a large error on the α for the corresponding peaks, which causes them to deviate from the linear fit line in red. Over the whole wavelength range of the probed spectrum, this rotation is quite significant (>15°). It is important to find the origin of the rotation, as this may result in systematic errors for the spectroscopic orientation analysis.

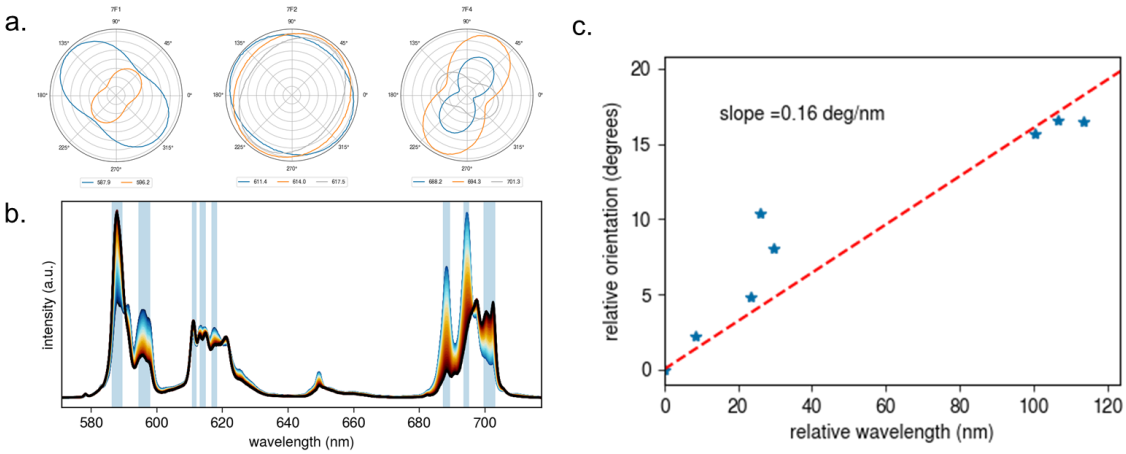

Figure 2.26 Polarized emission sample from nematic droplet in a sealed cell with 60 µm spacer. **a)** Polar diagrams of integrated intensities indicated by blue highlighted regions **b)** polarized emission **c)** Wavelength dependency on the relative orientation of the dumbbells in a).

In order to gain insight into the origin of this wavelength dependent rotation, several additional reference samples were investigated (**Figure 2.27a** and **Figure 5.36**). A different nematic sample (also sealed in a spacer cell) with a different orientation of $\vec{n}$ also showed a linear trend, but now the rotation happened in the other direction, as is seen from the negative slope in **Figure 2.27a**. We then tried aligning a droplet of the same nematic sample using an electric field. Even though $\vec{n}$ is identical to the previous sample, the rotation of the polar diagrams disappears and the polarization axes of all subpeaks have the same orientation. As the measurements with and without electric field were performed on the same nematic sample, we can assume the rod density is comparable. From the DOP, we can also assume that the order parameter is similar. The main difference is therefore that the electric fields helps to align $\vec{n}$ parallel to the surface, which may not be guaranteed in a spontaneous nematic domain. This may suggest that the rotation depends on the out-of-plane tilt angle of $\vec{n}$. However, it is unclear how this can induce the wavelength dependency.

We performed similar measurements inside nematic tactoids. We often observe that tactoids in a confinement cell are tilted (5-20°) with respect to the substrate. Although the DOP of the polar diagrams measured inside the tactoid is lower than that for the large nematic domains, we again observe the linear trend of the dumbbell orientation with respect to the wavelength (**Figure 2.27b**). Similarly, to the nematic, this trend disappears when a tactoid is aligned using the electric field.

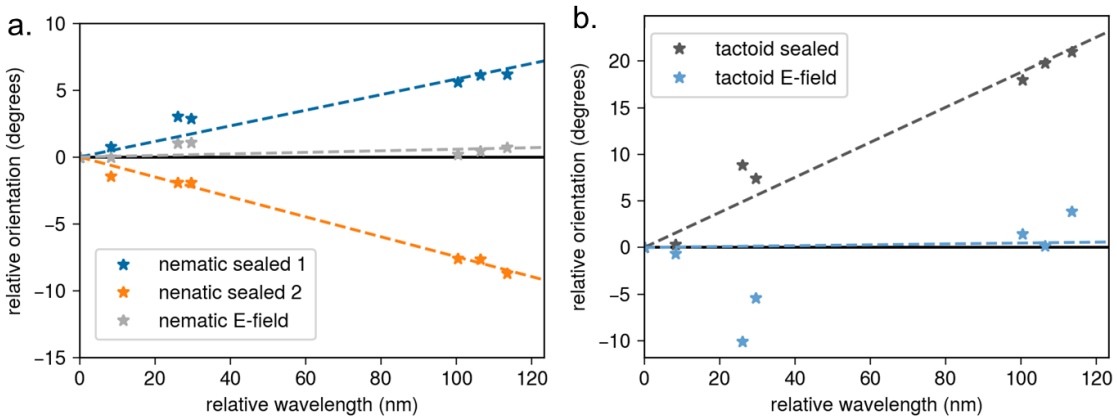

Figure 2.27 Wavelength dependency on the relative orientation of the dumbbells for various **a)** nematic and **b)** tactoid samples respectively. Polar diagrams of the integrated intensity of each peak for each sample can be found in the annex **Figure 5.36**.

There may be several origins to this phenomenon, but we suspect that it is linked to the large NA of the objective. It would be beneficial to perform a more comprehensive study of this effect its dependency of the tilt angle. If there is a clear trend between tilt angle and the rotation of the polarization state, it may provide an alternative method for determining the polar angle of nanorod assemblies. Independent measurements of the polar angle and order parameter is a big challenge and will be discussed in **section 2.4.1**. However, controlling the tilt angle whilst maintaining a high order parameter is challenging and cannot be achieved by applying a simple electric field.

Summary of chapter 2.3

$LaPO_4$:Eu nanocrystals are synthesized through hydrothermal methods in both rhabdophane and monazite phase. Resulting nanorods are highly polydisperse with a mean length of ~150 nm and width of ~8 nm. Suspensions in ethylene glycol (EG) exhibit liquid crystalline (LC) behavior and separate into a nematic and isotropic phase.

The accuracy of the orientation analysis depends on the accuracy of the reference spectra. A methodology for selecting the reference spectra is proposed, using automated Python scripts which can treat large amounts of measurements. Reference spectra are obtained from aligned thin films, nematic LC and under active alignment using an electric field. Their quality is evaluated by simulating the isotropic spectrum and by calculating the order parameter of measured isotropic sample. Finally, we find a wavelength dependent retardation of up to 20° across the PL emission spectrum. This disappears when applying an electric field, suggesting that it may be linked to an out of plane tilt of the director $\vec{n}$.

2.4 Orientation analysis methodology

As discussed in **chapter 2.1.1**, the 3D orientation can be obtained through area under the curve (AUC) ratiometry or by spectral fitting of the measured polarized emission. Although we previously demonstrated orientation analysis in both planar and homeotropic nanorod assemblies[12,36], until now, we did not succeed in characterizing systems with arbitrary $\vec{n}$ in three dimension. In this section the theoretical methodology without any assumption on the orientation of $\vec{n}$ will be derived and its limitations will be discussed. Then, the methodology will be demonstrated in LC assemblies with a known order parameter S, and in flow aligned nanorod suspensions for both a planar and non-planar $\vec{n}$.

2.4.1 Theoretical methodology

As discussed in **section 2.1.1** the polarized emission measured at a specific analyzer angle can be expressed as the sum of the projections of I_π and I_σ. Moreover, expressions for the polarized emission spectra can be formulated using two distinct coordinate systems, illustrated in **Figure 2.28**. θ, ϕ and γ, ψ are the polar and azimuthal angles with respect to the z-axis and y-axis respectively and are analogous to θ', ϕ' and θ, ϕ from **section 2.1.1**.

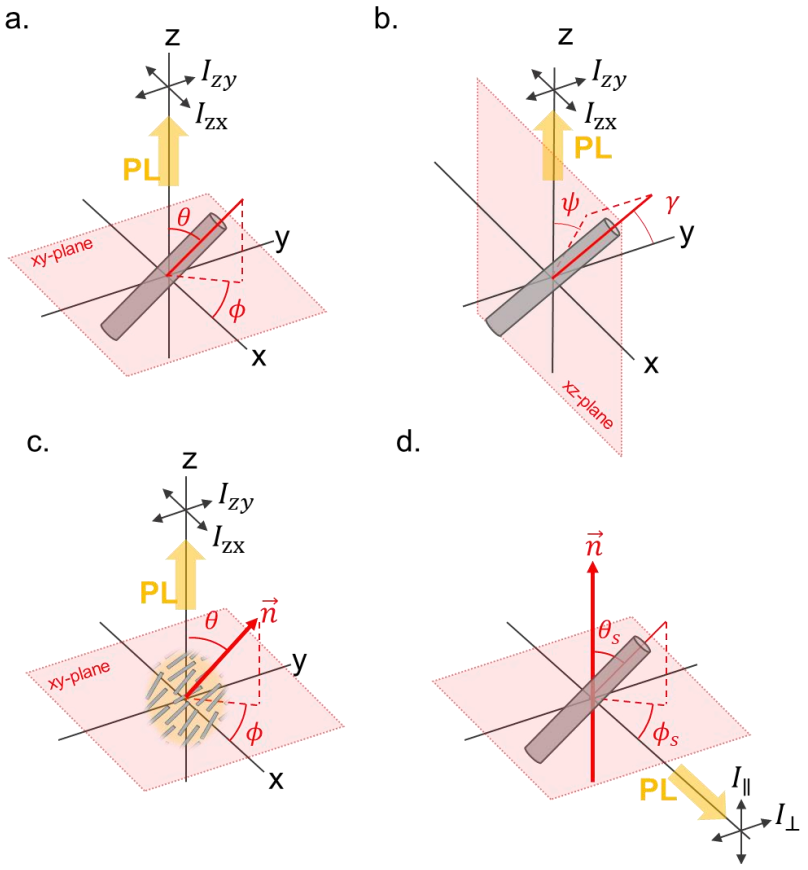

Figure 2.28 Schematic illustration of the various coordinate systems describing the orientation for **a-b)** a single nanorod **c)** the director $\vec{n}$ for an assembly of nanorods **d)** a single nanorod within the assembly. Azimuthal and polar angles **a,c)** θ, ϕ with respect to the z-axis **b)** γ, ψ with respect to the y axis **d)** θ_s, ϕ_s with respect to $\vec{n}$.

We can convert between the two coordinate systems using:

$$\gamma = sin^{-1}\sqrt{1 - sin^2\,\phi \cdot sin^2\,\theta} \quad \textbf{2.42}$$

$$\psi = cos^{-1}\left(\frac{cos\,\theta}{sin^{-1}\sqrt{1 - sin^2\,\phi \cdot sin^2\,\theta}}\right) \quad \textbf{2.43}$$

Depending on the application, it may be more convenient to use a specific coordinate system. In this section, derivation of the equations will be done based on coordinate system 1 (θ, ϕ). The equations for coordinate system 2 (γ, ψ) can be found in **annex 5.2**.

For a single nanorod, the emission spectra measured at orthogonal analyzers are described by **equations 2.16**-**2.17** (where θ',ϕ' correspond to θ, ϕ). Additionally, the emission measured with the analyzer at 45° with respect to the x-axis can be expressed as

$$I_{z45}(\lambda) = I_{\pi}(\lambda) \cdot sin^2\,\theta \cdot cos^2\left(\phi - \frac{\pi}{4}\right) + I_{\sigma}(\lambda) \cdot sin^2\,\theta \cdot sin^2\left(\phi - \frac{\pi}{4}\right) + I_{\alpha}(\lambda) \cdot cos^2\,\theta \quad \textbf{2.44}$$

Using the trigonometric relationships $cos^2\left(x - \frac{\pi}{4}\right) = \frac{1}{2} + \frac{1}{2} \cdot sin\,2x$ and $sin^2\left(x - \frac{\pi}{4}\right) = \frac{1}{2} - \frac{1}{2} \cdot sin\,2x$

$$I_{z45}(\lambda) = \frac{I_{\pi}(\lambda)}{2} \cdot sin^2\,\theta \cdot (1 + sin\,2\phi) + \frac{I_{\sigma}(\lambda)}{2} \cdot sin^2\,\theta \cdot (1 - sin\,2\phi) + I_{\alpha}(\lambda) \cdot cos^2\,\theta \quad \textbf{2.45}$$

For a collection of rods, $I_{\pi}(\lambda)$ and $I_{\sigma}(\lambda)$ can be replaced by $I_{\parallel}(\lambda)$ and $I_{\perp}(\lambda)$ respectively as defined in **equations 2.22**-**2.25**. Using $I_{\alpha,MD}(\lambda) = I_{\pi,MD}(\lambda)$ and $I_{\alpha,ED}(\lambda) = I_{\sigma,ED}(\lambda)$ the PL for each analyzer axis becomes, for MD transitions,

$$I_{zx,MD}(\lambda) = I_{\parallel,MD}(\lambda) \cdot (sin^2\,\theta \cdot cos^2\,\phi + cos^2\,\theta) + I_{\perp,MD}(\lambda) \cdot sin^2\,\theta \cdot sin^2\,\phi \quad \textbf{2.46}$$

$$I_{zy,MD}(\lambda) = I_{\parallel,MD}(\lambda) \cdot (sin^2\,\theta \cdot sin^2\,\phi + cos^2\,\theta) + I_{\perp,MD}(\lambda) \cdot sin^2\,\theta \cdot cos^2\,\phi \quad \textbf{2.47}$$

$$I_{z45,MD}(\lambda) = \frac{I_{\parallel,MD}(\lambda)}{2} \cdot (sin^2\,\theta \cdot (1 + sin\,2\phi) + 2\,cos^2\,\theta) + \frac{I_{\perp,MD}(\lambda)}{2} \cdot sin^2\,\theta \cdot (1 - sin\,2\phi) \quad \textbf{2.48}$$

and for ED transitions

$$I_{zx,ED}(\lambda) = I_{\parallel,ED}(\lambda) \cdot sin^2\,\theta \cdot cos^2\,\phi + I_{\perp,ED}(\lambda) \cdot (sin^2\,\theta \cdot sin^2\,\phi + cos^2\,\theta) \quad \textbf{2.49}$$

$$I_{zy,ED}(\lambda) = I_{\parallel,ED}(\lambda) \cdot sin^2\,\theta \cdot sin^2\,\phi + I_{\perp,ED}(\lambda) \cdot (sin^2\,\theta \cdot cos^2\,\phi + cos^2\,\theta) \quad \textbf{2.50}$$

$$I_{z45,ED}(\lambda) = \frac{I_{\parallel,ED}(\lambda)}{2} \cdot sin^2\,\theta \cdot (1 + sin\,2\phi) + \frac{I_{\perp,ED}(\lambda)}{2} \cdot (sin^2\,\theta \cdot (1 - sin\,2\phi) + 2\,cos^2\,\theta) \quad \textbf{2.51}$$

Additionally, for both types of dipole transition, I_{z45} can be expressed in terms of I_{zx} and I_{zy} such that

$$2 \cdot I_{z45}(\lambda) = I_{zx}(\lambda) + I_{zy}(\lambda) + \left(I_{zx}(\lambda) - I_{zy}(\lambda)\right) \cdot tan(2\phi) \quad \textbf{2.52}$$

Then by substituting the expression of $I_{\parallel}(\lambda)$ and $I_{\perp}(\lambda)$ from **equations 2.22**-**2.25** into **equations 2.46**-**2.51** and using the following definitions

$$x \equiv \langle cos^2\,\theta_s \rangle\,, y \equiv sin^2\,\theta\,, z \equiv cos^2\,\phi \qquad \textbf{2.53}$$

We find for MD transitions,

$$I_{zx,MD}(\lambda) = \frac{I_{\pi,MD}(\lambda)}{2} \cdot \big(1 + x + y \cdot (1 - 3x) \cdot (1 - z)\big) + \frac{I_{\sigma,MD}(\lambda)}{2} \cdot \big(1 - x - y \cdot (1 - 3x) \cdot (1 - z)\big) \qquad \textbf{2.54}$$

$$I_{zy,MD}(\lambda) = \frac{I_{\pi,MD}(\lambda)}{2} \cdot \big(1 + x + z \cdot y \cdot (1 - 3x)\big) + \frac{I_{\sigma,MD}(\lambda)}{2} \cdot \big(1 - x - z \cdot y \cdot (1 - 3x)\big) \qquad \textbf{2.55}$$

and for ED transitions,

$$I_{zx,ED}(\lambda) = \frac{I_{\pi,ED}(\lambda)}{2} \cdot \big(1 - x - z \cdot y \cdot (1 - 3x)\big) + \frac{I_{\sigma,ED}(\lambda)}{2} \cdot \big(1 + x + z \cdot y \cdot (1 - 3x)\big) \qquad \textbf{2.56}$$

$$I_{zy,ED}(\lambda) = \frac{I_{\pi,ED}(\lambda)}{2} \cdot \big(1 - x - y \cdot (1 - 3x) \cdot (1 - z)\big) + \frac{I_{\sigma,ED}(\lambda)}{2} \cdot \big(1 + x + y \cdot (1 - 3x) \cdot (1 - z)\big) \qquad \textbf{2.57}$$

The expressions for $I_{z45°}$ are of the same form as I_{zx} but with $z \equiv \cos^2 \phi - \frac{\pi}{4}$. Rewriting the expression in this way shows that the measured spectra always depend on the term $y \cdot (1 - 3x) \equiv sin^2\,\theta \cdot (1 - 3 \cdot \langle cos^2\,\theta_s \rangle)$. This implies that there are no unique solutions for $sin^2\,\theta$ and $\langle cos^2\,\theta_s \rangle$. This poses an important limitation to our orientation analysis methodology, as it is impossible to determine both the order parameter and the polar angle without making any assumptions. Instead, we can do the orientation analysis for two types of assumptions, either the order parameter is known (**section 2.4.2**) or the polar angle is known (**sections 2.4.4** for $\theta = 90°$ and **section 2.4.5** for arbitrary θ)

2.4.2 Measurement of three-dimensional orientation for a known order parameter

If the order parameter is known, the value of $\langle \cos^2 \theta_s \rangle$ is known and we can find the orientation either by a curve fit approach or by area under the curve (AUC) analysis. Both methods will be demonstrated using a liquid crystal sample (**Figure 2.29**). The nature of the LC structure and a full demonstration of 3D orientation tomography will be detailed in **chapter 3**.

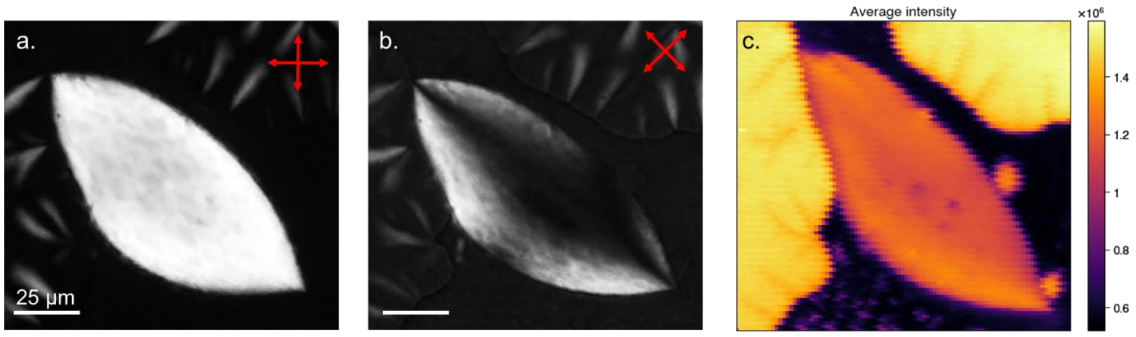

Figure 2.29 Liquid crystal sample used to demonstrate 3D orientation analysis containing a tactoid droplet and two flower domains surrounded by the isotropic phase. **a-b)** PLM images with crossed polarizers at 0° and 45° respectively. **c)** Total PL intensity averaged between the spectra measured at the 3 analyzer angles.

The example system consists of a nematic tactoid droplet placed between two flower-like nematic domains. As discussed in **chapter 1.1.1**, tactoids are a typical LC structure whereas the flower-like domain has not previously been reported. From our previous work, we expect the flower domain to be mostly close to homeotropically aligned, whereas the tactoid is expected to be planar with $\vec{n}$ following it's shape (see **Figure 2.8**). Polarized light microscopy (PLM) allows to approximate the orientation $\vec{n}$, as will be discussed in **chapter 3.3.1**. **Figure 2.29a-b** shows PLM images of the LC for two different orientations of the crossed polarizers. From the bright birefringence inside the tactoid, we can indeed assume that $\vec{n}$ is close to planar and the variation in intensity when rotating the crossed polarizers suggests that the $\vec{n}$ follows its contours.

Tomographic measurements of the emission spectra were performed by scanning over the sample in 1.25 µm steps. After scanning the full plane with the analyzer parallel to the x-axis, the scan is repeated for analyzer angles at 45° and 90°. Due to the high nanorod density, we only needed a small laser power of 1 mW and a relatively short exposure time of 20 milliseconds was enough to obtain spectra with excellent signal to noise ratio.

Mapping the PL intensity allows to identify the dense, well aligned regions (**Figure 2.29c**). This is because the PL intensity is directly proportional to the nanorod density, and the nematic (collectively aligned) phase of the LC has a higher density than the isotropic phase[2]. Although the flower domains remain dark for all polarizer angles, it is brightly luminescent which indicates a homeotropically (vertically) aligned nematic. This is therefore a suitable sample to evaluate the performance of the orientation analysis as $\vec{n}$ spans a wide range of θ and ϕ angles throughout.

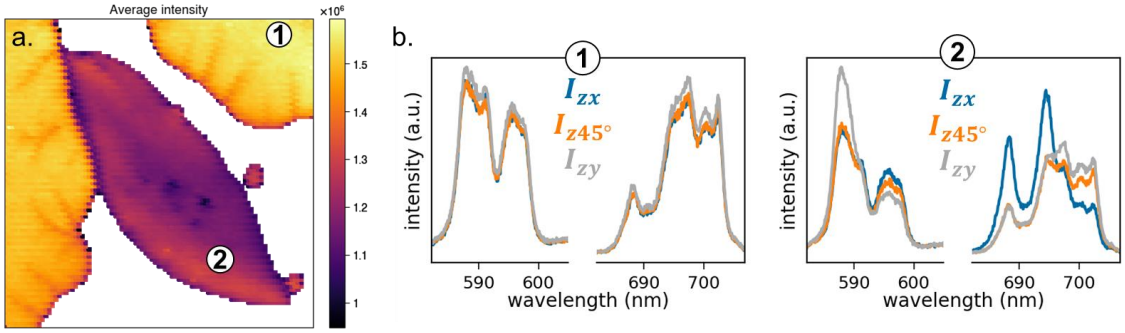

Figure 2.30 a) Average PL intensity. A mask has been applied such that the isotropic phase, which produces weak PL intensity, is hidden. **b)** Emission spectra I_{zx} (blue), $I_{z45°}$ (green) and I_{zy} (orange) for two different positions as indicated in **a**.

As the isotropic phase lacks collective orientation behavior, we apply a mask based on the PL intensity such that only the nematic domains are considered (**Figure 2.30a**). **Figure 2.30b-c** shows two examples of the emission spectra collected within the homeotropic flower regime and inside the tactoid for each analyzer axis. The baseline was subtracted using the procedure described in section **2.3.3**, but not normalized. As expected, the spectra in region 1 are not polarized but follow I_α such that for the MD transition the measured emission is identical to I_π and for the two ED transitions it is I_σ. In contrast, emission collected in the planar tactoid is polarized. In the case of the spectra shown in **Figure 2.30c**, we can deduce that the local absolute azimuthal orientation $|\phi|$ is close to 45°, as $I_{z45,MD} \sim I_{zx,MD}$ and $I_{z45,ED} \sim I_{zy,ED}$. The precise 3D orientation for each location can be found either by spectral fitting or AUC ratiometry using a Python script. Due to the low DOPs associated with the $^5D_0$-$^7F_2$ transition of the rhabdophane phase, only the $^5D_0$-$^7F_4$ transition is considered as the ED transition.

Spectral fitting

In order to find the values of $\sin^2\theta$ and $\cos^2\phi$ by spectral fitting approach, at least two different expressions from **equations 2.54-2.57** are required. The expressions for $I_{zx,MD}$ and $I_{zy,ED}$ are a function of $\sin^2\theta \cdot (1-\cos^2\phi)$ whereas $I_{zx,MD}$ and $I_{zy,MD}$ depend on $\sin^2\theta \cdot \cos^2\phi$. To have unique solutions, a combination of two types of expressions should therefore be used for the curve fit analysis. This means there are five different combinations to do the orientation analysis; the full spectrum for I_{zx} or I_{zy}, the MD or ED transitions of both I_{zx} and I_{zy} or both spectra for both dipoles. Here, the spectral fitting will be demonstrating using the full I_{zx}. A thorough discussion and comparison of the other possible combinations of measured spectra is given in **annex 5.3.1**.

For the spectral fitting, we only consider the main transition peaks, corresponding to 582-602 for MD and 682-702 nm for ED as seen in **Figure 2.31**. Normalization is not necessary as the spectral fitting is performed using a constant weighing factor to match the measured intensity to the intensity of the reference spectra. This is necessary to obtain a good fit for both MD and ED, as the relative intensity of

the $^5D_0$-$^7F_4$ compared to the $^5D_0$-$^7F_1$ may vary. The measured spectra are fit with the **expressions 2.54 and 2.56** multiplied with independent weighing factors for the MD and ED transition respectively. In order to find a unique solution, the value of $\langle \cos^2 \theta_s \rangle$ should be fixed. To estimate $\langle \cos^2 \theta_s \rangle$, we consider that S is constant throughout the sample and measure S_{homeo} in a homeotropic regime close to the substrate (see annex **Figure 5.37**) and set it to 0.9 (corresponding to $S = 0.85$). and the fitting applies bounds of [0,1] for both $\sin^2 \theta$ and $\cos^2 \phi$ and [0,∞] for the weighing factors. The resulting curve fit and corresponding $\sin^2 \theta$ and $\cos^2 \phi$ for positions 1 and 2 are shown in **Figure 2.31b-c**.

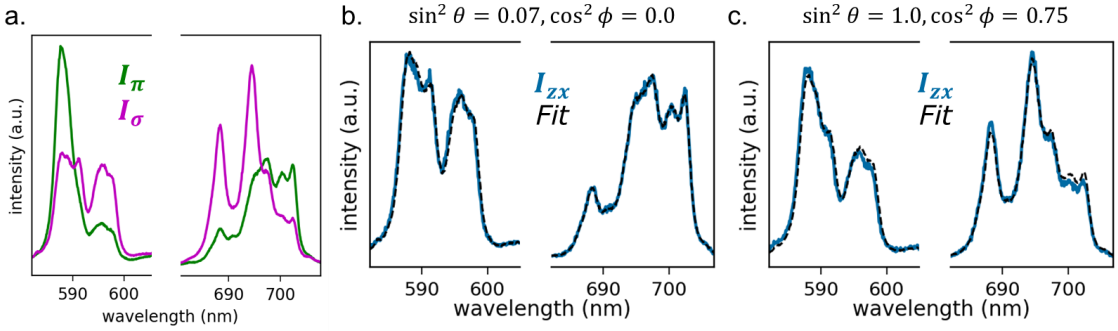

Figure 2.31 a) Reference spectra I_π and I_σ. **b-c)** example fits of the I_{zx} spectrum for positions 1 and 2 as indicated in **Figure 2.30a**.

Comparing I_{zx} at point 1 and 2, we can see that the curve fit for the spectrum at point 2 is slightly less accurate. This is most likely due to the saturations of the $\sin^2 \theta$ value at 1.0, which makes it impossible to find a perfect fit. Considering many curve fits throughout the sample (annex **Figure 5.38**), we see that as long as the value for $\sin^2 \theta$ is within the range [0,1] we always get a close to perfect curve fit. In the case where $\sin^2 \theta$ is at its limits, we still have a good curve fit with similar quality to the example at point 2 in **Figure 2.31**. Repeating the spectral fitting procedure for all positions results in the maps of $\sin^2 \theta$ and $\cos^2 \phi$ and the corresponding absolute angles $|\theta|$ and $|\phi|$ seen in **Figure 2.32a-d**. As expected, $\vec{n}$ inside the tactoid is fully planar, whereas it is homeotropic in the flower domain. We can also identify some small isotropic islands next to and near the bottom right tip of the tactoid.

Finally, the mirror angle is eliminated by comparing the intensity ratio of the two subpeaks of the MD transition for all three polarizer angles, as will be discussed in **section 2.4.3**. **Figure 2.32e** shows the found director field overlaid on the average PL intensity, where the orientation of bars corresponds to ϕ and their length to $\sin \theta$. We retrieve the expected azimuthal director profile for a colloidal tactoid, with $\vec{n}$ following the contours of the droplet[54]. The high spatial resolution of our microscopy setup also makes it possible to observe a slight deviation in this $\vec{n}$ profile near the interface of the two nematic domains.

A thorough discussion of the accuracy of the found $\vec{n}$ profile can be found in **annex 5.3.2.**

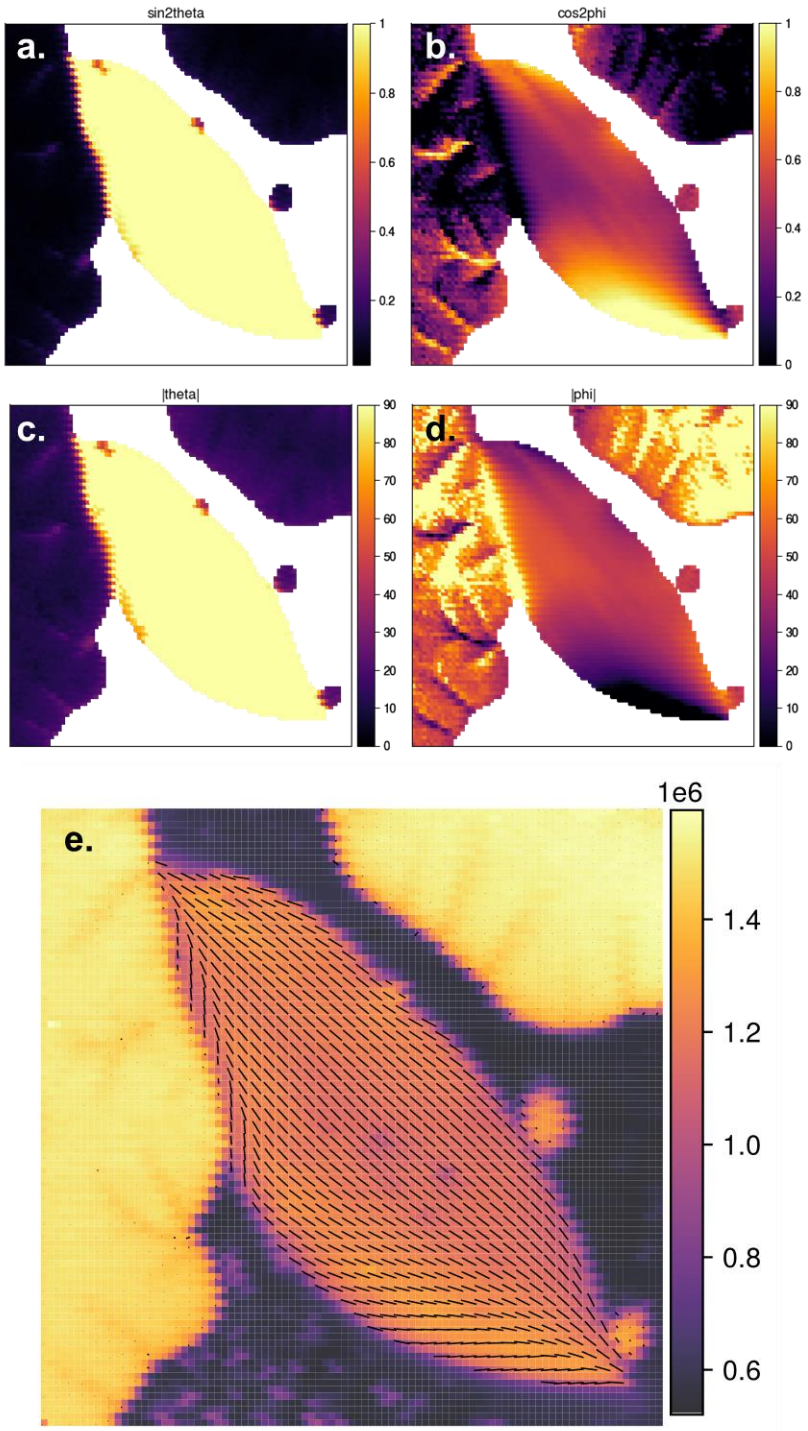

Figure 2.32 Calculated values found by the spectral fitting of I_{zx} **a)** $\sin^2\theta$ and **b)** $\cos^2\phi$ and corresponding absolute angles **c)** $|\theta|$ and **d)** $|\phi|$ **e)** $\vec{n}$ projected onto the xy-plane. The color indicates the average PL intensity.

Area under the curve ratiometry

In the second approach, we don't consider the complex line shape of the measure PL, but instead calculate the AUC (or integrated intensity) of two subpeaks per transition. We then compare the calculated values to the values corresponding to the same subpeaks in the reference spectra. We define the following constants

$$A \equiv I_{\pi,D1}, \qquad B \equiv I_{\sigma,D1}, \qquad C \equiv I_{\pi,D2}, \qquad D \equiv I_{\sigma,D2} \tag{2.58}$$

which correspond to the integrated intensity of the subpeaks for the reference I_π and I_σ spectra. **Figure 2.33a** shows the reference spectra with the subpeak ranges indicated in blue. The choice for the wavelength range considered as one subpeak is discussed in **annex 5.3.1**.

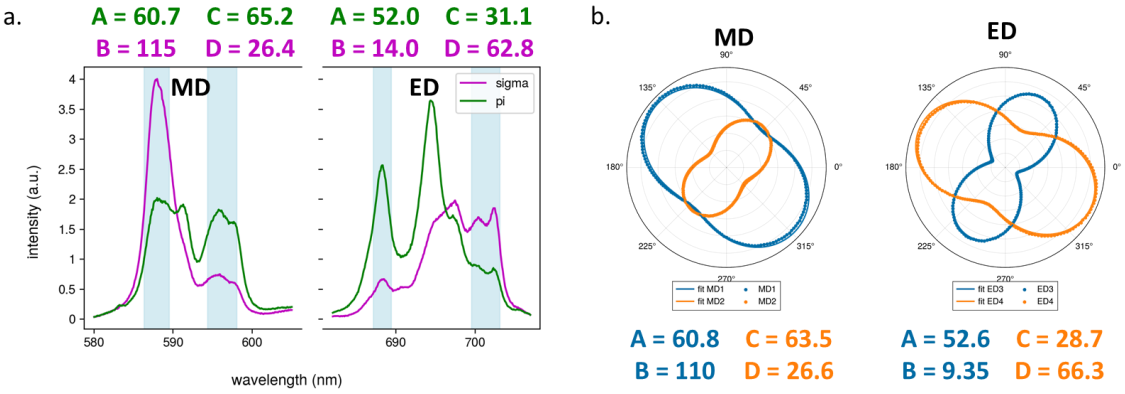

Figure 2.33 Calculation of area under the curve (AUC) for each subpeak of the reference spectra. **a)** I_π and I_σ reference spectra and the regions corresponding to the subpeaks highlighted in blue. The AUC values are found by integrating the I_π and I_σ spectra. **b)** Polar diagrams of the AUC for each subpeak corresponding to 180 different measurements. The reference AUC values are found by curve fitting each dumbbell to **expression 2.37**.

The A,B,C,D constants can either be extracted from the curve fit of the polar diagrams or by integrating the individual spectra, as is illustrated in **Figure 2.33**. For the MD transition both methods yield very similar values (typically below 5% difference), however for the ED transition the B and C value are significantly smaller when found through the curve fit approach. This occurs when there is a wavelength dependent rotation of the polarization state, as was discussed in **section 2.3.3**. It is therefore better to use the values found from the polar diagram fits, as they are not affected by the absolute orientation of each dumbbell.

Instead of comparing the absolute AUC values, we consider the ratio $k = \frac{I_{D1}}{I_{D2}}$ where I_{D1} and I_{D2} refer to the integrated intensity of two subpeaks from the same dipole transition. By taking the ratio of two subpeaks, there is no need for normalization and the analysis will not be affected by global intensity variations. **Figure 2.34** maps the AUC for each subpeak and the corresponding k-values for the measured I_{zx} spectra. Similar plots for I_{zy} and $I_{z45°}$ can be found in the annex (**Figure 5.40** and **Figure 5.41**). In

theory, the k-values cannot exceed the corresponding k-values of the reference. This means that we k-MD should be within 0.96-4.14 and k-ED within 0.14-1.83, which indeed seems to be the case.

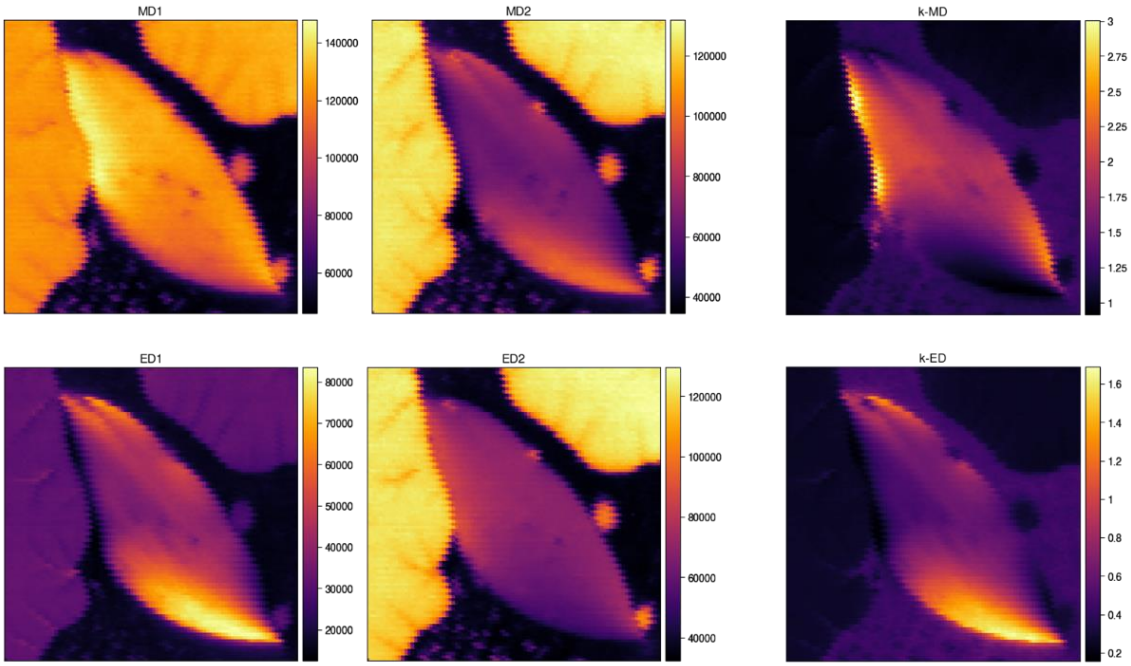

Figure 2.34 AUC for the two subpeaks of the MD and ED transitions and the corresponding k-values such that k-MD = MD1/MD2 and k-ED = ED1/ED2 for I_{zx}

Then to find the orientation from the measured k-values, we can rearrange the definitions for I_{zx} (**equations 2.54-2.57**) for each dipole such that for MD and ED transitions,

$$y \cdot (1-z) = \frac{\left(A_{MD} - k_{zx,MD} \cdot C\right) \cdot (1+x) + \left(B_{MD} - k_{zx,MD} \cdot D_{MD}\right) \cdot (1-x)}{(1-3x) \cdot \left(-A_{MD} + B_{MD} + k_{zx,MD} \cdot (C-D)\right)} \quad \textbf{2.59}$$

$$y \cdot z = \frac{\left(A_{ED} - k_{zx,ED} \cdot C\right) \cdot (1-x) + \left(B_{ED} - k_{zx,ED} \cdot D_{ED}\right) \cdot (1+x)}{(1-3x) \cdot \left(A_{ED} - B_{ED} - k_{zx,ED} \cdot (C_{ED} - D_{ED})\right)} \quad \textbf{2.60}$$

Similar equations for I_{zy} are found in the annex (**equations 5.18-5.19**). The values of $\sin^2\theta$ and $\cos^2\phi$ can be found by combining a together the expressions for the MD and ED transitions (**equations 2.59 and 2.60**) such that

$$sin^2\,\theta = y = \frac{\left(A_{MD} - k_{zx,MD} \cdot C_{MD}\right) \cdot (1+x) + \left(B_{MD} - k_{zx,MD} \cdot D_{MD}\right) \cdot (1-x)}{(1-3x) \cdot \left(-A_{MD} + B_{MD} + k_{zx,MD} \cdot (C_{MD} - D_{MD})\right)} + \frac{\left(A_{ED} - k_{zx,ED} \cdot C_{ED}\right) \cdot (1-x) + \left(B_{ED} - k_{zx,ED} \cdot D_{ED}\right) \cdot (1+x)}{(1-3x) \cdot \left(A_{ED} - B_{ED} - k_{zx,ED} \cdot (C_{ED} - D_{ED})\right)} \quad \textbf{2.61}$$

$$cos^2\,\phi = z = \frac{1}{y} \cdot \frac{\left(A_{ED} - k_{zx,ED} \cdot C_{ED}\right) \cdot (1-x) + \left(B_{ED} - k_{zx,ED} \cdot D_{ED}\right) \cdot (1+x)}{(1-3x) \cdot \left(A_{ED} - B_{ED} - k_{zx,ED} \cdot (C_{ED} - D_{ED})\right)} \quad \textbf{2.62}$$

Then using the estimated value for $x = \langle \cos^2 \theta_s \rangle$ (in this case S is assumed to be 0.85) and the k-values of I_{zx} (**Figure 2.34**), we find the $\sin^2 \theta$ and $\cos^2 \phi$ and corresponding $|\theta|$ and $|\phi|$ distributions shown in **Figure 2.35a-d**. Similar analysis can be performed on other combinations of k_{zx} and k_{zy}, or based on the equations formulated for coordinate system 2 (**Figure 2.28b**), as is discussed in detail in **annex 5.3.1**.

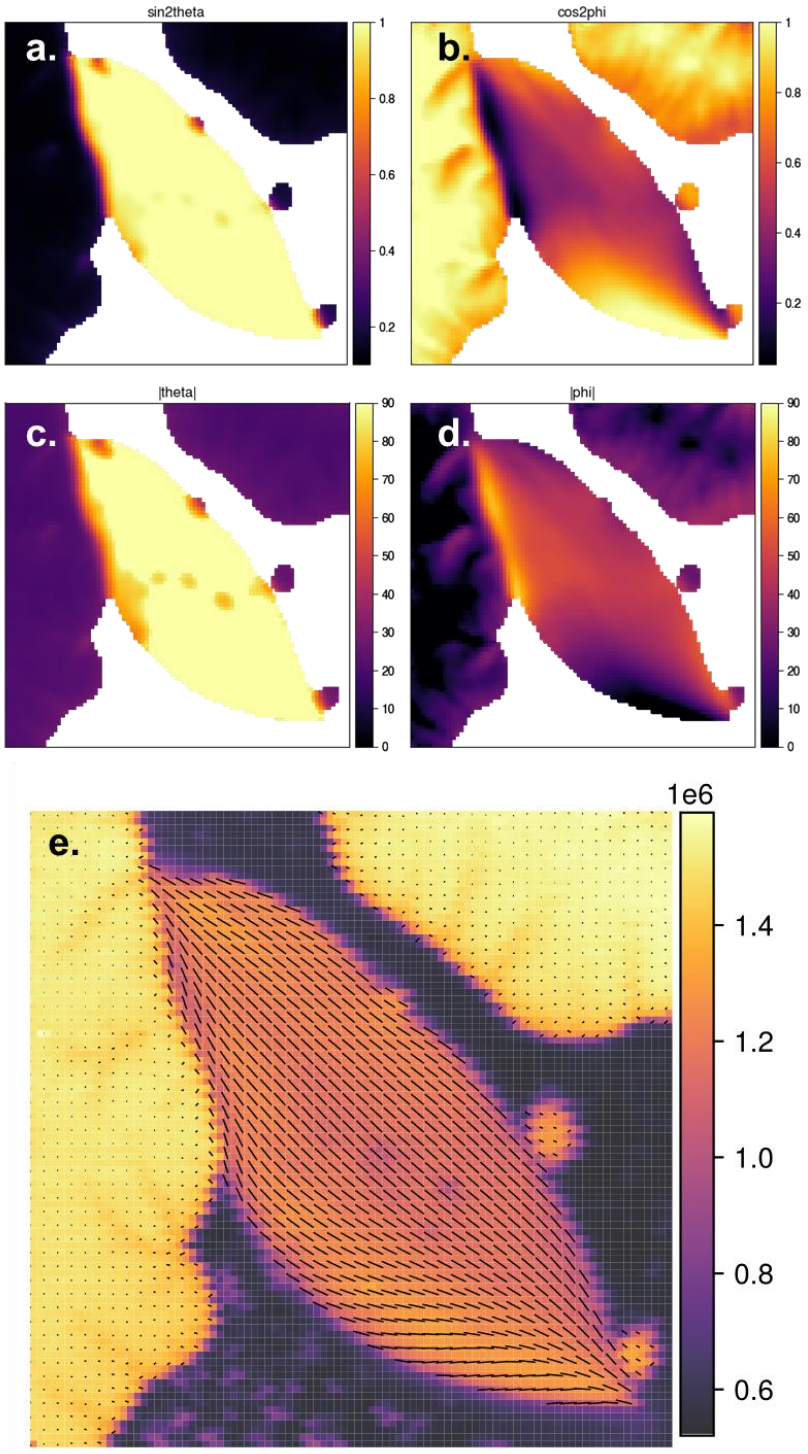

Figure 2.35 Calculated orientation found by AUC analysis using $k_{zx,MD}$ and $k_{zx,ED}$. **a)** $\sin^2 \theta$ and **b)** $\cos^2 \phi$ and corresponding absolute angles **c)** $|\theta|$ and **d)** $|\phi|$. **e)** Shows $\vec{n}$ projected onto the xy-plane. The color indicates the average PL intensity.

As the range of both $\sin^2(\quad)$ and $\cos^2(\quad)$ functions are [0,1], if the calculated values are outside of this range we set it to the closest extreme. Hence why $\sin^2\theta$ saturates to 1 for most of the tactoid. When $\sin^2\theta$ is small, meaning the orientation is homeotropic, the value for $cos^2\phi$ doesn't carry much physical meaning and we expect a large associated error. This is why $\sin^2\theta$ is calculated first and used as an input to find $\cos^2\phi$, rather than vise versa. The $1/\sin^2\theta$ dependency of **equation 2.62** explains why $\cos^2\phi$ as calculated by this AUC approach is always close to one in the homeotropic regions. The mirror angle of $|\phi|$ is eliminated and the projected $\vec{n}$ profile is plotted on top of the average PL intensity (**Figure 2.35e**). The projected director profile is quite comparable to that found by spectral fitting of I_{zx} (**Figure 2.32e**). However, $\sin^2\theta$ is consistently larger inside the homeotropic flower domain, with corresponding values $|\theta|$ around 35°.

Comparison of spectral fitting and AUC ratiometry

Finally, we compare the different spectral analysis techniques considered. Let's consider the orientation obtained by analysis of the I_{zx} spectra for both MD and ED peaks, shown in **Figure 2.32** and **Figure 2.35**. To compare the results, the absolute difference in the calculated orientation is plotted in **Figure 2.36**. Inside the homeotropic flower domain, there is generally a significant difference between θ_{SF} and θ_{AUC} of more than 10°. In fact, AUC ratiometry seems to generally give higher values of θ in homeotropic regions considering all other combinations of spectral segments. In terms of the tactoid region, θ is relatively consistent between the two methods, except for some specific regions near the tactoid/flower interface and the center. The total integrated intensity from I_{zx} is lower in these regions (see annex **Figure 5.44**), which could introduce an error especially for the AUC approach.

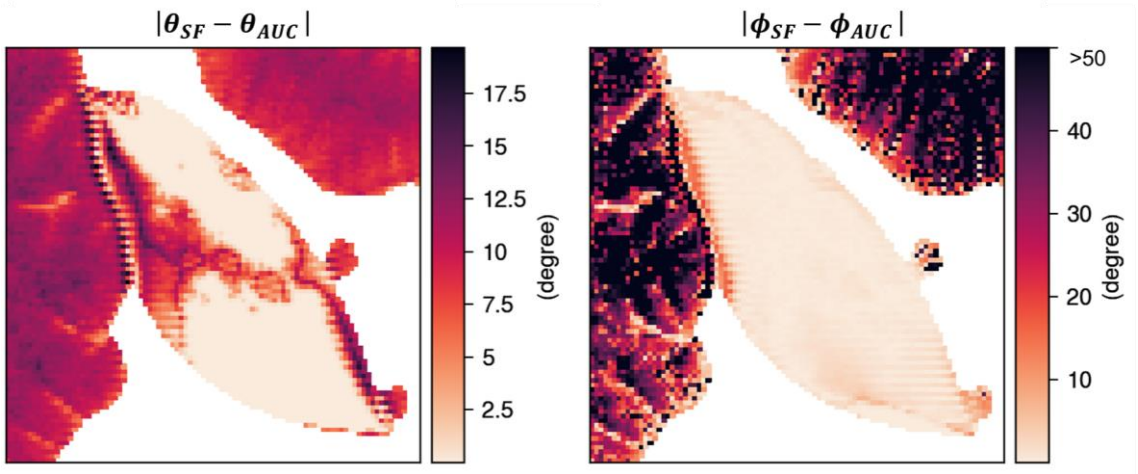

Figure 2.36 Difference between orientation calculated through spectral fitting and AUC ratiometry based on analysis of the I_{zx} spectrum.

In terms of the azimuthal orientation ϕ, there is almost no difference (< 5°) between the two methods when considering the planar regions inside the bulk of the tactoid. Comparing ϕ in the homeotropic

domains is not very meaningful, as its calculation is dominated by $\theta \to 0°$. This demonstrates that, the same spectrum will yield the same calculated value of ϕ, no matter if spectral fitting or AUC ratiometry is used.

2.4.3 Mirror angle discrimination

In order to distinguish between the mirror angles, we measure the spectrum with the analyzer oriented at 45° with respect to the x-axis. We then consider the k-values, which essentially represent the projection of the ratio of two emission dipole onto the observation plane. Even though the director may not be planar we can consider this projection to distinguish the mirror angles. This can be done by directly comparing 2 k-values to the reference polar diagram, as described in the **annex 5.3.3**, as we previously reported[26]. Here we report an alternative approach, using the definition for the azimuthal angle

$$\phi^* = -\frac{1}{2}\left(tan^{-1}\,\Sigma + \frac{\pi}{2}\cdot\frac{\Sigma}{|\Sigma|}\cdot\left(\frac{\Gamma}{|\Gamma|}+1\right)\right) \qquad \textbf{2.63}$$

where,

$$\Sigma = \frac{2\cdot k_{z45} - k_{zx} - k_{zy}}{k_{zx} - k_{zy}}\,, \qquad \Gamma = k_{zx} - k_{zy}$$

which is adapted from **expression 2.30.** Using the k-values instead of the absolute intensity is important, as it negates global intensity fluctuations based on the analyzer angle. **Figure 2.37** shows the calculated ϕ^* values based on evaluating **expression 2.63** for the k-values associated to the MD or ED transition. If $\vec{n}$ is close to homeotropic, all k-values should be close to identical. This will always generate $\phi^* = \pm 45°$, due to the fact that $\Sigma = 0$ and $\Gamma = 0$. This is indeed what is observed in **Figure 2.37**, for MD ϕ^* approaches $+45°$ and for ED it goes to $-45°$. We could also consider directly using ϕ^* as the azimuthal angle to form the director plot. Although the resulting director plot is quite similar to those found by spectral fitting, there are some slight disturbances near the edges of the tactoid (in annex **Figure 5.43**). Additionally, the difference between ϕ^* found from MD and ED is similar to that found by spectral fitting and may be attributed to the wavelength dependent rotation of the polarization axis.

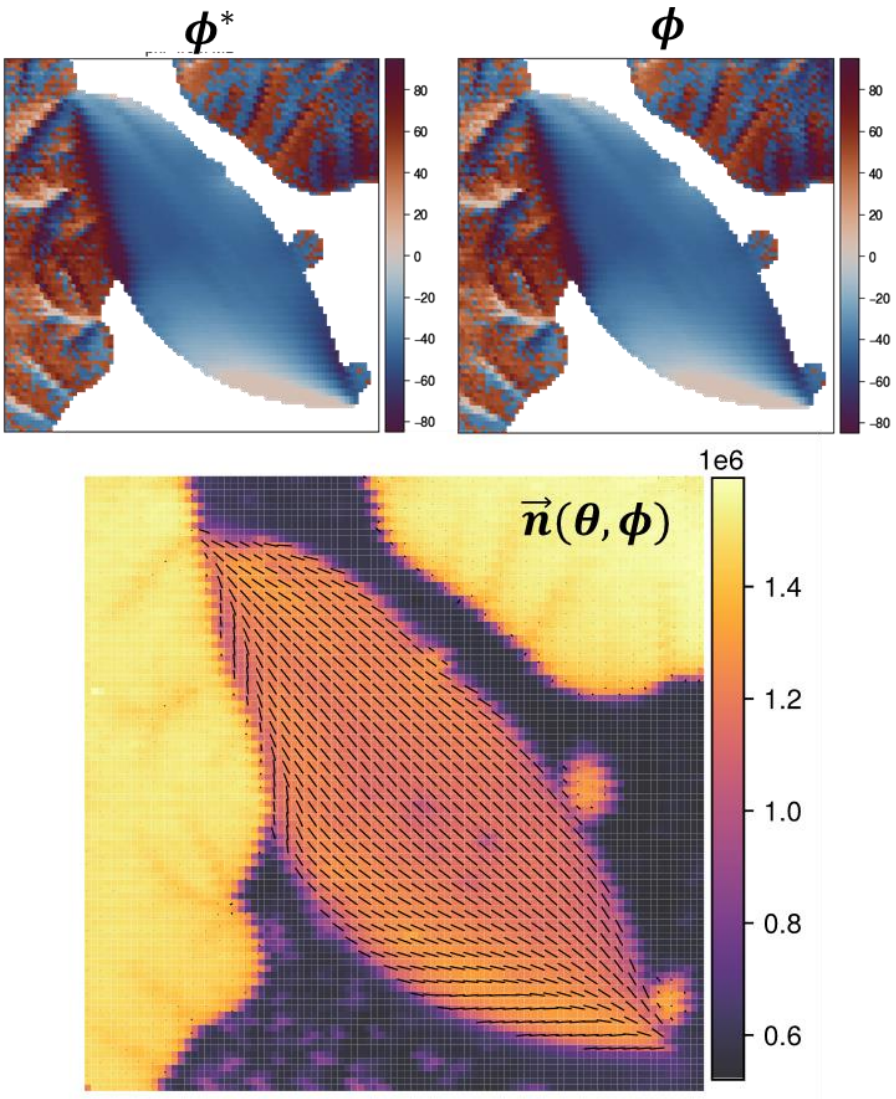

Figure 2.37 Mirror angle elimination based on $k_{zx,MD}$, $k_{zy,MD}$ and $k_{z45°,MD}$. ϕ^* is the azimuthal angle calculated from **equation 2.63**. $|\phi|$ was calculated using the spectral fitting method of both I_{zx} and I_{zy} and the sign of ϕ is then determined by the sign of ϕ^*.

Another approach is to only consider the sign of ϕ^*, but still calculate the value $|\phi|$ using either the spectral fitting or AUC approach. The second column in **Figure 2.37** shows ϕ calculated by a simultaneous spectral fit of I_{zx} and I_{zy} and by distinguishing the mirror angles based on the sign of ϕ^* from **equation 2.63**. In this way, we take advantage of the more sophisticated spectral fitting and avoid the issues associated to AUC or k-value analysis. Although this approach requires three measurements, the advantage is that it does not require the reference spectra I_π and I_σ (unlike the previous method). Moreover, as it is not based on discrete domains, the resulting profile of ϕ is much more uniform than that found by the previous approach.

Polar angle

Until now, there is no spectroscopic method to determine the sign of θ. Instead, careful consideration of the physical system and the associated boundary conditions can be used. As an example, for our LC system, we know $\vec{n}$ should be parallel to the isotropic-nematic interface and we expect a continuous change of the orientation throughout the sample. In the example shown here, the $|\theta|$ is either close to 0 or 90 so there is no significant difference between its two mirror angles. However, in **chapter 3** the mirror angle will be eliminated using the aforementioned boundary conditions.

2.4.4 Measurement of order parameter for a planar director

In order to measure the order parameter of an assembly of nanorods, we need to know the value of θ to obtain unique solutions. The simplest case would be a fully planar director ($\theta = 90°$), as this completely eliminates all $\sin^2\theta$ and $\cos^2\theta$ terms in the expressions for I_{zx}, I_{zy} and $I_{z45°}$ (**equations 2.46**-**2.51**). In this section we will therefor discuss the methodology for finding S assuming a planar director, both based on spectral fitting and AUC ratiometry. **Section 2.4.5** will cover the approach for any value of θ.

As an example system, we will use a microfluidic channel with a constriction, similar to what was used in our original work on orientation monitoring in flow[12]. By performing the measurement at the middle height of the channel, we can assume the director is planar due to the symmetric shear forces in the y-direction. The details of the experimental conditions can be found in **annex 5.1.2**.

As monazite has a higher DOP and luminescence intensity, we prefer to use it for flow experiments. However, the same approach discussed in this section is possible using rhabdophane and is demonstrated in **annex 5.3.5**. Unlike rhabdophane, monazite phase $LaPO_4$:Eu nanorods have an emission spectrum which is highly polarized both for the $^5D_0$-$^7F_2$ and $^5D_0$-$^7F_4$ ED transitions. The spectral analysis can therefore be performed using either transition. In this section, the more strongly polarized $^5D_0$-$^7F_4$ will be used for the demonstration, but a thorough discussion of the use of $^5D_0$-$^7F_2$ is given in the **annex 5.3.4**.

Spectral fitting

Using the assumption $\theta = 90°$, we can rewrite **equations 2.54**-**2.57** such that for MD transitions,

$$I_{zx,MD}(\lambda) = \frac{I_{\pi,MD}(\lambda)}{2} \cdot \big(1 + x + (1-3x)\cdot(1-z)\big) + \frac{I_{\sigma,MD}(\lambda)}{2} \cdot \big(1 - x - (1-3x)\cdot(1-z)\big) \qquad \textbf{2.64}$$

$$I_{zy,MD}(\lambda) = \frac{I_{\pi,MD}(\lambda)}{2} \cdot \big(1 + x + z\cdot(1-3x)\big) + \frac{I_{\sigma,MD}(\lambda)}{2} \cdot \big(1 - x - z\cdot(1-3x)\big) \qquad \textbf{2.65}$$

and for ED transitions,

$$I_{zx,ED}(\lambda) = \frac{I_{\pi,ED}(\lambda)}{2} \cdot \big(1 - x - z\cdot(1-3x)\big) + \frac{I_{\sigma,ED}(\lambda)}{2} \cdot \big(1 + x + z\cdot(1-3x)\big) \qquad \textbf{2.66}$$

$$I_{zy,ED}(\lambda) = \frac{I_{\pi,ED}(\lambda)}{2} \cdot \big(1 - x - (1-3x) \cdot (1-z)\big) + \frac{I_{\sigma,ED}(\lambda)}{2} \cdot \big(1 + x + (1-3x) \cdot (1-z)\big) \quad \textbf{2.67}$$

where $x \equiv \langle \cos^2 \theta_s \rangle$ and $z \equiv \cos^2 \phi$. Based on these expressions, we see that there are some combinations of x and z for which the spectrum is independent on x. For example, if $z = \frac{2}{3}$, $I_{zx,MD}(\lambda) = \frac{2}{3} \cdot I_{\pi,MD}(\lambda) + \frac{1}{3} \cdot I_{\sigma,MD}(\lambda)$ which is identical to the isotropic spectrum. This means that we cannot measure the order parameter using $I_{zx,MD}$ or $I_{zy,ED}$ if $\phi \sim 35°$ ($\cos^2 \phi = 2/3$). The same issue occurs for $I_{zx,ED}$ and $I_{zy,MD}$ when $\phi \sim 55°$ ($\cos^2 \phi$). Using the same logic, if $x = 0$ the calculated value of z will be either $\frac{1}{3}$ or $\frac{2}{3}$ depending on which expression was used to fit the data. However, there is no physical meaning to this, as an isotropic sample by definition doesn't have a director. We must consider these edge cases, in order to not misinterpret the results.

Due to the fact that the system is dynamic and the colloidal suspension is not perfectly homogeneous, there can be some fluctuations in the PL intensity, which is indeed observed in **Figure 5.2b-c**. In return, this means that between the three analyzer angles, there might be a significant difference in signal intensity. It is therefore necessary to normalize all the spectra before starting the curve fitting procedure. Besides the normalization, the procedure is exactly the same as was previously discussed for the LC sample, but using the **equations 2.64-2.67** instead. In order to minimize the impact of the problematic angles as much as possible, we should simultaneously fit at least two spectra recorded at different angles. However, due to the symmetry of the expressions for $I_{zx,MD}$, $I_{zx,ED}$ and $I_{zy,ED}$, $I_{zy,MD}$ respectively, simultaneous fitting of I_{zx} and I_{zy} does not work at the problematic angles either (no optimal fit is found). It is therefore necessary to include $I_{z45°}$ in the spectral fitting procedure. We can use the expressions

$$I_{z45,MD}(\lambda) = \frac{I_{\parallel,MD}(\lambda)}{2} \cdot (1 + sin\, 2\phi) + \frac{I_{\perp,MD}(\lambda)}{2} \cdot (1 - sin\, 2\phi) \quad \textbf{2.68}$$

$$I_{z45,ED}(\lambda) = \frac{I_{\parallel,ED}(\lambda)}{2} \cdot (1 + sin\, 2\phi) + \frac{I_{\perp,ED}(\lambda)}{2} \cdot (1 - sin\, 2\phi) \quad \textbf{2.69}$$

with the expressions of $I_{\parallel}$ and $I_{\perp}$ from **equations 2.22-2.25**. Additionally, by including $I_{z45°}$ in the curve fit, we can directly extract ϕ. This way, even if 2 out of the 4 spectral segments appear isotropic, there are still 2 other sections for which this is not the case. It may be even better to fit all 3 collected spectra simultaneously.

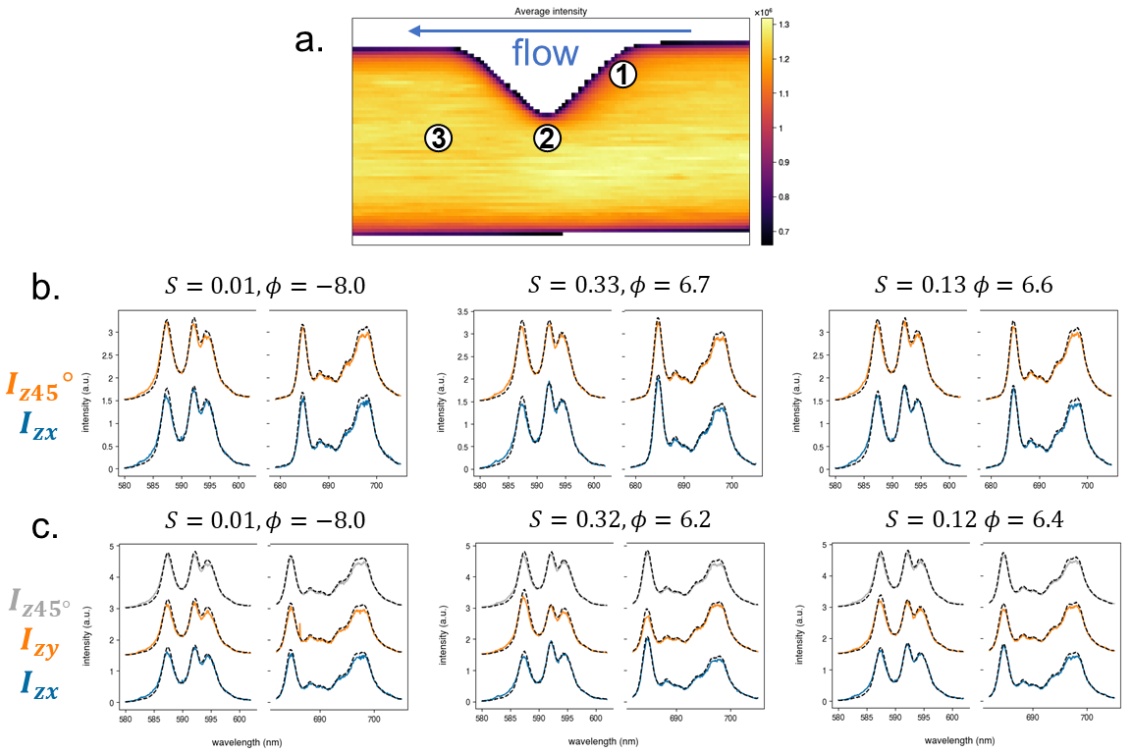

Figure 2.38 a) Average intensity in middle xy-plane of the channel **b-c)** Spectral fitting, indicated by black dashed lines, at three different positions in the microfluidic channel based on simultaneous fitting of **b)** I_{zx} and $I_{z45°}$ and **c)** I_{zx}, I_{zy} and $I_{z45°}$.

Figure 2.38 shows the spectral fitting spectra for different positions in the channel for simultaneous fitting of only I_{zx} and $I_{z45°}$ and with the additional I_{zy} spectrum. For both combinations of spectra, we obtain a good fit and the values are consistent between methods. The tomographic maps of S (in the annex **Figure 5.17**) of both combinations are also comparable, which means that for the spectral fitting approach, we do not need the inclusion of a third spectrum. This means the acquisition time can be reduced which is especially useful for dynamic samples.

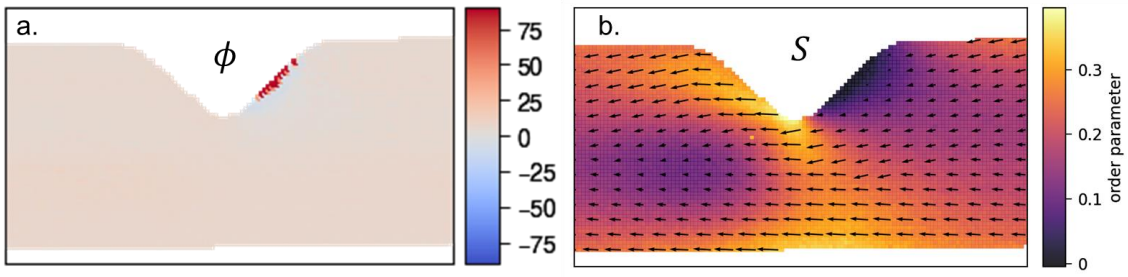

Figure 2.39 Results of spectral fitting of I_{zx} and $I_{z45°}$ **a)** In-plane director orientation ϕ **b)** Order parameter S. The direction of the arrows represents the local director $\vec{n}$ based on ϕ in a) and their length are proportional to S.

Finally, we consider the orientation of $\vec{n}$, which is found through the same spectral fit where ϕ is a fitting parameter. To eliminate the mirror angles of $-\phi$ and ϕ, we use the method based on the three k-values

outlined in **section 2.4.3.** From the spectral fitting, we find that $|\phi|\sim 10°$ throughout the channel (**Figure 2.39a**). However, in the sections of the channel where S is low, this doesn't have much physical meaning. **Figure 2.39b** shows $\vec{n}$ such that each arrows' length represents the magnitude of S.

Area under the curve ratiometry

Just as was done for the system with a known value of S, we can also perform the orientation analysis by ratiometric approach. As the peaks of the monazite spectrum are much narrower and well defined, we adapt the regions to be integrated such that the six subpeaks span from 586.7-588.1, 591.3-592.8, 611.0-612.2, 683.5-685.8 and 695.8-699.4 nm as indicated by the highlighted regions in **Figure 2.40**. The reference constants A,B,C,D (**equation 2.58**) are retrieved from the curve fit of the polar diagram for each subpeak in **Figure 2.40**.

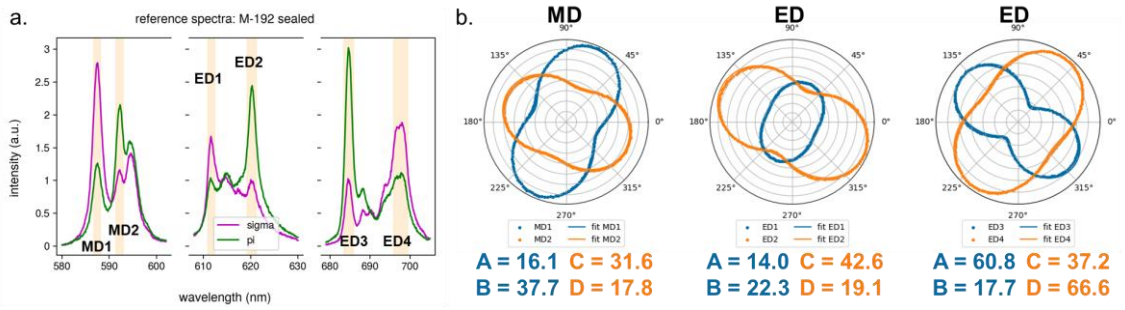

Figure 2.40 Calculation of area under the curve (AUC) for each subpeak of the reference spectra. **a)** I_π and I_σ reference spectra and the regions corresponding to the subpeaks highlighted in orange. **b)** Polar diagrams of the AUC for each subpeak corresponding to 180 different measurements. The reference AUC values are found by curve fitting each dumbbell to the dipolar model (**equation 2.35**).

We then calculate the AUC for each subpeak at each position (**Figure 2.41**). The resulting maps have been smoothened using a gaussian smoothing filter (the plots before smoothing can be found in the annex, **Figure 5.45**). We then consider the ratio $k = \frac{I_{D1}}{I_{D2}}$ where I_{D1} and I_{D2} refer to the integrated intensity of two subpeaks from the same dipole transition. Based on the reference, we find that the k-values should be within the ranges [0.51-2.12], [0.33-1.17] and [0.27-1.63] for the three transitions respectively. Indeed, from **Figure 2.41**, we see that all k-values stay within this expected range. We can also calculate the theoretical k-values for a fully isotropic sample using **equations 2.38-2.39** and we find $k_{iso,MD} = 0.86, k_{iso,ED1} = 0.73$ and $k_{iso,ED2} = 0.56$. We clearly observe some regions (near the center of the channel and at the upstream interface of the constriction) where the k-values match those of the isotropic spectrum and thus expect $S = 0$.

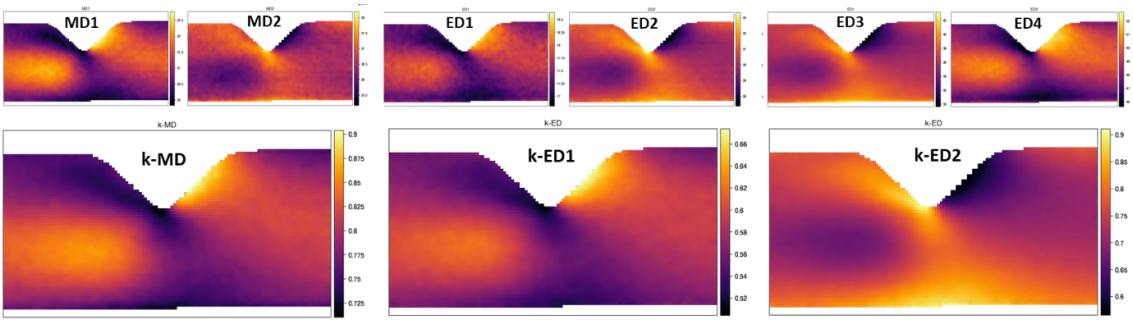

Figure 2.41 AUC for the two subpeaks of the MD and ED transitions based on the I_{zx} spectrum and the corresponding k-values such that $k_{MD} = I_{MD1}/I_{MD2}$, $k_{ED1} = I_{ED1}/I_{ED2}$ and $k_{ED2} = I_{ED3}/I_{ED4}$. A smoothing gaussian filter has been applied to improve the signal to noise ratio.

Using **equations 2.64**-**2.67**, we can then rearrange the definitions for k_{zx} for each dipole such that for MD and ED transitions,

$$(1-z)\cdot(1-3x)+x = \frac{A+B-k_{zx,MD}\cdot(C+D)}{-A+B+k_{zx,MD}\cdot(C-D)} \qquad \textbf{2.70}$$

$$z\cdot(1-3x)+x = \frac{A+B-k_{zx,ED}\cdot(C+D)}{A-B-k_{zx,ED}\cdot(C-D)} \qquad \textbf{2.71}$$

Similar expressions for are found in the annex (**equations 5.16-5.17**). We can then determine the values of $x \equiv \langle\cos^2\theta_s\rangle$ and $z \equiv \sin^2\phi$ by any combining an expression for $z\cdot(1-3x)+x$ with one for $(1-z)\cdot(1-3x)+x$. We can therefore use various combinations of k-values, but here we will just show the combination of $k_{zx,MD}$ and $k_{zx,ED}$. As there is no meaning to $cos^2\phi$ unless $S > 0$, it may therefore be best to first find x and then z. Summing **expressions 2.70 and 2.71** allows to find

$$x = 1 - \frac{A_{MD}+B_{MD}-k_{zx,MD}\cdot(C_{MD}+D_{MD})}{-A_{MD}+B_{MD}+k_{zx,MD}\cdot(C_{MD}-D_{MD})} - \frac{A_{ED}+B_{ED}-k_{zx,ED}\cdot(C_{ED}+D_{ED})}{A_{ED}-B_{ED}-k_{zx,ED}\cdot(C_{ED}-D_{ED})} \qquad \textbf{2.72}$$

$$z = \frac{1}{1-3x}\cdot\left(\frac{A_{MD}+B_{MD}-k_{zx,MD}\cdot(C_{MD}+D_{MD})}{-A_{MD}+B_{MD}+k_{zx,MD}\cdot(C_{MD}-D_{MD})} - 1\right) \qquad \textbf{2.73}$$

We can thus calculate the order parameter directly for **equation 2.72** by evaluating both an MD and ED transition, without needing to know the director orientation first. Afterwards, we can find $\cos^2\phi$ using the obtained value of $\langle\cos^2\theta_s\rangle$ and **equation 2.73**.

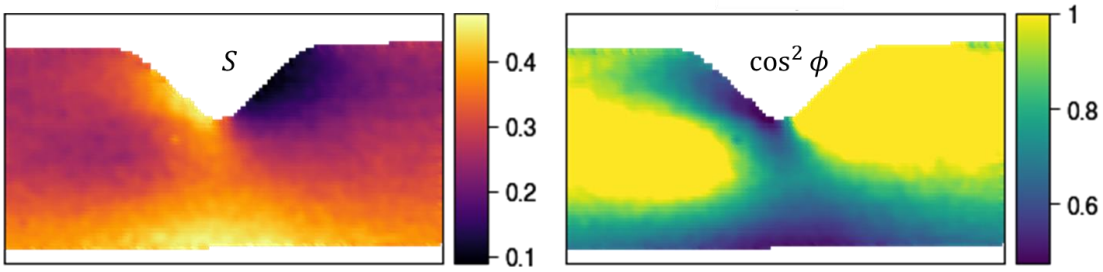

Figure 2.42 Order parameter S and $\cos^2\phi$ maps based on the AUC ratiometry using **equations 2.72-2.73**.

Upstream, on the right of the plot, we observe an almost constant gradient from high to low shear (from bottom to top) whereas we theoretically expect to see a symmetric profile with high shear near the walls and low shear near the center. Additionally, the value of $\cos^2\phi$ saturates to 1 for a large area in the channel, which seems inaccurate as well. This approach therefore cannot successfully reconstruct S and ϕ. Alternatively, we could use **equation 2.63** to find the value of ϕ based on the three k-values ($k_{zx,ED}$, $k_{z45°,ED}$ and $k_{zy,ED}$), which gives **Figure 2.43a**. This gives the most symmetric profile of ϕ compared to the other AUC and spectral fitting approaches. Note that close to the barrier $\phi \to 45°$, which is the value that emerges from **equation 2.63** when all k-values are equal (meaning $S = 0$). We then use $k_{zx,ED}$ with **equation 2.71** to calculate $\langle\cos^2\theta_s\rangle$ and S (**equation 2.15**), which is shown in **Figure 2.43b**. Using this approach, we retrieve the expected symmetric S profile on the right (upstream). Furthermore, the S profiles are smoother and more closely match those obtained by spectral fitting (**Figure 2.39b**).

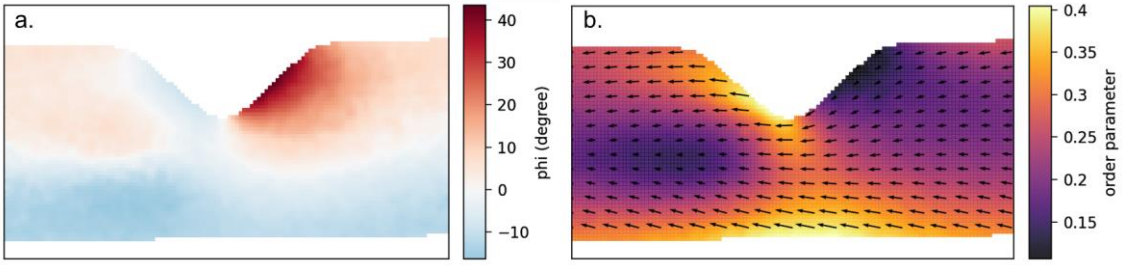

Figure 2.43 a) In-plane director orientation ϕ found by comparing $k_{zx,ED}$, $k_{z45°,ED}$ and $k_{zy,ED}$ and **equation 2.63**. **b)** Order parameter S found through **equation 2.63** . The arrows represent the local director $\vec{n}$ based on ϕ in a) and their length are proportional to S.

However, as the AUC analysis is only successful when finding ϕ using the k-values of three collected spectra, it requires an additional measurement for each position as compared to the spectral fitting approach.

Accuracy and comparison between spectral fitting and AUC ratiometry

Previously, we validated the orientation tomography method in microfluidics by comparing the experimental results to simulated profiles of S[12]. However, it is difficult to obtain such simulated profiles, as it requires a thorough understanding of the rheological and thermodynamic properties of the nanorod suspension, which may be slightly different for each sample. It is therefore not possible to quantitatively evaluate the accuracy in this work.

However, for the shearmetry, the most important factor is the consistency of the calculation of S. Even if there might be a systematic error on S, if this error is the same for the calibration curve linking S and the shear rate $\dot{\gamma}$ (discussed in **section 1.3**) and the measurements in unknown systems, the accuracy of $\dot{\gamma}$ will be maintained. Based on the fact that the qualitative profiles of S obtained through the spectral fitting (**Figure 2.39b**) and the AUC ratiometry (**Figure 2.43b**) are extremely similar, we can deduce that our approach yields consistent results. Considering that we'd expect $S \to 0$ in the center of the channel, we can expect the most accurate results by simultaneous spectral fitting of all three spectra recorded and considering the more strongly polarized $^5D_0$-$^7F_4$ ED transition.

In terms of the determination of ϕ, the approach comparing the three k-values seems to be most accurate, especially when S is small. This can be understood from the fact that when S is small, a change in ϕ will only result in a small perturbation in the spectra. The error on ϕ of the spectral fitting can therefore be significant for small S.

2.4.5 Measurement of order parameter for known polar angle

As discussed in **section 2.4.1**, it is not possible to retrieve both the order parameter S and the polar angle θ from the spectroscopic analysis. However, if we know or can reasonably estimate the profile of θ, we can use it to correct the calculated value of S. To demonstrate this, we consider an experiment where we scan the yz-cross section of a microfluidic channel (**Figure 2.44a**) while flowing a suspension of monazite $LaPO_4$:Eu nanorods under the same conditions as the previous example. Due to the symmetry along the y and z axis, the measured profiles of ϕ and S are expected to be symmetric as well. However, performing the spectral fitting analysis discussed before, we find that S is lower near the top and bottom walls than near the side wallsas seen in **Figure 2.44b-c**. This can be attributed to the fact that the assumption of a planar director only holds true near the center plane of the channel. In reality, we expect θ to follow a similar profile as that for ϕ due to the symmetry of the shear profile between the y- and z- axis.

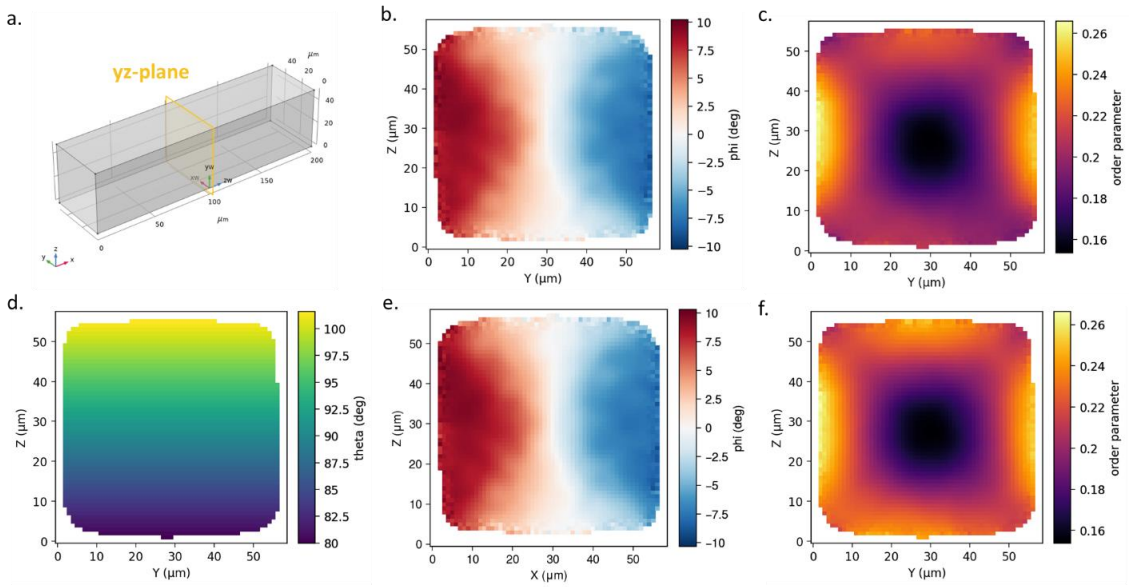

Figure 2.44 Orientation analysis with and without correction of the polar angle θ. **a)** Channel geometry and cross yz-cross section. **b-c)** Calculated profiles of ϕ and S based on spectral fitting assuming that $\theta = 90°$ everywhere. **d)** Estimated profile of θ based on the profile of ϕ at the middle height of the channel. **e-f)** Calculated profiles of ϕ and S based on spectral fitting using the estimated θ values.

Instead of using the previous expressions (for $\theta = 90°$) to fit the emission spectra, we should use the general **equations 2.54-2.57** with an estimated value of θ. We estimate the profile of θ to follow a linear relationship similar to the profile of ϕ at the middle height of the channel, such that $\theta \sim 80°$ at the bottom of the channel to $\theta \sim 100°$ near the top, as illustrated in **Figure 2.44d**. Using this θ as an input, we then repeat the spectral fitting procedure based and find ϕ and S (**Figure 2.44e-f**.). As expected, this finally results in a symmetric S profile such that S near the walls is always around 0.26.

Summary of chapter 2.4

Expressions for the measured polarized emission spectra are derived as a function of the reference spectra, without any assumption on the orientation of the director $\vec{n}$ or the order parameter S. All expressions contain the factor $\sin^2\theta \cdot (1 - 3\langle\cos^2\theta_s\rangle)$ and it is therefore impossible to independently find the polar angle θ and order parameter S through spectral analysis.

Orientation tomography of $\vec{n}$ in a highly aligned nematic LC is performed, assuming a fixed value of S. We compare the calculated values obtained through both spectral fitting and AUC ratiometry, and find that although both successfully reconstruct $\vec{n}$, the spectral analysis is more accurate, in particular for homeotropic domains. Several approaches of eliminating the mirror angles are discussed and compared.

Finally, orientation tomography in microfluidic channels is demonstrated using both monazite and rhabdophane $LaPO_4$:Eu suspensions for different known values of θ. As S is much lower in such systems than in the LC assemblies, a larger DOP is required for accurate and sensitive orientation measurements. The optimal methodology for shearmetry applications is therefore a spectral fitting of all spectra and considering the strongly polarized $^5D_0$-$^7F_4$ ED transition.

2.5 Conclusion

In this chapter, we discussed and demonstrated both the experimental and theoretical methodologies required for orientation tomography based on the spectroscopic analysis of lanthanide luminescence.

The improved optical configuration for polarization resolved micro-spectroscopy resulted in a spatial resolution of 0.5 µm (xy) by 1 µm (z) and we expect that further improvement in the axial resolution could be achieved by better controlling the pinhole position. The new configuration does not distort the polarization of the collected emission, as evidenced by dumbbell shaped dependency of the emission intensity as a function of analyzer angle for all peaks. However, we find a slight dependency on the analyzer angle of the isotropic emission. Further investigation is required to understand the origin of this phenomenon.

Interestingly, we found that in some cases there seems to be a wavelength dependent retardation, evidenced by the rotation of the dumbbells in the polar diagrams of the emission peaks. This can be up to 20° over the span of roughly 200nm. Initial experiments suggest that this effect is linked to the out-of-plane orientation $\vec{n}$, as it is not present in samples aligned by a planar electric field. It would be interesting to study this in a more controlled fashion as it might open up the possibility to obtain the value of the polar angle θ.

In the last section, we derive all the expressions for the polarized emission spectra without making any assumptions on the orientation of $\vec{n}$ or the value of S. We find that it is impossible to independently calculate the value of θ and S with the current methodology, and discuss its application for systems with a known S (demonstrated in highly aligned LCs) and for a known θ (demonstrated in microfluidic flows). Simultaneous spectral fitting of multiple polarized emission spectra shows the best accuracy and consistency, but area under curve (AUC) ratiometry achieves comparable results. It should therefore be possible to perform the orientation analysis using a simplified optical setup where the spectrometer is replaced by several detectors each collecting an emission peak selected using bandpass filters.

3 Orientation tomography of liquid crystal assemblies of $LaPO_4$:Eu nanorods

3.1 Introduction on liquid crystal assemblies

As discussed in **section 1.1.1**, suspensions of $LaPO_4$:Eu nanorods act as a liquid crystal (LC). To understand the spontaneous formation and evolution of self-assemblies observed in such suspensions, a general background on LCs and their thermodynamics is required. Here, we briefly introduce the different types of LCs and their phase behavior. We will discuss the role of topological defects and the free energy on the formation of topographies in LC assemblies. Finally, we give some examples of LC systems undergoing a defect morphogenesis, which can be used as a reference when considering the morphogenesis observed in the $LaPO_4$:Eu LC.

3.1.1 Liquid crystals

Liquid crystals (LCs) are dynamic soft materials which form mobile and ordered states through the self-assembly of their constituents. They typically consist of anisotropic molecules or particles suspended in a liquid medium. As a consequence, they exhibit anisotropic optical, magnetic and electrical properties associated with crystalline solids, but also isotropic properties such as fluidity and the inability to support shear associated to fluids[70,71]. External stimuli such as electric or magnetic fields as well as an applied shear can introduce/modify long range order. The dynamic, responsive nature of LCs enable their use for diverse applications, from display technologies and computing to soft robotics and shear monitoring[12,72–74].

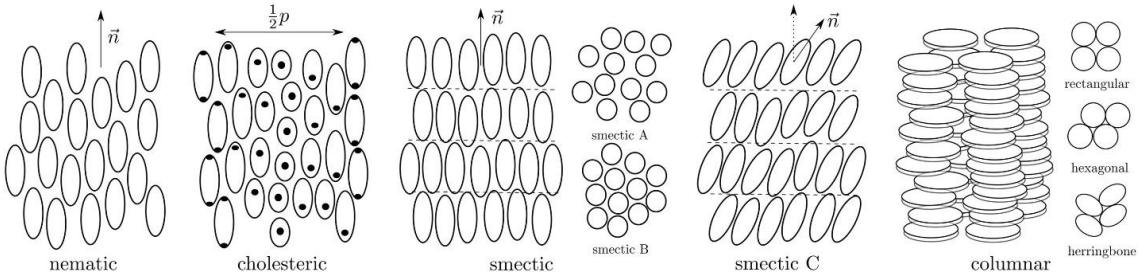

Figure 3.1 Ordered arrangements of the constituents in different liquid crystal phases. Figure from Andrienko (2018)[70].

Depending on the type of LC, there may be different types of ordered arrangement of their constituents, as depicted in **Figure 3.1**. The nematic phase corresponds to long range orientational order without the presence of positional order. The collective orientation in such systems is described by the director $\vec{n}$. For nematics there is no preferential orientation with respect to either end of the molecule/particle, so there is no meaning to the sign of $\vec{n}$. The cholesteric phase is similar, but with the addition of chirality as the

constituents rotate around their short axis. This generates a periodicity perpendicular to the plane of $\vec{n}$, which is characterized by the pitch p. In addition to orientational order smectic and columnar phases also exhibit positional order. The smectic phase consists of ordered layers which can freely slide over one another. Within smectics, we can distinguish the A phase ($\vec{n}$ perpendicular to each plane without positional order), B phase ($\vec{n}$ perpendicular to each plane and hexagonal order) and the C phase ($\vec{n}$ tilted in the plane). Finally, the columnar phase forms cylindrical structures with both orientational and positional order with different possible crystalline packing. Transitions between such phases can be triggered by various stimuli and have long been studied as it can act as a model system for other physical phenomena, such as cosmological phase transitions and magnetic vortexes in superconductors[75–77].

Phase transitions

Transitions between the disordered and/or differently ordered LC phases have long been of interest as a parallel for transitions occurring in magnetic and superconducting materials. LCs can transit from an isotropic phase to an ordered phase by a change in temperature (thermotropic) or concentration (lyotropic). For thermotropic LCs the ordered phases are stabilized by the enthalpic terms of the free energy, such that cooling results in a transition from isotropic to nematic phase[70]. For certain LCs, a smectic phase can be retrieved when cooling the nematic even further.

In this work, we mostly focus on lyotropic LCs of anisotropic particles. The behavior of a colloidal lyotropic LC is well described by the Onsager model for rigid rod-like particles[4]. Assuming no interparticle interactions, the free energy of the system depends on the rotational and translational entropies. The rotational entropy is maximum in the isotropic phase and decreases with an increase of the nematic order parameter. The translational entropy on the other hand is increased when the particles are more tightly packed together as this requires a collective alignment and is therefore higher in the nematic phase. At the isotropic-nematic phase transition, the two entropic terms balance each other. This allows us to determine the critical volume fraction $\Phi_{\mathrm{I-N}}$ for which the solution will spontaneously separate into an isotropic and nematic phase, which can be approximated as

$$\Phi_{\mathrm{I-N}} \sim 4D/L \qquad \textbf{3.1}$$

where D is the diameter and L is the length of the rods[78]. This means that rods with a larger aspect ratio will favor the formation of a nematic phase and thus exhibit lower $\Phi_{\mathrm{I-N}}$. In polydisperse samples, size fractionation is known to occur such that the average size in the isotropic phase is lower than that of the nematic phase[79].

3.1.2 Topological defects and topography

An important property of LC is that the ordered phases usually contain topological defects; discontinuities in the director field $\vec{n}$. Such defects can be easily observed by polarized light microscopy (PLM) as the

birefringence intensity gives information on the optical axis and thus $\vec{n}$. This has made LCs an excellent system to experimentally observe phenomena related to field theory. **Figure 3.2a** shows a PLM image of a thin LC layer sandwiched between microscope slides containing many topological defects. The observed pattern is known as the Schlieren texture, where each defect has several dark brushes which move continuously when rotating the crossed polarizers, indicating that the change in $\vec{n}$ is continuous as well[80].

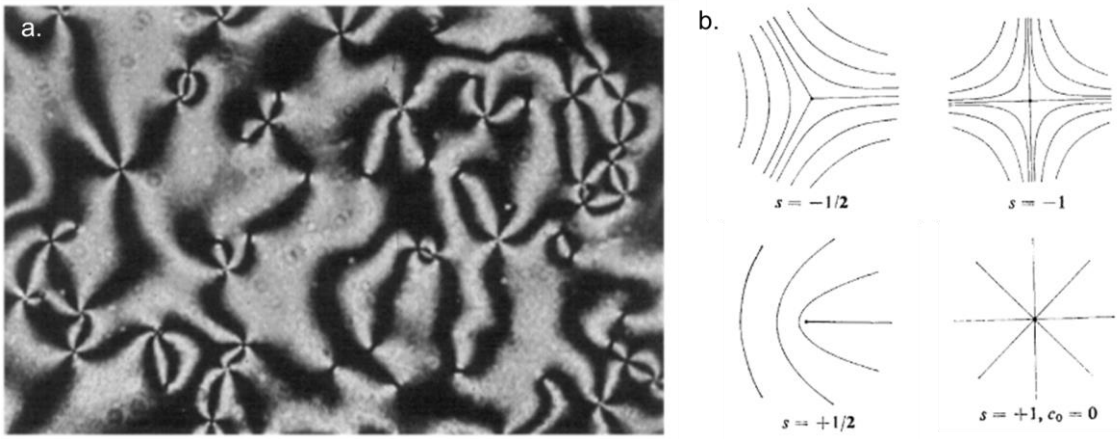

Figure 3.2 Defects in a 2D nematic. **a)** Schlieren texture of a 10 μm thick layer of 4-n-caproyloxy-4'-ethoxyazoxybenzene sandwiched between identical microscope slides. **b)** Illustrations of topological defects with different strengths s. Figures adapted from Nehring and Saupe (1972)[81].

Each defect can be classified by a topological strength s, and **Figure 3.2b** shows some examples which are typically observed in nematics. The magnitude $|s|$ of a defect can be determined by dividing the number of dark brushes by four[81]. Defects with $|s| > 1$ do not occur in nematic LC films as they are highly unstable[1]. The sign of the defect can be determined from the direction the dark brushes move when rotating the crossed polarizers, such that $s < 0$ when the brushes move in the opposite direction and $s > 0$ when they move in the same direction as the polarizers[81]. Connected defects usually have an opposite sign and may annihilate by merging.

In samples where the 2D nematic is exposed to symmetric boundary conditions (for example planar alignment) on each interface, the total sum of s of all defects in the sample tends to be zero. An example of this is the Schlieren texture in **Figure 3.2a**, where defects are connected to those of opposite sign. However, when the LC is exposed to conflicting boundary conditions, more complex defects can be observed resulting from the three-dimensional nature of $\vec{n}$[82]. A common example of this is a hybrid aligned nematic (or smectic) film, where at one side of the film $\vec{n}$ is planar to the surface and on the other it is perpendicular (i.e. homeotropic) to the surface. In practice, this can be achieved by placing an organic

LC on a liquid surface (such as water of glycerol)[22,83], or by interactions between the LC and functionalized substrate(s)[84–86].

Free energy of topological defects

The structure of defects and their stability are governed by the free energy associated to the assembly made up of the bulk and surface terms. The bulk term is described by the elastic free energy according to

$$f = K_{11}(\nabla n)^2 + K_{22}(n \cdot (\nabla \times n))^2 + K_{33}|n \times (\nabla \times n)|^2 \qquad \textbf{3.2}$$

where K_{11}, K_{22} and K_{33} are the splay, twist and bend elastic constants, illustrated in **Figure 3.3a**[70]. It is therefore minimal when n is uniform throughout the full domain and it cost energy to deviate from this distribution. The relative strength of the elastic constants plays an important impact on the defect structure and in particular determines where a defect is localized at the surface or can "escape" in the third dimension[87]. If the twist constant is dominant such that $K_{22} \gg K_{11}, K_{33}$, the defect will be localized at the surface (**Figure 3.3b**), whereas if bend is dominant and $K_{33} \gg K_{11}, K_{22}$ the defect will "escape" in the third dimension (**Figure 3.3c**)[87]. For lyotropic systems made of rigid rods, theory predicts that $K_{33} \gg K_{11}, K_{22}$ and in such systems we thus expect to see three-dimensional defect structures[88].

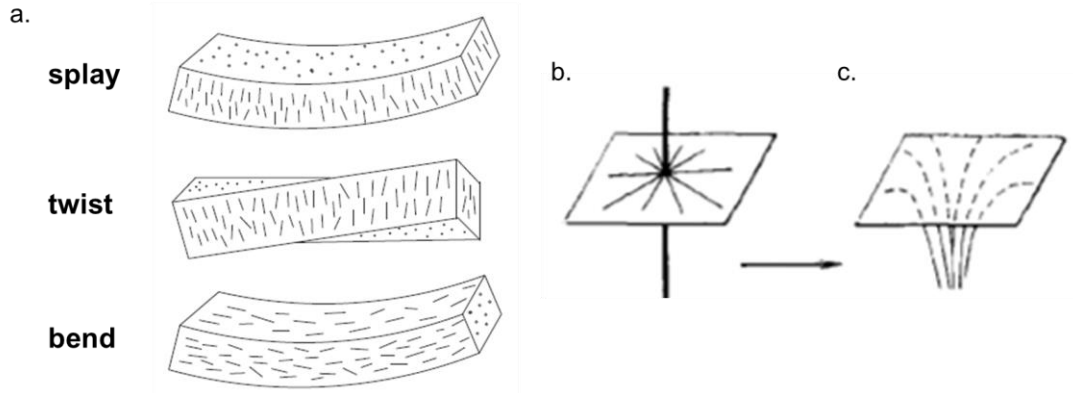

Figure 3.3 a) Illustration of the different types of elastic deformation. Figure from Andrienko (2018)[70]. **b)** Unstable +1 line disclination **c)** stabilized by "escaping" into the third dimension leaving only a point defect. Figures from Kurik and Lavrentovich (1988)[87].

The energy associated to the surface/interface has an isotropic and anisotropic component; the surface tension σ and anchoring strength W. The isotropic surface tension simply minimizes the total surface area, which may be achieved by deforming the bulk. Anisotropic anchoring occurs when there is a preferential orientation (known as the easy axis n_e) at the interface. In this case a deviation from n_e will result in an increase in the anchoring energy and thus the surface energy. Finally, the total free energy of the system can be expressed as

$$F = \frac{1}{2}\int_{\Omega} f(n, \Delta n)dV + \int_{\Omega}\left[\sigma - \frac{W}{2}(n \cdot n_e)^2\right]dA \qquad \textbf{3.3}$$

A defect is (meta)stable when this free energy is at a (local) minimum. Note that the first term concerns an integral over the volume, whereas the second term concerns only the surface. The relative strength of the elastic, surface and anchoring energies therefore determines not only the topology, but also the interfacial topography of the LC surrounding a defect.

Interplay between topography and topology

As an example, let's consider a hybrid aligned film (radial planar on the bottom and homeotropic on top) with a free surface on top (**Figure 3.4**)[84]. If surface tension is high, it resists the deformation of the interface resulting in flat topographies (**Figure 3.4a**). However, if the elastic energy is dominant, a divot will form to minimize the director gradient while maintaining the same total volume (**Figure 3.4b**). Finally, when the anchoring is relatively large, either a peak or divot can appear depending on the direction of the director splay at the substrate with respect to the point defect (**Figure 3.4c-d**).

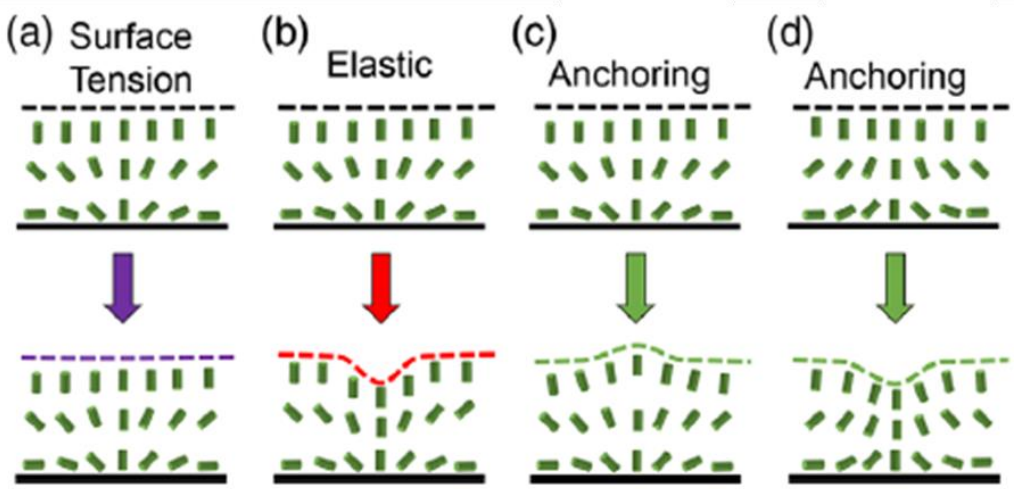

Figure 3.4 Schematic illustration of the impact of the different components of the free energy. **a)** A strong surface tension results in a minimization of the surface area and flat topology. **b)** Strong elastic energy prefers the minimization of the change in director and deforms the interface to achieve this. **c-d)** Relatively high anchoring strength creates strong boundary conditions at each interface and couples with the elastic energy to overpower the surface tension, creating a topography. A **c)** peak or **d)** divot appears depending on the direction of the director splay. Figure adapted from Ferris *et al.* (2021)[84].

Ferris *et al.* experimentally studied this effect using hybrid aligned films of 8CB (an organic thermotropic LC) on functionalized substrates containing a radial point defect[84]. Using optical profilometry, they reconstructed the topography of the top interface for different thicknesses of the film (**Figure 3.5**). For small film thicknesses, the elastic energy is dominant due to the large gradient in $\vec{n}$, resulting in a domelike topography which ensures a gradual transition in $\vec{n}$ along the z-direction (**Figure 3.5a**). In much thicker

films, the surface tension becomes more significant and we observe a conelike topography with almost no curvature (**Figure 3.5b**).

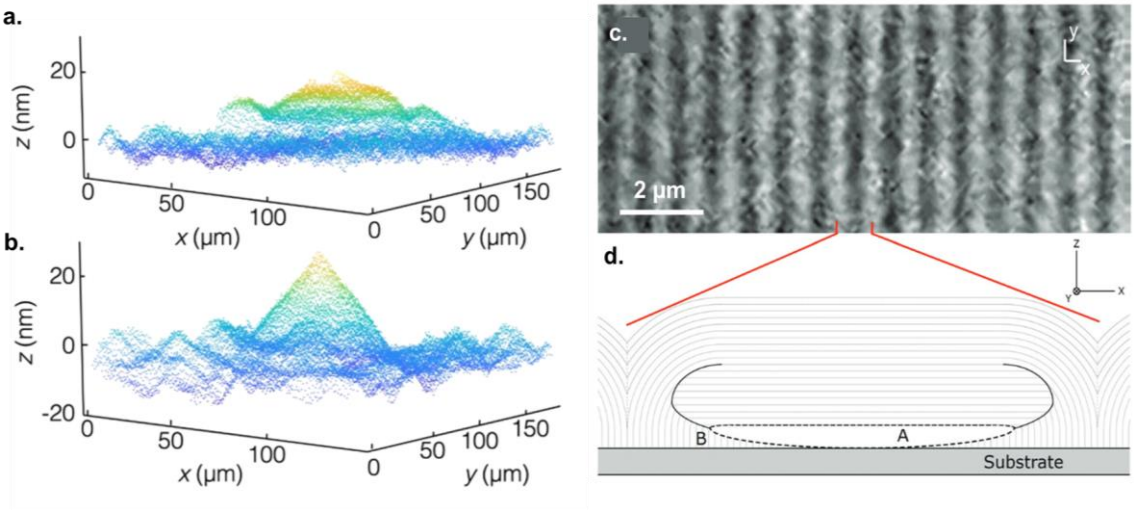

Figure 3.5 Examples of topography in LC films of 8CB, which exhibit homeotropic anchoring at the air interface. **a-b)** Nematic phase on a functionalized substrate with central point defect and degenerate planar anchoring **a)** Domelike topography for d=75 nm **b)** Conelike topography for d=660 nm. Figures adapted from Ferris *et al.* (2021)[84]. **c-d)** Smectic-A phase under on a rubbed substrate imposing unidirectional planar anchoring. **c)** Photomicrograph of formed oily streaks. **d)** Schematic representation of the LC structure with the lines representing the smectic layers. Figures adapted from Nemitz *et al.* (2016)[89].

Thin films of a smectic-A LC under hybrid boundary conditions also exhibit defects with an associated topography[89–91]. For such films, the unidirectional planar anchoring at the substrate and the conflicting homeotropic anchoring at the air interface result in the formation of oily-streaks, seen in **Figure 3.5c**. The oily streaks consist of an array of flattened hemicylinders where the smectic layers are bent to satisfy both boundary conditions, as illustrated in **Figure 3.5d**[89,91] The streaks exhibit topographical fluctuations, with the lowest height at the disclination lines (**Figure 3.5d**), of several tens of nanometers[90,91].

Such an interplay between topology and topography is of high interest, but it is challenging to observe their 3D structures by using optical methods due to the small characteristic lengths. In non-chiral organic LCs (such as the ones shown in **Figure 3.5**), topographic fluctuations are typically on the order of 10 to 100 nm[16]; well below the diffraction limit of light. This can be understood from the relatively high surface tension of organic LCs caused by the small size of their constituents. Using colloidal LCs of relatively large nanoparticles might therefore provide a more appropriate system, as will be discussed and demonstrated in **section 3.5**.

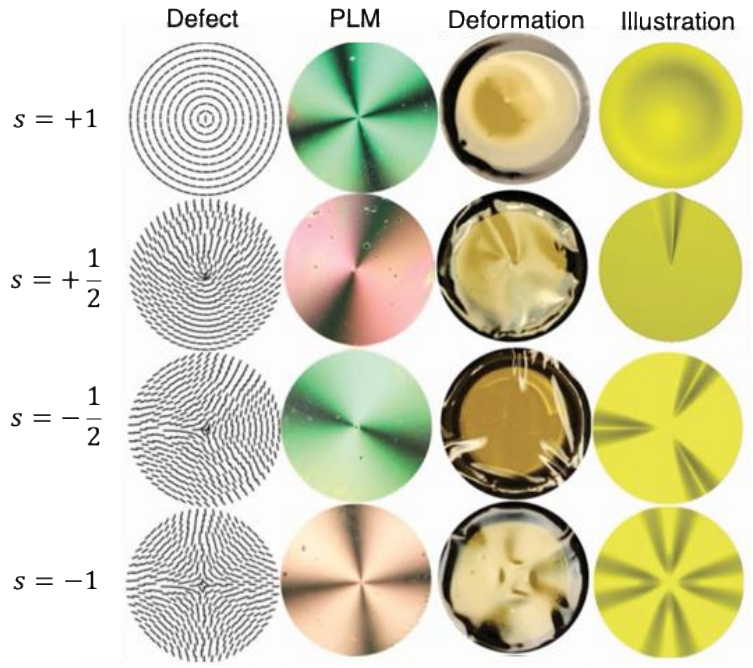

Figure 3.6 Impact of defect topology on the topography of a deformable LCN disk. Figure adapted from McConney *et al.* (2013)[92].

In the previous example, the defect at the origin of the topography was a simple point defect with $s = 1$. McConney *et al.* investigated how the strength of the defect impacts the topography using patterned liquid crystal polymer networks (LCN)[92]. Using a photopolymerization protocol, they patterned defects of different strengths, going as high as ± 10, into thin LCN disks. Triggered by external stimuli, the LCNs undergo reversible macroscopic deformation due to large changes in the order parameter[93], causing the appearance of topography (**Figure 3.6**). As seen in **Figure 3.6**, depending on the strength of the defect, different amounts of equally spaced valleys appear when triggering the deformation of the LCN. Consistent with the work of Ferris *et al.,* they find that a +1 defect results in a conical topography.

3.1.3 Morphogenesis of LC structures and defects

The morphogenesis of defects is particularly interesting for controlling the optical properties (such as the polarization and focal length) in functional materials like micolenses[94], and due to their analogy to other physical phenomena, such as cosmic string evolution[75]. Typically, studies focus on the formation and evolution of defects which occur during phase transition. For example, Kim *et al.* investigated the morphogenesis of defects and tactoid triggered by the I-N phase transition[5]. For this, they use di-sodium cromoglycate (DSCG) which is a commercial lyotropic chromonic liquid crystal (LCLC). LCLCs are made of aqueous suspensions of aromatic compounds with hydrophilic groups which tend to form stacks with $\vec{n}$ orthogonal to the molecular plane[95]. Under the right conditions, they form nematic tactoid droplets. PLM is used to image such tactoids and to reconstruct maps of the optical retardance and the $\vec{n}$, seen in **Figure 3.7**.

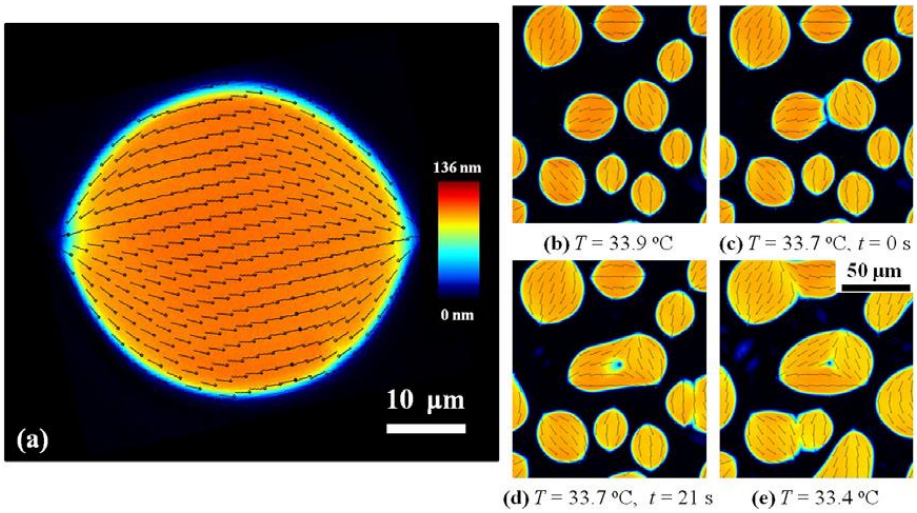

Figure 3.7 Lyotropic chromonic liquid crystal (LCLC) studied by PLM. Images show the calculated retardation and $\vec{n}$ **a)** A nematic tactoid **b-e)** Merging of tactoids and associated defect morphogenesis over time. Figure from Kim *et al.* (2013)[5]

Although LCLCs are a class of lyotropic LC, their phase behavior is also impacted by the temperature and the I-N transition occurs over a narrow temperature range[95]. Small changes in temperature trigger the coalescing of tactoids, seen in **Figure 3.7b-e**. This involves the merging of two or more domains with different orientations of $\vec{n}$ resulting in the formation of disclination lines, a process which is similar to the Kibble mechanism[96]. Moreover, these disclinations can evolve into point defects in the bulk (**Figure 3.7d-e**), due to the tangential anchoring at the I-N interface which conflicts with the internal $\vec{n}$.

Gim *et al*. followed the formation and morphogenesis of topological defects throughout the nematic to smectic-A transition in a hybrid aligned LC placed on water[22]. **Figure 3.8a-d** show PLM images taken with a first order retardation plate for different temperatures and thus different phases. Initially, point defects (boojum) with $s = \pm 1$ are observed in the nematic phase as seen in **Figure 3.8a**. The origin of this defect is the discontinuity of the degenerate planar anchoring on the bottom and the homeotropic anchoring on top, resulting in the defect structure illustrated in **Figure 3.8e**. Upon heating, a stripe-like pattern branching out from the center of the initial boojum appears (**Figure 3.8b**). Further heating triggers the phase transition to smectic-A and its characteristic focal conic domains (FCD) appear (**Figure 3.8c**). FCDs consist of parallel, curved layers with $\vec{n}$ aligned according to an easy axis (perpendicular for smectic-A) with respect to the layer[97], as illustrated in **Figure 3.8f**. Finally, these FCDs can turn into toric FCDs where each cone is titled with respect to the bottom substrate (**Figure 3.8d**).

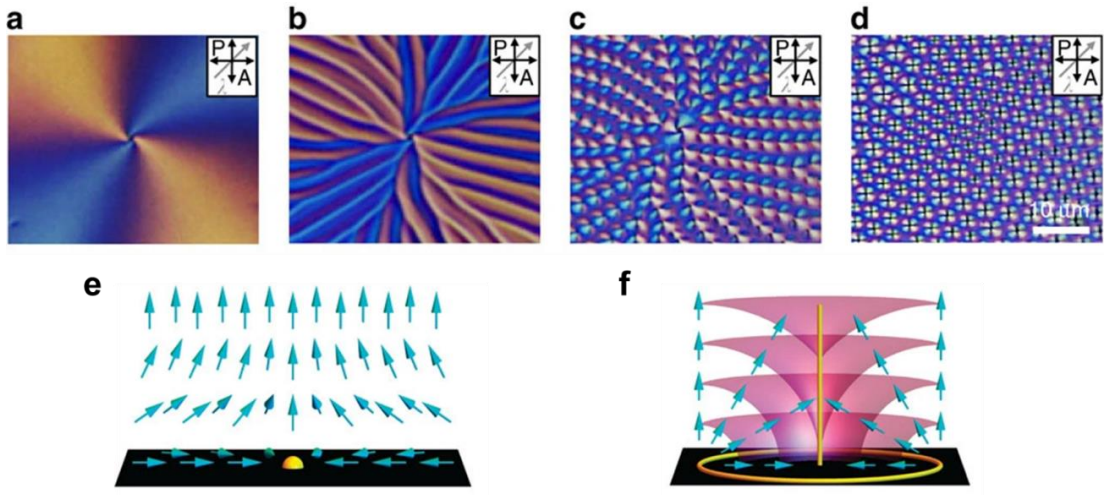

Figure 3.8 Morphogenesis of a defect during the nematic to smectic-A phase transition. a-**d)** PLM images with a first order retardation plate. **a)** nematic point defect **b)** nematic stripe pattern **c)** focal conic domains (FCD) **d)** toric FCDs **e)** Schematic representation of $\vec{n}$ (blue arrows) around a point defect with $s = 1$. **f)** Schematic representation of the layered TFD and $\vec{n}$ forming a conic structure. Figures adapted from Gim *et al.* (2017)[22].

Most previous studies of the evolution of defects have been focused on such organic (thermotropic) LC systems[22]. However, the transformation of defects in such systems takes place rapidly within (milli)seconds[98], making it practically impossible to observe the intermediate stages of morphogenesis. Additionally, defects and topographic domains in organics LCs have a small characteristic size on the nanoscale due to their small constituents and intrinsically high surface tension. It has thus been limited to characterize the defect core by optical methods[99,100].

Summary of chapter 3.1

Liquid crystals (LCs) are dynamic soft materials consisting of anisotropic molecules or particles in a liquid medium. They form organized phases controlled by temperature (for thermotropic LCs) or concentration (for lyotropic LCs) and can be aligned by external stimuli, making them of interest for a wide range of applications.

The collective orientation in LCs is denoted by the director $\vec{n}$ and discontinuities in its field are known as topological defects. Interfacial topographies may occur at the site of topological defects, depending on the relative strength of the bulk and surface forces. Additionally, defects may evolve over time (known as morphogenesis), especially when the LC is undergoing a phase transition. Most studies have been performed in organic, thermotropic systems in which the morphogenesis occurs rapidly and the defect size is relatively small. This makes it difficult to follow the structural changes throughout the morphogenesis.

3.2 Liquid crystal behavior of charge-stabilized $LaPO_4$:Eu nanorods

Here, we discuss the LC behavior of the $LaPO_4$:Eu colloidal suspensions. We first explain the different phases which can be observed and the conditions for spontaneous phase separation. Next, PLM imaging is used to observe the different LC phases and observed defect structures. Finally, we will discuss the morphogenesis from tactoids to streaks and flower domains observed when confining a biphasic LC between rigid walls.

3.2.1 Colloidal stability and phase separation of $LaPO_4$:Eu nanorod suspensions

*Suspensions of $LaPO_4$:Eu nanorods in EG, with 5% and 20% Eu^{3+} doping, were prepared in the rhabdophane phase according to the protocol in the **annex 5.1.1.** The size statistics of the resulting particles are found in **chapter 2.3.1, Figure 2.18**.*

As previously demonstrated in our group, the stability of the colloidal LC made of $LaPO_4$ nanorods is maintained without surface functionalization by the electrostatic repulsion due to the surface charge of the bare nanocrystals[2]. This system was shown to exhibit three different phases; isotropic, nematic and hexagonal columnar (as discussed in **section 1.1.1, Figure 1.1**)[2]. **Figure 3.9** shows a previously developed phase diagram based on the ion strength and the volume fraction Φ, with the dashed lines indicating the threshold for the isotropic-nematic phase transition for s-rods (large aspect ratio of $L/D = 23$) and lar- rods (smaller aspect ratio of $L/D = 18$) respectively[2]. The columnar phase was found for high Φ (>4%) and intermediate ionic strength, indicated by the diamonds in **Figure 3.9**. For sufficiently high salt concentrations, the suspension loses its LC behavior and forms a gel, indicated by the crosses in **Figure 3.9**. In this case, the high ionic strength overpowers the stabilizing electrostatic repulsion, resulting in the formation of aggregates[2].

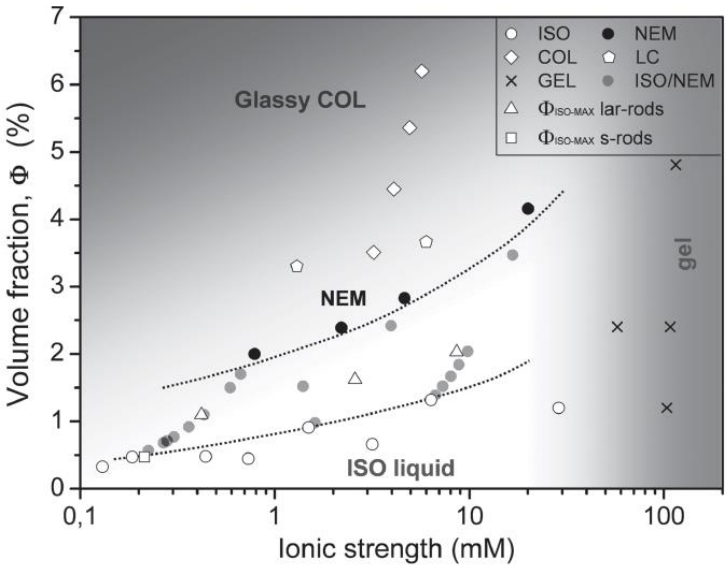

Figure 3.9 Phase diagram of $LaPO_4$ suspensions in ethylene glycol. Open circles represent isotropic, black circles nematic and grey circles a biphasic isotropic-nematic state of the s-rods. Open diamonds represent the columnar phase and open pentagons a pure LC state (columnar or nematic). Finally, the crosses represent a gel state. Figure from J-W. Kim. *et al.* (2012)[2]

As $LaPO_4$:Eu suspensions in EG are a type of lyotropic LC, transitions between the phases are triggered by Φ as described by Onsager's model (described in **section 3.1.1**)[4]. Indeed, as expected from **equation 3.1**, rods with smaller aspect ratio (lar-rods) were shown to have a higher Φ_{I-N} than those with a large aspect ratio (s-rods) (**Figure 3.9**). However, experimental values of Φ_{I-N} across the whole ionic range (**Figure 3.9**), were significantly lower than the theoretical value of $\Phi_{I-N}\sim 17\%$ based on **equation 3.1** (for $L/D = 23$). This can be explained by the fact that the Onsager model doesn't incorporate interparticle-interactions. Instead, D can be replaced by a larger effective diameter D_{eff} which considers the impact of electrostatic repulsion and steric hindrance, thus decreasing Φ_{I-N}. As the ionic strength impacts D_{eff}, it plays an important role in the phase behavior, as evidenced by **Figure 3.9**.

For most of the samples discussed in this work, the overall volume fraction Φ_{avg} is quite high, around 5%. Additionally, the ionic strength can be estimated to be on the order of 100 mM without dialysis in EG after the solvent transfer. Based on the phase diagram (**Figure 3.9**) we thus expect a mixture of nematic and isotropic phase or even a gel. Although some samples gellified shortly after the solvent transfer, dialyzing the gel in pure EG for several days to retrieve a (viscous) liquid state showing isotropic-nematic phase separation. No columnar phase was observed for these samples.

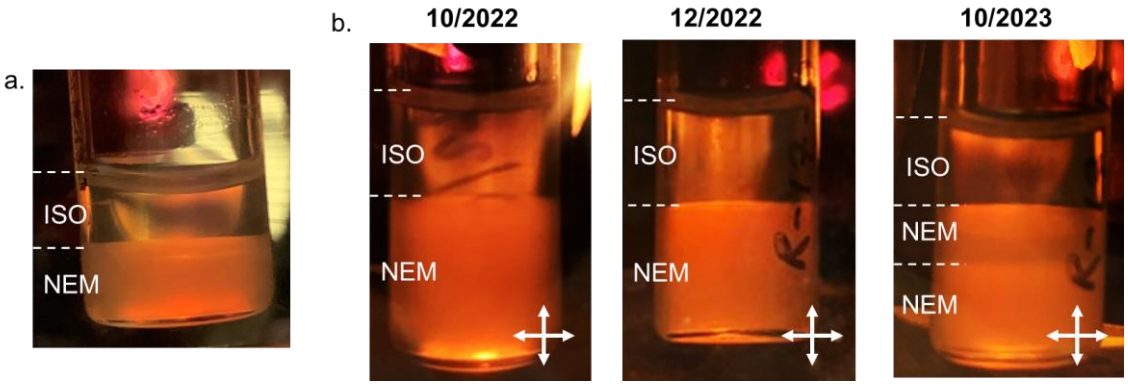

Figure 3.10 Phase separation of rhabdophane $LaPO_4$:Eu suspension in EG observed between crossed polarizers. **a)** $\Phi \sim 5.4\%$, 5% Eu doping and no EG dialysis. A stable biphasic isotropic-nematic equilibrium was maintained over several years. **b)** $\Phi \sim 5.1\%$, 20% Eu doping and 1 week dialysis in EG. Over time, the suspensions transitioned from a typical biphasic isotropic-nematic to a triphasic isotropic-nematic-nematic phase equilibrium after one year.

Figure 3.10a shows the typical biphasic phase separation of 5% doped $LaPO_4$:Eu in EG, with a isotropic phase on top and a brightly birefringent phase on the bottom, obtained after leaving the suspension in a vial for several weeks. In one case we found that a suspension which initially separated into two distinct phases in the vial appeared to have further separated into three phases after one year (**Figure 3.10b**). This occurred in a sample of 20% Eu doped $LaPO_4$ with $\Phi_{avg} \sim 5$ vol% which had been dialyzed in pure EG for 4 days. PLM images droplets taken from the bottom two phases confirm that both are nematic, as evidenced by the typical Schlieren textures (**Figure 5.49**). A similar triphasic isotropic-nematic-nematic equilibrium has been observed for polydisperse suspensions of boehmite rods[101] and for cellulose microfibril suspensions where the bottom nematic is chiral[102].

The origin of the isotropic-nematic-nematic phase equilibrium may be due to the polydispersity of the system. Theoretically, suspensions of rigid rods with a bimodal size distribution can exhibit this triphasic equilibrium when there is at least a factor of 3.167 difference between the two lengths, even for a small amount of longer particles[103]. Unlike the isotropic-nematic equilibrium, the nematic-nematic equilibrium is governed by the balance of orientational entropy and the entropy of mixing, rather than the orientation and translational entropies[103]. Generally, it is expected that the shorter nanoparticles remain in the isotropic phase and the larger particles in the nematic phase[4]. For a biphasic separation of the $LaPO_4$ colloidal LC this was indeed observed, with the average length being around 50% higher in the nematic phase[2].

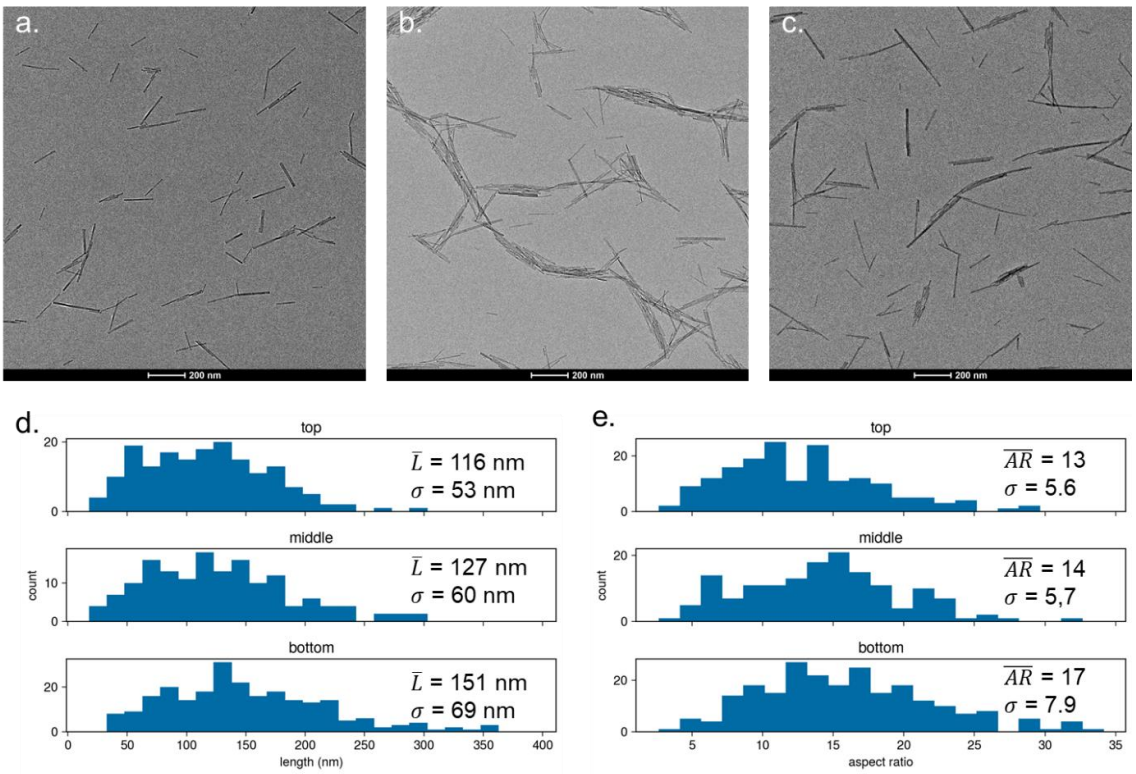

Figure 3.11 Nanoparticle size distribution for the three phases. **a-c)** Example TEM images with 200 nm scale bar of the top, middle and bottom phase respectively. **d)** Distribution of nanoparticle length including the average length $\bar{L}$ and standard deviation σ. **e)** Distribution of the length versus width aspect ratio including average aspect ratio $\overline{AR}$ and standard deviation σ.

In order to check both the dispersity and size of the nanorods, TEM images were taken on all three phases of the triphasic sample (**Figure 3.11a-c**). In general, the particles seem quite well dispersed, although we see some aggregates particularly in the middle phase (**Figure 3.11b**). However, this is likely due to the LC behavior being preserved when drop casting the (diluted) suspension on the TEM grid. Although there is no bimodal distribution of the size, we observe the average length increases when comparing the top (isotropic), middle (nematic) and bottom (nematic) phase (**Figure 3.11d**). Additionally, very large particles (length > 300 nm) are only observed in the bottom nematic phase. Finally, the aspect ratio is higher in the bottom nematic phase (**Figure 3.11e**).

3.2.2 Variety of liquid crystal textures observed by PLM

To observe the LC structures, we sandwich a droplet between two coverslips and image the birefringence pattern through PLM. **Figure 3.12** shows some typical configurations of the isotropic (I) and nematic (N) phase, similar to what was reported previously (**Figure 1.1**[2]). After the $LaPO_4$:Eu suspension has completely separated, most of the isotropic phase is removed from the vial so that only the nematic remains. As $\Phi_{\mathrm{nem}} > \Phi_{\mathrm{iso}}$, different Φ_{avg} can be obtained by controlling the relative amount of pure isotropic and nematic phase. At relatively low Φ_{avg}, many small nematic droplets, known as tactoids, form

and coalesce (**Figure 3.12a**). Further increasing Φ_{avg} causes the inversion of the distribution of the isotropic and nematic phase and anti-tactoids are formed (**Figure 3.12b**). When we take only the nematic phase, we observe a typical Schlieren texture as seen in **Figure 3.12c**. Similar Schlieren textures are observed when considering the pure nematic phases of the triphasic LC (annex **Figure 5.49**).

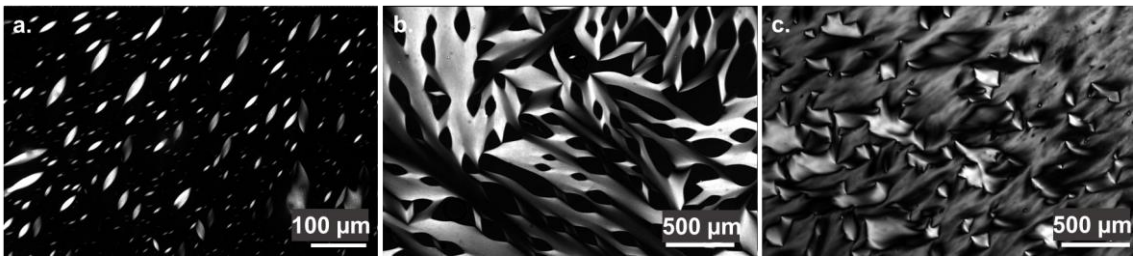

Figure 3.12 PLM images of the different phases observed of 5% doped $LaPO_4$:Eu LC sandwiched between microscope slide and coverslip. **a)** tactoids **b)** anti-tactoids **c)** Schlieren texture of the pure nematic.

Increasing the thickness of the nematic, by means of introducing a spacer between the two glass walls (see **annex 5.1.3**), produces new types of birefringent textures. If we consider the top nematic phase of the triphasic sample, we initially see a patch like pattern of different colors (**Figure 3.13a**). It is different from the Schlieren texture, as we don't see dark brushes, and seems more reminiscent of a marble texture[80]. After leaving the sealed sample at room temperature for one day, we observe the large uniform domain, with dark string-like features as well as several point defects and dark brushes (**Figure 3.13b**). The dark lines without brushes seem to correspond to inversion walls separating two domains of different $\vec{n}$, typical of a nematic thread texture[80].

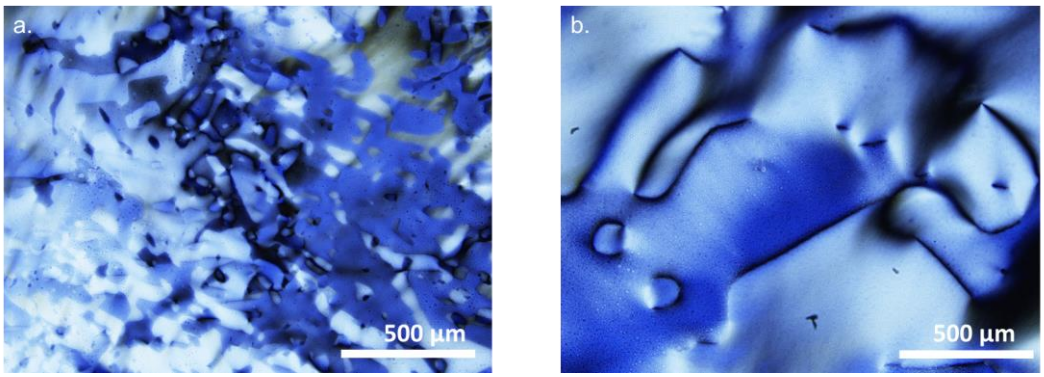

Figure 3.13 Evolution of the top nematic phase of the 20% doped $LaPO_4$:Eu triphasic LC within a confinement cell with 60 µm gap. PLM images taken after roughly **a)** one hour and **b)** one day.

We then consider the bottom nematic of the triphasic sample in a confinement cell, shown in **Figure 3.14**. Again, we see a marble-like texture, but with a smaller domain size and large fluctuations in color, from bright blue to bright yellow. The difference in color may be due to fluctuations in the out-of-plane component of $\vec{n}$, which impacts the effective birefringent for light propagating normal to the observation

plane. The several circular dark spots were confirmed to be air bubbles rather than isotropic phase based on the PL intensity (**Figure 5.50** in annex). After one day, the domains become more uniform and we can more clearly see narrow inversion walls (**Figure 3.14b**). Finally, after one week, the color domains became much larger, but we also see a speckle pattern which seems to be superimposed on top. Additionally, the inversion walls seem to connect and span over a much larger distance (**Figure 3.14c**).

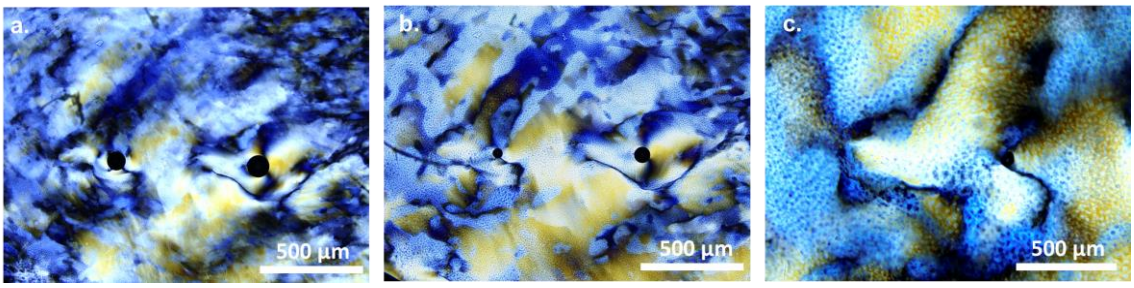

Figure 3.14 Evolution of the bottom nematic phase of the 20% doped $LaPO_4$:Eu triphasic LC within a confinement cell with 60 µm gap. PLM Images taken after roughly **a)** one hour, **b)** one day and **c)** one week.

Finally we consider the biphasic sample of the 5% doped $LaPO_4$:Eu LC with a 3:1 isotropic to nematic volumetric ratio. When directly sandwiched between two glass slides such a sample would generate tactoids and anti tactoids (as seen in **Figure 3.12**), but the addition of a spacer introduces completely new LC textures (**Figure 3.15**).

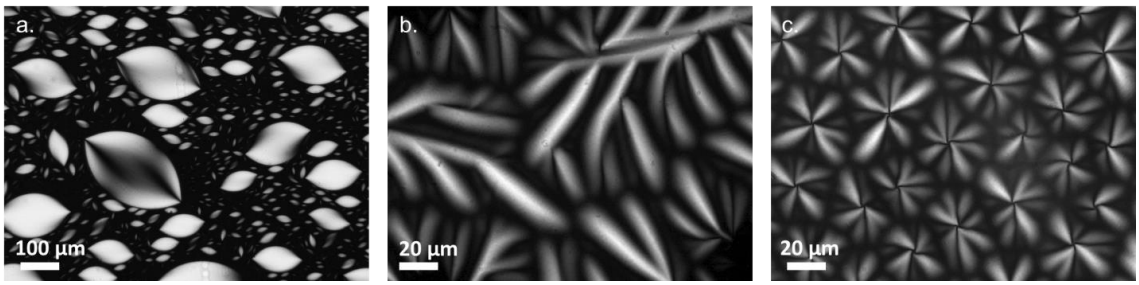

Figure 3.15 Structures observed of the biphasic 5% doped $LaPO_4$:Eu LC in a confinement cell with a 60 µm gap. PLM images of **a)** tactoids **b)** linear streaks **c)** flower.

In some regions, tactoids are observed (**Figure 3.15a**), but their size seems to be much larger than those observed without a spacer (**Figure 3.12a**). We also observe streak-like patterns which have a typical pitch of ~20 µm (**Figure 3.15b**) and flower-like patterns whose size is around 40-50 µm (**Figure 3.15c**). These structures were first discovered by Jeongmo Kim during his PhD, and seem to only occur for very specific conditions, as will be further discussed in the next section.

3.2.3 Morphogenesis of biphasic $LaPO_4$:Eu confined between rigid walls

The experiments discussed in this section were performed previously by Jeongmo Kim as part of his PhD.

Our group previously discovered that confining droplet of the biphasic $LaPO_4$ colloidal LC between two rigid walls (glass substrates) causes morphogenesis of the original nematic structures. **Figure 3.16** shows the evolution of the biphasic LC domains under the confinement between two glass walls with a 60 µm-thick gap as followed by the birefringence using PLM. Initially, we observe a typical I-N phase separation with the formation of strongly birefringent nematic tactoid droplets in the isotropic phase medium (**Figure 3.16**, 0.5 hours). The tactoids then continued to grow in size and coalesce (**Figure 3.16**, 0.7~1.3 hours). Contrary to most previous reports on colloidal biphasic LCs[54,55,104], the evolution did not stop at the tactoids' size growth. A new type of birefringence pattern started to appear and take over the edge of the tactoids (**Figure 3.16** 1.3~3.6 hours). Birefringent streaks with linear defects formed and grew until all of the tactoids were completely consumed. Finally, the linear defects reoriented towards single point defects, creating relatively dark and small flower-shaped domains (**Figure 3.16** 4.9~6.7 hours).

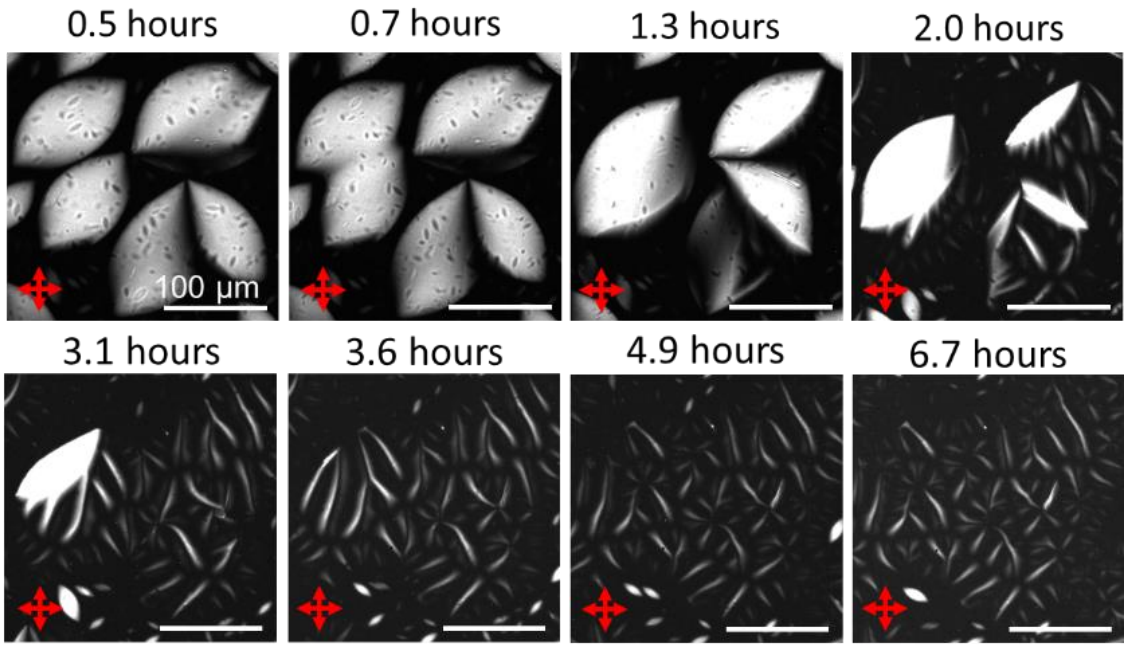

Figure 3.16 Time-lapse of the domain evolution of a biphasic colloidal suspension of $LaPO_4$:Eu nanorods dispersed in ethylene glycol confined in a 60 µm gap. Figure adapted from the PhD thesis of J-M. Kim[10].

This domain evolution depends strongly on the confinement parameters, such as the gap thickness (δ) and the surface chemistry of the walls. For instance, when δ was doubled to 120 µm (**Figure 3.17**), the tactoid droplets grew much bigger by merging completely with nearby ones, until only a single large nematic domain remained (**Figure 3.17** 0.2~2.3 hours). Afterward, linear defects were generated inside the nematic domain (**Figure 3.17** 3.0~13.6 hours). The evolution stopped with linear streaks as the final

structure (**Figure 3.17** 15.3~21.4 hours), which is similar to the fingerprint-like patterns often observed in organic LCs under homeotropic anchoring [8,22,105]. Further evolution to a flower-shaped domain was not observed, suggesting that such linear streaks are the (meta)stable configuration for the double-spaced confinement.

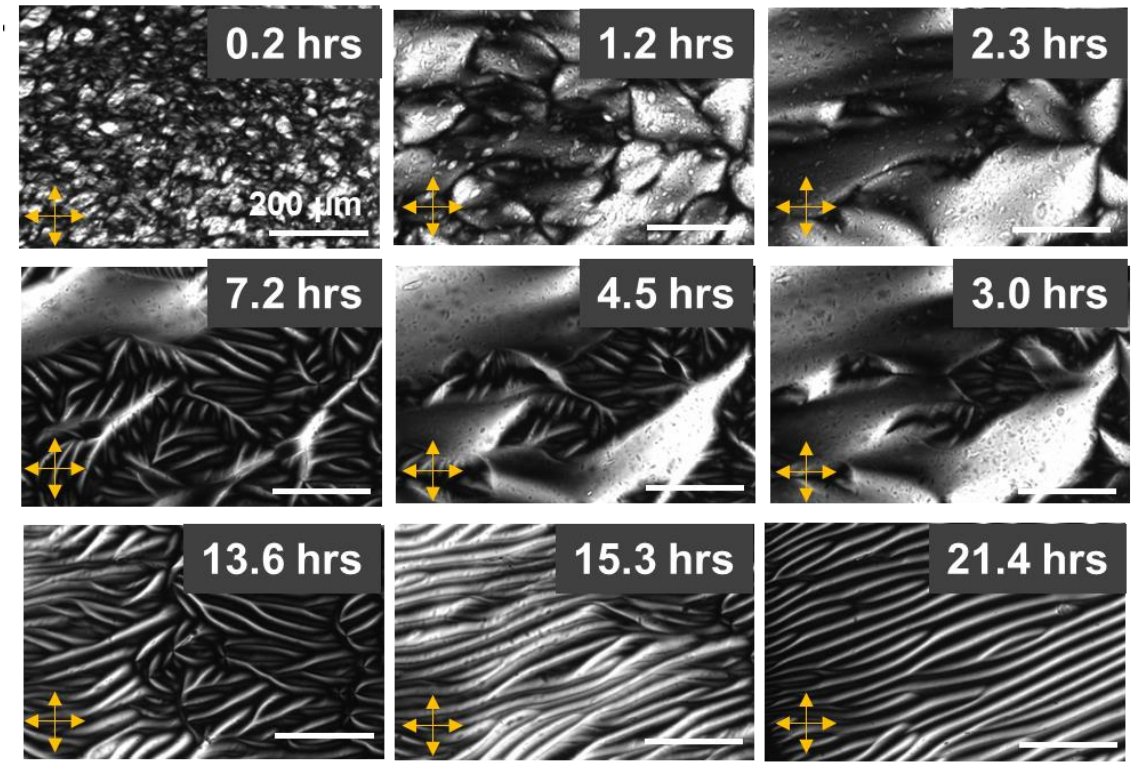

Figure 3.17 Domain evolution of biphasic LC observed in a cell with a 120 µm gap in a cell made of hydrophobic walls (through HDMS treatment of the microscope slides) with a 60 µm gap. Figure adapted from the PhD thesis of J-M. Kim[10].

When δ was kept as 60 µm and the surface chemistry of the confining glass walls was modified to be hydrophobic by a treatment with hexamethyldisilane (HMDS)[106], only the coalescence and growth of tactoids were observed without further evolution (**Figure 3.18**). Conversely, increasing the hydrophilic nature of the walls by means of UV-ozone treatment leads to the same domain evolution as in **Figure 3.16**. This implies that the interfacial chemistry at the confining walls is the driving force for the domain evolution resulting in the formation of the linear streaks and the novel flower-shaped structures.

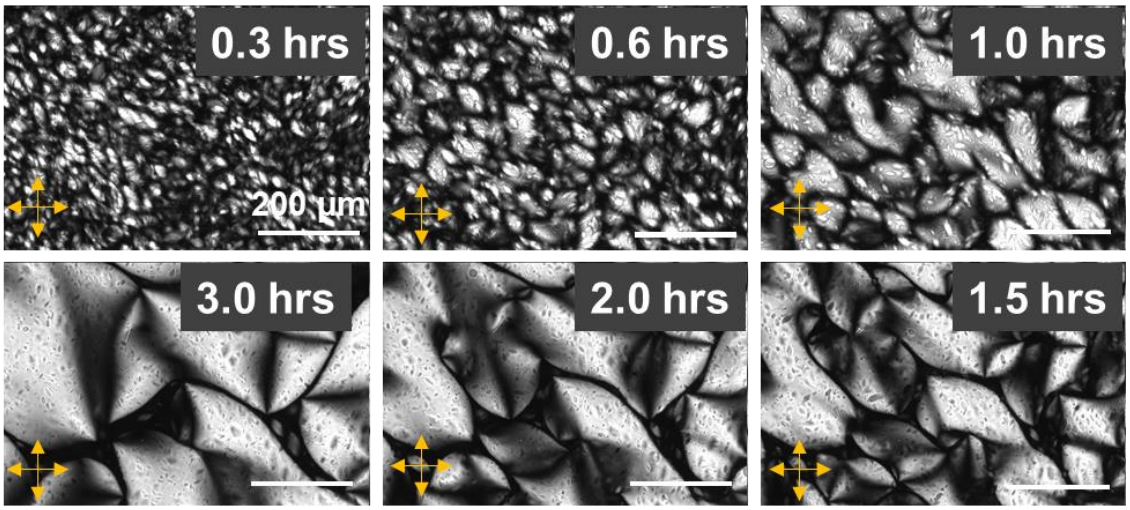

Figure 3.18 Domain evolution of biphasic LC observed in a cell made of hydrophobic walls (through HDMS treatment of the microscope slides) with a 60 µm gap. Figure adapted from the PhD thesis of J-M. Kim[10].

Summary of chapter 3.2

The colloidal $LaPO_4$:Eu LC is lyotropic and follows the Onsager hard rod model assuming an effective rod diameter based on the interparticle interactions. When left undisturbed, the suspensions naturally separate into an isotropic phase on top and nematic phase on the bottom. Under the right conditions, the bottom phase can further separate into two nematic phases with different densities and nanoparticle sizes.

We observe different textures by PLM imaging, including the Schlieren, marble and thread textures typical of nematic LCs. Moreover, when confining a biphasic droplet between rigid walls, a morphogenesis from tactoids to linear streaks and finally flower structures is observed. To understand the mechanism of the morphogenesis, a thorough analysis of the 3D structure of each domain is needed. Additionally, modeling of the free energy of each configuration can give insight into their stability.

3.3 Polarized light microscopy studies and numerical modeling of nematic tactoids

In order to model the free energy of the novel streak and flower structures, we need to have an indication of the relative strength of the elastic energy, surface tension and anchoring strength of our colloidal LC, allowing us to correctly evaluate **equation 3.3.** In this section, we therefor consider the structure of the well-known nematic tactoids and use experimental measurements of their size and director profiles to obtain the different energy contributions through numerical simulations.

3.3.1 Conventional orientation analysis from birefringence pattern

In order to approximate the (in-plane) director profile, we can use PLM imaging. Quantitatively, the light intensity $I(\alpha)$ of a birefringent medium measured for a given crossed polarizers orientation α can be expressed as:

$$I(\alpha) = I_0 \cdot \sin^2\big(2 \cdot (\phi - \alpha)\big) \cdot \sin^2\left(\frac{\pi \cdot \Delta n \cdot t}{\lambda}\right) \qquad \textbf{3.4}$$

where I_0 is the light intensity with parallel polarizers, ϕ is the azimuthal orientation of the director $\vec{n}$, Δn is the amount of birefringence, t is the thickness of the sample and λ is the wavelength of the light. The observed birefringence Δn is directly proportional to the order parameter S, but also the polar angle θ. It is therefore impossible to make quantitative measurements of S through the birefringence if θ is unknown. Nonetheless, collecting the intensity for a range of α allows to find the absolute in-plane orientation $|\phi|$ of the nematic by fitting the values to **expression 3.4**. An image taken with a first order retardation plate then allows to determine the sign of ϕ. Bright blue and yellow colors indicate $\vec{n}$ parallel and perpendicular to the slow axis of the retardation plate respectively.

Director profile of a tactoid

We use the outlined technique on the well-known tactoid structure. **Figure 3.19** shows PLM images taken with crossed polarized rotating in 15° increments (see red arrows) from 0° to 75°. The isotropic phase surrounding the tactoid does not produce any birefringence due to the random orientation of the nanorods and remains dark for all polarizer orientations. The nematic tactoid itself is strongly birefringent throughout and the measured intensity near the center is highest when the polarizers are between 45-60°, indicating that $\vec{n}$ is almost parallel to the x-axis, following the long axis of the tactoid. Near the edges of the tactoid the image taken with the first order retardation plate $\vec{n}$ shows bright blue and yellow colors, which indicate that ϕ is close to ±45° and $\vec{n}$ follows the contour of the I-N interface.

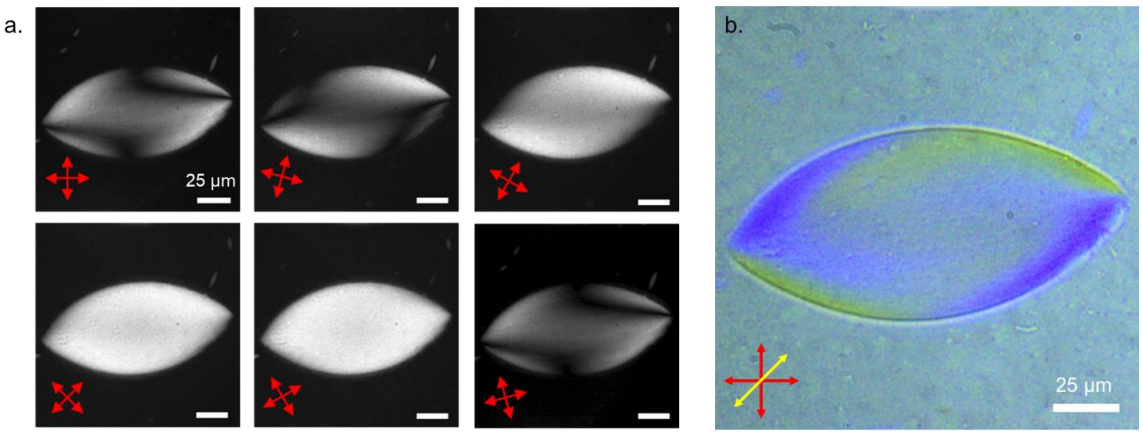

Figure 3.19 PLM images of a nematic tactoid droplet **a)** with crossed polarized rotating every 15° (see red arrows) and **b)** with a retardation plate whose slow axis is indicated by the yellow arrow**.**

To produce a quantitative profile of $\vec{n}$ we consider the absolute intensity fluctuations as a function of the polarizer orientation α. **Figure 3.20a** shows $I(\alpha)$ for nine different positions/pixels inside the nematic tactoid. To find the value of $|\phi|$, these points are first fit with the following function

$$I(\alpha) = A * \sin^2(2 \cdot (\phi - \alpha)) + B \qquad \textbf{3.5}$$

which is of the same form as **equation 3.4**, where A corresponds to the maximum intensity and B to the minimum (background) intensity. This gives an excellent fit to the data point as shown by the orange lines in **Figure 3.20a**. Repeating this procedure for all pixels in the image gives the profile of $|\phi|$ shown in **Figure 3.20b**. A mask has been applied based on the total intensity so that the isotropic phase is hidden. The periodicity of the function is $\pi/2$, which is reflected in the colormap. We see two lines of discontinuity, which corresponds to positions where $|\phi|$ is exactly 0 (and thus $\pi/2$).

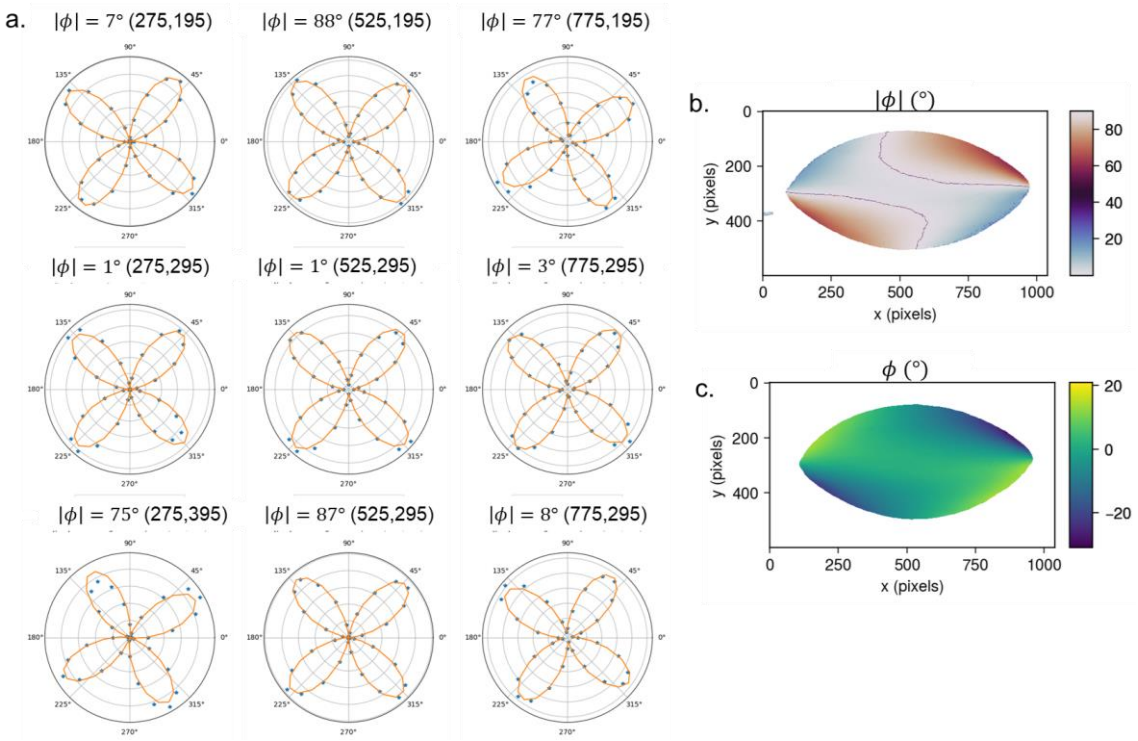

Figure 3.20 Orientation analysis procedure using PLM imaging. **a)** Plots of the intensity as a function of the polarizer angle for 9 different pixels inside the tactoid. The points are fit using equation **3.5** which results in the orange fit line and values of $|\phi|$. **b)** Plot of $|\phi|$ as calculated from the curve fit of the intensity. **c)** Plot of ϕ. Mirror angles were eliminated using the image taken with a first order retardation plate (**Figure 3.19b**).

To find the real orientation, we need to distinguish between $\phi = |\phi|$ and $\phi = |\phi| - \frac{\pi}{2}$, which is done using the image taken with the retardation plate (**Figure 3.19b**). We first consider the regions producing bright colors indicating and consider that the blue color means $\phi = |\phi|$, whereas the yellow color suggests $\phi = |\phi| - \frac{\pi}{2}$. Neither $\phi = 0°$ or $\phi = 90°$ produce any distinct color, so it is not possible to

distinguish between them based on the image in **Figure 3.19b**. One solution would be to take an additional image with the polarizers and retardation plate rotated another 45°. In this case, we simply consider that the profile of ϕ should be continuous and apply this as a condition to distinguish between the angles near $0°$ and $90°$. This finally results in a continuous profile of ϕ seen in **Figure 3.20c**. We can then plot the full profile of $\vec{n}$ as demonstrated in **Figure 3.21**. We observe that the tactoid has a bipolar prolate configuration, where $\vec{n}$ follows the I-N interface except for point defects (boojums) at either end, matching the expected structure for such colloidal LC tactoids[54].

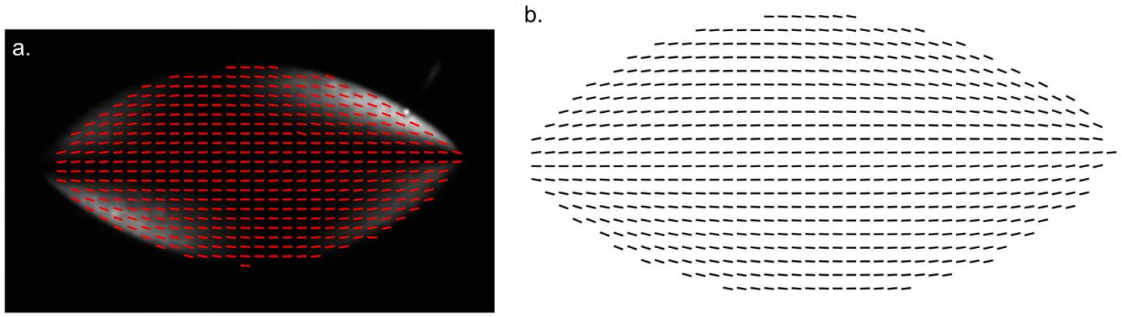

Figure 3.21 Reconstructed director profile in the tactoid **a)** Plotted on PLM image for $\alpha = 0$ **b)** On a white background.

Although these birefringence studies provide a rapid way to estimate the orientation, there are three main issues preventing the proper characterization of the internal structure of the LC. First, quantitative assessment of the azimuthal angle is tedious and requires a camera with large dynamical range. Secondly, as the birefringence only allows for the calculation of the projection $\vec{n}$ onto the observation plane, it cannot be used to determine the polar angle, and thus 3D orientation of $\vec{n}$. This also makes it impossible to distinguish between a homeotropic and isotropic configuration, as both appear dark at all polarizer angles. Finally, as the birefringence signal is collected throughout the depth of the sample, this method is not suited for tomographic mapping. To overcome these challenges, we can instead analyze the photoluminescence produced by the rare-earth doping of the nanorods, as will be demonstrated in **section 3.4.2**.

3.3.2 Numerical simulations to obtain the LC parameters

In order to model the energetics of the complex LC structures (linear streak and flower) we need to have some indication of the material properties (the elastic constant, surface tensions and anchoring strength) of our colloidal LC. We therefore perform numerical simulations of the observed tactoid structures, allowing us to extract the approximate material parameters (elastic constants, surface tension and anchoring strength) of our LC system. The simulations are based on the theoretical framework of Prinsen *et al.* which will be detailed below[107].

Theory of tactoid shape and director-field

As discussed in **section 3.1.2**, the free energy in a LC structure depends on the elastic energy in the bulk, and the surface tension and anchoring at the interfaces. Prinsen *et al.* formulated the energy functional of a tactoid as

$$F = \frac{\kappa}{2}\int_C [(\nabla \cdot n)^2 + |n \times \nabla \times n|^2] d^3x + \int_{\partial C} [1 + \omega(n \cdot s)^2] d^2x \qquad \textbf{3.6}$$

where κ and ω are dimensionless parameters, and s is the local outward normal[107]. κ describes the relative strength of the elastic and surface forces such that

$$\kappa = (K/\sigma)/\lambda \qquad \textbf{3.7}$$

where K is the elastic constant (assuming elastic isotropy such that $K = K_{11} = K_{22} = K_{33}$), σ the surface tension and λ is a characteristic length scale describing the size of the tactoid. The parameter ω captures the ratio of the anchoring strength W and σ such that

$$\omega = W/\sigma \qquad \textbf{3.8}$$

The equilibrium director field n and the shape of a tactoid corresponds to the minimum of the free-energy described by **equation 3.6** and can be classified based on the κ and ω parameters, as shown in the phase diagram of **Figure 3.22a**. No matter the shape of the tactoid, we can observe different types of director profiles depending on the material parameters. In the extreme cases, n is perfectly uniform (high κ and low ω) or n follows the tactoid surface into a boojum at either end, forming a bipolar director field (low κ and high ω). Based on the value of κ and ω, either one of these is expected to be more stable, and the transition between the two is indicated by the solid line in **Figure 3.22a**.

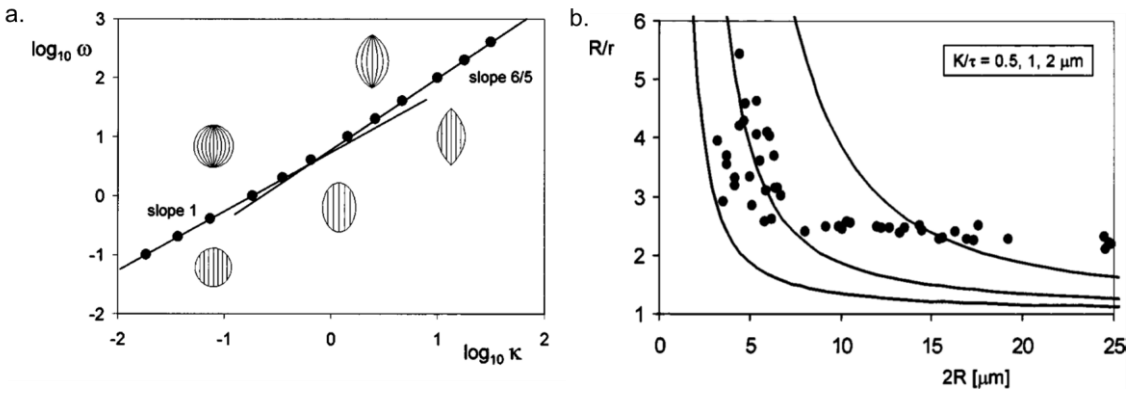

Figure 3.22 Theoretical structure of nematic tactoids. a) Phase diagram of tactoids as a function of the dimensionless parameters ω and κ. b) Plot of the aspect ratio R/r versus the characteristic length $2R$. Dots are experimental results and the solid lines are theoretical results for a bipolar director field with different values of κ/σ. Figures from Prinsen and van der Schoot (2003)[107].

In terms of the shape, we expect the tactoids be spherical for small values of κ and for them to become more elongated as κ increases (see **Figure 3.22a**)[107]. As an example. based on the phase diagram in **Figure 3.22a**, we can thus expect that our colloidal (elongated) tactoids have a higher κ than the (round) organic LCLC tactoid shown in **Figure 3.7**. This also means that larger tactoids tend to have smaller aspect ratios than small tactoids, as $\kappa \propto \lambda^{-1}$. This tendency was experimentally observed for tactoids formed in aqueous suspensions of fd virus and the polymer dextran considering **Figure 3.22b**[107]. Theoretically, the aspect ratio can be expressed as a function of of K/σ and the characteristic size considering a perfectly bipolar director configuration, as indicated by the solid lines in **Figure 3.22b**.

Modeling of tactoids and the determination of material parameters of the $LaPO_4$:Eu colloidal LC

The modeling of the tactoid energetics was performed by Prof. Timothy Atherton from Tufts University using the Morpho finite elements package.

To simulate the shape and director field n of a tactoid, minimization of **equation 3.6** is performed subject to a global volume constraint,

$$\int_C d^3x = V_0 \qquad \textbf{3.9}$$

and a local length constraint on the director,

$$n \cdot n = 1 \qquad \textbf{3.10}$$

We assume that the material parameters K, σ and W remain the same, no matter the configuration of the nematic. By analyzing the shape of the tactoids observed in our colloidal LC, we should be able to obtain the relative strength of these parameters. This can be achieved by two approaches: 1) Considering the general shape of a large amount of tactoids or 2) considering the director profile within a single tactoid.

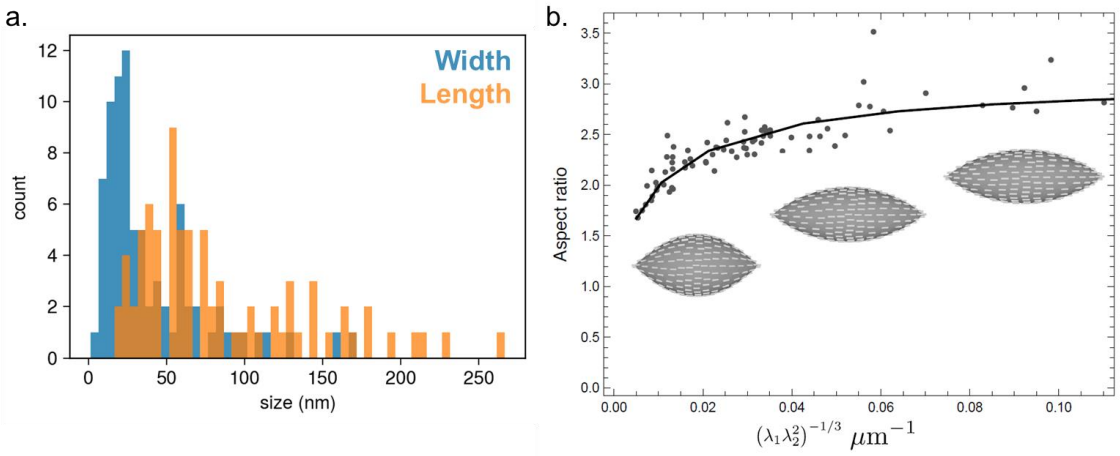

Figure 3.23 a) Distribution of tactoid length λ_1 and width λ_2 in a biphasic $LaPO_4$ LC measured from PLM images. **b)** Tactoid aspect ratio AR as a function of their inverse characteristic length scale. The experimental data are displayed as points and the theoretical fit as a solid line. Modeled tactoids shown for fitted value of ω = 2.48 and κ = 0.5, 3.5 and 7 respectively.

For the first approach, the length λ_1 and width λ_2 of 80 different tactoids were measured from PLM images (**Figure 3.23a**). Most tactoids have a size on the order of tens of µm, but much larger tactoids with λ_1 >250 µm are also observed. We assume the characteristic length scale λ as the cube root of the volume, assuming uniaxiality, such that $\lambda = (\lambda_1\lambda_2^2)^{1/3}$. We then plot their aspect ratio ($AR = \lambda_1/\lambda_2$) against the inverse of characteristic length scale in **Figure 3.23**. The resulting plot matches well with the previously reported relationship in **Figure 3.22b**.

The minimization of **equation 3.6**, considering the constraints of **equations 3.9**-**3.10**, was performed using the Morpho finite element package for values of parameters κ ∈ [0.01, 10] and ω ∈ [1, 10], bounds which were chosen from the observed range of experimentally observed aspect ratios. From the collection of 700 simulated tactoids, a model function describing $AR(\kappa, \omega)$ was learnt from the simulated tactoid data using linear interpolation in Mathematica. The interpolated function was fit to the experimental data with the ratio K/σ and ω as fitting parameters as shown by the solid line in **Figure 3.23**. Doing so, we obtained K/σ = 47.7µm and ω = 2.48.

For the second approach, we do not only consider the aspect ratio AR, but also the measured n, characterized by the azimuthal angle ϕ (**Figure 3.24a**). Essentially, we try to find out where our observed tactoids lie on the phase diagram in **Figure 3.22** and use it to extract κ, ω. More quantitatively, **equation 3.6** tells us that the energy depends on the dot product of n and the surface normal s through the term $\omega(n \cdot s)$. We consider the I-N interface, whose shape is found by performing a spline fit $y(x)$ (shown in red in **Figure 3.24a**) and derive the local surface tangent, defined in terms of the azimuthal angle $\phi_{interface}$ through

$$\phi_{interface} = \tan^{-1}(dy/dx) \qquad \textbf{3.11}$$

Note that this surface tangent is orthogonal to s. We find that along the spline of the tactoid, $\phi_{interface}$ changes linearly from +50° to -40° (see annex **Figure 5.51**).

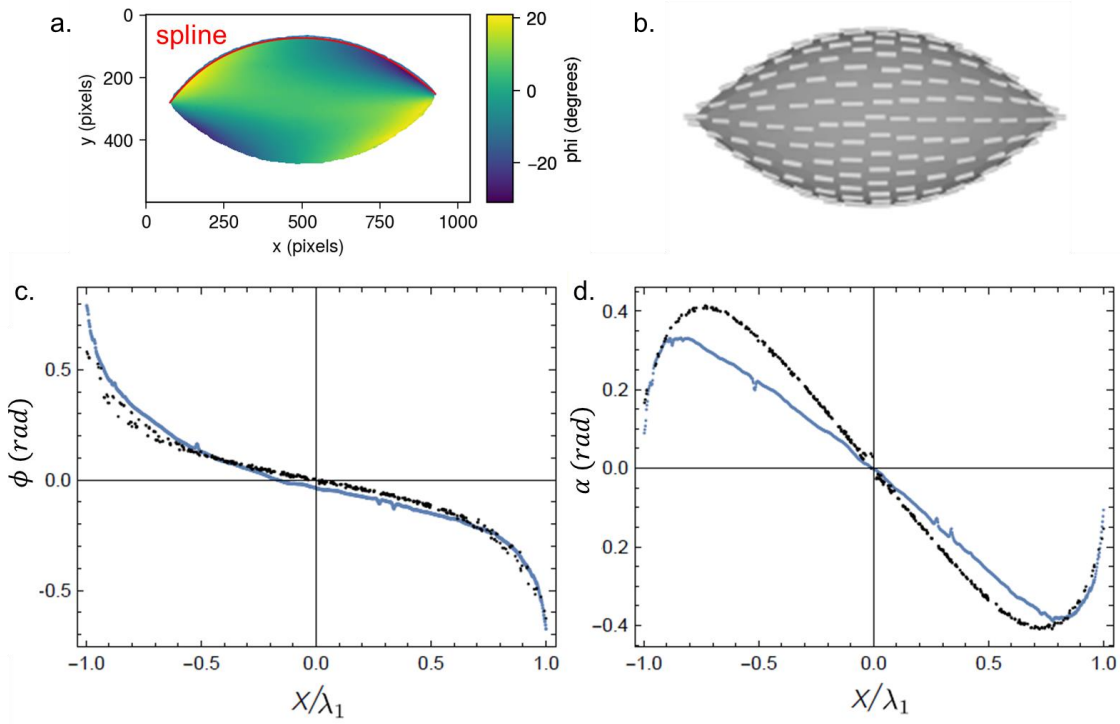

Figure 3.24 a) Plot of ϕ inside a tactoid measured using the PLM approach. The red line is a spline fit along the tactoid surface. **b)** Predicted tactoid configuration using fitted values of K/σ, ω and sizes. **c)** Reconstructed director angle relative to lab frame as a function of position x along the I-N interface and **d)** reconstructed angle α between the local tangent to the surface and the director angle. Experimental values in blue and data from simulated tactoid in black; positions are scaled by the length of the tactoid λ_1.

The tactoid in **Figure 3.24a** has a long axis λ_1 = 154µm and short axis λ_2 = 72µm; hence $\lambda = (\lambda_1\lambda_2^2)^{1/3}$ = 93µm and the AR = 2.14. Based on the on the values of K/σ and ω found using the previous approach, we can construct the simulated tactoid seen in **Figure 3.24b** with κ ≈ 0.5 and AR = 2. We compare the measured and simulated ϕ along the I-N interface in **Figure 3.24c**, and find an excellent agreement. Next, we plot the angle between the director and interface, such that $\alpha = \phi_{surface} - \phi$, seen in **Figure 3.24d.** While the agreement near the cusps of the tactoid is very good, it appears that the director distribution may mildly differ from the predictions of the above model. This is likely due to the incorrect assumption that the elastic constant is isotropic In reality, rod-like lyotropic systems are expected to have $K_{33} \gg K_{11}, K_{22}$[88].

Indeed, similar studies of cholesteric tactoids of amyloid fibrils confirmed such elastic anisotropy and found values for $K_{11}/\sigma = 6\ \mu m$, $K_{11}/\sigma = 8\ \mu m$ and $K_{11}/\sigma = 25\ \mu m$[108]. Additionally, they found $\omega =$

1.35[108]. These values are comparable to the values obtained for our colloidal $LaPO_4$:Eu LC (K/σ = 47.7µm and ω = 2.48). As both K/σ and ω are larger for the $LaPO_4$:Eu, we can expect that the surface tension σ is relatively weak compared to the amyloid fibril LC.

Summary of chapter 3.3

PLM imaging is used to experimentally obtain the (in-plane) director profile inside a nematic tactoid. We model the structure and size of the tactoids in order to extract the material parameters of our colloidal LC. In the first approach, we consider the aspect ratio as a function of the characteristic size of the tactoid and in the second approach we model $\vec{n}$ at the isotropic-nematic (I-N) interface. We find the ratio of the elastic constant and surface tension K/σ = 47.7µm and the ratio of anchoring strength to surface tension W/σ = 2.48. These parameters can then be used to model more complex structures, such as the streak and flower domains in the future.

3.4 Density mapping and 3D orientation tomography of a nematic tactoid

The PLM studies discussed in the previous section could only be used to approximate the in-plane component of the director throughout the depth of the sample. In order to characterize the 3D structure of the tactoid, we therefore need to apply the spectroscopic approach developed in **chapter 2.4.2**. Here, we will first demonstrate and validate the technique using the well-known nematic tactoid structure. In **section 3.5** the same approach will be applied to study the morphogenesis of the confined LC from tactoid to streak and flower.

Interactive, 3D plots are available as HTML files (which can be opened in a web browser) here: https://nostromo.polytechnique.fr/index.php/s/i3wHxigyrrdwzMj

3.4.1 Density mapping

Scanning fluorescence confocal microscopy measuring the total intensity allows to map the nanorod density in 3D. This can be done using the APD (avalanche photo-diode) or by integrating the collected spectra captured by the spectrometer. To demonstrate this, we consider a nematic tactoid in a confinement cell (**Figure 3.25a**). As the tactoids long axis is much larger than its thickness, the scanning was performed using 3 µm increments in the xy-plane and 1.5 µm steps in the z-direction. The collected spectra/APD images are processed using a Python script. A Gaussian smoothing algorithm is applied on the measured PL intensity in all three directions.

For lyotropic colloidal LCs, the nematic phase is significantly denser than the isotropic phase[4] and therefore results in a more intense luminescence intensity for the case of the $LaPO_4$:Eu suspensions. Indeed, considering **Figure 3.25b**, the average PL intensity inside the nematic tactoid is roughly 2 times higher as compared to the surrounding isotropic phase. This is consistent with the colloidal density difference observed in our previous studies (see phase diagram **Figure 3.9**)[2]. This intensity difference is consistent throughout the depth of the sample as seen in **Figure 3.25c**. Such a high contrast of PL intensity allows to perform a tomographic mapping of the nematic domain and create a volumetric 3D reconstruction of the I-N interface topography (**Figure 3.25d**).

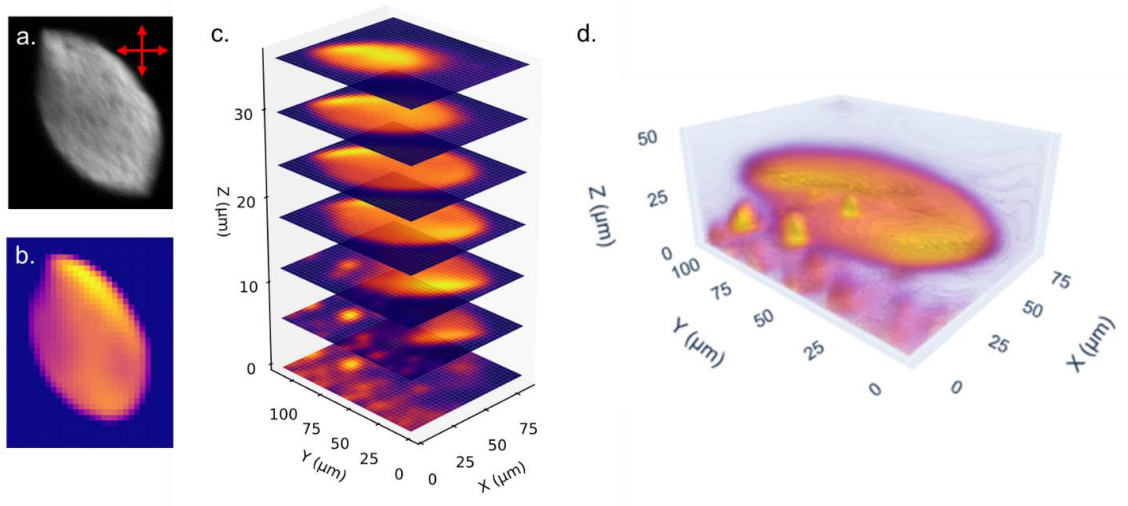

Figure 3.25 Density mapping of a tactoid in confinement cell. **a)** PLM image taken with crossed polarizers (red arrows). **b)** PL intensity map near the center xy-plane of the tactoid, image is 90 µm by 111 µm in size. **c)** PL intensity maps for several depths in the sample, illustrating the tomographic imaging. **d)** Reconstructed nanorod density throughout the 3D volume showing a large, slightly tilted tactoid and some dense islands on the substrate. (Interactive 3D figure available).

The selected tactoid was slightly tilted with respect to the horizontal plane (**Figure 3.25d**), which could not be retrieved by PLM imaging. It has a typical bipolar prolate shape[54], with a flattened elliptical cross section (rather than circular), likely due to the limited depth in the confinement cell. Interestingly, we found small nematic islands scattered underneath the tactoid. Formation of such nematic islands has not been observed by using conventional PLM (**Figure 3.25a**), suggesting their homeotropic alignment. The origin of these islands and their role in the formation of flower-like LC domains will be discussed in **section 3.5**.

3.4.2 Three-dimensional orientation tomography of a nematic tactoid

Polarization resolved confocal micro-spectroscopy enables the 3D mapping of $\vec{n}$ as was demonstrated in **chapter 2.4.2**. Emission spectra are collected with the analyzer parallel to the x and y-axis (I_{zx} and I_{zy}) as

well as at 45° with respect to the x-axis ($I_{z45°}$). The order parameter is approximated at a constant value of 0.85, based on measurements of S_{homeo} near the substrate in a homeotropic region (annex, **Figure 5.37**). The 3D orientation is determined through a simultaneous spectral fitting of the $^5D_0$-$^7F_1$ (MD) and $^5D_0$-$^7F_4$ (ED) transitions of the I_{zx} and I_{zy} spectra, according to the protocol in **annex 5.3.1**, examples of which are shown in **Figure 3.26a-b**. The mirror angles of ϕ are eliminated by comparing the ratio of the first and second MD peak for all three spectra, as described in **section 2.4.3**. We assume that $\vec{n}$ should be tangential at the I-N interface and use this assumption to eliminate the mirror angle of θ. The reference spectra I_π and I_σ were obtained from a large nematic domain in a confinement cell (**Figure 2.31a**).

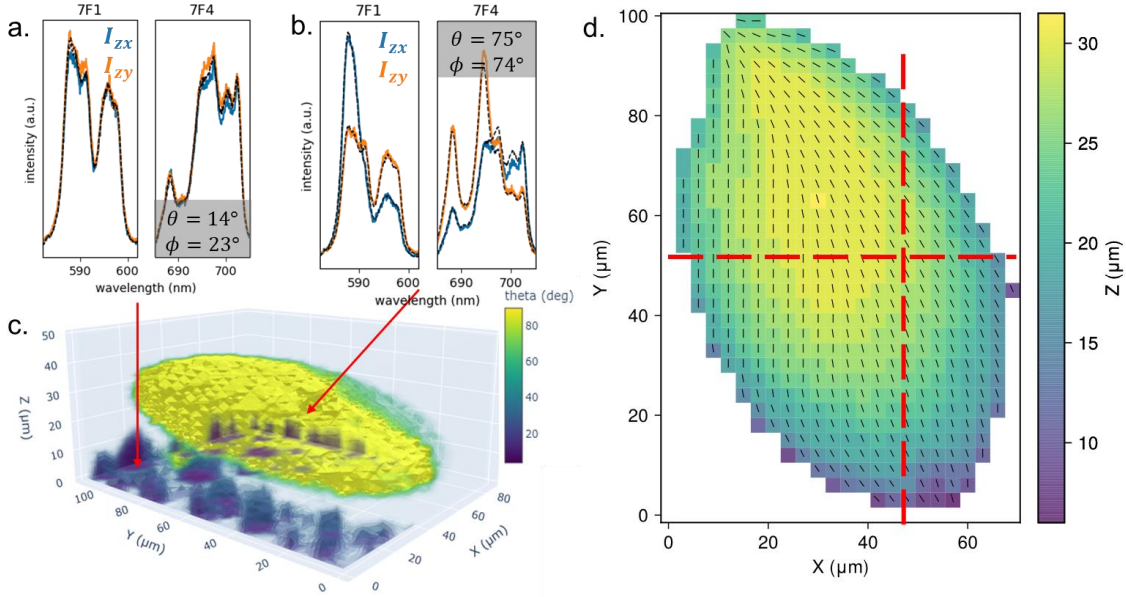

Figure 3.26 3D orientation tomography inside the nematic tactoid. **a-b)** Measured emission spectra and the orientation calculated by spectral fitting (black dashed line) at two positions as indicated by the red arrows. **c)** 3D plot of $|\theta|$ throughout the nematic volume. (Interactive 3D figure available). **d)** $\vec{n}$ projected on the top I-N interface of the tactoid. The color indicates the z-position. Red dashed lines correspond to the cross-sections plotted in **Figure 3.27**.

Figure 3.26c shows the calculated polar angle ($|\theta|$) throughout the whole nematic volume. We find that $\vec{n}$ is mostly planar inside the tactoid, whereas the nematic islands forming on the bottom substrate exhibit vertical homeotropic orientation. This spectroscopic method also successfully reconstructs $\vec{n}$ at the I-N interface of the tactoid (**Figure 3.26d**) as it matches $\vec{n}$ found through PLM measurement in 2D (**Figure 3.21**) for a similar tactoid. However, now we can also visualize the 3D topography of the I-N interface, indicated by the color scale in **Figure 3.26d**, which was not possible by PLM. $\vec{n}$ follows the contours of the tactoid and converges into a boojum on both ends.

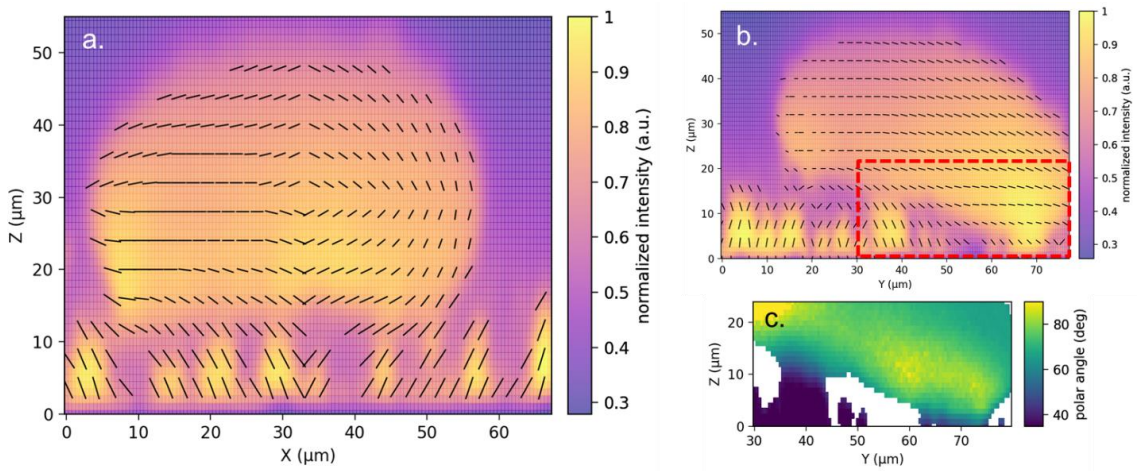

Figure 3.27 High resolution (0.5 µm by 1 µm increments) tomographic scans of the xz plane and yz plane indicated by the red dashed lines in **Figure 3.26d**. **a-b)** $\vec{n}$ projected on the **a)** xz plane and **b)** yz plane, such that the length of the bars represents to the out-of-plane orientation. The color represents the normalized PL intensity. **c)** $|\theta|$ within the region indicated by the dashed red box in b).

To get a more precise understanding of $\vec{n}$ inside the volume of tactoid, we perform tomographic measurements on the yz- and xz cross sections at the center of the tactoid with the maximum spatial resolution (corresponding to 0.5 µm steps in x and y and by 1 µm steps in z). The mirror angle of θ has been eliminated by considering that $\vec{n}$ should be parallel to the I-N interface. **Figure 3.27** shows the resulting PL intensity maps and the calculated $\vec{n}$ field. From the xz cross section, we clearly see that $\vec{n}$ is tangential to the I-N interface, particularly on the right side (**Figure 3.27a**). However, there is a clear discontinuity where the sign of θ changes which indicates that there is some error on the calculation of $|\theta|$. This may be linked to the assumption that the order parameter S is constant throughout the whole nematic domain. As discussed in **section 2.4.1**, S and $\sin^2\theta$ cannot be determined independently, and an error on the assumed value of S therefore results in an error on $\sin^2\theta$. The slight tilt of $\vec{n}$ in the homeotropic islands may also be linked to this issue, as there is no physical reason to expect a tilted easy axis for the anchoring due to the homogeneous nature of the substrate.

3.4.3 Inverse simulation of birefringence patterns from the measured $\vec{n}$

Based on the calculated orientation in the tactoid, we should be able to reconstruct its birefringence patterns as would be observed using PLM, as was demonstrated in **annex 5.3.2** for a 2D dataset. The expected light intensity should follow the previously discussed **expression 3.4**. It should be noted that the Δn depends on the polar angle θ, as well as the order parameter S. Here, we consider S to be constant throughout the nematic domain and we approximate that $\Delta n \propto \sin^2\theta$. The intensity as a function of the orientation of the crossed polarizers α is therefore

$$I(\alpha) \propto \sin^2\theta \cdot \sin^2\big(2 \cdot (\phi - \alpha)\big) \cdot t \qquad \textbf{3.12}$$

where t is the thickness of the nematic phase, which may be different for each xy-position due to the 3D shape of the tactoid. Additionally, we consider that the isotropic phase (identified by its low PL intensity) doesn't produce any birefringence and mask it for the calculations. Using the 3D orientation measured throughout the whole volume of the tactoid, this results in the generated PLM images in **Figure 3.28**.

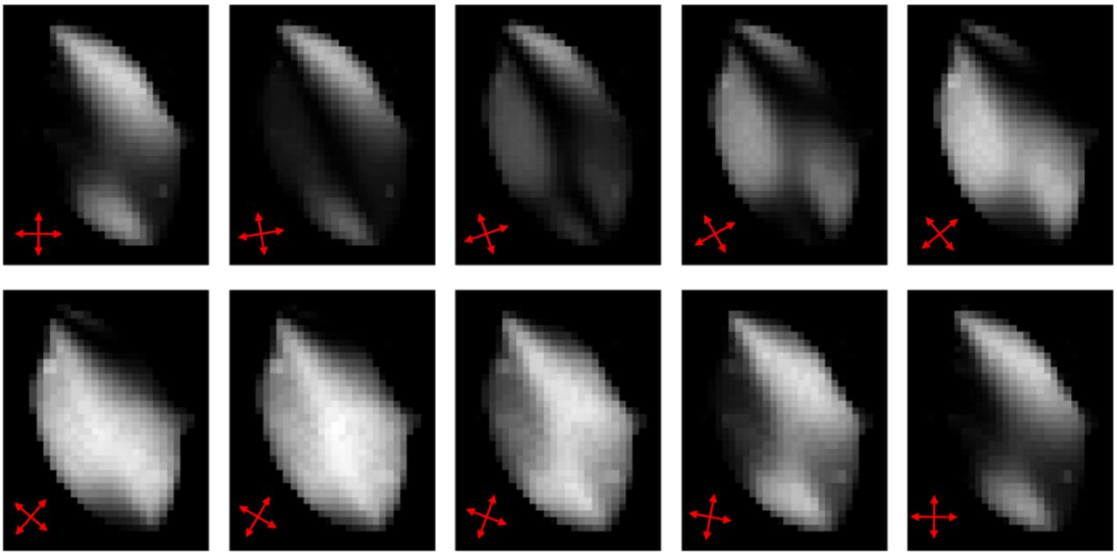

Figure 3.28 Simulated intensity based on the found orientation through spectral fitting as would be observed between crossed polarizers (red arrows) using PLM. Each image is 90 µm by 111 µm in size.

We retrieve continuous profiles for all angles, which looks similar to previous PLM studies of the tactoid in **Figure 3.19a**. Such patterns are commonly reported for colloidal tactoids with bipolar director fields[54], which validates the spectroscopy based orientation tomography technique. Unfortunately, there is no full PLM study of the same tactoid discussed in this section, making it difficult to make a quantitative comparison between simulation and experimental observation. We will demonstrate the birefringence simulation of two other 3D datasets, including the flower structure, in **section 3.5.3**.

Summary of chapter 3.4

Density and 3D orientation tomography through confocal micro-spectroscopy is demonstrated in a large nematic tactoid. Mapping the PL intensity throughout the 3D volume allows to distinguish between the bright, high density nematic and surrounding isotropic phases. This allows us to observe the titled tactoid in the confinement gap and also uncovers the presence of nematic islands formed on the substrate, which were not observed through PLM. The 3D director $\vec{n}$ is reconstructed throughout the nematic volume by polarization resolved spectroscopy. We retrieve the expected bipolar configuration inside the tactoid and find homeotropic alignment in the nematic islands. Finally, simulations of the birefringence patterns further validate the accuracy of the orientation tomography technique.

3.5 Orientation tomography following the confinement-induced LC morphogenesis

As discussed in **section 3.2.3**, we found the formation of unique LC textures resembling linear streaks and flowers when confining the biphasic LC between rigid walls. Moreover, we observed a morphogenesis from tactoids to streaks and finally flowers, which only occurred when the walls were hydrophilic and the space between them was 60 μm[10]. Here we characterize the 3D structure of the different structures observed and use the obtained insights to formulate the mechanism responsible for the morphogenesis.

3.5.1 Estimation of the in-plane orientation through polarized light microscopy

We use the PLM approach demonstrated in **section 3.3.1** to approximate the projected $\vec{n}$ for the linear streak and flower. **Figure 3.29a** shows the linear streak domain observed for different crossed polarizer orientations. We observe narrow birefringent streaks surrounded by regions which appear dark for all polarizer angles and don't show bright colors when imaging with a first order retardation plate (**Figure 3.29b**). We finally find that $\vec{n}$ mostly follows the direction of the streaks **Figure 3.29b**. However, from **Figure 3.29b** we also see some regions (bottom and right) where there seems to be a lot of splays as the color changes abruptly from blue to yellow.

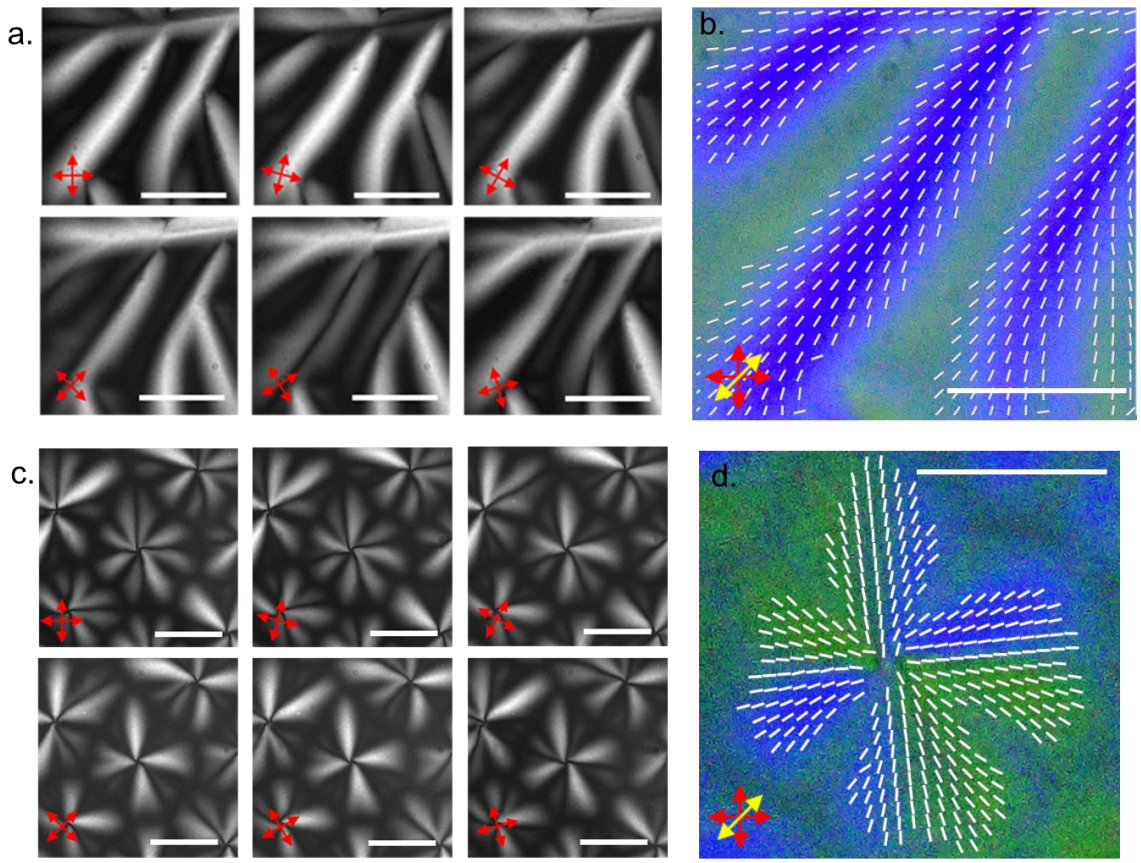

Figure 3.29 Polarized light microscopy (PLM) study of the linear streaks **(a-b)** and flower-shaped **(c-d)** domains. **a**,**c)** PLM images taken with crossed polarized rotating every 15° (see red arrows) . **b,d)** PLM images with a retardation plate whose slow axis is indicated by the yellow arrow. White bars represent the director profiles reconstructed from the birefringence and retardation images. A mask is applied to exclude regions without strong birefringence, indicating either an isotropic or homeotropic alignment. Similar figures for a tactoid structure are found in **section 3.3.1**.

As shown in **Figure 3.29c**, the flower domain typically consists of four strongly birefringent streaks radiating from a dark singularity in the center and dark blurry flower-shaped contour. For the center of the flower, we observe four dark brushes rotating in the opposite direction to the crossed polarizers, indicating a point defect with strength -1. The flower-shaped outline is especially clear in the image with the retardation plate, and each petal seems to consist of two sections with mirrored orientation radiating out from the center (**Figure 3.29d**). This is confirmed by the calculated $\vec{n}$ which shows four distinct petals (**Figure 3.29d**). The surrounding areas are hidden, as they do not show birefringence at any angle of crossed polarizers. Such dark regions indicate the presence of either the isotropic regime or the homeotropic nematic regime involving a complex 3D structure. Therefore, an alternative 3D characterization method is essential to analyze the morphology and topology (profile of $\vec{n}$) of these new nematic domains.

3.5.2 Tomographic density mapping

To understand the 3D structure of each nematic configuration, we first perform a tomographic mapping of the nanorod density, as was previously demonstrated for the early stages of the morphogenesis with a floating tactoid (**Figure 3.25**). In this case, the tactoid had not merged with any other (homeotropic) nematic domains and consequently displayed a slightly flattened, symmetric rugby ball shape. In this section, we will consider a tactoid as it is merging with an existing flower domain, the linear streaks and finally the flower structure.

Tactoid morphing into a flower domain

The next step observed in the morphogenesis was the disappearance of the tactoids as they are consumed by a streak or flower-like domain. **Figure 3.30a** shows such a tactoid as it evolves into a flower domain. A tomographic mapping of the PL intensity, with step size 2.5 µm x 2.5 µm x 2 µm), was performed throughout the sample (**Figure 3.30b-e**). From the xy-scan taken at the middle plane, we can see that the PL intensity is comparable in the tactoid and the flower domain. Surprisingly, we observe that almost a third of the tactoid has a significantly weaker PL intensity and thus lower nanorod density than the rest of the nematic (**Figure 3.30b,e**).

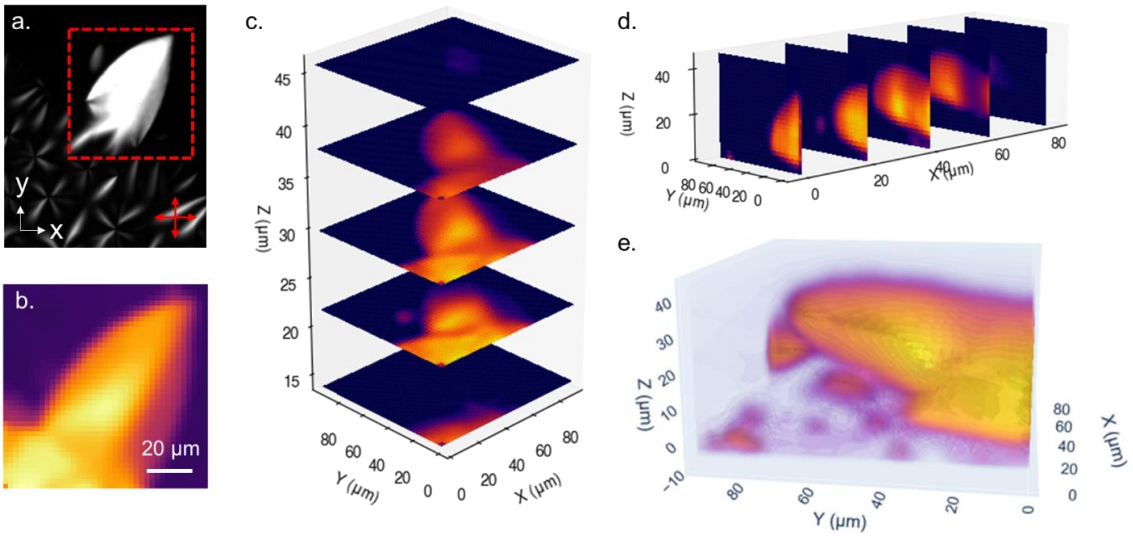

Figure 3.30 Density mapping of a tactoid merging with a flower domain. **a)** PLM image taken between crossed polarizers. The region of interest for the PL measurements is indicated by the red dashed outline. **b-e)** PL intensity maps with a scanning resolution of **b)** PL intensity map near the center height of the tactoid. **c-d)** PL intensity maps for various xy and xz cross sections. **e)** Reconstructed nanorod density throughout the 3D volume (interactive figure available).

The cross sections and 3D reconstruction reveal that the tactoid is tilted and does not contact the substrate anywhere (**Figure 3.30d-e**). Even the part which seems to have already merged into a streak or flower pattern does not reach to the bottom substrate. Some nematic islands are observed on the substrate which do not contact the tactoid.

Linear Streaks

Next, we consider the linear streaks, the intermediate phase observed during the morphogenesis, shown by the PLM image in **Figure 3.31a**. Taking PL images at different depths in the sample reveals a non-flat topography and that the brightly birefringent streaks correspond to a lower luminescence intensity as seen in **Figure 3.31b**. From the high-resolution (step size of 0.5 µm x 1 µm) cross section xz-planes in **Figure 3.31c**, we observe that the nematic regions are all sat on the bottom substrate surface while the isotropic phase fills the above volume of the gap. We find a highly spiky topography of the I-N interface where the streaks form sharp ridges, which is linked to the dark outline in the PLM image.

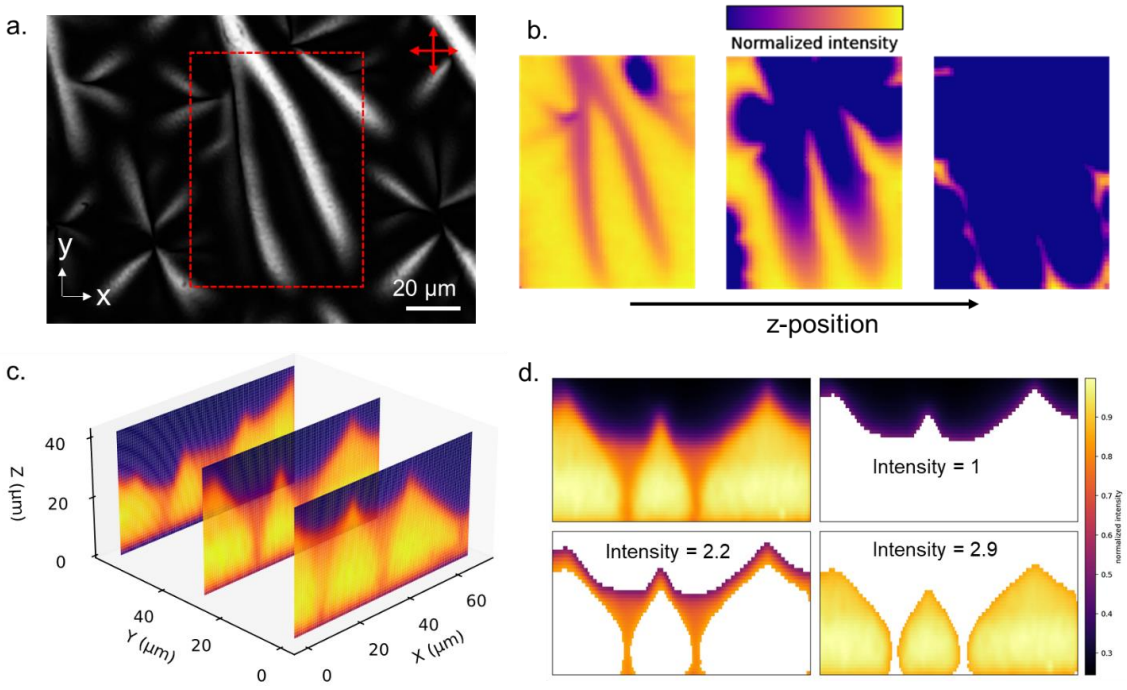

Figure 3.31 Density mapping of linear streak. **a)** PLM image taken between crossed polarizers (red arrows). The region of interest for the PL measurements is indicated by the red dashed outline. **b)** PL intensity maps at different z-positions (roughly z=20,30,40 from left to right) **c)** PL intensity maps for various xz cross sections. **d)** PL intensity map of the middle xz cross section (top left) and its separation of the three domains; isotropic (top right), low density nematic (bottom left) and high density nematic (bottom right). The average intensity with respect to the isotropic is calculated.

Based on the PL intensity, we can distinguish two distinct nematic domains with different densities, as illustrated in **Figure 3.31d**. The brightly birefringent parts of the streaks (**Figure 3.31a**) correspond to the valleys whose PL intensity (i.e. nanorod density) is 30% lower compared to the denser nematic region (**Figure 3.31d**). The vertical section of dense nematic regions (**Figure 3.31c-d**) displays a half tactoid-like shape that are vertically posed side by side. The intermediate regions fill the sharp valleys connecting the inflection points of neighboring ridges rendering energetically favorable menisci. As the bottom part of the gap is occupied entirely by the nematic domains, the dark regions observed by PLM (**Figure 3.31a**) are

expected to be due to a homeotropic alignment rather than isotropic domains. The planar alignment of $\vec{n}$ seems to exist only inside the birefringent, low-density nematic regions.

Flowers

Finally, we consider the flower structure previously characterized by PLM and map its PL intensity (**Figure** 3.32). First, high-resolution cross-sectional scans at the center of the flower were performed, with a 0.5 µm step size in the lateral and 1 µm in the axial direction (**Figure 3.32b-c**). We see that the intermediate low-density nematic domains disappeared while forming the flower-shaped domains from the initial streaks (**Figure 3.32b-c**). Only the brightly luminescent sharp ridges remain with the curvature of I-N interface becoming almost linear except the sharp edge points (**Figure 3.32b-c**)**.** Additionally, we can see a thin defect core reaching down to the bottom substrate at the center.

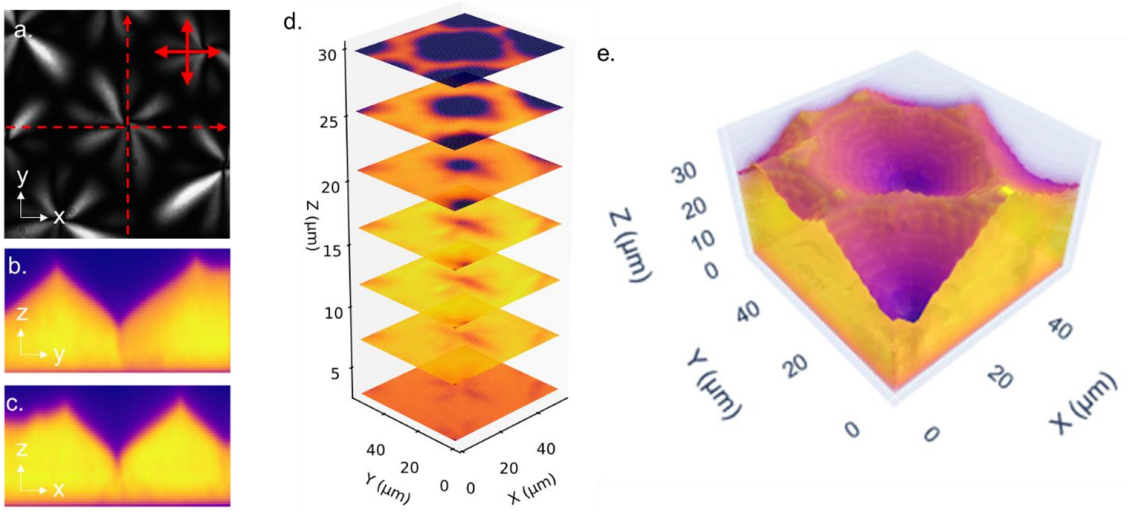

Figure 3.32 Density mapping of flower structure. **a)** PLM image taken between crossed polarizers (red arrows). **b-c)** High resolution PL intensity maps at the middle yz and xz plane respectively (see dashed lines in **a**). **d)** PL intensity maps for various xy cross sections. **e)** Reconstructed nanorod density throughout the 3D volume (interactive figure available).

We then performed tomographic scanning throughout the 3D volume with larger step size (1.25 µm x 1.25 µm x 1.5 µm). Comparing the different xy-cross sections shows that the nematic fully covers the substrate with a minimum thickness of around 15 µm (**Figure 3.32d**). From the 3D reconstruction in **Figure 3.32e**, we see that the I-N interface of a flower has a central crater surrounded by contouring ridges. The altitude of the I-N interface thus varies largely from the center to the contour from 15 to 35 µm within the confinement gap of 60 µm. The ridges are remarkably sharp indicating the presence of linear defects. From the measured PL intensity, which is 2 times higher than the isotropic, we find that the nanorod density of the flower domain matches that of the initial tactoid. The PLM analysis of the birefringence pattern shows that a flower is composed of four symmetric petals radiating out from the center, while

there exist a certain gap between petals (**Figure 3.29f**). In order to further investigate the complex topology of this system, a 3D orientation analysis of the local $\vec{n}$ is required.

3.5.3 Three-dimensional orientation tomography

Next, we apply the spectroscopic orientation tomography previously demonstrated in **section 3.4.2** to the different structures observed during the morphogenesis.

Tactoid morphing with flower

Figure 3.33a shows the projected $\vec{n}$ mapped over the top interface of the tactoid merging with the flower domain. For the most part, $\vec{n}$ follows the contours of the tactoid and the edges of the streaks, as expected from our previous results. However, we observe a discontinuous change in $\vec{n}$ on the right side, which corresponds to the region of low PL intensity (see **Figure 3.30**). This does not seem to be due to an error in the calculation, as the same discontinuity is observed from the experimental PLM images in **Figure 3.33b-c** and the simulated images in **Figure 3.33d-e**. Although the interface is strongly curved, it varies continuously across the tactoid, and topography alone can therefore not explain the abrupt change in $\vec{n}$. Instead, as the line defect directly follows the direction of the streak which the tactoid is merging into (see **Figure 3.30a**), it seems to be due to the remaining strain associated to the morphogenesis. This strain may also explain the local decreased rod density of the bottom right region in the tactoid, as observed in **Figure 3.30**.

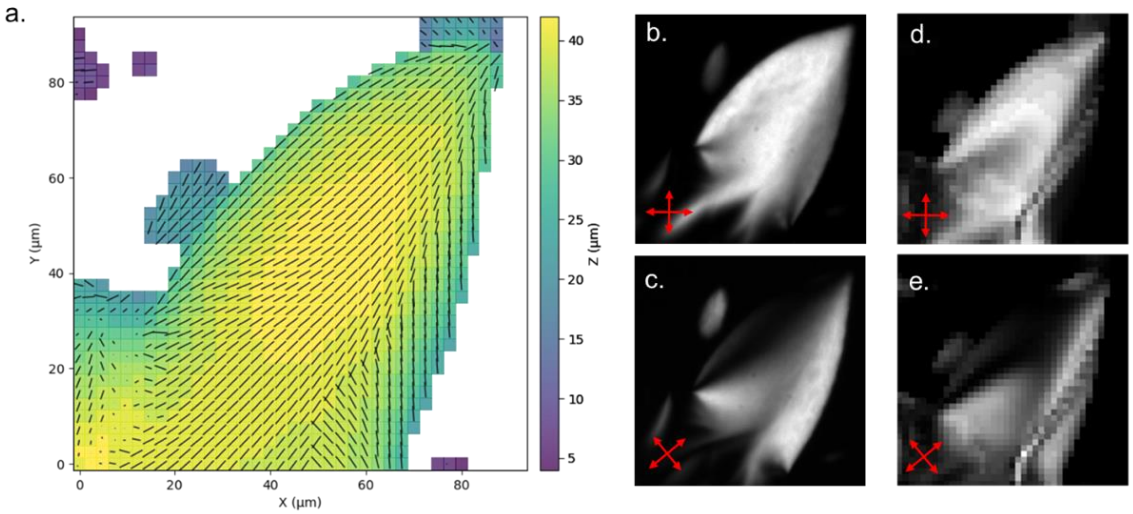

Figure 3.33 a) Projected $\vec{n}$ on the top of the I-N interface. The color corresponds to the z-position. **b-c)** PLM images taken with crossed polarizers at 0° and 40° respectively. **d-e)** Simulated birefringence pattern based on the calculated 3D orientation throughout the nematic volume for crossed polarizers at 0° and 40° respectively.

This is more clearly seen when considering the variation in polar angle $|\theta|$ across the I-N interface (**Figure** 3.34**a**). We can see two distinct planar regimes, separated by a slightly tilted domain at the same position

as the discontinuity seen in the PLM images. Considering the cross-section and full volume, we see that where the side of the tilted tactoid approaches close to the bottom substrate, the homeotropic anchoring propagates upwards (**Figure 3.34b-c**). It seems closely approaching the bottom substrate is required to trigger the morphogenesis, as the part far above the substrate preserves the planar orientation of $\vec{n}$. Remarkably, the initially isotropic domain between tactoid and substrate forms some homeotropic islands (**Figure 3.34b,c**) that grow up to connect with the tactoid and form an almost continuous domain even before the complete touchdown. This observation evidences that the strong homeotropic anchoring force and the resultant elastic strain dominates the morphogenesis and the topological evolution.

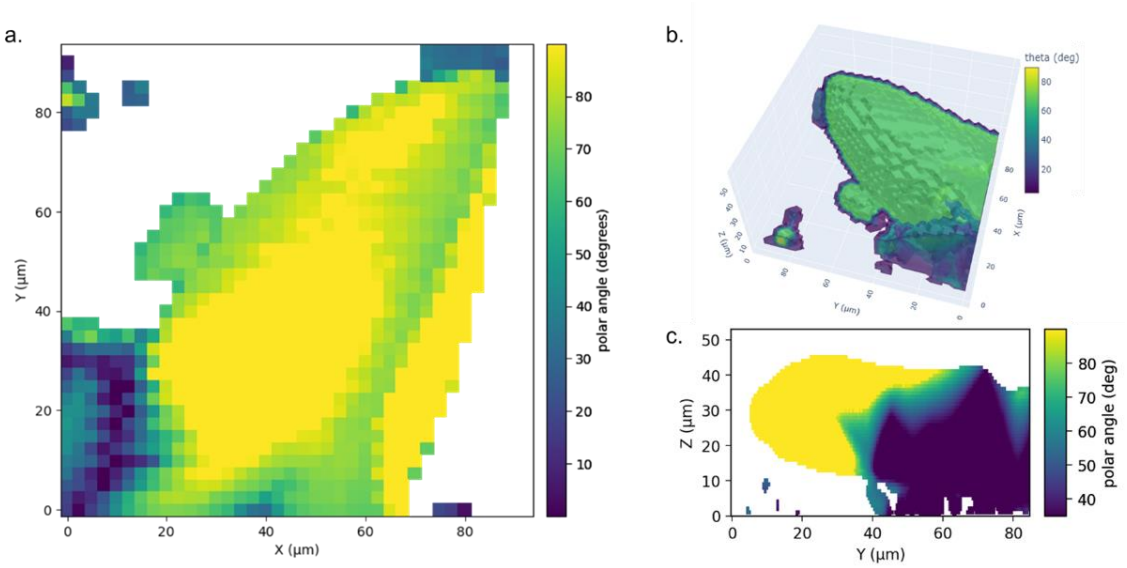

Figure 3.34 Polar angle θ throughout the tactoid merging with flower domain. **a)** θ on the top of the I-N interface, matching the z-positions in **Figure 3.33a b)** θ throughout the volume. (Interactive 3D figure available) **c)** θ for the yz-cross section at the center x-position.

Linear Streaks

The linear streaks, generated after the complete evolution of the tactoids, display globally homeotropic alignment except in the low-density region between the ridges associated with bright birefringence (**Figure 3.35**). **Figure 3.35a** shows that $\vec{n}$ follows the length of the birefringent streaks, which is consistent with the results from the PLM analysis discussed earlier. The branching into smaller streaks is paired with significant splay in the $\vec{n}$ field, which was also predicted from the PLM imaging with a first order retardation plate (**Figure 3.29b**). The cross-sectional view in **Figure 3.35b** shows within the less dense region, $|\theta|$ changes gradually from ~45-90° connecting neighboring ridges. This large gradient in $\vec{n}$ may be responsible for the low density of nanorods in this region and its further transformation to the final flower-shaped domains in order to reduce the elastic energy.

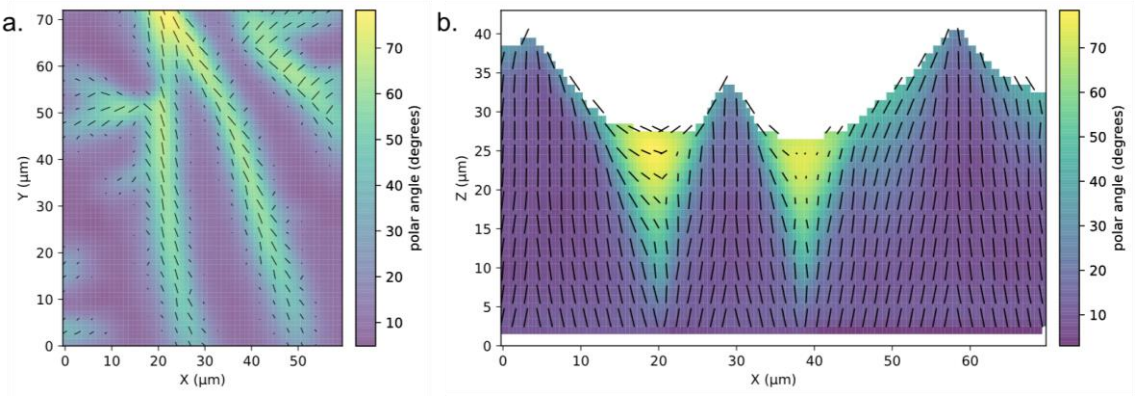

Figure 3.35 Orientation tomography in linear streak corresponding to **Figure 3.31**. The color represents θ and the bars the projection of $\vec{n}$ onto the plane such that the length indicates the out of plane orientation. **a)** xy plane near the center height **b)** xz plane at y = 30 µm.

Flower

We indeed find that this low-density, high-strain region is eliminated in the flower-shaped domains (**Figure 3.36a**). In the flower, the homeotropic orientation at the bottom gradually changes to planar with respect to the I-N interface, similarly to $\vec{n}$ inside the tactoid**.** The central singularity is exceptionally clear, showing a fully homeotropic alignment persisting from the bottom substrate to the I-N-interface (**Figure 3.36a**). **Figure 3.36b** displays the polar angles on the I-N interface seen from the top, which clearly outlines the flower with four distinct petals. When considering the alignment throughout the whole volume (**Figure 3.36c**), we find that the bulk is fully homeotropic and $\vec{n}$ only changes close to the I-N interface in the walls of the craters. The sharp ridge tops corresponding to the contour of the flower are also linear defects with perfectly homeotropic orientation. This is reminiscent of the topography induced in thin organic nematic films, where the center of the point defects corresponds either to the peak or valley of the topography (see **Figure 3.4**)[84]. This reveals that the elastic energy is competing with the surface energy in our colloidal LC.

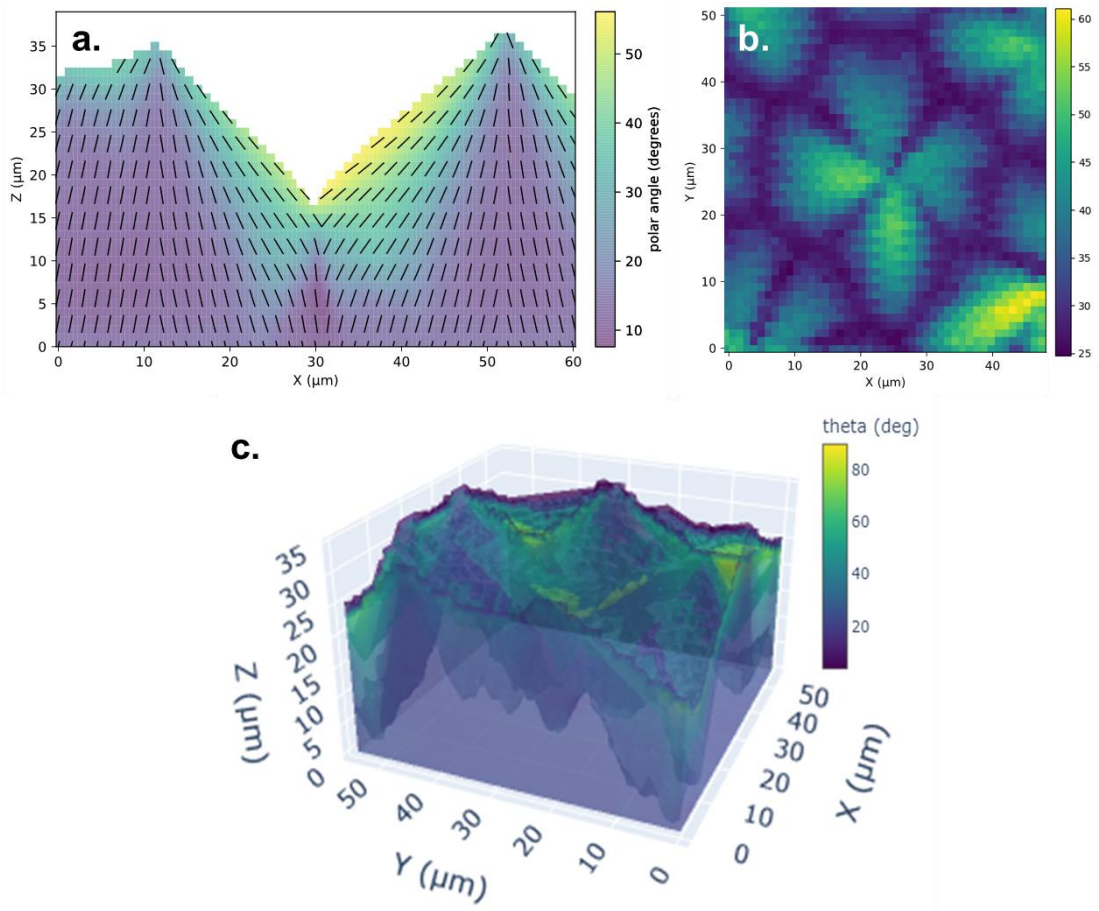

Figure 3.36 Orientation tomography in flower domain, corresponding to **Figure 3.32**. **a)** $\vec{n}$ projected on central xz-cross section **b)**$|\theta|$ on the I-N interface. **c)** $|\theta|$ throughout the nematic volume (interactive 3D figure available).

Finally, **Figure 3.37a** shows the director field at the I-N interface as seen from above, showing a radial distribution in four orthogonal sections (petals) reproducing **Figure 3.29f** obtained by PLM. The gaps between petals correspond to the homeotropic ridges, and therefore don't show a projection on the interface in **Figure 3.37a**. To confirm the correct analysis of $\vec{n}$, we can compare the simulated PLM images to those measured experimentally, as seen in **Figure 3.37b-e**. Although the profile is less smooth, we generally find a good agreement between simulated and experimental results.

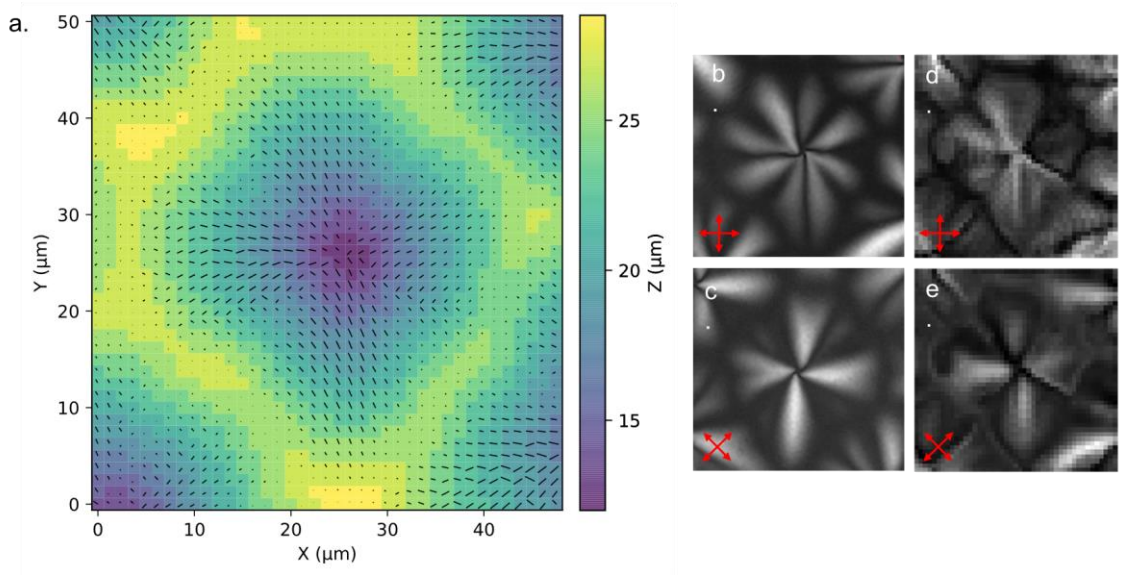

Figure 3.37 a) Projected $\vec{n}$ on the top of the I-N interface. The color corresponds to the z-position. **b-c)** PLM images taken with crossed polarizers at 0° and 45° respectively (indicated by red arrows). **d-e)** Simulated birefringence pattern based on the calculated 3D orientation throughout the nematic volume for crossed polarizers at 0° and 45° respectively.

The radial orientation of $\vec{n}$ in the flower-shaped domain is reminiscent of the focal conic domain (FCD) seen in nematic films close to the transition to smectic A phase when subjected to hybrid anchoring conditions (discussed in **section 3.1.2**)[22,109]. However, the 3D tomography reveals that our flower-shaped domain has a more complex and peculiar topology and interfacial topography. In fact, the anchoring conditions of flower-shaped domain are inversed compared to that of FCD which have planar anchoring at the substrate and homeotropic anchoring at the air interface. The interface of FCD is expected to be flat due to the dominating contribution of surface tension. By contrast, the elastic energy dominates the presented colloidal LC resulting in the dramatic topographical fluctuation of I-N interface as observed.

As discussed in **section 3.1.2**, disk shaped films including a -1 point defect have been shown to morph into a topography with 4 outwardly radiating valleys surrounding a protruding center (see **Figure 3.6**)[92]. The defect core in our flower structure also has a strength of -1, which seems to also produce a four-fold symmetric topography even though it is a 3D volumetric defect structure. In our case, morphing the I-N interface of the bulk nematic domain that is homeotropically anchored at the bottom. Therefore, the defect core flowing out into the third dimension seems to minimize the elastic free energy of the volume maintaining the dominant homeotropic alignment[87]. We note that all types of observed defects (core, ridge, boundary between flowers) are perfectly homeotropic along with the anchoring at the bottom substrate.

3.5.4 Morphogenesis mechanism and stability

Based on the demonstrated structural characterization in 3D, we propose a mechanism responsible for the observed morphogenesis under confinement (illustrated in **Figure 3.38**). The origin of the topological evolution is the conflicting anchoring conditions at the two interfaces. At the nematic-wall interface, interactions between the charged tip of the crystalline $LaPO_4$:Eu nanorods[2] and the hydrophilic glass surface induce strong homeotropic anchoring, although the chemical origin of this anchoring is not yet understood. At the I-N interface the tangential orientation is favored as governed by the elastic anisotropy of the nematic phase[110]. If the anchoring strength is sufficiently high compared to the elastic energy, a tactoid becomes anchored to the substrate, causing the formation of local defects. Gradually, the rods in the tactoid reorient from a planar to homeotropic alignment. As this anchoring happens simultaneously at different positions, linear defects appear where multiple domains intersect through the Kibble mechanism[111]. The planar regimes remaining in those linear defects experience large stresses, associated with the strong director gradient. Over time, a new thermodynamically stable configuration is established by minimization of the elastic free energy, eliminating this planar regime. A delicate balance of the elastic energy, anchoring force and surface tension result in the remarkable crater-like topology formed around arrays of central point defects. Preliminary modeling of the flower structure (**annex 5.4**) underscores the importance of the relatively low surface tension compared to the more common organic LCs.

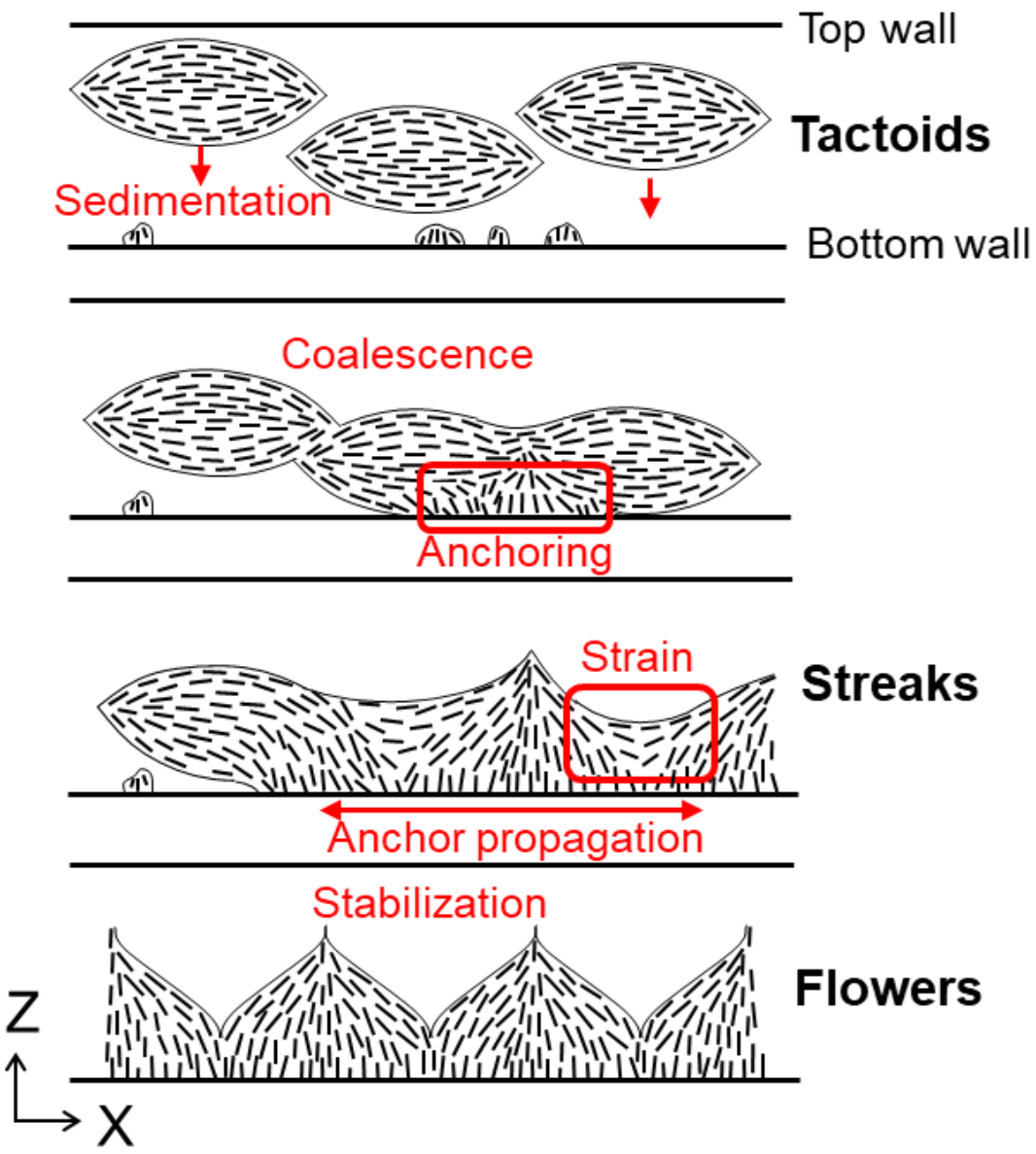

Figure 3.38 Illustration of the proposed morphogenesis mechanism. Nematic tactoid droplets form and sediment due to gravity and homeotropic islands nucleate on the substrate. Contact between these two domains trigger a homeotropic anchoring of tactoids. The tactoids continue to coalesce combined with a propagation of the homeotropic anchoring. The conflicting boundary conditions, planar at the I-N interface and homeotropic at the substrate surface, result in high strain regions forming streak patterns. Finally, a crater like topography is formed minimizing the strain and stabilizing the structure.

Increasing the hydrophobicity of the surface seems to decrease the surface anchoring strength, which is consistent with previous reports[112]. When the anchoring strength decreases, the bulk elastic energy and surface tension become the dominating factors and tactoids no longer anchor to the substrate (**Figure 3.18**). Doubling the spacer thickness increases the total nematic volume, which decreases the relative impact of the surface tension and results in long linear streaks which minimize the elastic energy while

maintaining homeotropic anchoring (**Figure 3.17**). The formation of the complex flower structure therefore requires a delicate balance of the elastic energy, surface tension and anchoring strength.

Summary of chapter 3.5

We studied the 3D structures observed throughout the morphogenesis from tactoid to linear streak and finally flower. The high spatial resolution achieved by the confocal setting reveals that the hybrid boundary conditions, with homeotropic anchoring at the substrate and a planar anchoring at the I-N interface, result in the formation of linear streaks which morph into flower-shaped four-fold symmetrical topological defects with crater-like topography. The large topography seems to be a result of the relatively high elastic energy and anchoring forces as compared to the surface tension.

3.6 Conclusion

We explore a lyotropic colloidal LC of anisotropic $LaPO_4$:Eu nanocrystals dispersed in ethylene glycol (EG). At sufficiently high volume fractions, the LC typically separates into an isotropic (I) and nematic (N) phase, but in some conditions even an I-N-N equilibrium appears.

When confining a biphasic droplet of the $LaPO_4$:Eu LC between hydrophilic walls, we observe the formation of tactoids and subsequent evolution into streak- and flower like patterns. We apply the spectroscopic orientation tomography developed in **chapter 2** to characterize the 3D structures throughout the morphogenesis. The final flower structure exhibits four-fold symmetric craters which have extreme topographical fluctuations, on the order of tens of microns. Such large topographies have never been observed in organic LCs and can be understood from the fact that colloidal LCs have a relatively low surface tension. Hence, the colloidal LC and its large scale defects and 3D interfaces provides a unique opportunity to study the complex interplay between bulk elastic forces and surface tension.

We combine experimental PLM studies of tactoids and simulated tactoid structures to retrieve the relative strength of the elastic energy, anchoring strength and surface tension of the $LaPO_4$:Eu LC. Using the found parameters, we can simulate the more complex streak and flower structures. First results of the modeling of the flower structure in a cylindrical geometry shows that the relatively small surface tension is indeed responsible for the large topography observed. To more closely match the experimental results, we should include the elastic anisotropy and consider a more representative geometry (for example with four-fold symmetry rather than radial symmetry).

4 Shearmetry in a kinetic energy harvesting system based on selective ion sweeping

4.1 Shearmetry using non-Newtonian suspensions of $LaPO_4:Eu^{3+}$ nanorods

The high shape anisotropy of the $LaPO_4$:Eu nanocrystals allows them to be easily aligned by external forces. An interesting application arising from this property, is the measurement of shear stresses in microfluidic flows, as was introduced in **chapter 1.3.** In this section, the fundamental theory explaining the relationship between alignment and applied shear stress will be discussed. Additionally, we consider the rheological behavior of the suspension in order to refine the calibration procedure.

4.1.1 Monitoring shear using anisotropic nanoprobes

In 1939, Peterlin and Sutart formulated the orientation theory which describes the optical (as well as electrical and magnetic) behavior of a collection of rigid ellipsoidal particles in a continuous fluid medium[113]. The orientation of each particle, as defined by its major axis, with respect to the streamlines can be defined as $\xi(\theta, \phi)$, where θ is the angle with respect to the normal to the streaming plane and ϕ as the angle between its projection and the direction of the velocity gradient (**Figure 4.1a**). We also consider that the shape of the ellipsoids is described by the length of its two semi-axes a and b (**Figure 4.1b**). Finally, it should be noted that the theory discussed below is only valid for dilute suspensions and neglects interparticle interactions. It can therefore not be applied to dense LC samples described in **Chapter 3**, but can be used to describe the behavior of a dilute isotropic phase.

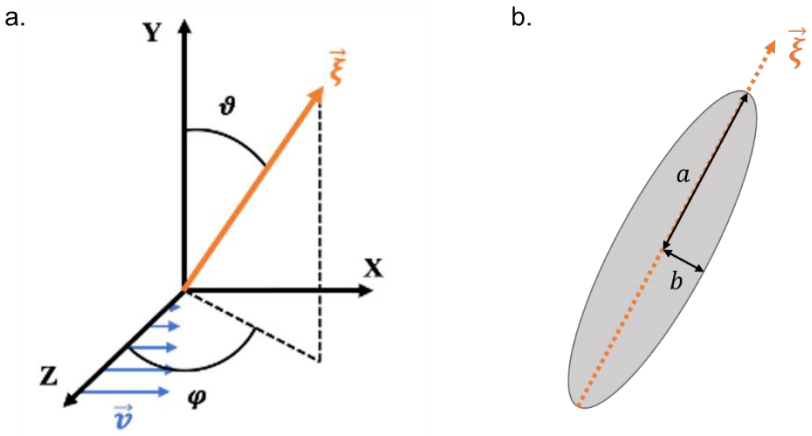

Figure 4.1 a) Orientation of the major axis of an ellipsoidal particle $\xi(\theta, \phi)$d in a coordinate system with principle axes X,Y,Z. X is in the direction of the streamlines, Z is in the direction of the velocity gradient and Y is normal to the streaming plane. Figure adapted from Cerf and Scheraga (1952)[44]. **b)** Dimensions of an ellipsoidal particle.

The collective orientation of an ensemble of such ellipsoids is captured in the distribution function $F(\theta, \phi, t)$, which describes the distribution of the orientation of particles in an ensemble at a given time. Its evolution is described by Fick's equation:

$$\frac{\partial F}{\partial t} = \Omega \Delta F - \nabla F \omega \qquad \textbf{4.1}$$

where t is time, Ω is the rotary diffusion constant, Δ is the Laplacian operator and ω is the angular velocity. The first term captures the effect of Brownian motion which is opposed by the effect of the hydrodynamic forces according to the second term. Brownian motion favors a completely random orientation, and its strength is characterized by Ω which can be calculated using the equations of Perrin such that,

$$\Omega = \frac{3kT}{16\pi\eta_0 a^3} \cdot \left(-1 + 2\ln\frac{2a}{b}\right) \qquad \textbf{4.2}$$

where k is the Boltzmann constant, T the absolute temperature, η_0 the solvent's viscosity[114]. Smaller particles thus have a larger associated Ω, which results in rapid diffusion and homogenization of the orientation distribution. On the other hand, hydrodynamic forces cause the particles to align with the streamlines and their effect on the orientation distribution are captured by ω, which is described by its two components

$$\omega_\theta = \frac{1}{2} \cdot R \cdot \ G \cdot \sin\theta \cdot \cos\theta \cdot \sin 2\phi \qquad \textbf{4.3}$$

$$\omega_\phi = \frac{1}{2} \cdot (1 + R\cos 2\phi) \qquad \textbf{4.4}$$

where G is the velocity gradient and R is a form factor which depends on the axial ratio of the ellipsoid ($R = \frac{p^2-1}{p^2+1}$ with $p = \frac{a}{b}$). In the case of simple shear, where the velocity profile is two-dimensional ($v_z = 0$), the shear rate $\dot{\gamma}$ is simply equal to the velocity gradient G. In situations with a strong velocity gradient (and thus high shear), the particle responds rapidly as ω_θ is large. This means that the particles can quickly respond to changes in the direction of the streamlines and corresponds to a high degree of alignment within the ensemble.

For small particles (a < 1µm) steady state is achieved very quickly and we can approximate $\frac{\partial F}{\partial t} = 0$[44]. Under this steady-state condition, **equation 4.1** can be solved numerically which yields

$$F = \sum_{j=1}^{\infty} R_j \left[\frac{1}{2}\sum_{n=0}^{\infty} a_{n0,j} P_{2n} \cos 2m\phi + \sum_{n=1}^{\infty}\sum_{m=1}^{\infty} \left(a_{nm,j}\cos 2m\phi + b_{nm,j}\sin 2m\phi\right) P_{2n}^{2m}\right] \qquad \textbf{4.5}$$

where P_{2n} are Legendre polynomials of the first kind, and P_{2n}^{2m} are their derivatives of the 2m order[113]. The $a_{nm,j}$ and $b_{nm,j}$ coefficients are functions of the relative impact of the shear forces and Brownian motion, described by the factor $\alpha = G/\Omega$, and for simple shear $\alpha = \dot{\gamma}/\Omega$. Based on the distribution F, we can also find the orientation factor f which describes the degree of order within the ensemble (previously referred to as the order parameter S) such that

$$f = \frac{16\pi}{5}\left[\left(\sum_{j=1}^{\infty} a_{11,j}\right)^2 + \left(\sum_{j=1}^{\infty} b_{11,j}\right)^2\right]^{1/2} \qquad \textbf{4.6}$$

f is thus a function of the coefficients of the distribution function, which depend on α. If shear forces dominate ($\alpha \gg 1$) the ellipsoids will all align in the same direction and f will approach 1. In the opposite case when rotational diffusion is dominant, particles will orient randomly and $f = 0$. The full dependence of f on α can be found through the numerically calculated $a_{11,j}$ and $b_{11,j}$ coefficients, as shown in **Figure 4.2a**[23]. For simple shear, **Figure 4.2a** therefor demonstrates the stress-optical law by showing $f(\dot{\gamma}/\Omega)$ for such a system. **Figure 4.2b** shows how the aspect ratio p affects the orientation factor (for $\alpha = 5$). As expected from the dependency of Ω and ω on p, large aspect ratios result in a higher degree of alignment. We also see that $f(\alpha)$ is (close to) linear for low values of α and its slope depends on p.

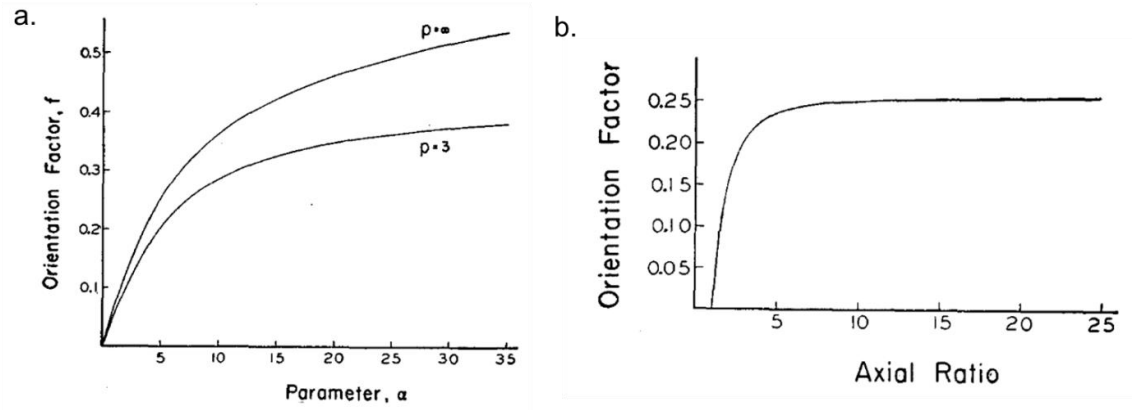

Figure 4.2 Orientation factor f based on numerical calculations for **a)** as a function of α (the ratio between the velocity gradient G and rotary diffusion constant Ω) for different aspect ratios p. **b)** as a function of p for the case of $\alpha = 5$. Figures from Scheraga *et al.* (1951)[23].

Additionally, in a flowing system where the particles align along the streamlines, the birefringence Δn can also be used to determine f by using the relationship

$$\Delta n = \frac{2\pi \cdot \phi}{n_0} \cdot (g_1 - g_2) \cdot f \qquad \textbf{4.7}$$

where ϕ is the volume fraction of the particles in the solvent, n_0 is the refractive index of the solvent at rest and $(g_1 - g_2)$ is the optical factor, which depends of the refractive indices of the particles and solvent, the shape of the ellipsoid and the intrinsic anisotropy of the field[44,113]. Δn is therefore directly

proportional to the orientation factor and the (optical) properties of both solvent and particles and follows the stress-optical law such that $\Delta n(\dot{\gamma}/\Omega) \propto f(\dot{\gamma}/\Omega)$.

Optical measurements of the $LaPO_4$:Eu nanorod suspensions through PLM can be used to directly measure Δn, using **equation 3.4** and assuming the director $\vec{n}$ is parallel to the observation plane and follows the streamlines. Additionally, using the spectroscopic analysis of the polarized PL as described in **chapter 2.4.4**, f (equivalent to the order parameter S) can be measured directly. As discussed in **section 1.3,** a calibration curve of $f(\dot{\gamma})$ and $\Delta n(\dot{\gamma})$ can therefore be established through measurements in a simple channel with known $\dot{\gamma}$ (**Figure 1.12c**). Previously in our group, the calibration curve was obtained by measuring the global emission spectra throughout the channel using a low magnification, conventional microscope without a pinhole[12,38]. However, as the calculated value of the orientation factor f using the spectral analysis of the PL can vary depending on the optical setting, it should be better to do both the calibration and measurement using the same optical setup. Moreover, we previously assumed that dilute nanorod suspensions (Φ<1%) act as classical Newtonian fluids, but recent results showed that they are actually shear thinning[38]. In the next section, we will propose an alternative approach, using the same optical configuration and considering the rheological properties of the suspension.

Apparent shear and the impact of the Peclet number

As previously discussed in **section 2.1.1**, the first demonstration of tomographic shear rate mapping was performed in a microfluidic channel with a cylindrical constriction[12]. By spectral analysis of the polarized PL of $LaPO_4$:Eu^{3+} a map of the order parameter S, equivalent to f, could be reconstructed. Then by combining this map with the established calibration curve, it could be converted to a map of $\dot{\gamma}$, as seen in **Figure 4.3a**. For laminar flow, we would expect the profile of $\dot{\gamma}$ to be fully symmetric around the constriction (**Figure 4.3b**), but clearly this is not what was obtained. The origin of this discrepancy can be attributed to the fact that the response of the nanorods to the change in the streamline direction is not instant, but instead occurs on the diffusion time scale $\tau_d = \Omega^{-1}$. Therefore, if the nanorods are advected faster than this time scale, the rotational inertia creates an apparent shear rate $\dot{\gamma}_{app}$ which does not match the real $\dot{\gamma}$ imposed by the flow. This impact of this effect is quantified by the non-dimensional Peclet number

$$Pe = \frac{U}{H\Omega} \qquad \textbf{4.8}$$

which is the ratio of τ_d and the advection time scale $\tau_a = H/U$, where H is the characteristic length (in this case the height of the channel) and U the flow velocity.

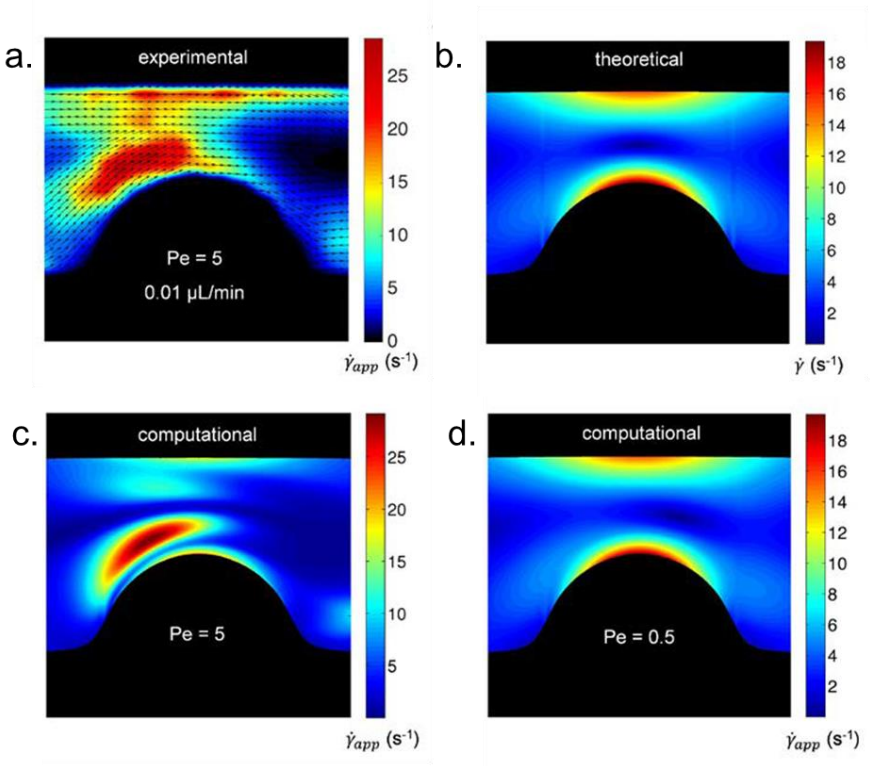

Figure 4.3 a) Experimental map of the apparent shear rate $\dot{\gamma}_{app}$ around a cylindrical constriction in a microfluidic channel obtained through spectral analysis. **b)** Theoretical map of the shear rate $\dot{\gamma}$ under laminar flow **c-d)** Simulated map of $\dot{\gamma}_{app}$ taking into consideration the orientational inertia through the Peclet number Pe for **b)** $Pe = 5$ and **d)** $Pe = 0$. For all plots the flow direction is from left to right. Figure from J-W. Kim *et al.* (2017)[12].

A large Pe suggests that advection dominates, such that the rotation of the particles is relatively slow with respect to their displacement, and thus a large mismatch between $\dot{\gamma}_{app}$ and $\dot{\gamma}$. Simulations of $\dot{\gamma}_{app}$ as a function of Pe show a good agreement with the experimental profile using $Pe = 5$, as seen in **Figure 4.3c**. Ideally, we want to minimize the discrepancy as much as possible, which requires $Pe < 1$, such that the measured $\dot{\gamma}_{app}$ matches the theoretical $\dot{\gamma}$ (**Figure 4.3d**). Decreasing Pe whilst maintaining the same flow conditions requires an increase in the rotary diffusion coefficient Ω. From **expression 4.2**, this can be achieved by reducing the size of the particles, as $\Omega \propto 1/a^3$ (where a is the half-length). Although not the focus of this work, our group has therefore been working on synthesizing smaller nanorods whilst maintaining a high aspect ratio, thus alleviating the distortion in measurements of $\dot{\gamma}$.

4.1.2 Calibration curve including the rheological properties of the nanorod suspensions

In this section, an alternative calibration approach considering the rheological properties of the suspension is performed with the confocal microscopy setup. We use a straight channel with square cross section and collect the PL spectra at the middle plane using the confocal microscope. In parallel, numerical simulations considering the complex rheology of the nanorod suspension are performed, which allow to

provide a theoretical profile of $\dot{\gamma}$. We then match the calculated profile of f to the simulated profile of $\dot{\gamma}$ to obtain the calibration curve.

Shear thinning and simulations of the shear profile

We recently characterized the rheology of our nanorod suspensions and found significant shear thinning behavior[38]. We can thus not assume Newtonian behavior in the simulation and should include the viscosity as a function of the shear rate $\mu(\dot{\gamma})$ in the COMSOL model. To do so, we first need to find the expression describing $\mu(\dot{\gamma})$. We approximate that the nanorod suspensions behave like a generalized Newtonian fluid, meaning that the viscosity μ is a function of the instantaneous shear rate $\dot{\gamma}$, but is not affected by any history effects. Furthermore, the shear stress τ is simply the product of the viscosity $\mu(\dot{\gamma})$ and $\dot{\gamma}$. The Carreau model is often used to describe the rheology of suspensions of nanoparticles[115,116], and states that,

$$\mu(\dot{\gamma}) = \mu_\infty + (\mu_0 - \mu_\infty) \cdot (1 + (\lambda \cdot \dot{\gamma})^2)^{\frac{n-1}{2}} \qquad \textbf{4.9}$$

where μ_∞ is the viscosity at infinite shear, μ_0 the viscosity at zero shear, λ is the relaxation time (under low shear conditions) and n is a dimensionless number. Generally, if $n < 1$ the fluid is shear thinning, if $n = 1$ it is Newtonian, and if $n > 1$ it is shear thickening. Shear thinning behavior following this model has previously been reported for aggregates of silica particles suspended in mineral oil with n ranging from 0.35 to 0.72 depending on the particles' volume fraction[117].

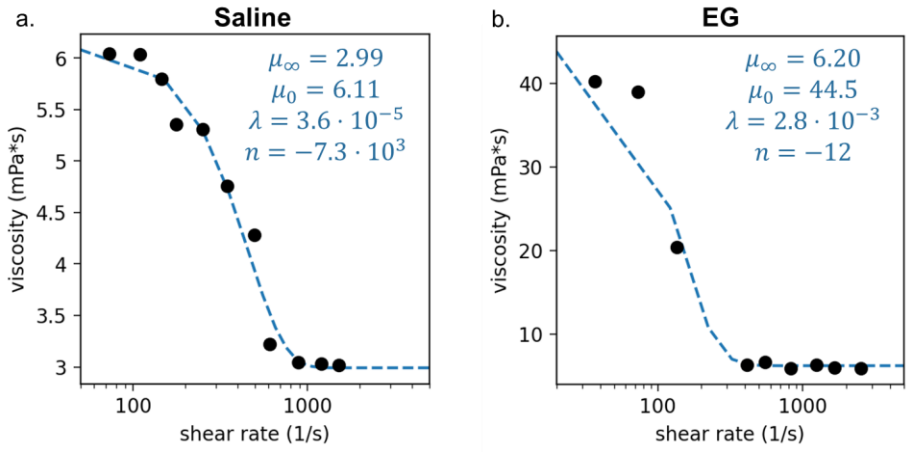

Figure 4.4 Shear thinning behavior of nanorod suspensions in **a)** saline and **b)** ethylene glycol (EG). The datapoints are fit using the Carreau model (**expression 4.9**). The measurements of the viscosity were performed by Zijun Wang[38].

Figure 4.4 shows the experimentally measured viscosity for $LaPO_4$:Eu suspension in a saline solution and in ethylene glycol (EG). For both types of suspensions, the μ remains constant after a certain threshold of $\dot{\gamma}$, indicating that the suspensions act as Newtonian fluids for sufficiently high $\dot{\gamma}$. The data was fit using the Carreau model as is indicated by the blue dashed lines. We find a decent fit for the saline suspension, but

a poor fit for the EG suspension. Moreover, the best fit value of n is negative, which doesn't have physical meaning and is inconsistent with previously reported values for similar colloidal suspensions. Restraining the fitting parameters to positive values doesn't generate any successful fitting either. Fitting the data points with other models such as the power law, Bingham-Papanastasiou and Casson, also did not provide adequate fits. This suggests that the fluid may not really act as a generalized Newtonian fluid but has a more complex rheological behavior. Alternatively, this discrepancy could be due to viscosity measurement errors or insufficient datapoints.

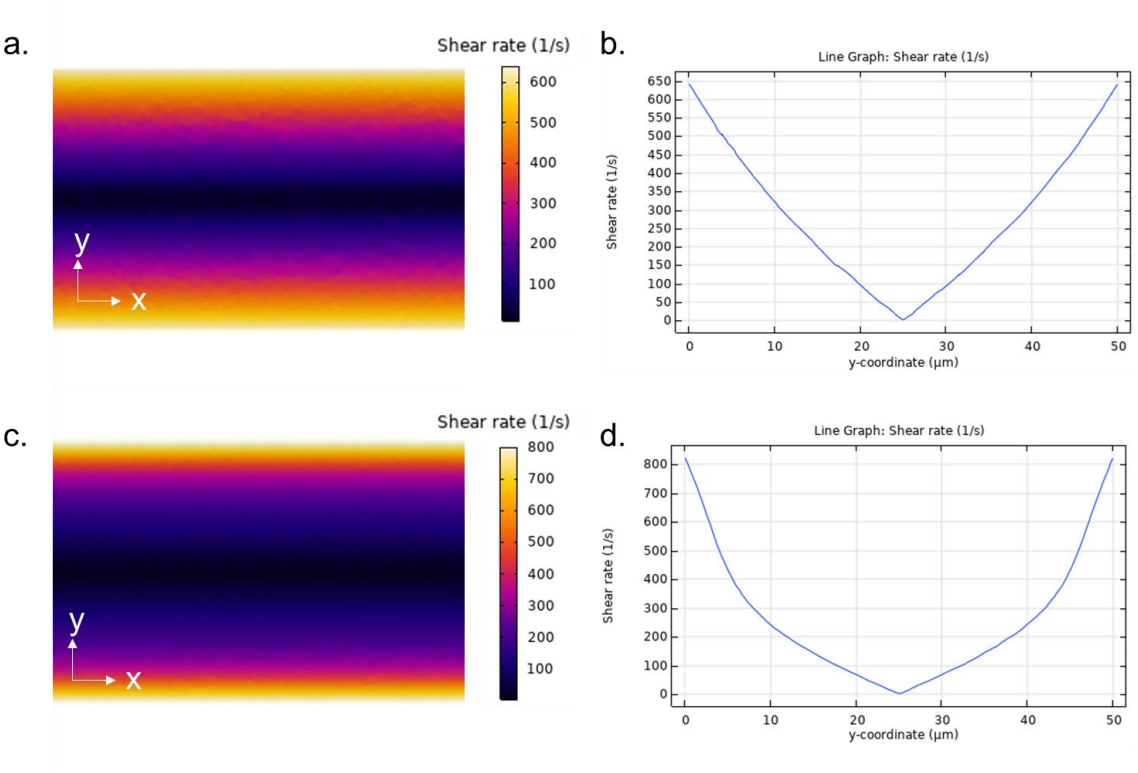

Figure 4.5 Simulated profiles of the shear rate $\dot{\gamma}$ at the middle plane of a channel with square cross section with width and height of 50 µm for 400 nL/min flow. **a-b)** Using a Newtonian fluid with $\mu = 6.12\ mPa \cdot s$**c-d)** Using a non-Newtonian fluid with $\mu(\dot{\gamma})$ from the experimental fit in **Figure 4.4a.**

Even though the fit parameters are not in line with the expected values, the fit line does describe $\mu(\dot{\gamma})$ for the saline suspension relatively well, and we can thus use the fit parameter to model the non-Newtonian behavior in the COMSOL model. **Figure 4.5** shows a comparison of the simulated $\dot{\gamma}$ profile at the middle height of a square channel for a Newtonian (top row) and shear thinning fluid (bottom). The model is evaluated for a flow rate of 500 nL/min, such that the range of $\dot{\gamma}$ matches the strongly shear thinning behavior of the saline suspension (**Figure 4.4a**). As expected, including the shear thinning behavior in the model drastically impacts the simulated $\dot{\gamma}$ profile. This emphasizes the importance of including the rheological behavior in the evaluation of the calibration curve.

Calibration curve

The second step to constructing the calibration curve, is to obtain the orientation factor for different values of $\dot{\gamma}$. To do this, we performed a tomographic measurement of the PL spectra of a suspension of rhabdophane $LaPO_4$:Eu nanorods in EG ($\Phi \sim 0.9$ %) within a straight microfluidic channel with 50 μm x 50 μm cross section at different flow rates. We then calculate the orientation factor f (equivalent to the order parameter S) using the spectral analysis detailed in **section 2.4.4**. **Figure 4.6a** shows the f profile obtained by the area under the curve (AUC) approach and **Figure 4.6a** the simulated profile for the same flow rate. To make the calibration, we consider the average f as a function of the y-position in the channel, indicated by the green points in **Figure 4.6c**. By averaging across the different x-positions, we decrease the measurement error. Then, for each y-position, we match the measured f to the simulated $\dot{\gamma}$ from the COMSOL model indicated by the blue line in **Figure 4.6c**. Finally, this allows us to reconstruct $f(\dot{\gamma})$ in **Figure 4.6**.

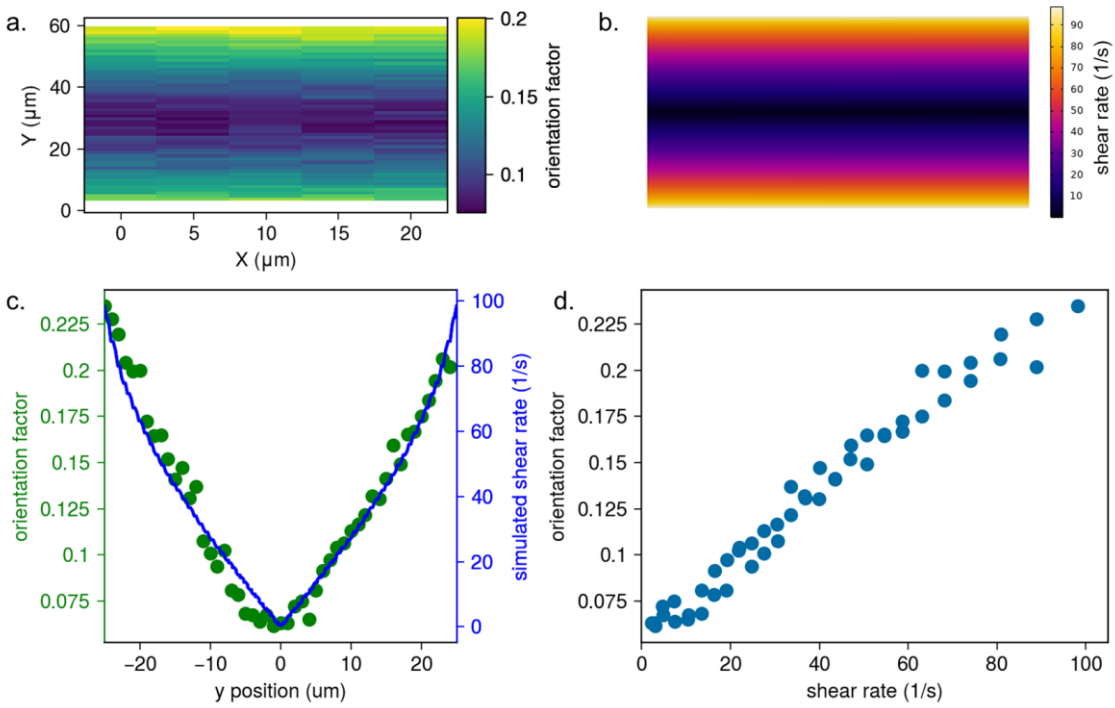

Figure 4.6 Calibration measurements at the middle xy-plane of a square microfluidic channel while flowing a rhabdophane phase 20% doped $LaPO_4$:Eu EG suspension at 100 nL/min. **a)** Orientation factor f measured using area under the curve (AUC) analysis of the polarized emission spectra. **b)** Simulated shear rate $\dot{\gamma}$ considering the previously measured rheological behavior. **c)** Average of **a-b)** plotted as a function of the y-position in the channel. **d)** Constructed relationship between f and $\dot{\gamma}$

We repeat the same procedure for two other flow rates at 10 nL/min and 50 nL/min and plot the obtained $f(\dot{\gamma})$ in **Figure 4.7a**. We generally find a good correspondence between the different flow rates, except for the measurements corresponding to the center of the channel. For example, the minimum value of f

is ~0.08 for 100 nL/min, ~0.03 for 50 nL/min and ~0.02 for 10 nL/min (see annex **Figure 5.52**). Theoretically, the shear rate should be zero at the center of the channel, however, experimentally it is essentially impossible to measure exactly at the center height of the channel. Moreover, as the focal volume is on the order of 1 µm^3, part of the collected PL will come from slightly aligned rods above and below the middle height. This effect is exacerbated at high flow rates, where the gradient of $\dot{\gamma}$ is very high near the center of the channel. To create the calibration curve, we therefor only consider the measurements relatively close to the wall, where the accuracy will be highest. The datapoints in **Figure 4.7b** are all obtained within 15 µm from each wall, whereas **Figure 4.7a** shows all measurements including those corresponding to the center of the channel.

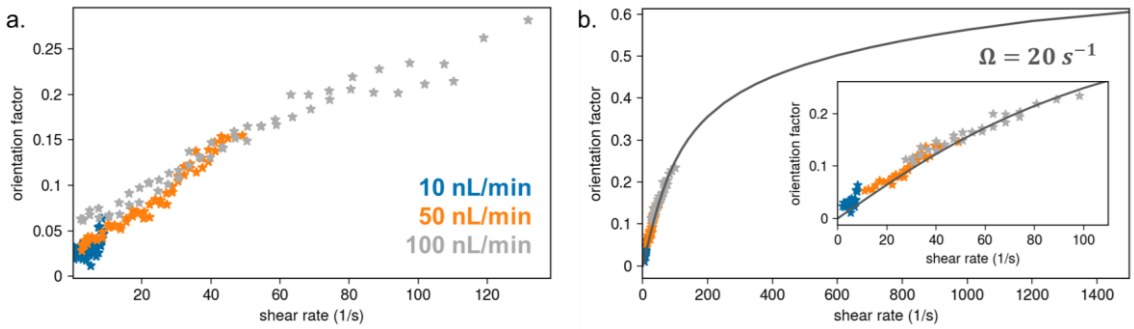

Figure 4.7 Calibration curve of rhabdophane phase 20% doped $LaPO_4$:Eu suspension in EG. **a)** f versus (simulated) $\dot{\gamma}$ based on experiments done at different flow rates. **b)** Calibration curve based on the stress-optical law. The measured values are fit with the numerical solution reported by Scheraga *et al.* and gives the rotary diffusion coefficient Ω[23].

To obtain the full calibration curve, the data points should be fit to the numerical model reported by Scheraga *et al.* which describes the relationship between the f and the parameter $\alpha = \dot{\gamma}/\Omega$ for anisotropic particles with a given aspect ratio p (see **Figure 4.2**). Based on the TEM characterization, the average $p = 13 \pm 6$ within the nanorod suspension, so we use the numerical solution reported for $p = 10$[23]. We obtain a good fit when setting $\Omega = 20\ s^{-1}$, as indicated by the line in **Figure 4.7b**. Using equation **Figure 4.2** and the average half-length $a = 58$ nm and half width b = 4.5 nm found from TEM imaging, annex **Figure 5.57**), we can estimate the theoretical value of $\Omega \sim 23\ s^{-1}$, which corresponds well with the experimentally obtained value. To improve the accuracy, the experiment should be repeated at even higher flow rates, such that there are experimental points corresponding to the strongly curving part of the calibration curve.

Comparison between rhabdophane and monazite suspensions

The downside of using rhabdophane nanorods as shear probes is that they have a less strongly polarized emission spectrum compared to monazite, which can enhance the measurement error. However, besides their luminescence properties, there is also a difference in morphology between the two types on

nanorods, which impacts their response to the shear. Monazite phase $LaPO_4$:Eu nanorods are slightly longer ($a = 141 \pm 55$ nm) and have a two times larger $p = 28 \pm 11$ than the previously discussed rhabdophane rods[3]. This makes them easier to align, which explains why even for a low flow rate (10 nL/min) we see strong alignment (see **Figure 4.8a**).

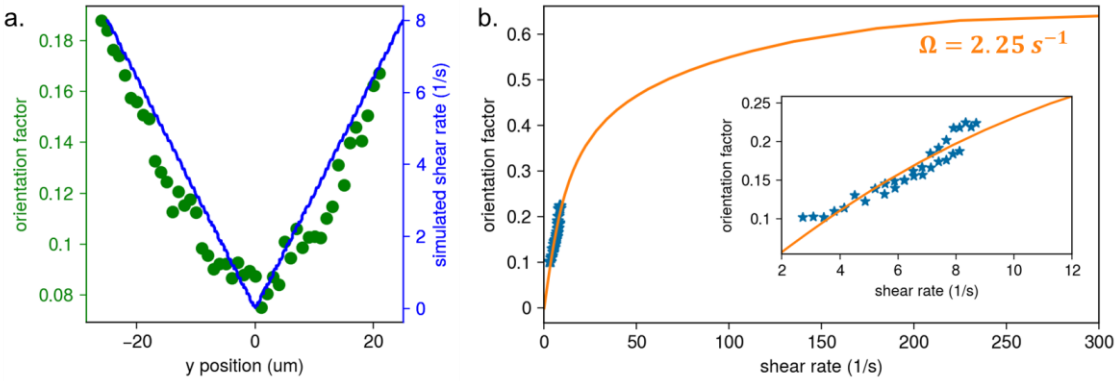

Figure 4.8 Calibration curve of monazite phase $LaPO_4$:Eu in EG based on PL measurements for a flow rate of 10 nL/min. **a)** Orientation factor f measured using area under the curve (AUC) analysis of the polarized emission spectra. **b)** Approximate calibration curve based on the stress-optical law assuming rotary diffusion coefficient Ω[23].

Although it is necessary to repeat the measurements at higher flow rates to obtain a reliable calibration curve, we can use the few measured points to estimate the value of Ω to be on the order of few s^{-1} based on the fit shown in **Figure 4.8b**. The approximated calibration curve in **Figure 4.8b** is consistent with the one reported using the previous method[38].

Whereas monazite rods can be aligned at relatively low flow rates rhabdophane rods barely showed any alignment at the same flow rates, as seen in **Figure 5.52**. This can be attributed to the fact that the rhabdophane nanorods are smaller and have a lower aspect ratio (**Figure 5.57**). As a result, the monazite suspension therefore has a 10 times smaller rotary diffusion compared to the rhabdophane suspension. This can also be seen from the fact that a value of $f = 0.2$ is achieved with rhabdophane for $\dot{\gamma} = 80\ s^{-1}$ (**Figure 4.7b**), whereas for monazite it is around $\dot{\gamma} = 8\ s^{-1}$ (**Figure 4.8b**).

Summary of chapter 4.1

Orientation theory describes the collective orientation, quantified by the orientation factor f, of anisotropic particles under flow as a function of the ratio between the velocity gradient G and rotary diffusion coefficient Ω. In the case of simple shear, G is equal to the shear rate $\dot{\gamma}$, which means there is a theoretical relationship $f(\dot{\gamma})$. As the birefringence Δn is directly proportional to f, as similar relationship of $\Delta n(\dot{\gamma})$ can be established. For $LaPO_4$:Eu suspensions, both relationships can be obtained experimentally, by measuring f through the spectroscopy of its PL or by measuring Δn using PLM for known values of $\dot{\gamma}$. Here, we establish the calibration curve $f(\dot{\gamma})$ which considers the shear thinning rheology of the $LaPO_4$:Eu suspensions, which finally allows to probe $\dot{\gamma}$ in unknown systems.

4.2 Introduction on flow based kinetic energy harvesting

As we want to apply our shearmetry technique for the study of a kinetic energy harvesting system, we will first give a general introduction to the electrochemical system under investigation and how it relates to the state of the art. All the energy harvesting systems discussed in this chapter are based on the movement of charges which originate from the electric double layer (EDL) formed at a charged surface. To understand how these systems convert energy, we will first consider the structure and properties of the EDL.

4.2.1 The electric double layer

The EDL is formed to compensate for the excess charges present on the solid-liquid interface. These charges can be from an external potential for a conductor (**Figure 4.9a**) and/or due to ionized surface groups (**Figure 4.9b**). The EDL can be divided into two main layers, as indicated in **Figure 4.9**. The inner layer, known as the Stern layer, closest to the charged surface consists of counter ions and solvent molecules which are specifically adsorbed, meaning they are kept at the surface through chemical bonds. The rest of the EDL is formed by the diffuse layer which extends to the bulk and consists of ions attracted to the surface by long range electrostatic forces. The Stern layer is not affected by flow shear, as the charges are strongly bound to the solid surface. However, the diffuse layer can be disturbed by flow, such that it slides over the Stern layer.

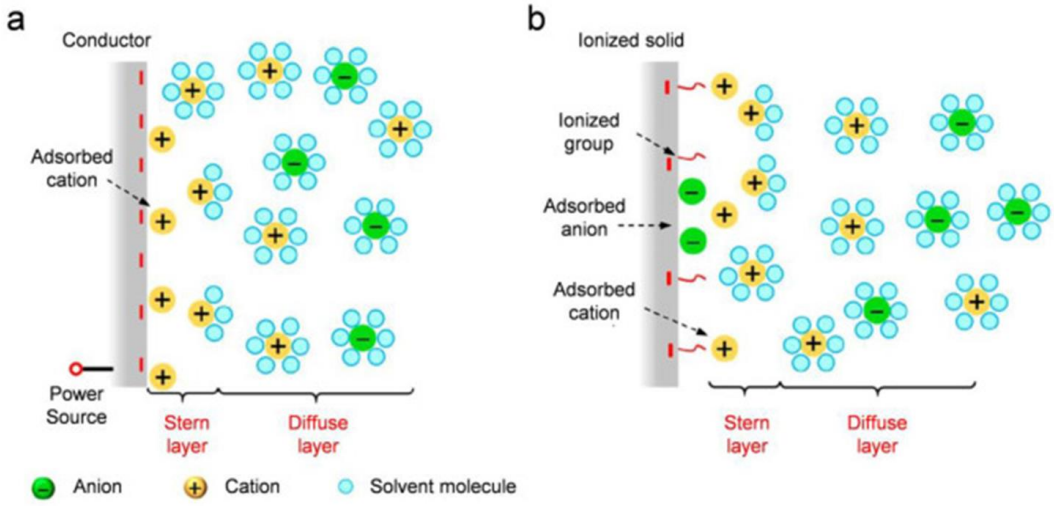

Figure 4.9 Schematic representation of the electric double layer (EDL) formed at the surface of a charged **a)** conductor **b)** ionized solid. Figure from Hu *et al.* (2024)[118].

The size of the diffuse layer is characterized by the Debye length, such that

$$L_D = \sqrt{\frac{\epsilon\epsilon_0 kT}{2n_0 z^2 e^2}} \qquad \textbf{4.10}$$

where ϵ is the dielectric constant, ϵ_0 the vacuum permittivity, k the Boltzmann constant, T the absolute temperature, n_0 is the concentration of ions, z the ionic charge magnitude and e the elementary charge[119]. This implies that for a distance greater than L_D, Ψ_0 is effectively screened and ions are no longer affected by the potential. For dilute, aqueous electrolytes at room temperature, $\epsilon = 78.49$ so

$$L_D \sim 0.304/\sqrt{zC^*} \qquad \textbf{4.11}$$

where $C^*$is the bulk electrolyte concentration in mol/L and L_D is given in nm. For typical electrolytes at room temperature, L_D is on the order of several nanometers up to a micron depending on the ionic strength of the solution.

EDL capacitance and pseudo-capacitance

The capacitance, the ability to store electric charge, is an important metric when considering materials for energy applications. A common way to measure the capacitance is through cyclic voltammetry in which the current response is recorded over a linear potential sweep[119]. **Figure 4.10** shows an example of a cyclic voltammogram obtained for N-doped mesoporous carbon[120]. As EDL capacitance is mostly independent on the potential bias, the voltammogram is expected to be rectangular in shape, indicated by the pink region in **Figure 4.10**. However, the presence of redox reactions at the electrode interface can

add a pseudo-capacitance, as indicated in green. Such materials are actively explored as supercapacitors for energy storage applications[121].

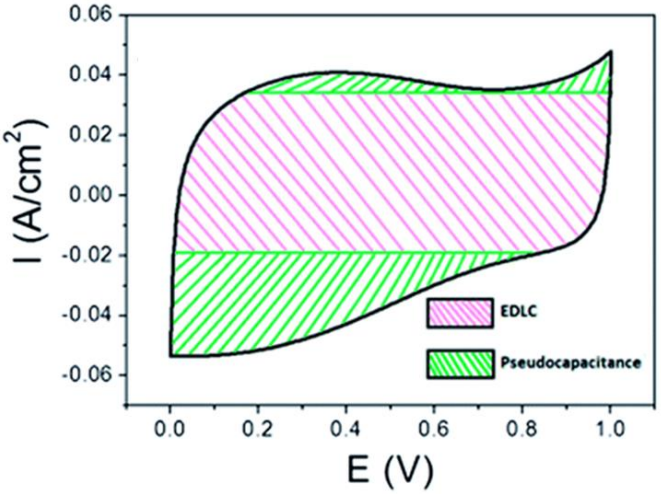

Figure 4.10 Example of cyclic voltammetry performed on a N-doped mesoporous carbon electrode. Figure from Hu *et al.* (2014)[120].

In the next section we will discuss how the EDL is impacted by flows and how this can be used to convert kinetic into electrical energy.

4.2.2 Hydrovoltaic energy harvesting

There are various approaches to harvesting the mechanical energy of flows, but here we focus on hydrovoltaics which generate energy based on interactions at the solid-liquid interface, involving the EDL[122]. Finally, the selective ion sweeping system introduced in **chapter 1.4** will be discussed in more detail and compared to the other systems.

Streaming current/potential

A common approach to harvesting energy from flows is by utilizing the concept of ion selectivity, which implies that in channels with charged walls the counter-ions (opposite charge to wall) are transported preferentially over the co-ions (same charge as wall). In the case where the pore size, or distance between the walls, is on the same order as L_D, the EDL originating from the different walls will overlap, excluding most of the co-ions from entering the pore, as illustrated in **Figure 4.11a**[123]. Evidently, when forcing an electrolyte to flow through such pores, a potential difference between in- and outlet will be built up as an excess of counter-ions accumulate downstream, while the majority of co-ions remain upstream. Fundamental studies in single silica nanochannels showed that the current increases linearly with the applied pressure/flow under steady state conditions (**Figure 4.11b**)[124]. This concept and its application for energy harvesting has been known and explored for more than half a century[125], but recent advances in nanofabrication techniques and the societal interest in energy conversion has reinvigorated this research

field. This involves the development of large scale permeable membranes with high ion-selectivity, which is actively explored using 2D materials such as nanoporous graphene[126] and single layer molybdenum disulfide (MoS_2)[127].

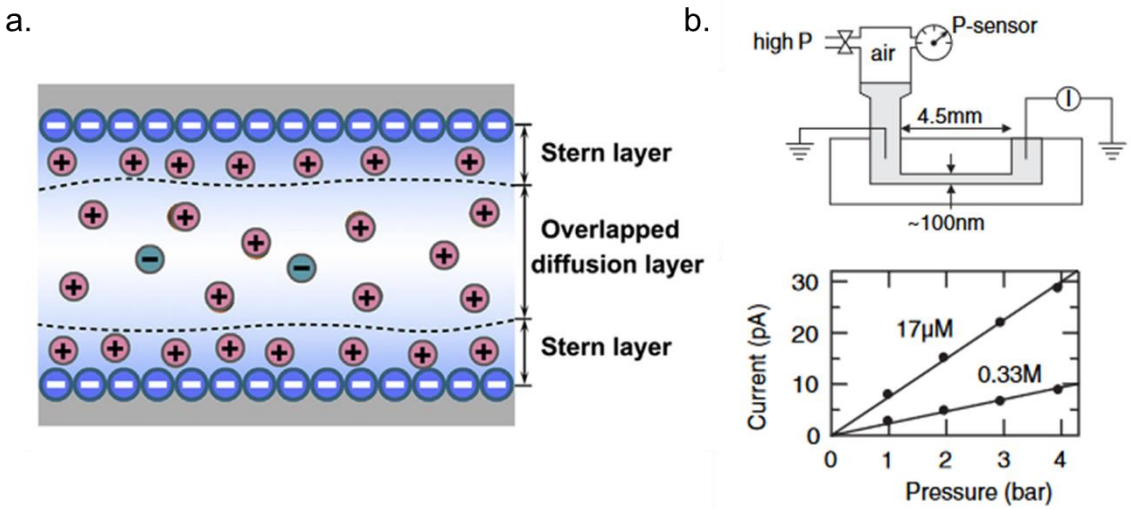

Figure 4.11 a) Schematic illustration of the charges in small channel with charged walls. Due to the overlapping EDLs, co-ions are almost completely excluded from the channel. Figure from Xiao *et al.* (2019)[123] **b)** Example of streaming current from a single silica nanochannel. Figures adapted from van der Heyden *et al.* (2005)[124].

Zhang *et al.* demonstrated that this can also be achieved on the larger scale, in a system consisting of a PDMS microfluidic channel containing an array of micropillars and electrodes at the in- and outlet (**Figure 4.12a-b**)[128]. Theoretical calculations based on single channels suggest that the highest efficiency is achieved when $L_D \sim 0.5$ times the channel height h, but that a smaller streaming current can still be observed even if the EDLs don't overlap at all ($L_D \ll h$)[129]. Zhang *et al.* did not report h for their microfluidic system, but from the SEM images in **Figure 4.12b** we can estimate h to be on the order of 10 µm. This means that for $L_D \sim h$, the ion concentration C should be on the order of 10^{-9} M. Interestingly, they found a much higher optimal value of $C \sim 10^{-5}$, corresponding to $L_D \sim 100$ nm (**Figure 4.12c**). Finally, they found a linear relationship between the flow rate and streaming current (**Figure 4.12d**), which is in agreement with other experimental studies in single channels[124]. It is therefore important to consider that streaming current can be present in relatively large PDMS channels, even when the characteristic size is larger than L_D.

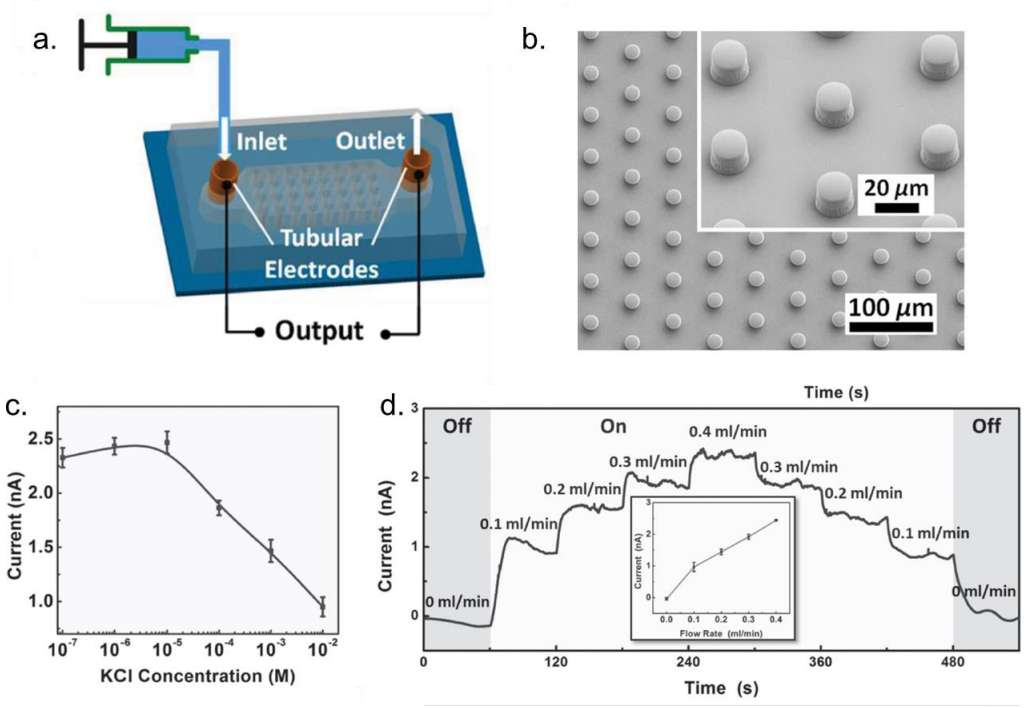

Figure 4.12 Streaming current in PDMS microfluidic channel. **a)** Schematic illustration of the device consisting of a microfluidic channel with an array of pillars and electrodes at the in- and outlet. **b)** SEM image of the micropillars taken at a 30° tilt. **c)** short circuit current as a function of the salt concentration for a flow rate of 0.1 ml/min. **d)** Current for different flow rates. Inset shows the average current as a function of flow rate. Figures from Zhang *et al.* (2015)[128].

Triboelectric nanogenerators (TENGs)

The triboelectric effect, the generation of electrostatic surface charges when two different materials come into contact, has been known for centuries, with the first reports dating back to ancient Greece[130]. This surface charge generates an EDL through contact electrification (CE). Over the last decade, much research has been focused on the development of triboelectric nanogenerators (TENGs) which use these liquid-solid interactions as a way to harvest kinetic energy[131]. The main advantages of solid-liquid TENGs compared to more traditional solid-solid systems is their increased effective surface area and increased current generation duration[132,133].

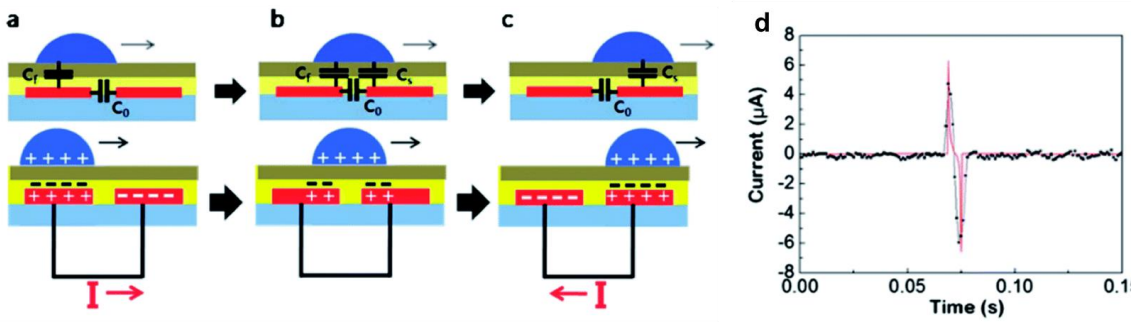

Figure 4.13 An example of a TENG: Water motion active transducer (WMAT). **a-c)** Schematic illustration of the energy harvesting cycle. As the droplet moves from one electrode to the next, it transports surface charges generated due to CE. **d)** Current generated by a single droplet. Figures from Kwon *et al.* (2014)[134].

A common approach is to use the movement of droplets over dielectric surfaces[118]. As an example, Kwon *et al.*, demonstrated a water motion active transducer (WMAT), a type of TENG, which utilizes the surface charges arising when a water droplet comes into contact with a dielectric surface, here the polymer poly-4-vinyl phenol (PVP)[134]. The device consists of two electrodes covered by PVP and a hydrophobic layer and the operating principle is shown in **Figure 4.13a-c**. Upon contact, the droplet accumulates positive surface charges due to the negative polarity of the PVP, and positive charge accumulates on the electrode to maintain electron neutrality, generating a current (**Figure 4.13a,d**). The droplet, and its EDL, moves to the second electrode and the process is repeated, generating an opposite current (**Figure 4.13c-d**)**.** However, such a system generally creates short current pulses, as seen in **Figure 4.13d**.

Selective ion sweeping

As discussed in **chapter 1.4**, the group of Prof. Seok Woo Lee at NTU recently proposed a novel approach based on selective ion sweeping in a hybrid cell containing a battery-type and a supercapacitor electrode[50]. An EDL is formed at the capacitor electrode when the two electrodes are brought into electrical contact due to the difference in their electrochemical potential. When exposed to electrolyte flow, only ions in the EDL of the supercapacitor are removed, which generates a potential difference and allows to generate power.

The selective ion sweeping based energy harvesting cycle consists of several steps illustrated in **Figure 4.14a**. When a flow is applied, the anions are swept of the capacitive electrode, causing a positive potential bias. This generates a positive current (**Figure 4.14b**), as an equal number of cations are expelled from the battery electrode in response. This continues until a pseudo equilibrium is achieved, where the number of ions on both electrodes remains constant. Once the flow is stopped, the system will go back to the equilibrium state through the adsorption of anions and absorption of cations which balance out the electrochemical potential difference inherent to the electrode materials. During this process, a negative

current is generated until the equilibrium state is retrieved (**Figure 4.14b**). Typically, the total current density is on the order of a few µA cm^{-2} which can last 10-30s per flow cycle, as seen in **Figure 4.14**.

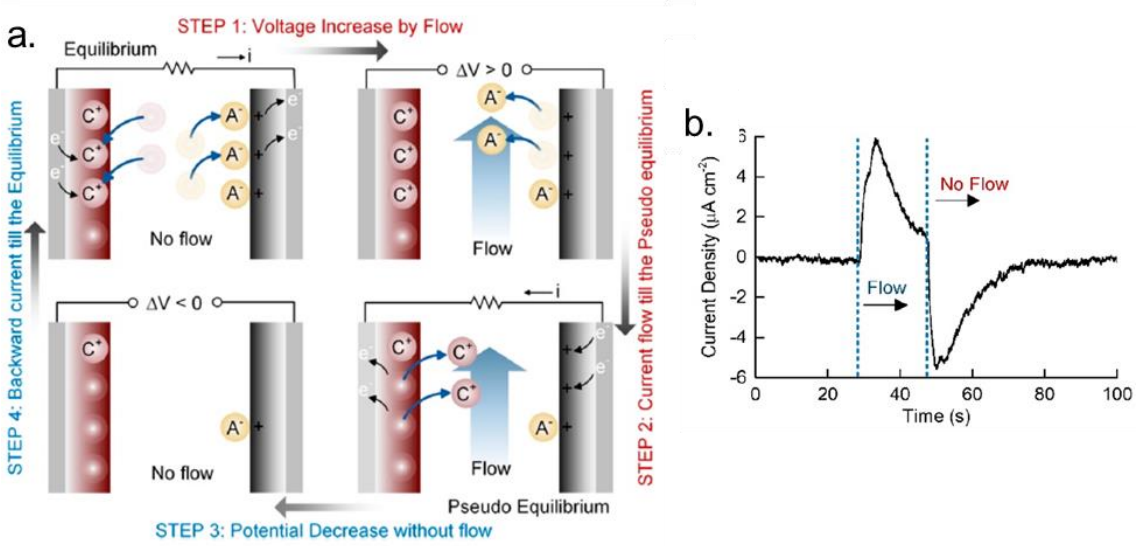

Figure 4.14 Description of the energy harvesting in a hybrid cell **a)** Schematic illustration of the four steps. Step 1: Flow sweeps anions in the EDL of the capacitive electrode, generating a positive potential bias ΔV. Step 2: Cations are expelled from the battery electrode coupled positive current until a pseudo-equilibrium is reached. Step 3: As the flow is stopped, the potential difference is increased. Step 4: A backward current is generated as the cations intercalate in the battery electrodes and anions re-adsorb in the EDL of the capacitive electrode. **b)** Typical current response induced by applying a flow for 20 seconds. Figures from Jung *et al.* (2020)[50].

They demonstrated this mechanism both by exposing the capacitive electrode to a jet flow (directed orthogonally to its surface) and to a shear flow (with flow parallel to the surface), and found a similar current response. This independence on flow direction makes the approach distinct from streaming current where the direction of the flow determines the polarity of the current response. Moreover, whereas the EDL movement associated to TENGs are generally due to wetting/dewetting, here a constant contact between solid and liquid is maintained. Although all processes involve the movement of charges associated to the EDL, the exact mechanisms seem slightly different. This makes ion sweeping an interesting alternative approach which could potentially be used to harvest irregular, low frequency oscillations such as human movements.

Summary of chapter 4.2

The electric double layer (EDL) is formed in response to surface charges at the liquid-solid interface and plays an important role in flow based kinetic energy harvesting systems. Only the outer diffuse layer of the EDL is affected by shear flow, whereas the inner Stern layer contains ions strongly bound to the solid surface.

Different approaches exist to convert mechanical to electrical energy from liquid movement, such as streaming current and triboelectric nanogenerators (TENG). Recently, our collaborators as NTU demonstrated a novel approach, based on the sweeping of ions in the EDL of a capacitive electrode under flow. Using a hybrid cell consisting of a capacitive and battery-type electrode, they demonstrated that this effect can be used to generate power. In order to optimize the energy harvesting efficiency, it is crucial to understand the role of the interfacial shear stresses believed to trigger the ion sweeping. In this work, we therefore aim to apply our shearmetry technique based on the spectroscopy of luminescent nanorods to develop the fundamental understanding of the ion sweeping phenomena.

4.3 Design of microfluidic device for selective ion sweeping

To address the application of small, wearable devices, it is interesting to miniaturize the previously demonstrated selective ion sweeping energy harvesting system. Moreover, in order to make *in situ* shear measurements using the luminescent nanoprobes, the system should be compatible with the confocal microscope setup. To achieve this we incorporated planar electrodes into a microfluidic channel, as illustrated in **Figure 4.15**. We also considered several other configurations, discussed in **annex 5.5.**

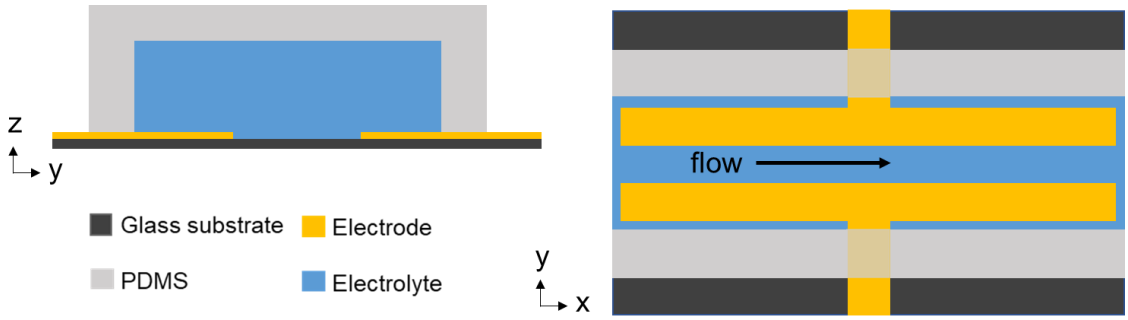

Figure 4.15 Schematic illustration of the microfluidic channel with incorporated electrodes. Here a straight channel with rectangular cross section is shown, but more complex geometries may be explored as well.

In this section, we will first discuss the different strategies for achieving selective ion sweeping in such a microfluidic system. Then we will discuss the electrode materials considered and finally on the design of a microfluidic channel which could induce high shear anisotropy between the two electrodes.

4.3.1 Strategies for selective ion sweeping in microfluidic systems

In order to generate a net current as a response to shear flow on two electrodes, the ion sweeping should be considerably faster on one than the other. In the case of the hybrid cell, this is achieved due to the fact that only the charges in the EDL of the capacitive electrode are swept, whereas the ions incorporated in the battery electrode are unaffected by the flow (**Figure 4.16a**). In principle, this could be achieved by simply incorporating a battery and capacitive electrode in a straight microfluidic channel. However, as will be discussed in **section 4.3.2**, producing a micro-patterned battery electrode suitable for the microfluidic system is challenging.

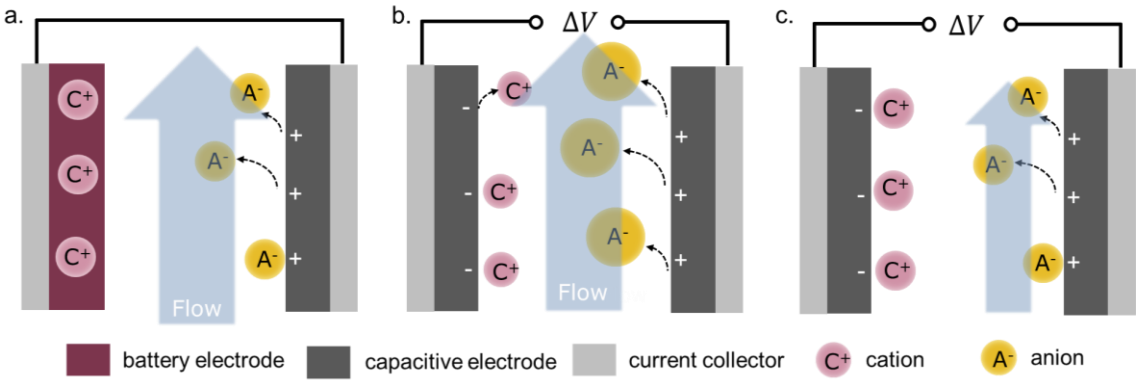

Figure 4.16 Schematic illustration of selective ion sweeping in different systems. The cations and anions drawn represent the diffuse layer of the EDL. **a)** Hybrid cell with battery and capacitive electrode. Ions are only swept from the EDL of the capacitive electrode. **b)** Cell with two capacitive electrodes, both exposed to flow. Larger anions may be swept faster than the smaller cations. **c)** Cell with two capacitive electrodes but only one of them is exposed to strong interfacial shear forces

Instead of a hybrid cell, we consider a system with two identical capacitive electrodes whose EDL are formed due to an external applied bias. To induce selective ion sweeping, we could replace one of the ions by much larger ions, molecules or even charged nanoparticles (**Figure 4.16b**). In this case, even if the two electrodes are exposed to the same flow conditions, the larger charged species may be removed faster. We briefly explore this concept in a simple straight channel, as will be discussed in **section 4.4.2**.

Alternatively, if only one of the two electrodes is exposed to (high) flow shear, we'd expect a difference in sweeping rate (**Figure 4.16c**). In a macroscopic beaker cell setup this may be achieved by placing the electrodes far apart and aiming the jet flow on only one of them. In a microfluidic system with incorporated electrodes, this requires a suitable design of the channel geometry, which carefully optimizes the shear anisotropy. In **section 4.3.3** such geometries will be explored and in **section 4.4.3** and **section 4.5.2** the current response due to the shear anisotropy between capacitive electrodes will be discussed.

4.3.2 Electrode materials

In order to replicate the initial system demonstrated by our collaborators, we wanted to incorporate both a capacitive electrode and a battery electrode. For the initial proof of concept, we planned to use hybrid system of a (capacitive) metal electrode and a battery Prussian blue analogue (PBA) electrode. There are various PBA analogues, but copper hexacyanoferrate (CuHCFe) was selected based on its stability in aqueous solutions and low overpotential during charge and discharge cycles[135]. In a different system we wanted to try to achieve the selective ion sweeping based on flow conditions alone, using two identical capacitive electrodes. The first challenge was therefore to make miniaturized electrodes which could be fitted inside a microfluidic channel.

Initial trials were done using platinum electrodes printed on glass microscope slides. However, due to the poor adhesion between PDMS and platinum, leaking and subsequent delamination of the PDMS occurred easily. Glass and PDMS are able to form strong bonds through the silanol groups created by oxidization of the surface (through plasma or UV/ozone treatment)[136], but such groups are not available on most metal surfaces. The two main approaches to improving the bonding between PDMS and metals are 1) the introduction of a third layer which acts as an adhesion promotor and 2) through additional surface functionalization of the PDMS and/or metal[137,138]. However, both methods require additional steps in the fabrication procedure, and we therefor chose to simply change the electrode material.

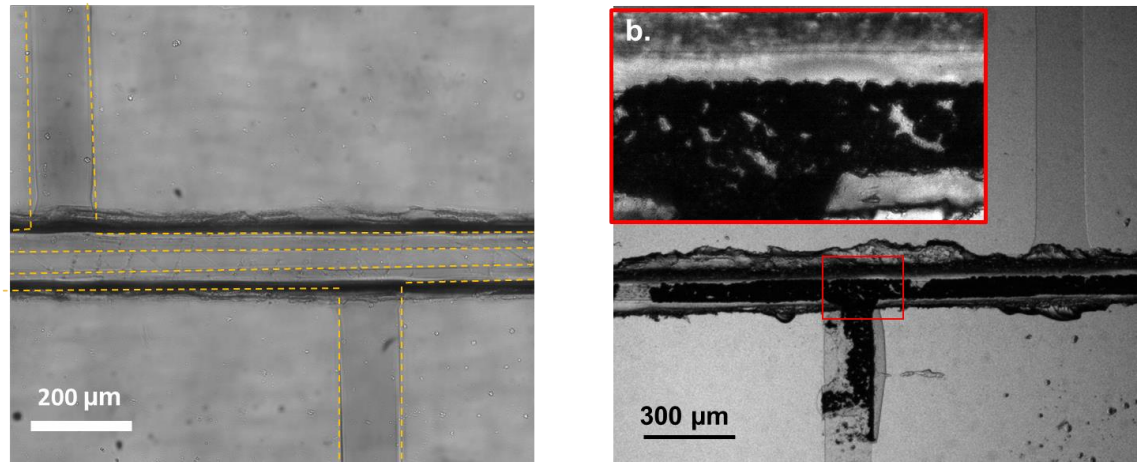

Figure 4.17 Planar electrodes with a straight, rectangular channel on top. **a)** two ITO electrodes indicated by the yellow dotted lines **b)** one ITO electrode (top), one ITO+CuHCFe electrode. The inset shows the formation of relatively large, cubic particles rather than the formation of a homogeneous thin film.

We switched to indium tin oxide (ITO) electrodes, as good adhesion between glass and ITO could be achieved after UV/ozone treatment. Additionally, it's transparency in the visible spectrum should allow us to make optical measurements through it and close to the electrode surface[139]. Moreover, initial experiments show that the presence of the ITO does not impact the shear measurements performed

through spectroscopy of $LaPO_4$:Eu nanorods (discussed in **annex 5.7**). **Figure 4.17a** show an example of two of such electrodes with a straight microfluidic channel on top. To avoid damaging the ITO, we always use NO_3^- as the anion in the electrolyte which has been shown to increase the reduction potential and thus helps maintain the electrode integrity when a (high) potential bias is applied[140].

In order to make the battery electrode, we tried starting with an ITO electrode and growing a thin film of CuHCFe on top. The idea was to selectively deposit the CuHCFe on the part of the electrode exposed to the flow, so we could still take advantage of the good adhesion strength between the ITO and PDMS. We initially tried achieving this by consecutive electrodeposition of $Cu(NO_3)_2$ and $K_3Fe(CN)_6$ precursors in aqueous solution. However, this method resulted in the deposition of relatively large, cube shaped particles (**Figure 4.17b**). This made the electrode much bulkier than anticipated, which could potentially cause short circuits and would thus require larger channels. Additionally, the large surface roughness would also affect the flow through the channel, which may make the shear measurements unreliable.

As an alternative approach, we therefore decided to start with two identical capacitive electrodes and try to induce selective sweeping through a difference in interfacial shear between the two electrodes, rather than relying on a chemical difference as previously demonstrated[50]. However, as the two electrodes would have the same electrochemical potential, the formation of a (significantly large) EDL will require an applied potential bias.

4.3.3 Optimization of shear anisotropy in microfluidic channels

To design appropriate channel geometries, we first try to optimize the shear anisotropy through numerical simulations using COMSOL. Next, we try to fabricate the designed channels and when successful make experimental shear measurements considering the birefringence produced by flowing $LaPO_4$:Eu nanorod suspensions. As a convention, we place the counter electrode (CE) under high shear, and the working electrode (WE) under low shear.

Simulations of the shear profile

The simplest way to reduce shear stress on the WE is to prevent any direct flow across the length of the electrode. This can be achieved by using small compartments or pores which extend from the main channel over the WE, as seen in **Figure 4.18a**. Indeed, the numerical simulations predict that the shear stresses on the CE will be 10^4 times higher than those on the WE. However, in practice this design is difficult to use for the ion sweeping experiment as the narrow pores cannot be filled fully due to the high capillary pressures required. Forcing the electrolyte to enter such pores causes leaks or detachment of the pore walls. Moreover, a large portion of the WE area would be covered with PDMS, which could limit the electrochemical performance of the cell. Widening the pores would alleviate these issues, but the large shear ratio is lost when increasing pore size.

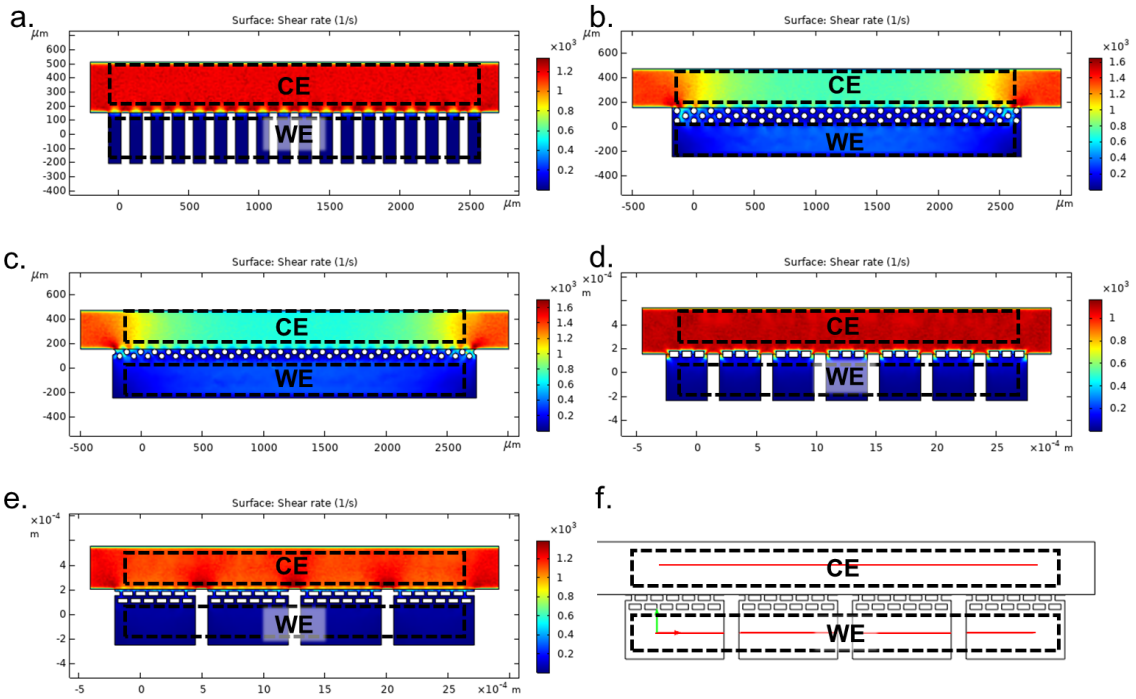

Figure 4.18 a-e) Profiles of simulated shear rate at bottom surface of channel for different geometries. The position of the working electrode (WE) and counter electrode (CE) are indicated by the black dashed lines. The average shear rate is evaluated using a line average along the center position of each electrode as marked by the red lines in **f)**.

Table 4.1 Quantitative analysis of the shear profiles shown in **Figure 4.18**.

Channel	Average shear CE (S^{-1})	Average shear WE (S^{-1})	ratio
a)	1192	$2.35 \cdot 10^{-2}$	$5 \cdot 10^{4}$
b)	827	302	2.7
c)	775	305	2.5
d)	1058	31.7	33
e)	1152	28.9	40

To avoid covering the electrode with PDMS, another design using cylindrical barriers was explored. This geometry was inspired by a microfluidic membrane system previously reported by Biswas *et al*[141]. The cylindrical barrier dimensions were limited by the gap between the electrodes (80 µm) and the minimum gap size producible using the lithography method, which was estimated around 20 µm. With these restrictions, an optimization was done to design channels with either 2 or 3 rows of cylindrical pillars, as shown **Figure 4.18b,c**. For both designs the shear ratio was rather low, around 2.5-2.7. In practice, these channels were difficult to fabricate accurately, as the small and round features were easily over etched during the mold fabrication, resulting in smaller or shorter pillars. This made the pillars easy to remove under flow and made the shear ratio even smaller than the simulations.

The final channel designs are a combination of the previous two, containing large pores which are shielded from the flow using one or two rows of barriers, see **Figure 4.18d,e**. The rectangular barrier shape, as opposed to the round one, allows for more reliable etching and better bonding with the glass due to the larger contact area. Using this design large shear ratios can be achieved whilst maximizing the exposed surface area of the WE. Although the narrow pores with a single row of barriers (**Figure 4.18d**) is expected to produce a slightly smaller shear ratio than the one with wider pores with a double row of barriers (**Figure 4.18e**) its simpler structure made it more reliable to fabricate. We therefor tried our sweeping experiments in both types of channels.

Experimental shear measurements through flow birefringence

In order to confirm that the channels fabricated indeed show a high shear ratio, PLM imaging of the nanorods under flow were performed. Although PL can provide higher accuracy shear measurements close to the electrode surface, birefringence allows us to make qualitative measurements on a large field of view within a few seconds and can thus be used to rapidly evaluate the quality of the microfluidic channels. As previously discussed in **section 4.1.1**, the birefringence Δn is a function of the shear rate $\dot{\gamma}$ and we can approximate this as a linear relationship at low flow rates. Moreover, the intensity I observed between crossed polarizers is directly proportional Δn (**equation** Error! Reference source not found.), m eaning that we can use the measurement of I to approximate the shear ratio between the two electrodes.

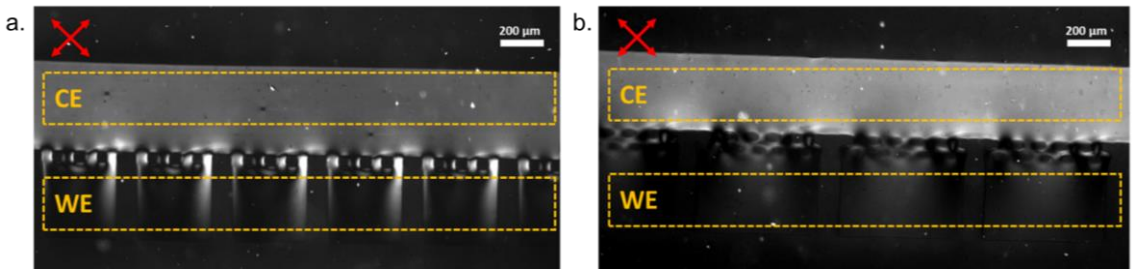

Figure 4.19 Birefringence of nanorods under flow in different microfluidic channels observed between crossed polarizers (red arrows) **a)** 5-S and **b)** 6-L. The position of where the CE and WE will be are marked in yellow.

Figure 4.19 shows the birefringence observed between crossed polarizers from the flow of nanorods in two different geometries labeled as 5-S (**Figure 4.19 a**) and 6-L (**Figure 4.19 b**). Both show more intense birefringence in the top section (where the CE would be), as expected from the simulations. Comparing the average light intensity above each electrode, we find that 5-S and 6-L exhibit shear ratios of 23 and 13 respectively. This is contrary to the simulations, which predicted 6-L would have a 20% higher shear ratio. This is likely due to issues in the fabrication process, as some of the rectangular barriers in the 6-L (**Figure 4.19b**) aren't as sharply defined as the square barriers of 5-S (**Figure 4.19a**). We therefore expect that the

5-S barrier geometry will result in the strongest flow induced electrochemical response when incorporating the electrodes.

Summary of chapter 4.3

We design a microfluidic energy harvesting device compatible with the confocal microscopy setup required for *in situ* shear measurements. The device consists of transparent ITO electrodes with a PDMS microfluidic channel on top. We focus on generating selective ion sweeping by playing on the flow conditions, rather than relying on a difference in electrode materials. Numerical simulations are performed in order to find an optimal design for the microfluidic channel, maximizing the difference in interfacial shear stresses experience by the two electrodes under flow. Two of the best geometries are tested experimentally by monitoring the flow birefringence of $LaPO_4$ nanorod suspensions, and we find that the optimal geometry induces >20 times higher shear on one of the electrodes than the other. We expect that such a high shear anisotropy is enough to induce a selective ion sweeping current.

4.4 Electrochemical characterization of flow-induced selective ion sweeping

In this section, we will first verify that no a flow induced current response can be observed in a straight channel, where the interfacial shear stresses are similar on both incorporated electrodes. Next, we will test the designed anisotropic channels in order to see if the high shear anisotropy can induce selective ion sweeping. We characterize the electrochemical response for a variety of flow conditions and electrolytes.

4.4.1 Experimental methodology for electrochemical measurements

Figure 4.20 shows the experimental setup used to carry out all electrochemical measurements. A potentiostat in the two-electrode configuration, where the working electrode (WE) is connected to the electrode experiencing low shear stresses and the counter electrode (CE) to the electrode exposed to high shear stresses. To ensure a stable electrical contact, wires are attached to the exposed end of the ITO electrodes on the glass using silver paste (**Figure 4.20c**). Due to the lack of a reference electrode (RE) inside the channel, the RE is directly connected to the CE. After the electrolyte is first introduced to the anisotropic channel, a slight back pressure is applied until all air bubbles are eliminated. For flow experiments, a motorized syringe pump is used to control the flow rate.

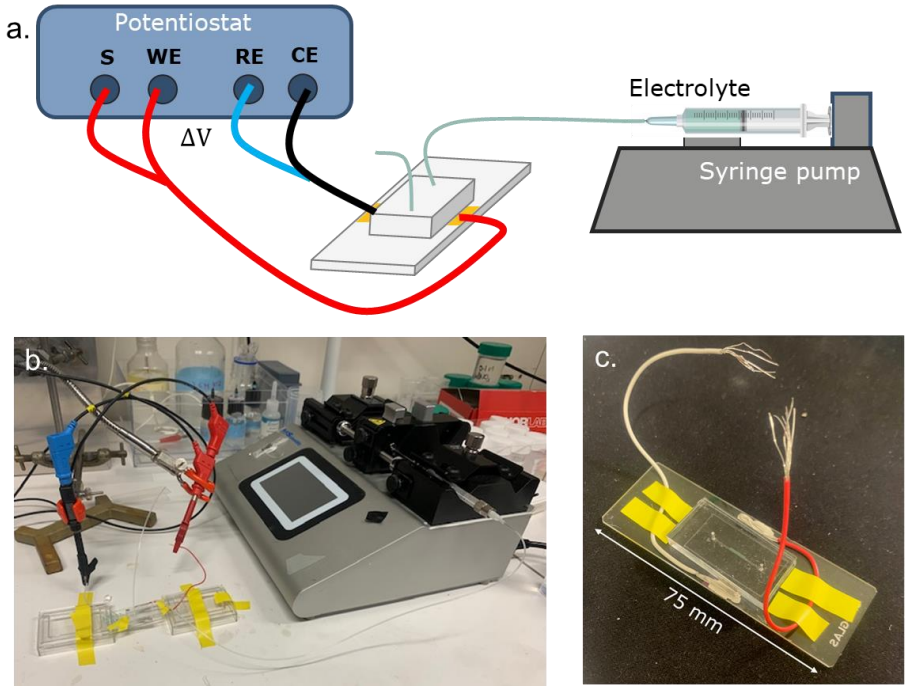

Figure 4.20 Experimental setup for electrochemical characterization of ion sweeping device. **a)** Schematic illustration **b)** image of the experimental setup. **c)** Image of the ion sweeping device consisting of a microfluidic channel with incorporated electrodes.

Constant potential amperometry measurements were done using an interval time of 0.05 seconds of followed by a Savitzky Golay smoothing function. Cyclic voltammetry was performed using a scan rate of 0.0495 V/s and a step size of 0.0099 V such that the interval time was around 0.2 s to minimize background noise.

Capacitance measurements

We use the cyclic voltammetry measurements to approximate the capacitance of the electrodes. **Figure 4.21a** shows an example of the voltammogram obtained in the microfluidic channel with two ITO electrodes. From the slightly tilted shape of the voltammogram, we can deduce that the ITO doesn't act as a pure EDL capacitor (which would produce a purely rectangular loop), but that some H^+ or OH^- ions get specifically adsorbed due to redox reactions at the electrode surface, making it a pseudocapacitor[142]. In this work we refer to the pseudo-capacitance when mentioning the capacitance of the electrodes.

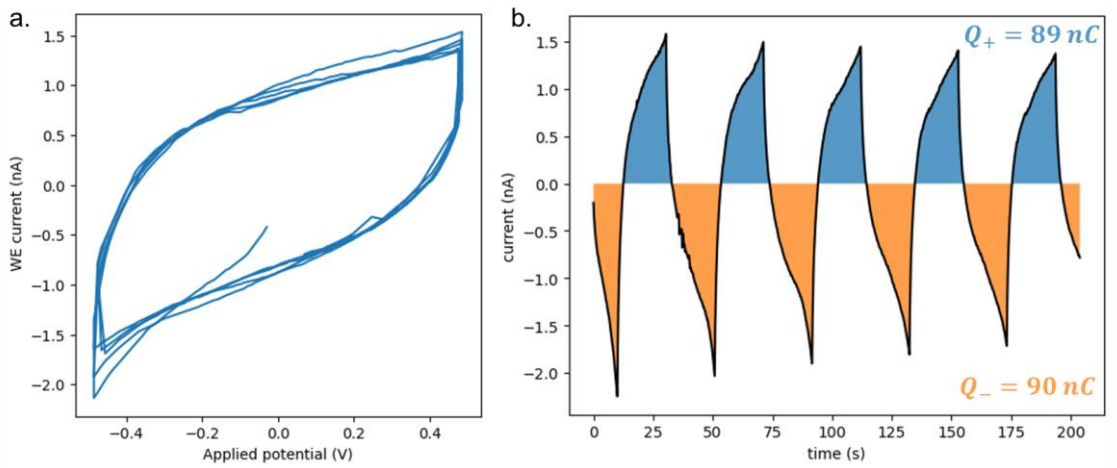

Figure 4.21 Cyclic voltammetry to obtain pseudo-capacitance. Performed in a microfluidic channel with two ITO electrodes with surface area 2.6 mm^2 each in an electrolyte of 0.1 M $NaNO_3$ at pH 8. **a)** Plot of the current while sweeping the potential between ±0.5 V for 5 consecutive cycles. **b)** Current versus time.

The capacitance, the ratio between the total charge Q and the applied potential ΔV, can be found by integrating the current I measured while sweeping the voltage and using the expression

$$C = \frac{Q}{\Delta V} = \frac{\int Idt}{\Delta V} \qquad \textbf{4.12}$$

We assume that the charging and discharging capacity are identical (due to the symmetry in electrodes) and integrate the positive and negative current as indicated by the shaded regions in **Figure 4.21b** to find the total charge per cycle

$$Q = \frac{Q_+ + |Q_-|}{N} \qquad \textbf{4.13}$$

where N is the number of cycles. For the example shown in **Figure 4.21**, $Q = \frac{89+90}{5} = 35.8\ nC$ and $\Delta V = 1\ V$ (from -0.5 to +0.5 V), which gives $C = 35.8\ nF$.

4.4.2 Electrochemical characterization in a straight channel

In order to confirm that selective ion sweeping only occurs when CE and WE are exposed to different flow conditions, we first characterize the electrochemical response under flow in a simple straight channel with rectangular cross section of 800µm by 33µm (**Figure 4.23a**). The two embedded ITO electrodes have a 300 µm width and 2.9 mm length and are separated by 85 µm.

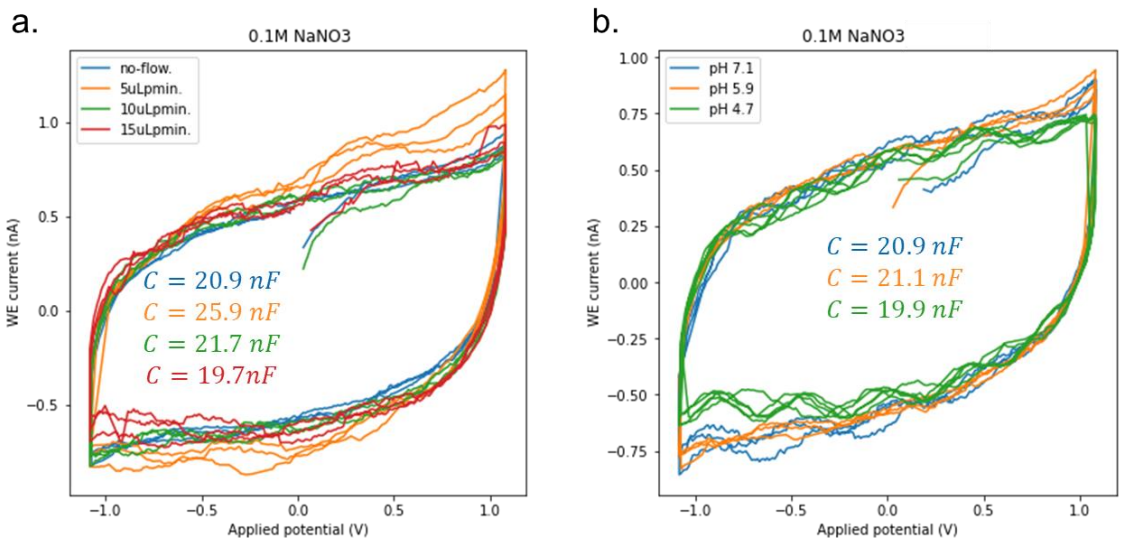

Figure 4.22 Cyclic voltammetry of 0.1M $NaNO_3$ on ITO electrodes in straight channel. **a)** under different flow conditions **b)** in different pH.

Cyclic voltammetry with and without flow is performed to see if the presence of flow affects the capacitance of the electrodes. From **Figure 4.22a**, we don't observe any significant difference in either the shape of the voltammogram or the associated capacitance, with all constant flow rates (including no flow) displaying a capacitance of ~5.2 nF. This may indicate that the ion sweeping is a kinetic process, and it doesn't affect the EDL under prolonged, steady flow. Or, that the kinetics of charging are faster than those of sweeping, which means no response to the flow can be seen due to the relatively fast scan rate. Changing the pH also doesn't seem to impact the capacitance, as there is only a slight difference between the acidic and neutral pH (**Figure 4.22b**).

Next, we consider the current response in the straight channel under flow. Whilst applying a potential of ± 1V a 0.5M solution of $NaNO_3$ is flowed with flow rate of 5µL/min for 15 seconds. In the first experiment, the flow starts only 30 seconds after the potential has been turned on, resulting in **Figure 4.23b-c**. This is not enough time to fully charge the electrodes, as we still see the exponential decay in the current, characteristic of capacitive charging. We therefore repeat the same experiment but wait much longer until the baseline current approaches zero (**Figure 4.23d-e**).

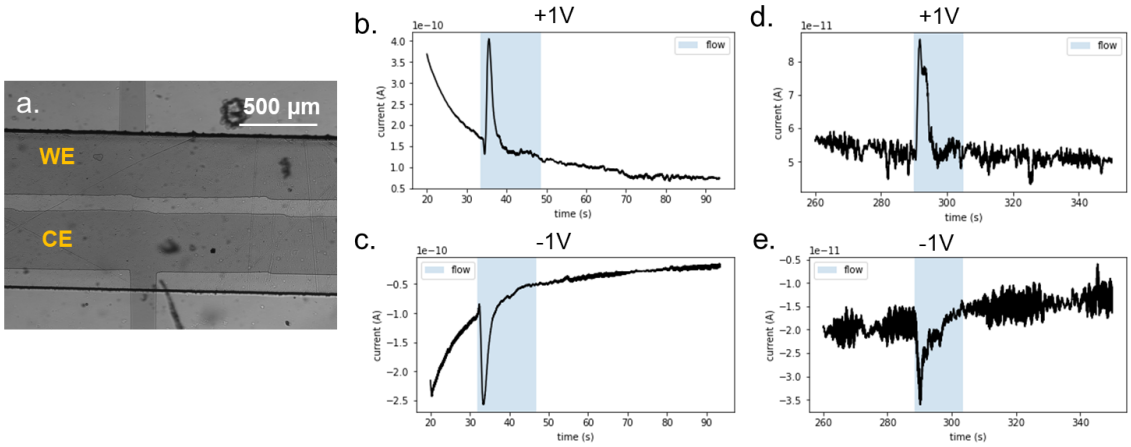

Figure 4.23 Characterization of electrochemical response in straight channel. **a)** Image of the ITO electrodes incorporated in a rectangular channel **b-e)** Current response when applying a ± 1V bias and a 15 second flow pulse (indicated by blue region) after **b-c)** 30 seconds and d-**e)** 4.5 minutes.

When applying the flow, a small peak in the current lasting a few seconds is observed for both charging conditions. This peak always has the same sign as the charging current and the intensity seems to be proportional to the baseline current. Similar experiments were repeated with various electrolytes, but always yielded the same type of current response, as discussed in **annex 5.6**. Additionally, we tried to induce size-based selective ion sweeping, by using tetrabutylammonium (TBA^+) as the cation of the electrolyte. We thought that the large hydrodynamic radius of TBA^+ (3.84 Å) might make it easier for the ion to be swept as compared to the smaller NO_3^- (1.29 Å) ion[143,144] and thus induce a slight amount of selective ion sweeping. However, the current response was similar to that with $NaNO_3$ shown in **Figure 4.23d-e**.

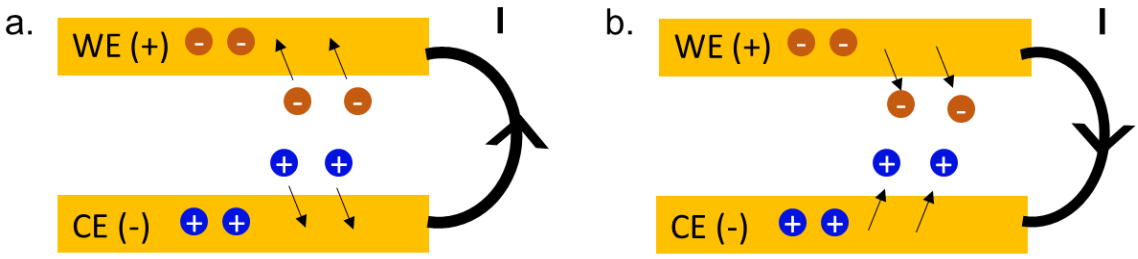

Figure 4.24 Schematic illustration of the current response in a cell with two capacitive electrodes and a positive potential difference due to **a)** charging of the EDLs and **b)** removal of ions from the EDLs (discharge). The charging and discharging current have opposite polarity indicated by the arrows.

To understand the origin of the small current peak observed at the onset of the flow we consider the expected current for the charging and discharging of the two EDLs (on each electrode), as illustrated in **Figure 4.24**. When the potential is applied, ions start forming the EDL on both electrodes which results in

a current with the same sign as the applied potential (**Figure 4.24a**). This process generates the exponentially decaying charging current seen in **Figure 4.23b-c**. Then, if we imagine that the flow triggers the removal of ions from both capacitive electrodes we would observe a current response with opposite polarity to the charging current, as illustrated in **Figure 4.24b,** followed by an opposite current once the flow is stopped as ions re-adsorb (**Figure 4.24a**). However, we always see a current with the same sign as the charging current and observe no response to the stopping of the flow. Based on this observation, it seems that the flow simply temporarily increases the charging rate, which may be due to homogenization of the ion concentration, rather than sweeping ions.

To conclude, we do not see a current response indicating selective ion sweeping in straight channels even when the cation is larger than the anion. Instead, a short increase in the charging current is observed, which is likely due to a homogenization of electrolyte near the electrode surface. Additionally, the current is not affected by the stopping of the flow.

4.4.3 Electrochemical characterization in anisotropic channels

Next, we investigate if selective ion sweeping can be achieved by exposing chemically identical electrodes to different amount of interfacial shear stresses. To do so, several microfluidic channels with incorporated ITO electrodes were made (illustrated in **Figure 4.25a**). Electrodes were roughly 300 µm wide with an 80 µm gap between them and either 2500, 5000 or 9000 µm long. Based on the simulations and birefringence results, 2 different channel geometries were chosen for initial testing as shown in **Figure 4.25b-c**.

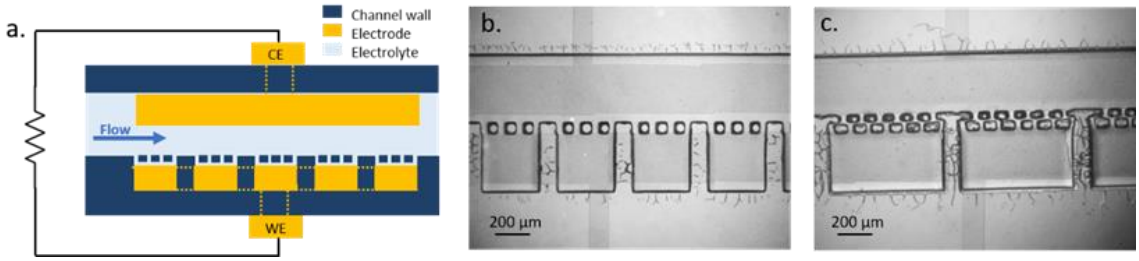

Figure 4.25 Selective ion sweeping device based on anisotropic shear conditions. **a)** Schematic of the device from the top view. **b)** and **c)** images showing two different channel geometries on top of two parallel ITO electrodes.

Effect of applied potential

Initially, we assumed that applying a potential difference between the electrodes would be necessary for enough charges to be present in the EDL to see a response to the flow. For a positive potential, we expected anions at the WE and cations to be present at the CE. According to our hypothesis, applying a flow would primarily sweep the cations on the CE and we should thus observe a positive current, as illustrated in **Figure 4.26a**. Similarly, applying negative potential means sweeping anions at the CE and thus negative current (**Figure 4.26b**). We therefore applied a potential bias for all initial experiments, of

+/- 0.5V. **Figure 4.26c** shows the current response for both a positive (black) and negative (red) potential bias when applying a flow pulse (highlighted in blue). These experiments confirmed that, contrary to the straight channel, a significant current can be observed in an anisotropic channel as a response to a flow.

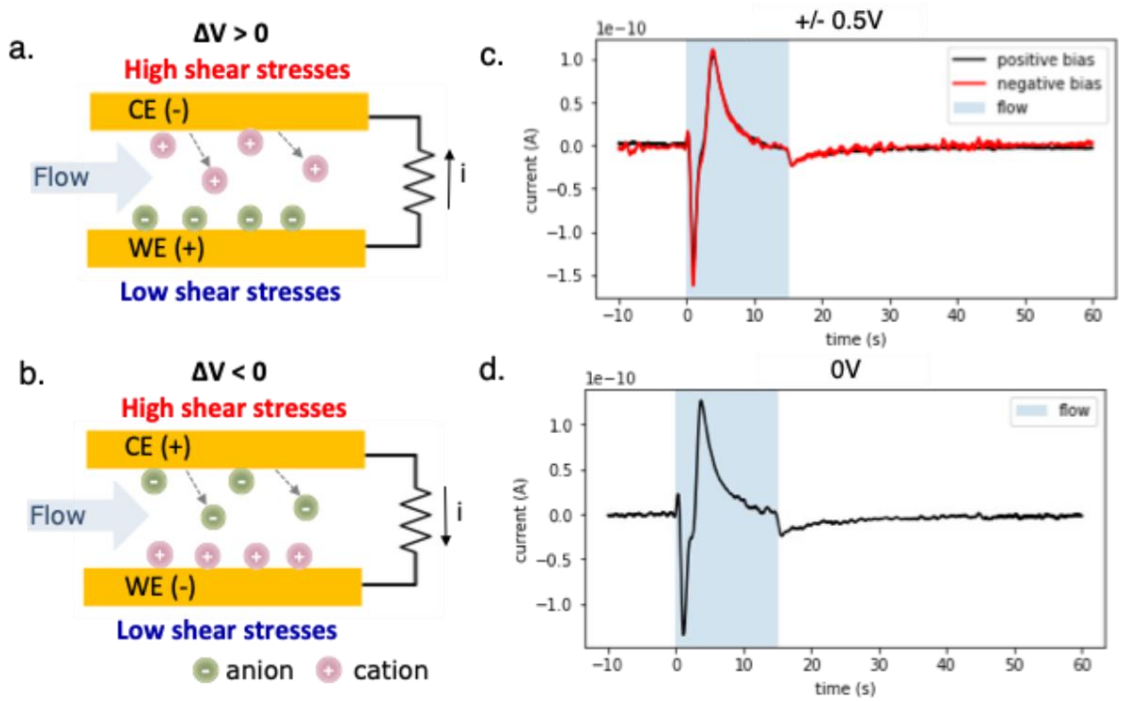

Figure 4.26 a-b) Initial hypothesis of the ion sweeping for a positive or negative bias respectively. The flow will sweep the ions on the CE which produces a current whose sign depends on the nature of ions swept. **c-d)** Current response when flowing 0.5M $NaNO_3$ at 2 µL/min for 15 seconds under a potential bias of ±0.5V or 0V respectively through an anisotropic channel (geometry **Figure 4.25c**).

Contrary to our hypothesis, we observed that the current response is not affected by the sign of the applied potential, as can be seen in **Figure 4.26c**. This suggests that no matter the potential applied, the sign and the amount of the charges swept is always the same. This means that the current cannot be caused by sweeping the ions on the CE, as changing the sign of the potential should change the charge of the ions in the EDL and thus the charges swept. To verify that the current is not dependent on the charges adsorbed on the CE, we repeated the experiment while setting the potential difference at 0V. Although the relative intensities of the current peaks change, the total charge (found by integration) remains unchanged when changing the potential (0.44±0.1 nA for ± 0.5V and 0.46±0.1 nA for 0V). This suggests that the presence of a potential bias simply affects the kinetics of the measured phenomena.

Impact of flow rate

Figure 4.27a shows the current response induced by a 15 second flow pulses at different flow rates without any applied potential bias. We always observe an initial negative current peak, followed by a second, positive peak. The current of the positive peak may reach zero during the flow, in which case no

response to stopping the flow is observed. However, for slow enough flow rates (< 4 µL/min) the current decreases more rapidly after the flow is stopped. This is more clearly observed in the annex **Figure 5.24**.

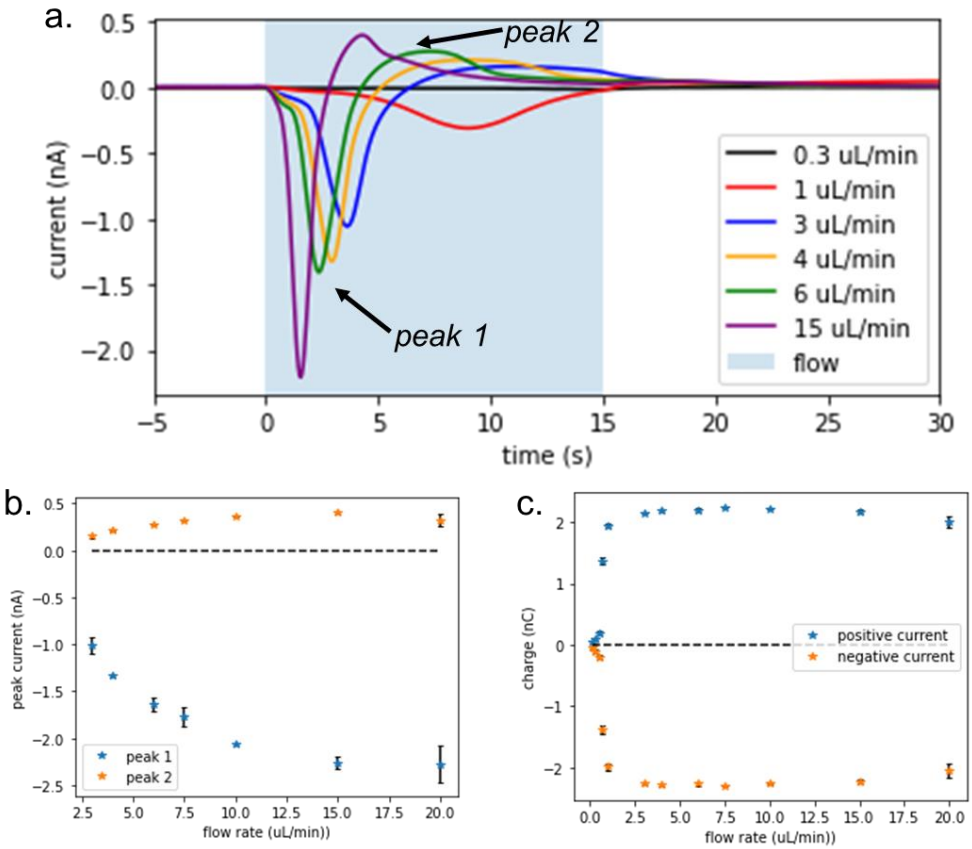

Figure 4.27 Electrochemical response to 15 second flow pulse over the CE in anisotropic channel (geometry **Figure 4.25b**) for $\Delta V = 0$. Using NaOH at pH 8.6 as the electrolyte. **a)** Current response at various flow rates **b)** Peak current and **c)** total charge (integrated current) for the first and second peak as indicated in **a)**.

To better understand the flow dependency, we plot the peak current and total charge, found by integrating the current, for the first and second peak observed as a function of the flow rate (**Figure 4.27b-c**). The peak current increases with the flow rate but is much higher for the negative peak. Although the peak current keeps increasing with the flow rate, we see that the total charge saturates to ~2.3 nC when the flow rate exceeds 5 µL/min (**Figure 4.27b-c**). This suggests that the flow rate only impacts the kinetics, but that there is a finite amount of charge which can be swept. However, as the experiments were done without any applied bias, we do not expect a large EDL on either electrode. In fact, experiments performed with an applied potential bias of ±0.5V give comparable results (as discussed in **annex 5.6.2**), further indicating that the response is not related to the EDL formed on the capacitive electrodes.

Sample deterioration and ionic strength

As the characteristic size of the EDL is affected by the concentrations of ions in the electrolyte[119], we then repeated the same experiments using different concentrations of $NaNO_3$ in the same channel. To make sure the ionic strength was not impacted by previous electrolytes, the channel was flushed several times with pure deionized water. For both concentrations of 0.05M and 0.5M the currents were much smaller than for the initial experiments with 0.1M $NaNO_3$. Repeating the initial experiment with 0.1M $NaNO_3$ also resulted in a much lower current response than the first experiment.

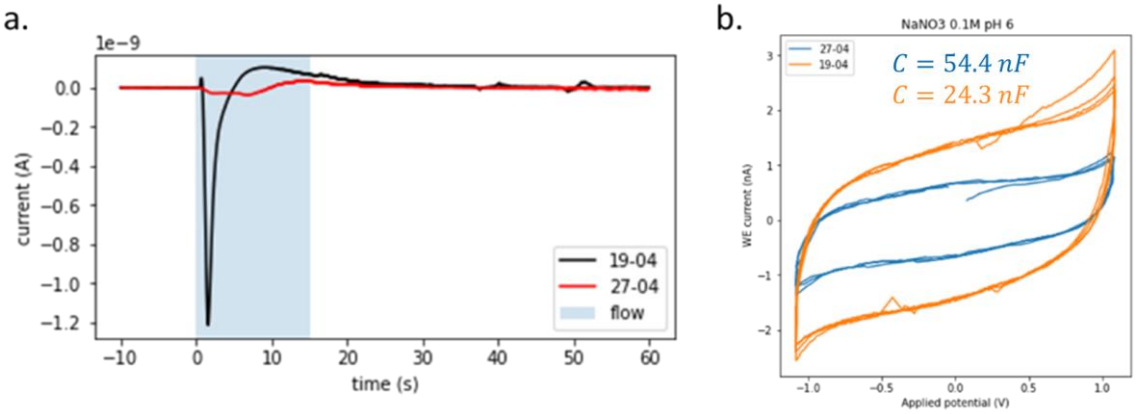

Figure 4.28 Loss of performance over time seen by difference of measurements taken on one week apart. **a)** Shows the current response to 15 seconds of flow at 15 µL/min. **b)** Voltammograms in 0.1 M $NaNO_3$ and the calculated capacitances.

The performance of the microfluidic electrode devices deteriorated significantly over time, as current response dropped significantly, shown in **Figure 4.28a**. The decrease in performance seems to be related to the electrodes (rather than the channel itself) as the pseudo-capacitance, calculated from the voltammogram in **Figure 4.28b**, dropped from 54.4 nF to 24.3 nF over one week of experiments. This loss in capacitance may be due to ions becoming permanently trapped at the ITO interface, acting as a kind of passivation layer. Additionally, it is well known that contamination of the ITO surface can strongly affect its electrical performance, specifically it's work function[145]. The many cycles of flushing of the channel are paired with removal and reattachment of the tubing, which could introduce (organic) impurities into the channel as the experiments were not done in an ultra-clean environment. This makes it difficult to make quantitative comparisons between the experiments done at different times, and for now doesn't give conclusive insight into the performance dependency of ionic strength.

Open circuit potential

Until now, only current measurements were discussed, but measurements of the open circuit potential V_{oc} may provide additional insight into the electrochemical response to the flow. **Figure 4.29** shows the measured V_{oc} before, during and after a flow pulse is applied for a duration of 1 minute, for various flow

rates. We should consider that this experiment is done without any reference electrode, and the absolute value of V_{oc} is therefore not reliable. For higher flow rates, V_{oc} increases rapidly from the onset of the flow, then slowly starts to decrease while the flow continues and finally undergoes an exponential decay when the flow is stopped. If we consider the derivative of V_{oc}, seen in the bottom row of **Figure 4.29**, we retrieve similar profiles to the previously obtained current profiles measured. This suggests that current measured in the previous experiments is simply there to compensate the change in potential between the two electrodes, a purely capacitive process (without the involvement of chemical reactions).

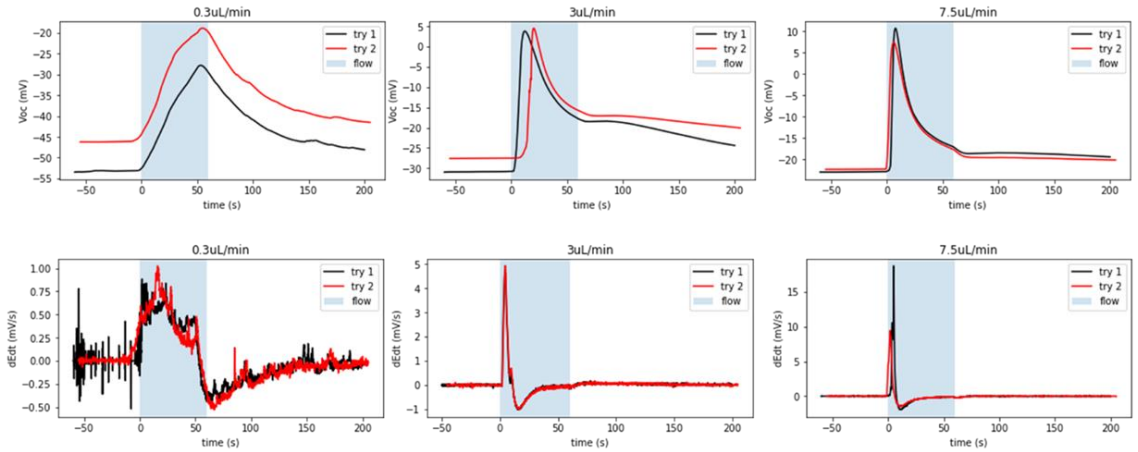

Figure 4.29 Open circuit potential V_{oc} measurements for a 1 minute flow pulse at different flow rates in an anisotropic channel (geometry **Figure 4.25c)** using 0.1M $NaNO_3$ at pH 7.1. The measurement is repeated a second time after 15 minutes of no flow. The top row shows V_{oc} and the bottom row its time derivative.

Based on these results, we can propose an alternative hypothesis regarding the nature of the current response illustrated in **Figure 4.30**. First, as we expect ITO to have a negative surface charge for experiments done at pH 8[146], anions may be the dominant ions in the EDL for both CE and WE at equilibrium. If a flow is applied, anions are predominantly swept from the CE, corresponding to a negative current. As a response, anions will leave the WE in order to return to equilibrium, corresponding to positive current. When the flow is stopped, the EDL of each electrode will be restored at the same rate, such that there is no net current. This means that the surface charge of the ITO rather than the accumulation of electrons/holes at the electrode surface dominates the sweeping behavior. To test this hypothesis, we more closely study the flow response as a function of the pH, effectively changing the surface charge of ITO.

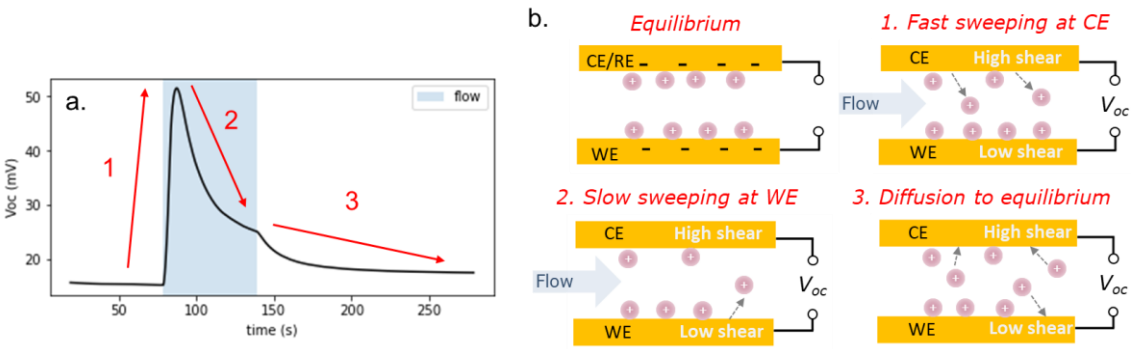

Figure 4.30 a) Open circuit potential V_{oc} measured while applying a 7.5 µL/min flow for 1 minute in anisotropic channel (geometry **Figure 4.25**c). The electrolyte used is 0.1M $NaNO_3$ at pH 8. **b)** Schematic illustration of the hypothesis explaining the V_{oc} behavior under flow. Cations are absorbed to both electrodes due to ITO's negative surface charge and will be more rapidly swept of the CE due to the high shear stresses causing an increase in V_{oc}. Slow sweeping at the WE causes the V_{oc} to decrease and when the flow is stopped cations diffuse back to the electrodes at a similar rate.

Effect of pH

ITO is known to have a negative surface charge under basic conditions and a positive surface charge in acidic conditions[146,147]. It is challenging to obtain the exact point of zero charge (PZC) for ITO, as it depends on the exact composition, but is has been reported to be at a pH of 8.5 for ITO nanoparticles in solution[147] and has been estimated to lie between pH 6-7 for bulk ITO[146]. This means it will be positively charged for previously investigated neutral and acidic conditions and negatively charged under (very) basic conditions. We therefor expect cations instead of anions on the ITO surface in highly basic conditions and consequently expect the current response to start with a positive current peak (due to sweeping of cations on CE). Close to the PZC, we expect to see no effect from the flow if there is no potential applied, as there shouldn't be many ions in the EDL.

To investigate this hypothesis, we characterized the current response as a function of the pH of the electrolyte. Additionally, we wanted to see if deionized water without any salt would produce a (stronger) current response. We thus started the first experiment in a new anisotropic channel with pure MilliQ water, labeled as pH 6.4 in **Figure 4.31a**. Solutions with different pH by adding NaOH or HNO_3 were prepared (without additional salt) and the experiments were repeated. **Figure 4.31a** shows that even for ultrapure deionized water, a current response similar to previous results is observed. **Figure 4.31** shows the current response for different pH while applying a 15 second flow pulse of 3 µL/min. Contrary to our expectations, the first large peak remained negative for all pH values. However, a small peak immediately after starting the flow can sometimes be observed which is positive for pH 4.7 and 6.4 and negative for pH = 10.

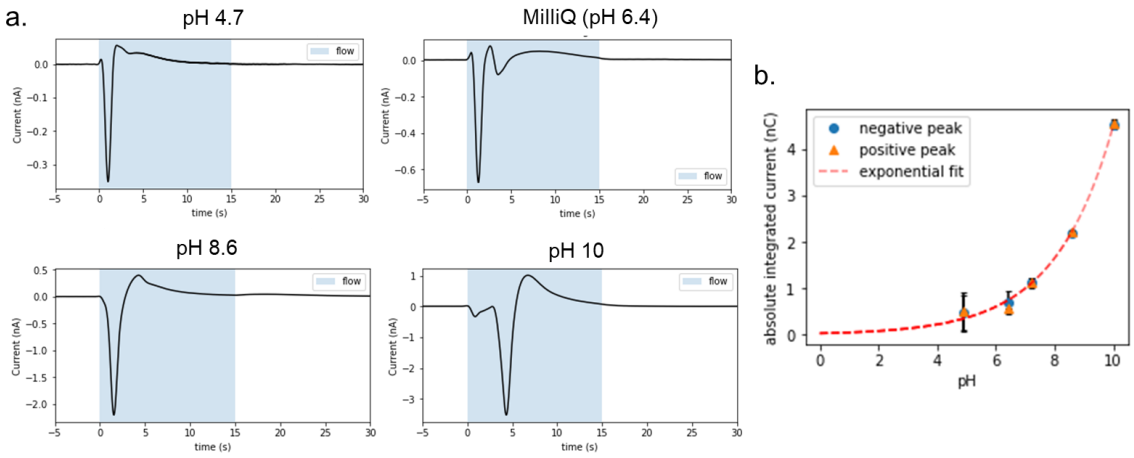

Figure 4.31 Effect of pH on current response under 15 seconds of 15 µL/min flow without an applied bias in anisotropic channel (geometry **Figure 4.25**b). **a)** I-t curves at various pH **b)** total positive and negative charge (integrated current) as a function of the pH fit with an exponential curve.

Moreover, the total integrated current (as well as peak current) seemed to increase exponentially with pH (**Figure 4.31b**). We previously found that the pH did not have a significant effect on the capacitance of the electrodes in the straight channel (see **Figure 4.22b**), however when performing cyclic voltammetry in the anisotropic system we do see significant variation as seen in **Figure 4.32a**. To check that this variation is not due to sample deterioration, we repeated the measurement at pH 10 after completing all other measurements and found a similar value for the capacitance as before (see annex **Table 5.1**). Interestingly, the capacitance is lowest for the highly basic pH, which provided the largest integrated current. As these experiments were done without adding additional salt, the difference in current response could also be linked to the different ionic concentrations. We therefore repeated the measurements with 0.1M $NaNO_3$ for pH 4.7-8 and find similar values (**Figure 4.32b-c**). The pH therefore does play an important role, but not in the way we expected.

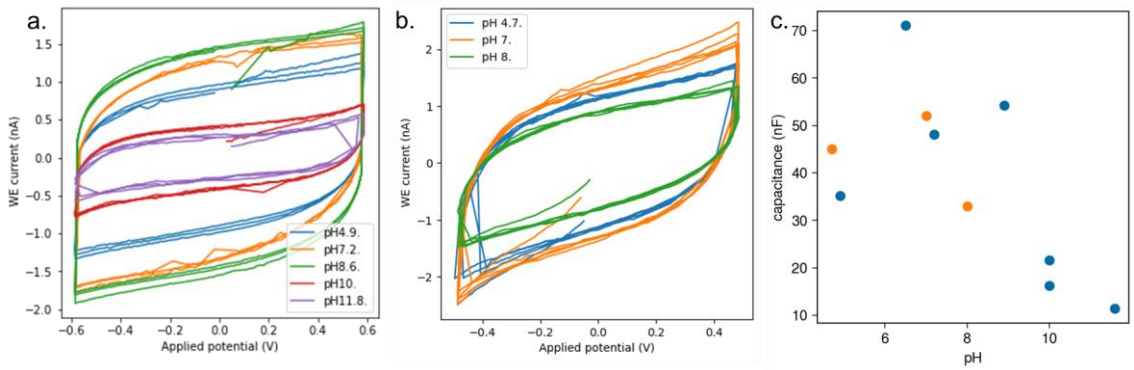

Figure 4.32 Cyclic voltammetry at different pH levels. **a)** Deionized water, pH adjusted by adding either NaOH or HNO_3. **b)** 0.1 M $NaNO_3$ solutions, pH adjusted by NaOH and HNO_3. **c)** Plot of the capacitance as a function of the pH obtained from a-b). Calculated capacitance values are found in the annex: **Table 5.1** and **Table 5.2**.

For PDMS, the PZC has been reported to be around a pH of 4.1[148]. To eliminate the possible effect of streaming current originating from interactions with the PDMS walls of the channel, we therefore repeat the experiments using a commercial buffer solution with pH = 4.1 in a new channel. First, we verify the state of the electrodes by voltammetry and find a capacity of 34 nF (**Figure 4.33a**), which is relatively high and signifies that the electrodes have not been passivated/deteriorated.

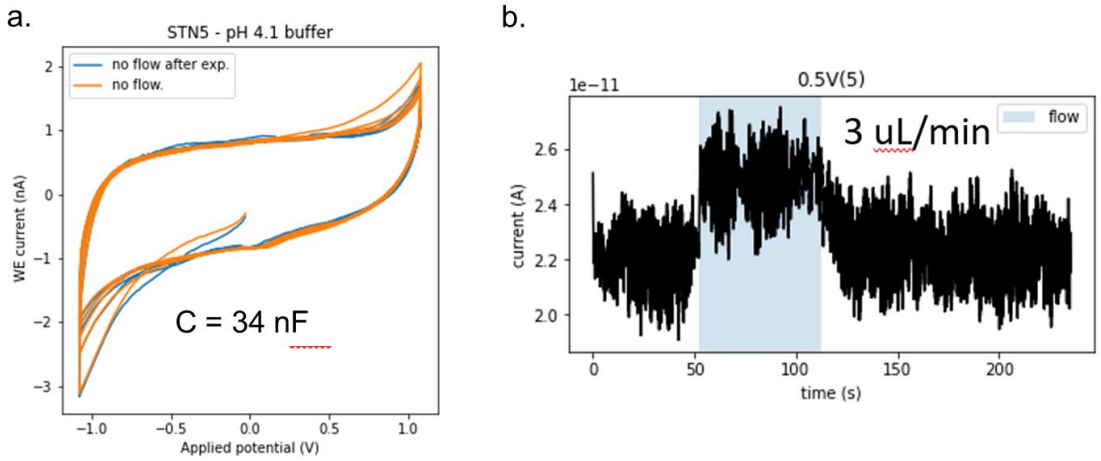

Figure 4.33 Experiments with commercial buffer solution of pH=4.1 as the electrolyte. **a)** Cyclic voltammogram before and after the flow experiment. **b)** Current response when applying a 0.5 V bias and a 60 second long flow pulse at 3 µL/min.

Figure 4.33 shows the current response under a 0.5 V bias when applying a flow. Indeed, we observe almost no response (~4 pA), whereas at higher pH the response for the same flow rate was on the order of 10 nA. This makes it likely to be related to the generated streaming current, rather than the ion sweeping occurring on the capacitive electrodes. It is possible that selective ion sweeping does occur, but that the magnitude of the current is too low compared to the streaming current. Additionally, it is also possible that the expected sweeping performance of ITO is deteriorated at such acidic conditions. To get a quantitative estimation of the expected current and its dependence on the pH, experiments on macroscopic sized ITO electrodes in a beaker cell were performed, as will be discussed in the next section.

Effect of electrode material

To verify that the observed currents are not dominated by the nature of the electrode surface, we made some similar devices using gold electrodes. If (some of) the charges swept under flow are present due to interactions at the interface of the ITO, we expect a decrease in current response when on gold electrodes as compared to the ITO. Gold was selectively deposited on part of the ITO electrodes and the anisotropic PDMS channel was attached on top. An image of the resulting assembly can be found in the annex, **Figure 5.54**. As the PDMS does not adhere to gold, the placement of the channel was chosen to maximize PDMS-glass contact. When flushing the channel with electrolyte, no leaking or detachment of the PDMs was

observed. The capacitance of the gold electrodes was measured using cyclic voltammetry (see annex **Figure 5.55**) at 145 nF, which is almost three times as high as the typical capacitance of the ITO electrodes with the same surface area.

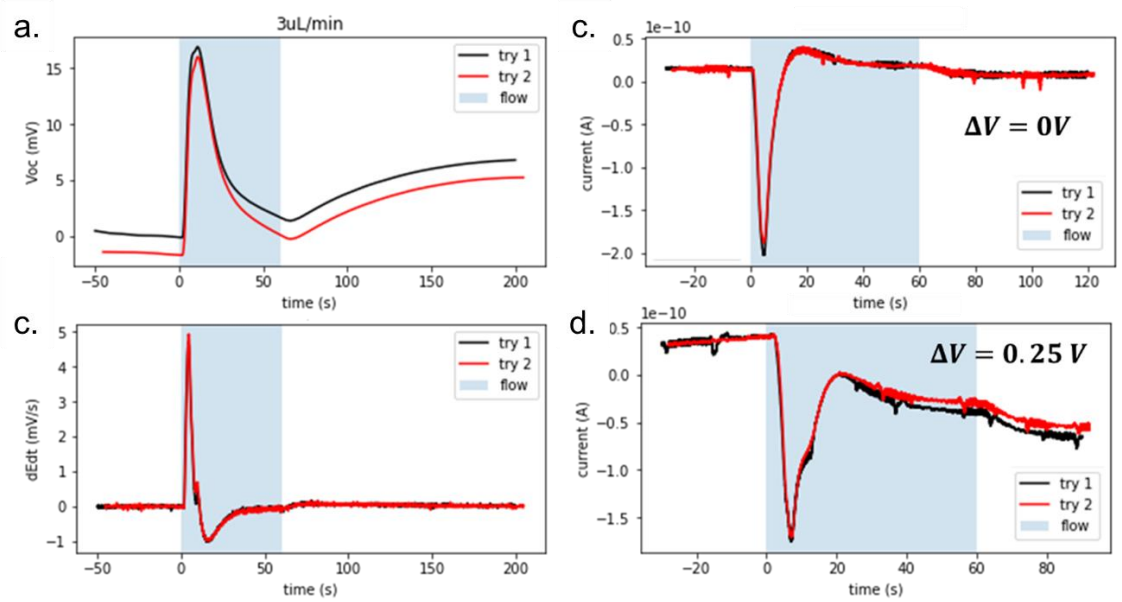

Figure 4.34 Gold electrodes in 0.1M $NaNO_3$ solution at pH 7 when applying a 3 µL/min flow for 60 seconds. **a)** V_{oc} and **b)** its derivative dE/dt. c-**d)** current response under flow for different applied potentials

For the initial experiments, the electrolyte was 0.1M $NaNO_3$ with pH 7. **Figure 4.34b-c** shows the measurements of the V_{oc} and its time derivative when applying a 3 µL/min flow pulse. We see a sharp increase in V_{oc} at the onset the flow, followed by as slower decrease as the flow continues, which is similar to the response previously observed on ITO electrodes (see **Figure 4.29**)**.** The current response when maintaining a 0V potential bias (**Figure 4.34d**) also has the same sharp negative peak followed by a less intense positive peak as the one for ITO electrodes. This evidences that the electrochemical response is not related to the surface charge of the ITO. Moreover, applying even a small potential causes the distortion of the current response, as seen in **Figure 4.34e**. Unlike the ITO, the current response therefor does depend on the applied potential. This could be due to the enhanced capacitance (three times higher than ITO) or could indicate the presence of chemical reactions at the gold surface.

Final hypothesis: streaming current

Based on the above observations, in particular the independence on the (polarity of the) applied potential bias, it is unlikely that the measured current originates from changes in the EDL on the capacitive electrodes. Considering that the current is minimized near the PZC of the channel walls, we expect that the response is instead linked to a streaming current due to the surface charge of the PDMS. At pH > 4, the PDMS has a negative surface charge[148], which promotes a preferential transport of cations, similarly

to what demonstrated by Zhang *et al.* (see **Figure 4.12**)[128]. However, in streaming current devices, the electrodes are positioned at the in- and outlet, whereas in our system they are parallel to the flow. Moreover, the current response is mostly constant whilst the flow is applied (**Figure 4.12d**) whereas we always see two current peaks of opposite sign with a net-zero charge (**Figure 4.27c**).

In the straight channel, both electrodes are affected by the streaming current equally, so no net current is detected. In the anisotropic channel this is not the case and we identify two main possible mechanisms for the net currents observed. First, the flow of electrolyte passes around the rectangular PDMS barriers (seen in **Figure 4.25**) and thus cause a small flow from one electrode to the other, similar to streaming current. The net-zero charge could be explained from the fact that as the flow passes the barrier it first moves from CE to WE and then in the opposite direction. The second possibility is that the EDL of the capacitor is affected in a similar fashion to those of the PDMS, resulting in a sweeping of cations. As the flow continues. This is essentially the same mechanism as shown in **Figure 4.30b**, but instead of being caused by the surface charge of ITO it is due to the PDMS.

Summary of chapter 4.4

In straight channels, where the shear rate should be similar on both electrode surfaces, we do not observe a significant response to flow. Small current peaks (<0.1 nA) are observed, but seem to be due to a temporary increase in the capacitive charging rate. In the anisotropic channels we do observe a current response with peak currents up to several nA. However, this response is independent on the polarity of the applied bias and is therefore different from the capacitive ion sweeping previously demonstrated. As the current is minimized near the point of zero charge (PZC) of PMDS, we attribute this to streaming current originating from the EDL formed at the PDMS surface.

To achieve measurable selective ion sweeping behavior in a microfluidic system, the device should be redesigned in such a way that the streaming current is minimized. In the next section we will therefore investigate alternative geometries. To inform the new design, we first investigate the sweeping behavior on macroscopic ITO electrodes.

4.5 Redesign of the microfluidic device based on characterization of ion sweeping on macroscopic electrodes.

Based on the surprising results in the previous section, which seem to suggest that the observed current is related to surface charges of the PDMS channels rather than to the EDL formed on the charged electrodes, we decided to perform additional experiments in a macroscopic beaker cell setup. First, this would allow us to characterize the current response without the presence of PDMS and give an idea of

the expected order of magnitude of the current for the small electrodes. Moreover, we initially expected that the current response due to selective sweeping due to the shear anisotropy on two capacitive electrodes would be the same to that in a hybrid cell with a battery electrode. To verify this, we repeat the beaker cell experiments with two ITO electrodes as the WE and CE whilst applying a jet flow on the WE (described in **annex 5.1.8**). Finally, based on the results on macroscopic electrodes, we redesign the microfluidic device.

4.5.1 Electrochemical characterization under jet flow on macroscopic electrodes

Experiments in the macroscopic beaker cell were performed at the Lee's Nano Energy Laboratory (NTU, Singapore) together with Donghoon Lee under supervision of prof. Seok Woo Lee.

The main goal of the macroscopic, beaker cell experiments was to see if the initial hypothesis of selective ion sweeping on charged ITO electrodes (described in **Figure 4.26a-b**) would hold true. As a reminder, based on this hypothesis we expect to see a positive current for a positive applied potential when applying the flow to the WE, as it means that there are anions absorbed to the WE and their removal by the flow creates holes which will attract electrons from the CE. This is indeed what was observed by Jung *et al.*, as seen in **Figure 4.14b**, where anions are swept from the WE (in this case their initial adsorption is due to the electrochemical energy difference of the two electrode materials)[50]. We thus wanted to confirm that a similar response can be observed in a cell with two ITO electrodes under a constant potential bias, while applying flow only to one of them.

To mimic the conditions in the previously discussed microfluidic system, we perform the first experiments in a two-electrode setup with identical ITO electrodes and an electrolyte of 1 mM KNO_3 around pH 7. This setup does not include a RE, which means that the exact value of the applied potential bias cannot be guaranteed. We were not able to perform a cyclic voltammetry experiment, but based on the capacitance measured in the microfluidic sample (see **Table 5.2**), estimate the capacitance to be around 5 µF for an electrode with surface area of 1 cm^2. During the experiment, a constant potential is applied and the current is collected. Using the jet setup (**Figure 5.5a-b**), flow pulses are applied at different flow rates for 1 minute, spaced by 20 minutes of no flow to make sure an equilibrium state is achieved before starting each flow. **Figure 4.35a** shows the current response for applied potentials of ±300 mV and ±500 mV and flow rates from 1 to 20 mL/min.

NB: In this case, the flow is always applied on the WE, whereas in the previously discussed microfluidic systems, the flow was applied to the CE. This means that the sign of the current is inverted with respect to the previous results.

As expected, we see that the sign of the current triggered by flow always matches the sign of the applied potential. This suggests that it is indeed the sweeping of the ions in the EDL which is responsible for the current response. At the onset of the flow the current increases rapidly and it slowly decreases as the flow continues. At higher flow rates, we can observe a narrow current spike followed by a plateau of an almost constant current. Due to the limited time to perform the experiments, the flow pulse was kept relatively short but increasing the flow time would likely maintain this current. This plateau, or saturation current, was previously reported to scale exponentially with the applied potential and linearly with the flow rate[50].

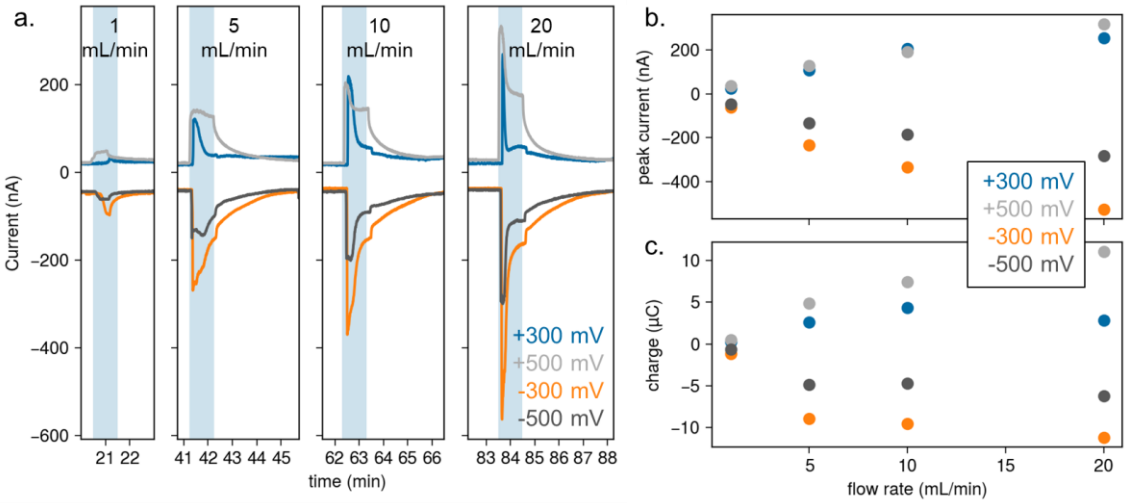

Figure 4.35 Effect of applied bias and flow rate in beaker cell experiment. **a)** Current response when applying jet flow on the WE in an ITO|ITO cell for different applied potentials. The presence of flow is indicated by the highlighted regions in blue. **b-c)** Peak current and integrated current (charge) during the flow pulse, after subtracting a constant baseline.

Unlike the initial reports in a hybrid cell by Jung *et al.* we do not see a reversal of the current after the flow is stopped[50]. Instead, we see an exponential decay in the current, typical of capacitive charging, until the original baseline is retrieved. This may be due to the fact that the potential bias always keeps the same sign as it is controlled actively, whereas for the hybrid cell the initial bias originates from the electrochemical potential difference which changes as the battery electrode discharges. Additionally, the kinetics of ion adsorption and ion intercalation may be different, which could also explain the back current when the flow is stopped in the hybrid cell. However, the re-adsorption rate on the identical capacitive electrodes can be expected to occur at the same rate, and no back current is seen. Importantly, this means that the current response is distinct from that of the hybrid cell, contrary to our initial hypothesis.

In order to quantitatively investigate of the flow rate and potential, we consider the peak current as well as the charge (**Figure 4.35b-c**). No matter the applied bias, the peak current seems to be directly proportional to the flow rate. This is in line with previously reported results for both selective ion sweeping and streaming current devices[50,124,128]. Increasing the applied potential should result in the augmentation

of ions in the EDLs of both electrodes. The charge is calculated by integrating the current over the duration of the flow and does not include the effect of the decay current after the flow is stopped. Considering the positive potential, we see that the peak current is almost identical for both 300 mV and 500 mV, but that the charge is larger for the higher potential. This may indicate that a similar number of ions is rapidly swept as an immediate response to the flow and that under sustained flow more ions continue to be swept but its rate depends on the size of the EDL. For a potential bias of ±500 mV, the charge swept by the highest flow rate is around 12 µC. Assuming a capacitance of 5 µF, the charge moved during the one minute flow pulse therefore corresponds to almost 5 times the total charge in the initial EDL (2.5 µC). Of course, it is possible that the capacitance is grossly underestimated, but either way the charge seems very large compared to that in the microfluidic systems.

Effect of electrode size

In the previous section, we confirmed that a flow induced current is observed for a two electrode cell with identical ITO electrodes, although different from the current in a hybrid cell. However, the behavior in the microfluidic system discussed in **section 4.4.3** is distinctly different, as the current response under flow is unaffected by the applied potential and the net charge is always zero. We hypothesized that the current measured in the microfluidic system is dominated by the streaming current generated by interactions with the charged PDMS channel walls. Even if selective ion sweeping does occur on the ITO electrodes, the resulting current might be too small compared to the streaming current from the PDMS. To estimate the magnitude of the expected current response from ion sweeping, we characterized the current response as a function of the surface area of the WE using the beaker cell setup.

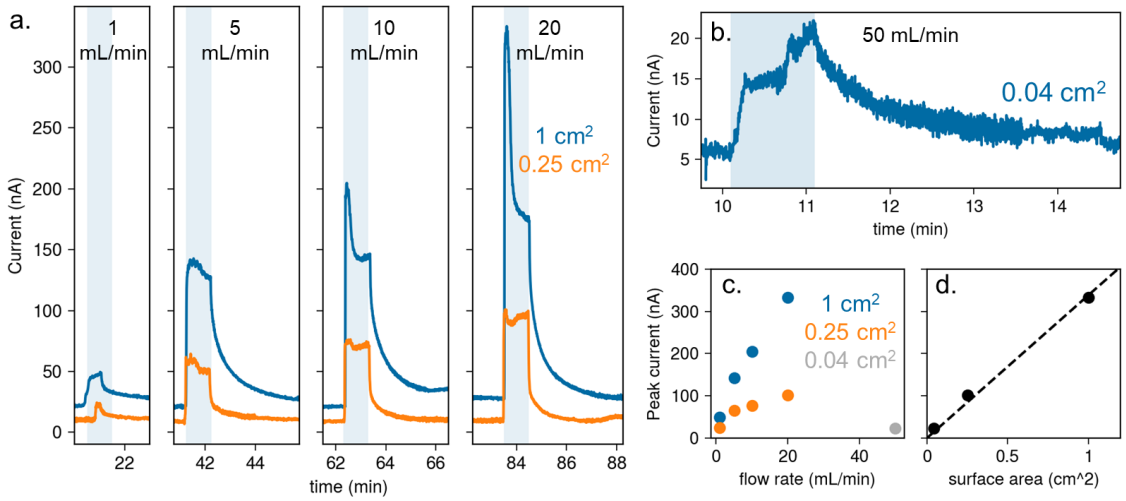

Figure 4.36 Current as a function of the surface area A under jet flow (indicated by blue highlighted regions). **a)** Current response for different flow rates for A of 1 and 0.25 cm2 **b)** Current response for a 50 mL/min flow rate for A = 0.04 cm2. **c)** Peak current as a function of the flow rate and surface area. **d)** Peak current measured at the maximum flow rate as a function of A.

Jet flow experiments were performed in a two-electrode configuration using 1 mM KNO_3 and an applied bias of 500 mV. The surface area of the CE is kept constant, but the effective surface area of the WE is varied by masking part of the surface (see **Figure 5.5c**). **Figure 4.36a** shows the current response for surface areas of 1 cm^2 and 0.25 cm^2 and flow rates of 1 to 20 mL/min. A much larger flow rate (50 mL/min) was required to see any noticeable response on the 0.04 cm^2 area, as seen in **Figure 4.36b**. Generally, we see a linear increase in the peak current with the flow rate (**Figure 4.36c**) and the current seems to be directly proportional with the surface area of the WE (**Figure 4.36d**).

Although we cannot directly compare the quantitative amount of the shear forces due to the jet flow in the beaker cell and the laminar flow in the microfluidic channel, we can use the beaker experiments to approximate the order of magnitude of the expected current in the previous microfluidic system. The surface area of the electrodes in the microfluidic channel were on the order of 1 mm^2, which means we can expect a current on the order of several nA based on **Figure 4.36b-d**, assuming the shear forces are comparable.

Effect of pH

Finally, we investigate the role of the electrolyte pH on the sweeping behavior in the beaker cell. **Figure 4.37** shows the current response to 1 minute long flow pulses while applying a positive bias for pH 4 and pH 10 solutions of 1mM KNO_3. For both, the current response to the flow is always a positive current whose magnitude increases with the flow rate, similar to the previous results in pH 7. For the experiments with pH 10, high flow rates produce very sharp but short current spikes, whereas the response for pH 4 is more constant. For both, the magnitude of the peak current is an order of magnitude smaller than that measured using pH 7 electrolyte.

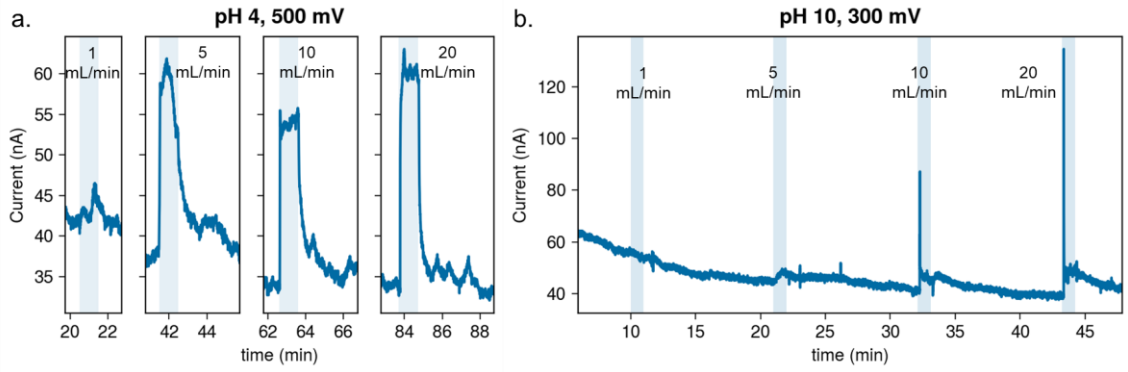

Figure 4.37 Current response for 60 second flow pulses at various flow rates using 1 mM KNO_3 at **a)** pH 4 and **b)** pH 10.

In the microfluidic experiments, the maximum current response was observed for a pH of 10 (see **Figure 4.31**). However, in the beaker cell the current is decreased drastically at pH 10 (**Figure 4.37b**) as compared

to similar experiments done at pH 7 (**Figure 4.37a**). This again suggests that the processes measured in the microfluidic and beaker cell are not the same. Additionally, when applying a 500 mV potential bias, the baseline current kept increasing (see annex **Figure 5.56**), indicating a continuous reaction occurring, which may have also been the case in the microfluidic channel but with such a small current it might not have been noticeable.

4.5.2 Redesign of kinetic energy harvesting device

Based on the beaker cell experiments, we can conclude that the previous microfluidic systems were dominated by another phenomena than ion sweeping on the capacitive electrode. Firstly, because based on the surface area dependency (**Figure 4.36**), we only expect a weak current from ion sweeping in the previous microfluidic system with small electrodes. Secondly, the pH dependency (see **Figure 4.31b**) and previously reported PDMS systems[128] suggests that the measured current is linked to streaming current generated by the PDMS surface charges. To be able to make meaningful shear characterization, we should therefore redesign the microfluidic channel to minimize the impact of streaming current and maximize the contribution of capacitive ion sweeping. It may also be necessary to passivate the channel surface, to eliminate the influence of streaming current on our measurements. This may be done by coating the PDMS surface with a passivating layer, such as PTFE[149] or HDMS, or by incorporating additives to the PDMS mixture before casting the channels[150]. However, it will be challenging to selectively passivate the channel walls without coating the electrodes whilst maintaining a strong bond between the PDMS and glass. Instead, we focus our effort to minimize the streaming current and maximize ion sweeping purely based on the design of the channel and electrodes.

Usually, in streaming current devices, the two electrodes are placed at the in- and outlet, whereas in our case both electrodes are parallel to the flow direction. We thought that maybe the small PDMS barriers used to enhance the shear anisotropy (see **Figure 4.25**) could be the origin of the streaming current, as they are reminiscent of the pillars used by Zhang *et al.* (see **Figure 4.12**)[128]. Their presence greatly enhances the total PDMS surface area and creates a small amount of flow from the CE to WE. We therefore tried to redesign the microfluidic channel without such barriers, whilst maintaining a high shear ratio.

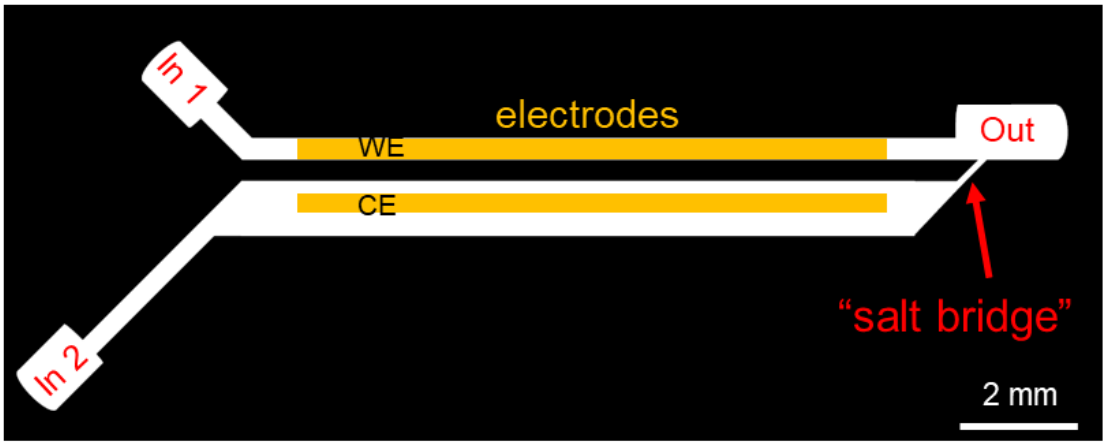

Figure 4.38 Top view of the channel design consisting of two parallel channels connected by a narrow channel for ion transfer.

Figure 4.38a shows a simple design, of two parallel channels connected only near the outlet by a narrow channel acting as a "salt bridge" to allow for ion exchange. The channel has two inlets, the first one is for actively creating a flow over the WE, and the second inlet is just to fill the bottom channel with electrolyte and was plugged after filling to prevent any flow over the CE. In this case, there are no complex PDMS pillars/barriers and there is no direct flow possible between the two electrodes. However, this channel produced a similar response to the initial microfluidic system; when flowing over the CE, the current response is always negative, no matter the applied potential (see annex **Figure 5.59**). Similarly, flow on the WE always produce positive current peaks. The streaming current therefor does not seem to be due to the specific channel design as simplifying the channel geometry does not change the current response.

The next strategy we explored was to enhance the relative contribution of the ion sweeping, by significantly increasing the surface area of the electrodes. We made ITO electrodes of 500 µm wide and 3 cm long each which are spaced 400 µm apart. This size is maximized according to the restricted dimensions of the substrate used for the confocal microscopy measurements. We also redesign the microfluidic system, such that the connection between the channels is in the center, allowing for better ion transfer between the two electrodes, as illustrated in **Figure 4.39a**. After the bottom channel has been filled with electrolyte, the two bottom inlets are sealed of using tape, preventing flow over the bottom electrode. The channel height is fixed at 33 µm, and based on the COMSOL simulations we expect that the shear is almost 18 times stronger on the top electrode (**Figure 4.39b**).

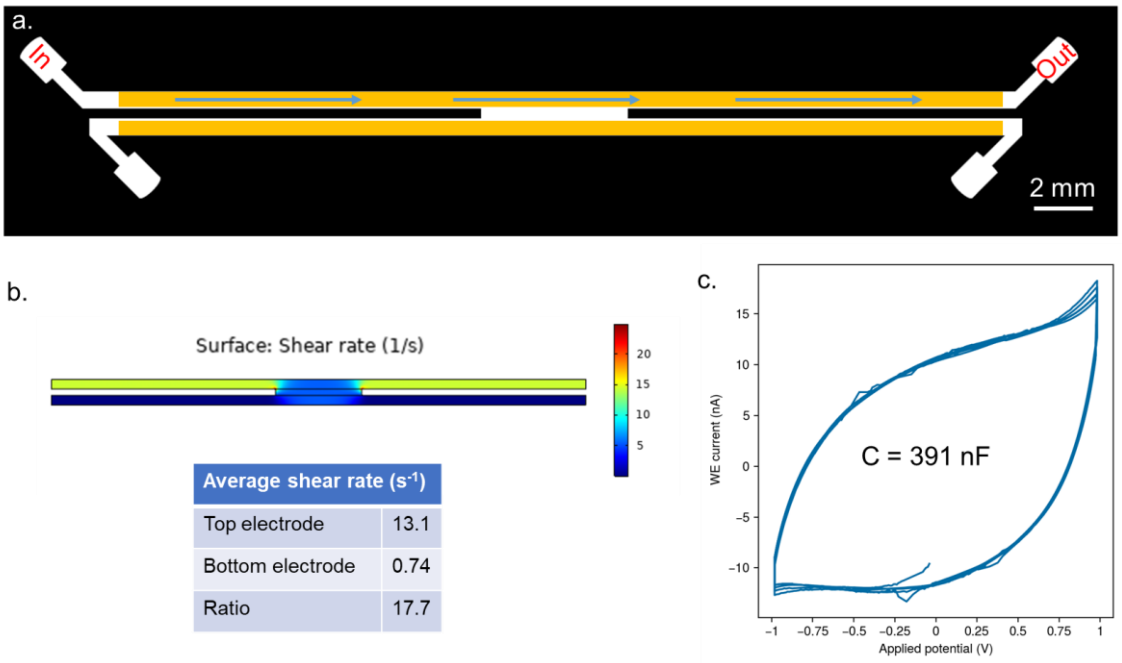

Average shear rate (s^{-1})	
Top electrode	13.1
Bottom electrode	0.74
Ratio	17.7

Figure 4.39 a) Top view of the channel design consisting of two parallel channels connected by through a central connection for ion transfer between the electrodes (indicated in yellow). The bottom two inlets are used solely for filling the bottom channel and are sealed during flow experiments, such that the flow only follows the top channel. **b)** COMSOL simulation of the shear rate at the bottom surface of a 33 µm high channel for a constant flow rate of 10 µL/min. The average shear rate is evaluated along each electrode position. **c)** Cyclic voltammetry measured using 10 mM $NaNO_3$ and the calculated capacitance.

The electrodes in this new design each have a 5 times higher surface area than those used for the microfluidic experiments in **section 4.4.3**. Consequently, the capacitance is around 10 times larger as well (see **Figure 4.39**). **Figure 4.40a** shows the current response to 60 second flow pulses in such a channel for both a negative and positive 1V bias. Unlike all previous microfluidic systems, we now observe that the sign of the current changes with the sign of the potential, which is consistent with the macroscopic beaker cell experiments. This suggests that we finally succeeded to measure selective ion sweeping associated to the charges in the EDL of the capacitive electrode. Interestingly, we do not see a clear dependency between flow rate and peak current and total charge, as it remains mostly constant within the measured range of 3-15 µL/min (**Figure 4.40b-c**). The maximum charge removed during the 60 second flow pulse is around 30 nC, corresponding to ~8% of the capacity at 1V.

Based on the beaker cell experiments (see **Figure 4.36**) we may expect a peak current on the order of tens of nA for a surface area of 0.15 cm^2. However, in the microfluidic system, the largest peak current is only ~1 nA. observed for the smallest flow rate, so it is possible that decreasing the flow rate even further will enhance the current response. Additionally, the current seems to reach an almost steady plateau during the flow pulse, it would be interesting to see how long this current can be maintained under continuous

flow. Additional experiments, varying the flow rate and duration will therefore be needed to better understand the mechanism.

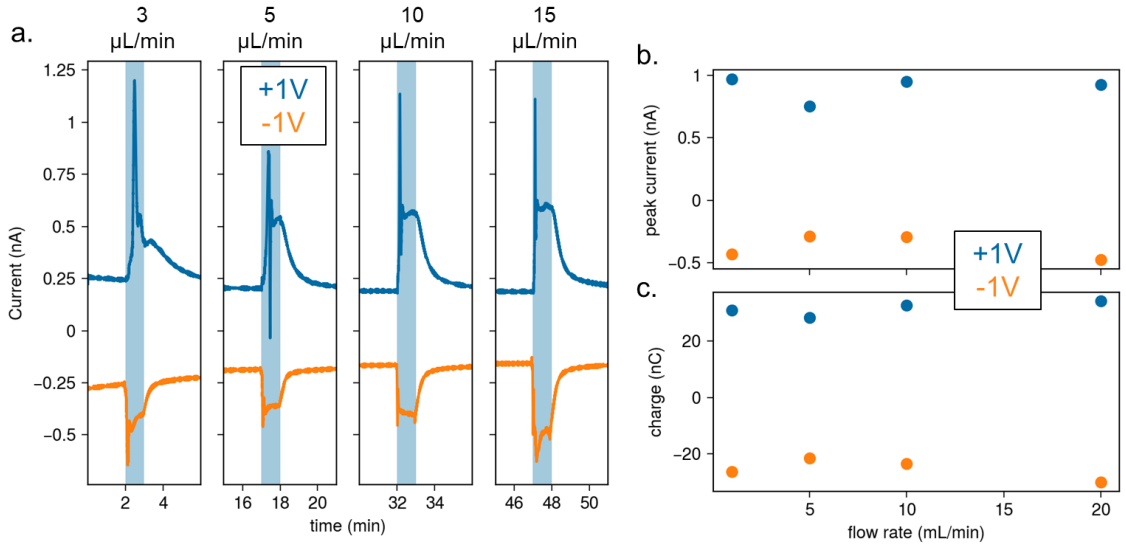

Figure 4.40 Effect of the applied bias on the current response under flow in microfluidic channel depicted in **Figure 4.39a**. **a)** Current response to 60 second flow pulses at various flow rates for an applied potential of ±1V. **b)** Peak current and **c)** charge (integrated current during flow) as a function of the flow rate.

Summary of chapter 4.5

The ion sweeping phenomenon is studied by application of a jet flow on macroscopic ITO electrodes in a beaker cell. As expected, we observe a positive current response for a positive potential bias and a negative current for negative bias. However, unlike the hybrid cell with a battery electrode, we do not see a reversal in the current once the flow is stopped. The peak current and total charge increase linearly with the flow rate and seem to be directly proportional to the electrode surface area. Based on these results, we expect that the electrode's surface area in the previous microfluidic systems was too small to generate a significant sweeping current.

Finally, by increasing the electrode surface area and changing the channel geometry, we achieve selective ion sweeping through a difference in shear conditions on capacitive electrodes. Unlike the beaker cell, we do not observe a clear trend in the current as a function of the flow rate. Further studies of the flow dependency are required for the full electrical characterization of the system.

4.6 Conclusion

Here we investigate a novel kinetic energy harvesting system based on selective ion sweeping on capacitive electrodes, first reported by our collaborators at NTU. Under flow, ions in the diffuse layer of the EDL may be swept away, and if this process only occurs on one electrode in a circuit, it can be used to generate a current. Although the initial demonstration was performed in a hybrid cell, containing capacitive and battery-type PBA electrodes, we try to replicate the effect in a cell with identical capacitive electrodes purely based on a difference in shear conditions. A flow induced current is observed both on macroscopic electrodes in a beaker cell and in a microfluidic system with incorporated electrodes. However, we do not see a back current when stopping the flow, which makes the response distinct from the previously reported hybrid cell.

Recently, we succeeded in fabricating PBA thin films on top ITO micro-patterned electrodes (**annex 5.1.9**). This should finally make it possible to replicate the hybrid cell configuration in the microfluidic system. This would eliminate the need for an external bias, as the difference in electrochemical potential between the two materials generates the EDL on the capacitive electrode. We hope to achieve such a microfluidic hybrid cell in the future.

In parallel, we further develop our shearmetry technique and include the rheological properties of the nanorod suspension in the calibration procedure. Initial results show that shearmetry can be performed close to the ITO surface without any distortions (**annex 5.7**). The next step is to combine the two advancements and perform *in situ* shearmetry during the ion sweeping in the microfluidic energy harvesting device.

Conclusion and perspectives

Overall, this work highlights the versatility of $LaPO_4$:Eu nanorods: they spontaneously form never-before-seen LC assemblies, can be used as orientation probes and make it possible to measure shear stresses in microfluidic flows.

The existing spectroscopy-based orientation analysis methodology was further developed, making it more accurate and robust. A main limitation which remains is that we cannot obtain both the order parameter and out-of-plane orientation independently. For the application in LC tomography, this requires the assumption of a known and constant order parameter throughout. However, in complex LC structures where the director changes drastically throughout the volume, this assumption cannot be accurate. One way we may get insight into the out-of-plane angle is the wavelength dependent retardation which was sometimes observed in nematic LCs. Characterizing this effect as a function of the director tilt could therefore be interesting to explore.

The improved methodology helped us to gain valuable insight into the previously unknown LC structures. The high resolution of the confocal microscopy setup allowed us to precisely map the isotropic-nematic interface, revealing remarkably sharp ridges and peaks in the streak and flower structures. The orientation tomography revealed that the hybrid boundary conditions, homeotropic at the substrate and tangential at the isotropic-nematic interface, are the driving factor for the morphogenesis from tactoid, to streak and finally flower domains. Moreover, from the simulated and observed tactoids, we learned that the anchoring strength and elastic energy are more dominant than the surface tension in our colloidal LC. Some initial work on simulating the more complex linear streak and flower structures has been done, but to improve the accuracy we should consider the elastic anisotropy and adapt the shape of the unit cell domain.

Now that we understand the origin of the complex LC structures, we can start to control it actively. For example, we could introduce an orientational surface treatment of the substrate and in turn favor long streaks, similar to the oily-streaks seen in smectic LCs. Using our colloidal LC would likely result in much larger topographical fluctuations on the order of tens of microns compared to tens of nanometers for organic LCs.

The high shape anisotropy of the $LaPO_4$:Eu makes them easily aligned by external forces, which we have been exploiting to probe the shear stresses in microfluidic flows. In this work, we demonstrated that the $LaPO_4$:Eu suspension are slightly shear thinning and proposed an adapted calibration procedure for the existing shearmetry technique. With this advancement as well as the improvements in the spectroscopic methodology, the steady-state shear monitoring has become much more reliable. The next step will be to adapt the technique for time dependent shearmetry. For this, it will be crucial to characterize the response

time, which will likely depend on the nanoparticle morphology and the rheological properties of the suspension.

At the beginning of my PhD I set out to apply the shearmetry technique to study the ion sweeping phenomenon demonstrated by our collaborators at NTU. Reproducing their hydrovoltaic system in a microfluidic channel proved much harder than expected, and I therefore did not get to do any *in situ* shear measurements. Finally, at the end of my PhD, we managed to create a microfluidic device with incorporated electrodes whose electrochemical response matches that of a similar macroscopic system. We showed that a current can be generated in a cell of identical capacitive electrodes, purely based on an anisotropy in shear conditions. It should now be possible to simultaneously monitor the shear close to the electrode surface and the electrochemical response of the device. Moreover, we would like to replace one of the capacitive electrodes with a battery-type one, so that we no longer need to apply a potential bias to see the ion sweeping effect.

Résumé en français

Les nanoparticules et les molécules luminescentes jouent un rôle crucial dans l'étude des objets et des processus à l'échelle micro- et nanoscopique. Elles sont particulièrement importantes dans les situations où une méthode d'imagerie non destructive et peu invasive est nécessaire, comme pour l'imagerie biologique et d'autres systèmes dynamiques. En particulier, la capacité à mesurer l'orientation tridimensionnelle des objets à l'échelle micro- ou nanoscopique est essentielle pour une grande variété de domaines de recherche. Par exemple, les mesures d'orientation autour des défauts observés dans les cristaux liquides pourraient aider à optimiser les dispositifs actifs et fournir des informations fondamentales sur les phénomènes d'autoassemblage. Le suivi des dynamiques d'orientation est également essentiel pour comprendre divers mécanismes biologiques, tels que le repliement des protéines. Pour répondre à ce besoin, notre groupe a développé des nanocristaux qui émettent une luminescence fortement polarisée. Nous avons précédemment démontré que la collecte de leur émission polarisée est une méthode efficace, rapide et simple pour déterminer l'orientation tridimensionnelle des nanocristaux anisotropes uniques. Dans ce travail, nous montrons qu'une telle méthode peut être étendue à la caractérisation d'assemblages de nanoparticules et à l'étude de ses applications.

Micro-spectroscopie confocale résolue en polarisation

L'imagerie tomographique à haute résolution des lanthanides ne peut pas être réalisée avec des microscopes confocaux conventionnels en raison de la grande différence entre les longueurs d'onde d'excitation et d'émission (200-300 nm) et des durées de vie longues (~10^{-3} s) de leur luminescence. Dans ce travail, un microscope confocal personnalisé est développéé qui permet une micro-spectroscopie résolue en polarisation. Pour résoudre l'aberration chromatique, nous ajustons manuellement la collimation du laser d'excitation afin de correspondre au plan focal de l'émission. Le balayage tomographique est réalisé à l'aide d'une platine piézoélectrique avec une vitesse de balayage ajustée à la durée de vie longue. Une optimisation minutieuse des composants optiques et de l'alignement assure un contrôle précis de la polarisation de l'émission collectée. Enfin, en cartographiant l'intensité de la luminescence d'un nanocristal unique de $NaYF_4$:Eu, nous démontrons une résolution spatiale d'environ 590 nm et 950 nm dans les directions latérale et axiale, respectivement.

Tomographie de l'orientation collective dans un cristal liquide

Les suspensions de nanobâtonnets colloïdaux $LaPO_4$:Eu forment des phases cristallines liquides à des fractions volumiques suffisamment élevées. Dans cet état, les nanobâtonnets forment des autoassemblages ordonnés tout en conservant leurs propriétés liquides. Lorsqu'une goutte de ce cristal liquide est confinée entre deux parois rigides, des défauts apparaissent en raison des conditions de

frontière contradictoires aux interfaces. De plus, nous constatons que ces défauts subissent une morphogenèse et forment enfin des structures jamais rapportées auparavant.

En utilisant la luminescence polarisée provenant de l'ion Eu^{3+}, nous avons pu reconstruire la structure interne du cristal liquide à divers stades de la morphogenèse des défauts. Cela se fait par analyse spectral de la luminescence polarisée mesurée en utilisant les composants principaux obtenus à partir d'un échantillon de référence. Nous démontrons d'abord la technique dans le tactoïde bien connu et récupérons son profil de directeur attendu suivant les contours de la gouttelette. La cartographie tomographique de l'orientation dans les structures linéaires intermédiaires et finales en forme de fleur a révélé un ancrage vertical à l'interface du substrat, couplé à d'importantes variations topographiques. La structure en forme de fleur présente une topographie semblable à un cratère, avec le directeur rayonnant à partir des cratères sous forme de quatre pétales. Sur la base de nos observations, nous proposons que ce soit l'équilibre délicat entre l'énergie élastique, la force d'ancrage et la tension superficielle qui donne lieu à de telles structures complexes en trois dimensions.

Caractérisation du cisaillement dans un système hydrovoltaïque microfluidique

Lors de l'écoulement d'électrolytes sur une électrode capacitive, les ions adsorbés sur la surface sont balayés par la contrainte de cisaillement interfaciale. Si ce balayage ionique se produit sur une seule électrode d'un circuit, il induit une polarisation en potentiel et peut ainsi générer un courant électrique. Ce principe a été démontré par nos collaborateurs à NTU (Singapour) dans une cellule hybride ; avec une électrode capacitive et une électrode batterie. Cependant, le mécanisme de balayage ionique n’est pas bien compris, ce qui freine le développement. Le but de cette partie de la thèse était donc de caractériser la réponse électrique en fonction de cisaillement interfacial pour faire progresser la compréhension du balayage ionique et de permettre l'optimisation du système.

Le premier objectif était de reproduire le phénomène de balayage sélectif dans un système microfluidique. Pour ce faire, des canaux microfluidiques sont construits contenant deux électrodes capacitives avec une géométrie qui expose qu’une seule électrode à des vitesses de cisaillement élevées. Des simulations numériques ont été utilisées pour trouver la géométrie optimale du canal entraînant la plus grande anisotropie de cisaillement. La réponse électrochimique a été caractérisée dans les canaux résultants en variant les propriétés de l'électrolyte, les matériaux des électrodes et la vitesse de l'écoulement. Nous avons vérifié la production d'un courant électrique sous écoulement, similaire au balayage ionique macroscopique développé à la NTU.

Les premières démonstrations des mesures de cisaillement dans de tels canaux ont été réalisées avec succès. À l'avenir, nous espérons caractériser complètement la réponse électrochimique en fonction du

cisaillement et utiliser ces informations pour concevoir des systèmes de récupération d'énergie cinétique plus efficaces.

5 Annex

Table of contents of the annex

5.1 Methods

5.1.1 Synthesis of $LaPO_4$:Eu suspensions

Preparation of rhabdophane $LaPO_4$:Eu nanorod suspensions

$LaPO_4$ nanorods, with 5% and 20% Eu^{3+} doping, were prepared in the rhabdophane phase by a solvothermal synthesis method as previously reported[2]. Aqueous precursor solutions of $(NH_4)_2HPO_4$, $La(NO_3)_3{\cdot}6H_20$, $Eu(NO_3)_3{\cdot}H_20$ with 100mM concentration were prepared and cooled down to 0 °C by placing the solutions on ice for 30 minutes. A stoichiometric solution with total volume of 70 mL was prepared and mixed by shaking the container. A milky solution with precipitated seed particles was prepared and transferred to an autoclave to be heated at 160 ℃ for 3 hours. The preferential growth along the c-axis of the crystal generates highly anisotropic rod-shaped nanocrystals. Synthesized rod particles were then separated by centrifugation at 1000 RPM for 1 hour and re-dispersed in 40 mL of acidic water (pH2 adjusted with HNO_3) by vortex mixing until homogeneous. Next, the suspension was dialyzed in pH2 water for two days to remove the remaining ions of the precursors in order to avoid aggregation. To further enhance the colloidal stability, the nanorods are transferred to 3 mL of ethylene glycol (EG) using a rotary evaporator.

Preparation of monazite $LaPO_4$:Eu nanorod suspensions

Monazite phase $LaPO_4$ nanorods with 5% and 20% Eu^{3+} doping were prepared by a hydrothermal microwave synthesis method as previously reported[3]. Aqueous precursor solutions of $(NH_4)_2HPO_4$, $La(NO_3)_3{\cdot}6H_20$, $Eu(NO_3)_3{\cdot}H_20$ with 50mM concentration were prepared as well as 0.01M HNO_3 (pH2 water). A total volume of 22 mL of the precursors were combined in a microwave tube with 20% excess of the phosphate precursor, forming a milky solution of seed particles. The mixture was then heated in a microwave reactor at 160°C for 2 hours with maximum power and stirring, growing highly anisotropic nanocrystals. After cooling down to room temperature, the products were collected by centrifugation at 8000g for 20 minutes. The nanorods were then redispersed in 5mL of pH2 water and mixed by vortex mixer until fully homogeneous. Finally, the suspension was dialyzed for 2 days in pH2 water and transferred to ethylene glycol by distillation using a rotary evaporator.

Determination of volume fraction Φ

The volume fraction Φ_{aq} of the aqueous suspension before the solvent transfer is calculated by measuring the weight of 1 mL before and after drying overnight at 80°C. The final Φ_{EG} is estimated based on Φ_{aq} and the difference in solvent volumes.

Liquid crystalline behavior and particle aggregation

For colloidal suspensions of both rhabdophane and monazite $LaPO_4$:Eu nanorods, we observe liquid crystal (LC) behavior indicated by strong birefringence under alignment. Moreover, the suspensions separate after a few days to weeks, depending on the exact synthesis parameters, such that a dense, aligned nematic phase fills the bottom of the vial with an isotropic phase above (see **Figure 5.1**). A perfect phase separation, observed by a lack of nematic droplets in the nematic phase, usually takes >1 month to observe. For the microfluidic flow experiments, the isotropic phase is diluted to ~0.5-1 vol% and for the LC samples the biphasic sample is mixed thoroughly. This preparation of the LC structures and its behavior will be discussed in more detail in chapter x.

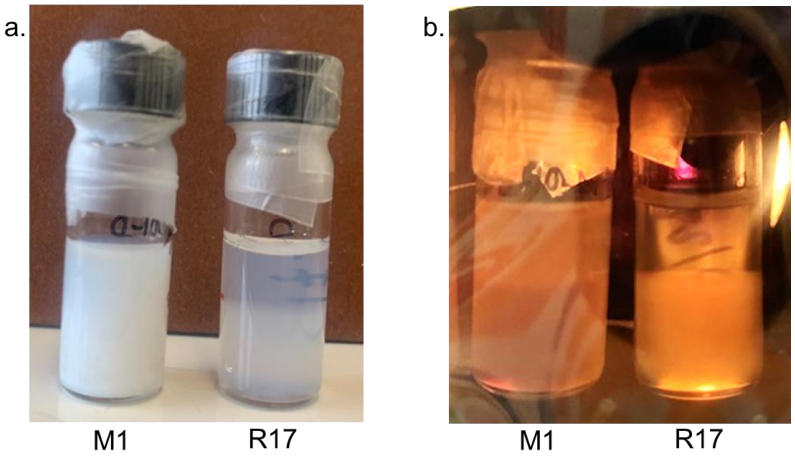

Figure 5.1 Phase separation of colloidal LC suspensions of monazite (M1) and rhabdophane (R17) $LaPO_4$:20%Eu nanorods. **a)** Regular image **b)** image taken between crossed polarizers.

Rhabdophane suspensions are typically quite translucent, with even the dense nematic phase remaining fairly semi-transparent, both for 5% and 20% europium doping. Considering the two vials shown in **Figure 5.1**, we see that the monazite sample (M1) is much less transparent than the rhabdophane one (R17). In fact, all of the monazite samples I synthesized appeared milky, and didn't show good LC behavior (such as the formation of large nematic domains when confining a droplet between coverslips). This indicates the formation of large aggregates, which was confirmed by dynamic light scattering (DLS) and transmission electron microscopy (TEM) shown in the annex (**Figure 5.33**).

However, we had previously demonstrated the preparation of monazite suspensions with excellent colloidal stability and LC behavior[3]. At the time it was unclear why the synthesis always resulted in aggregation, but it may be due to the high doping percentage which could distort the crystal structure due to the difference in size between the Eu^{3+} and La^{3+} ions. As the synthesis and in particular the phase separation requires a significant amount of time, I opted to use previously prepared samples. Flow

experiments using monazite presented in this work were therefore performed using suspensions of 5% doped $LaPO_4$:Eu synthesized by Zijun Wang and Marcello Bonetti.

5.1.2 Experimental conditions for flow experiments

The channel has a 50-by-50 µm cross section and a triangular constriction as shown in **Figure 5.2a**. A suspension with volume fraction ϕ_{frac}~0.9% of nanorods is flowed through the channel at a constant flow rate using a syringe pump. It should be noted that the associated nanorod density is significantly smaller than those in the nematic domains, which lowers the PL intensity and we typically need longer exposure times to maintain a good signal to noise ratio. However, as the nanorods flow through the laser excitation spot, we can safely apply higher laser power (~20mW), which we have observed destroyed the LC systems under prolonged exposure.

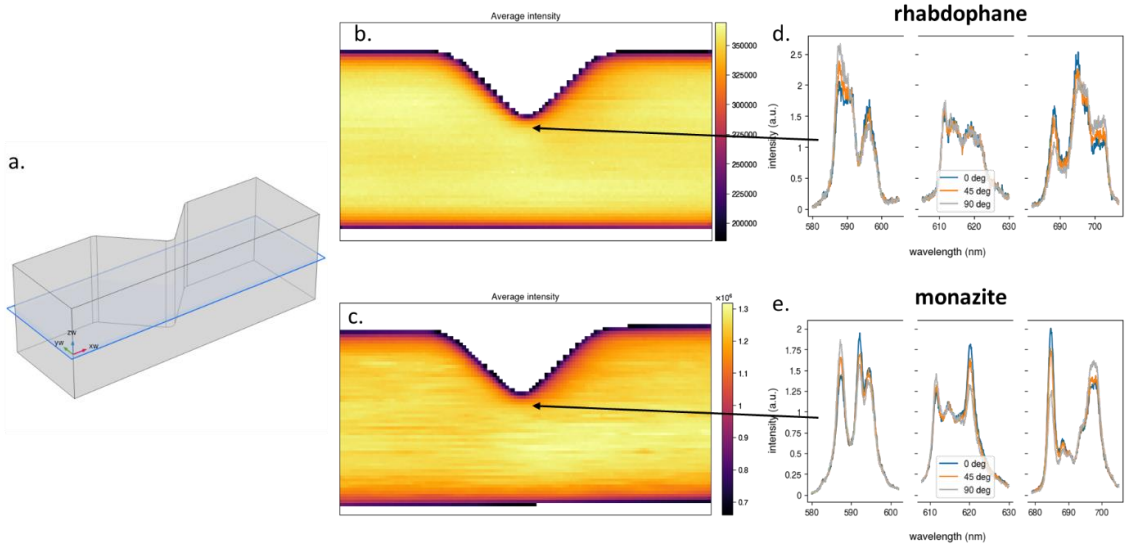

Figure 5.2 a) Geometry of the microfluidic channel and the middle xy-plane. The cross section is 50-by-50 µm. **b-c)** PL intensity map when flowing suspensions of rhabdophane and monazite $LaPO_4$:Eu rods respectively. The exposure time for the monazite sample is 4 times longer, which explains the improved signal to noise ratio. **d-e)** Polarized PL near the tip of the constriction.

For such experiments we therefor prefer to use monazite phase nanorods, which not only have a better DOP, but have a stronger PL emission which improves the signal to noise ratio and lowers the necessary exposure time per position. **Figure 5.2b-c** shows PL intensity maps of rhabdophane and monazite samples with similar volume fractions obtained by scanning at the middle plane with 1 µm step size using 20 mW laser power. To obtain the same degree of alignment, the flow rate for the rhabdophane rods was 100 nL/min whereas 10 nL/min for the monazite rods. This difference in response to the shear originates from the difference in the size and shape or the nanorods, as is discussed in **chapter 4.1.2.**

5.1.3 Preparation of confinement cell

To observe the LC behavior under confinement, we create a confinement cell as illustrated in **Figure 5.3**. A microscope slide and coverslip are cleaned thoroughly using a detergent (100 times diluted), ethanol and distilled water, as impurities may interact with the LC. To create the confinement cell, an opening of roughly 1 cm by 1 cm is cut in a piece of scotch tape with a measured thickness of 60 µm, which is then attached to the microscope slide. A small droplet (3-5 µL) of the LC is placed in the center and the coverslip is placed on top. In the case of biphasic samples, the suspension is first strongly vortexed to remix and homogenize it. The as-prepared cell was sealed with UV glue to preserve the solvent from evaporating. An example of the LC in confinement cell is shown in **Figure 5.3b**. In some cases, the LC is directly sandwiched between the microscope slide and coverslip (without a spacer) and then sealed.

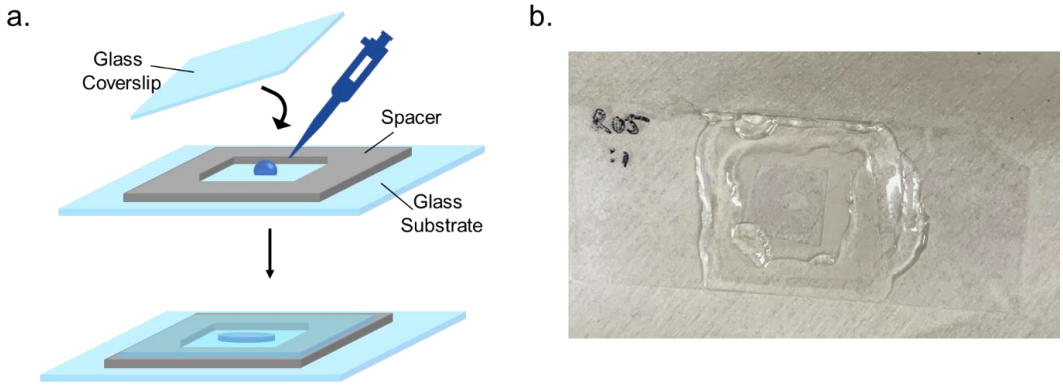

Figure 5.3 a) Illustration of the preparation of confinement cell **b)** Image of a confinement cell consisting of a glass substrate and coverslip, tape (as a spacer) and UV cured glue.

5.1.4 Fabrication of microfluidic channels

Microfluidic channels were prepared using soft lithography method. To create the molds, a curable resin sheet (33 um or 50 um thickness) is attached to a cleaned microscope slide by lamination at 100 °C. It is then covered with a printed film mask and cured using UV lamp. The uncured resin is then removed by etching in an aqueous potassium carbonate bath (2% by mass) for few minutes. Excess etching solution is rinsed off using DI water and the resulting mold is then cured again under the UV lamp. Polydimethylsiloxane (PDMS) is prepared by mixing the pre-polymer and curing agent and degassing under vacuum. It is then poured over the prepared molds and degassed again to remove all air bubbles. The PDMS is then cured by baking at 65 °C overnight. The PDMS channels are peeled from the mold and cleaned together with glass microscope slides using water and ethanol. The channels are then attached to the glass after UV/ozone cleaning at 50°C for 15 minutes. To enhance the PDMS to glass bond, the channels are then baked in an oven at 90 °C overnight.

5.1.5 Preparation of ITO electrodes by lithography

All the electrodes made through lithography used in this work were fabricated by Donghoon Lee, a PhD student in Lee's Nano Energy Laboratory of the Nanyang Technological University, Singapore.

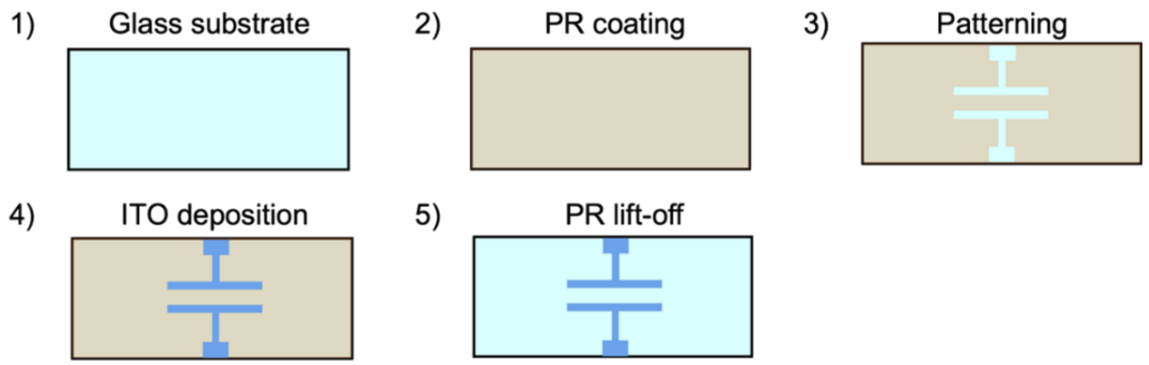

Figure 5.4 Electrode preparation procedure of ITO electrodes. Figure provided by Donghoon Lee.

The electrodes were fabricated using a maskless lithography system (Illuminaid Co., Ltd.). **Figure 5.4** describes the electrode preparation process. A thin glass substrate, compatible with the confocal microscopy setup, is selected and undergoes a sequential cleaning process involving acetone, isopropanol (IPA), and deionized (DI) water. Following cleaning, the substrates are subjected to oxygen plasma treatment to enhance adhesion with the photoresist (PR). A positive PR, AZ5214 (Clariant), is then spin-coated onto the substrates. The desired pattern is defined using 405 nm UV light exposure. To further improve the bonding between the exposed regions and the indium tin oxide (ITO), oxygen plasma treatment was performed. A 100 nm thick layer of ITO was deposited by sputtering. The ITO layer functions both as a current collector and a counter electrode.

5.1.6 COMSOL simulations

Numerical simulations were performed to evaluate different channel geometries for the optimization of the anisotropic shear conditions. The three-dimensional laminar flow (stationary) module of COMSOL was used with the following parameters: fluid material was ethylene glycol, channel height of 33 µm, fully developed flow with flow rate 8e-11 m^3/s (4.8 µl/min) at the inlet, atmospheric pressure at the outlet. All simulations shown are for channels which correspond 300 µm wide, 2500 µm long electrodes with an 80 µm gap.

5.1.7 Flow birefringence measurements

Birefringence measurements can be used to rapidly assess the shear profile in the microfluidic channels under flow. This provides a method for evaluating the quality of the fabricated channels and to confirm

the numerical simulation results. Nanorod suspensions are prepared according to the protocol in section **5.1.1** and the suspension is dialyzed in pure EG for several days. For the flow experiments, the isotropic phase is diluted to 0.8 vol% using pure EG. The suspension is introduced to the channel using a motorized syringe pump at a constant flow rate. The channel is placed on a conventional microscope and viewed between crossed polarizers oriented 45° with respect to the flow direction. Images are captured using a CCD camera after several minutes of flow to ensure a steady state has been reached.

5.1.8 Experimental setup for jet flow experiments

Flow is applied using a motorized pump which connects a plastic syringe to a tube with small nozzle to provide fast jet flow directly on the WE (**Figure 5.5a-b**). Experiments are done with ITO as the WE and the CE is either ITO or PBA thin films deposited on glass. Some experiments are done in a two electrode setup, and some in a three-electrode setup with a standard Ag/AgCl as the RE. The effective surface area of the WE is controlled by masking the excess area with tape, as seen in **Figure 5.5c**. The electrolyte for all experiments is 1 mM KNO_3.

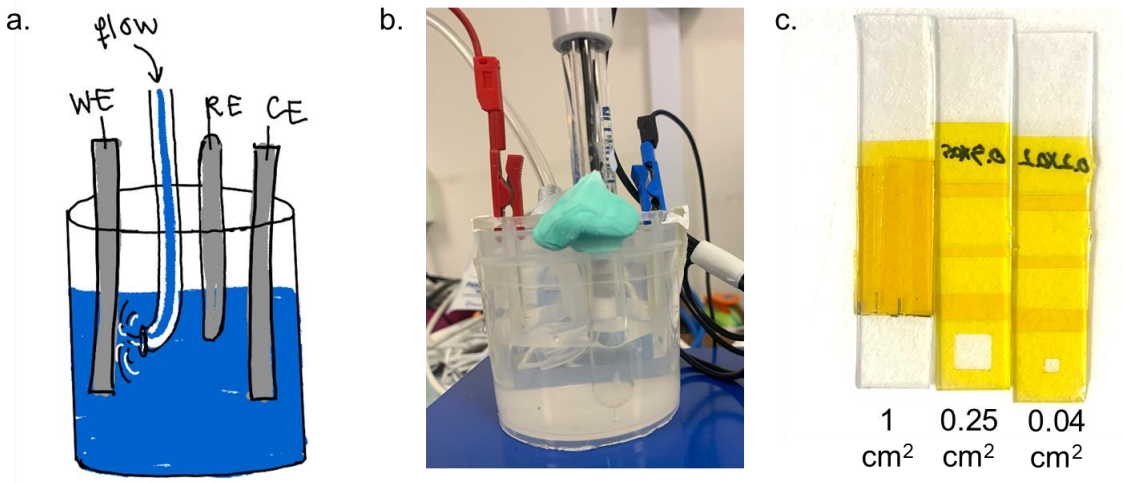

Figure 5.5 Experimental setup for beaker cell experiments. **a)** Schematic illustration of the three-electrode cell with a jet flow on the WE. The flow is initiated by a motorized syringe pump. **b)** image of the experimental setup. **c)** ITO covered glass with controlled exposed surface area using tape, used as the WE.

5.1.9 Fabrication of microscopic PBA electrodes

All the electrodes made through lithography used in this work were fabricated by Donghoon Lee (NTU).

Initially, we did not succeed in making PBA electrodes, as discussed in **section 4.3.2**. However, Donghoon Lee developed a protocol for the preparation of CuHCFe thin films which could be applied both to macroscopic and microscopic electrode geometries. The CuHCFe thin-film was prepared using a two-step deposition method, described in **Figure 5.6a**. For integration with the microfluidic channel, the CuHCFe

was deposited on an ITO electrode acting as current collector and prepared using the protocol in **annex 5.1.5**. The positive photoresist (PR) is reapplied to cover both the ITO and glass surface. Using UV exposure, the PR is cured selectively and after it is removed, a 10 nm layer of copper (Cu) was deposited on one side of the electrode via sputtering. The rest of the PR is then lifted and a droplet of $K_3Fe(CN)_6$ is placed to cover the Cu surface and left at room temperature for ~12 hours, to form the CuHCFe thin film. As seen in **Figure 5.6b**, such a film contains hundreds of CuHCFe cubic nanocrystals.

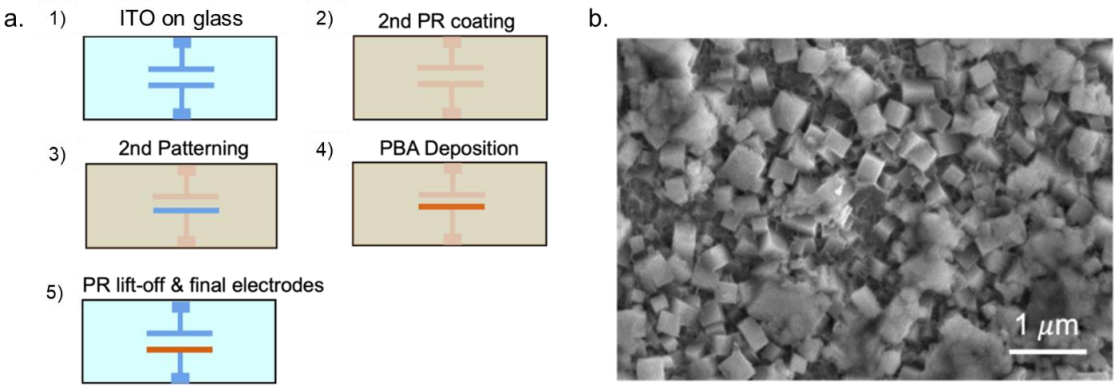

Figure 5.6 Preparation of PBA electrode. **a)** Process of creating PBA electrodes on existing ITO electrodes **b)** SEM image of CuHCFe thin film. Figures provided by Donghoon Lee.

Next, to charge the PBA electrode, it is then connected to the potentiostat as the WE in a three-electrode setup with Ag/AgCl as RE and platinum as the CE. To avoid inhomogeneous deposition, the RE should be symmetric with respect to the CE and WE. A droplet of the electrolyte of choice (in this case 1 mM KNO_3) is placed to cover all electrodes. Cyclic voltammetry is then performed with a scan rate of 10mV/s, seen in **Figure 5.7**. We observe two clear charge and discharge peaks centered at ~0.9 V and ~0.8 V respectively. Several cycles are required until a stable pattern is achieved, as there may be some reactions occurring when first applying the potential. Indeed, additional peaks are observed around 1V and 1.1V which can be attributed to reactions between residual precursors.

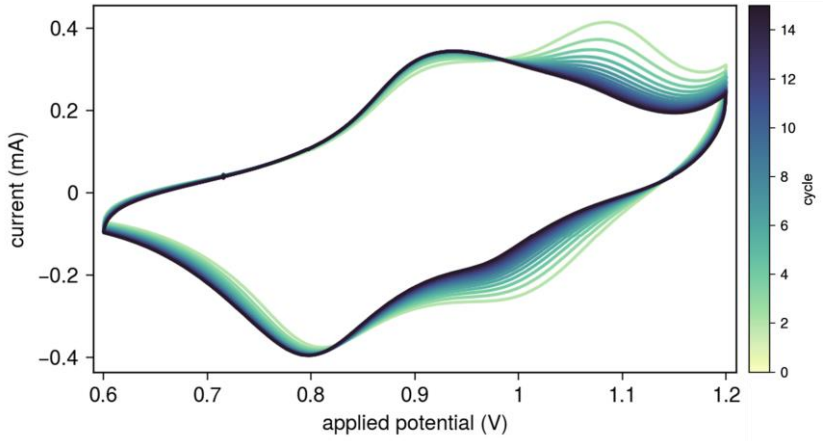

Figure 5.7 Cyclic voltammetry of PBA (CuHCFe) thin film, with Ag/AgCl RE and Pt CE and a scan rate of 10mV/s.

5.2 Extended orientation equations

Coordinate system 2 - (γ, ψ)

Conversion from coordinate system 1 (ϕ, θ)

$$\theta = cos^{-1}(sin\,\gamma \cdot cos\,\psi) \quad \textbf{5.1}$$

$$\phi = sin^{-1}\left(\frac{cos\,\gamma}{\sqrt{1 - sin^2\,\gamma \cdot cos^2\,\psi}}\right) \quad \textbf{5.2}$$

The polarized emission can be found by adapting the expressions for a single particle (**equations 2.1**-**2.2** where θ, ϕ correspond to γ, ψ) by replacing $I_\pi(\lambda)$ and $I_\sigma(\lambda)$ with $I_\parallel(\lambda)$ and $I_\perp(\lambda)$, such that for MD transitions,

$$I_{zx,MD}(\lambda) = I_{\parallel,MD}(\lambda) \cdot sin^2\,\gamma + I_{\perp,MD}(\lambda) \cdot cos^2\,\gamma \quad \textbf{5.3}$$

$$I_{zy,MD}(\lambda) = I_{\parallel,MD}(\lambda) \cdot (cos^2\,\gamma + sin^2\,\gamma \cdot cos^2\,\psi) + I_{\perp,MD}(\lambda) \cdot sin^2\,\gamma \cdot sin^2\,\psi \quad \textbf{5.4}$$

and for ED transitions,

$$I_{zx,ED}(\lambda) = I_{\parallel,ED}(\lambda) \cdot sin^2\,\gamma \cdot sin^2\,\psi + I_{\perp,ED}(\lambda) \cdot (cos^2\,\gamma + sin^2\,\gamma \cdot cos^2\,\psi) \quad \textbf{5.5}$$

$$I_{zy,ED}(\lambda) = I_{\parallel,ED}(\lambda) \cdot cos^2\,\gamma + I_{\perp,ED}(\lambda) \cdot sin^2\,\gamma \quad \textbf{5.6}$$

We set the following definitions:

$$x \equiv \langle cos^2\,\theta_s \rangle, \qquad u \equiv sin^2\,\gamma, \qquad w \equiv cos^2\,\psi \quad \textbf{5.7}$$

Then by substituting the definitions of $I_\parallel, I_\perp$ from **equations 2.22**-**2.25** and rearranging:

or MD transitions,

$$I_{zx,MD}(\lambda) = \frac{I_{\pi,MD}(\lambda)}{2} \cdot \big(2 - 2x - u \cdot (1 - 3x)\big) + \frac{I_{\sigma,MD}(\lambda)}{2} \cdot \big(2x + u \cdot (1 - 3x)\big) \quad \textbf{5.8}$$

$$I_{zy,MD}(\lambda) = \frac{I_{\pi,MD}(\lambda)}{2} \cdot \big(1 + x + u \cdot (1 - 3x) \cdot (1 - w)\big) + \frac{I_{\sigma,MD}(\lambda)}{2} \cdot \big(1 - x - u \cdot (1 - 3x) \cdot (1 - w)\big) \quad \textbf{5.9}$$

and for ED transitions,

$$I_{zx,ED}(\lambda) = \tfrac{I_{\pi,ED}(\lambda)}{2} \cdot (1 - x - u \cdot (1 - 3x) \cdot (1 - w) + \tfrac{I_{\sigma,ED}(\lambda)}{2} \cdot (1 + x + u \cdot (1 - 3x) \cdot (1 - w)) \quad \textbf{5.10}$$

$$I_{zy,ED}(\lambda) = \tfrac{I_{\pi,ED}(\lambda)}{2} \cdot (2x + u \cdot (1 - 3x)) + \tfrac{I_{\sigma,ED}(\lambda)}{2} \cdot (2x - u \cdot (1 - 3x)) \quad \textbf{5.11}$$

Again, each expression depends on $u \cdot (1 - 3x) \equiv \sin^2 \psi \cdot (1 - 3\langle \cos^2 \theta_s \rangle)$, so there is no unique solution for S and ψ.

Assuming the value of x is known, the previous equations can be rearranged in terms of the ratiometric k-values such that, for MD transitions,

$$u = 2 \cdot \frac{\big(A_{MD} - k_{zx,MD} \cdot C_{MD}\big) \cdot (1 - x) + \big(B_{MD} - k_{zx,MD} \cdot D_{MD}\big) \cdot x}{(1 - 3x) \cdot (A_{MD} - B_{MD} - k_{zx,MD} \cdot (C_{MD} - D_{MD}))} \quad \textbf{5.12}$$

$$u \cdot (1 - w) = \frac{\big(A_{MD} - k_{zy,MD} \cdot C_{MD}\big) \cdot (1 + x) + \big(B_{MD} - k_{zy,MD} \cdot D_{MD}\big) \cdot (1 - x)}{(1 - 3x) \cdot (-A_{MD} + B_{MD} + k_{zy,MD} \cdot (C_{MD} - D_{MD}))} \quad \textbf{5.13}$$

and for ED transitions

$$u \cdot (1 - w) = \frac{\big(A_{ED} - k_{zx,ED} \cdot C_{ED}\big) \cdot (1 - x) + \big(B_{ED} - k_{zx,ED} \cdot D_{ED}\big) \cdot (1 + x)}{(1 - 3x) \cdot (A_{ED} - B_{ED} - k_{zx,ED} \cdot (C_{ED} - D_{ED}))} \quad \textbf{5.14}$$

$$u = 2 \cdot \frac{\big(A_{ED} - k_{zy,ED} \cdot C_{ED}\big) \cdot x + \big(B_{ED} - k_{zy,ED} \cdot D_{ED}\big) \cdot (1 - x)}{(1 - 3x) \cdot (-A_{ED} + B_{ED} + k_{zy,ED} \cdot (C_{ED} - D_{ED}))} \quad \textbf{5.15}$$

AUC equations for planar director based on I_{zy}

$$z \cdot (1 - 3x) + x = \frac{A + B - k_{zy,MD} \cdot (C + D)}{-A + B + k_{zy,MD} \cdot (C - D)} \quad \textbf{5.16}$$

$$(1 - z) \cdot (1 - 3x) + x = \frac{A + B - k_{zy,ED} \cdot (C + D)}{A - B - k_{zy,ED} \cdot (C - D)} \quad \textbf{5.17}$$

5.3 Extended methodology studies

5.3.1 Spectroscopic analysis using different spectra for a fixed order parameter

Beyond the spectral fitting of I_{zx}, it can also be performed using the other possible combinations of **equations 2.54**-**2.57**. **Figure 5.8** shows corresponding spectral fitting results for the same 2 positions as discussed prior (**Figure 2.30a**). For all the combinations of just two spectral segments, we observe close

to perfect agreement between the fit and the data. Fitting the both full spectra for simultaneously results in a slightly less accurate curve fit, which may indicate that the two measured spectra are not exactly corresponding to orthogonal polarization component. This becomes more evident when considering the found orientation from each curve fit method.

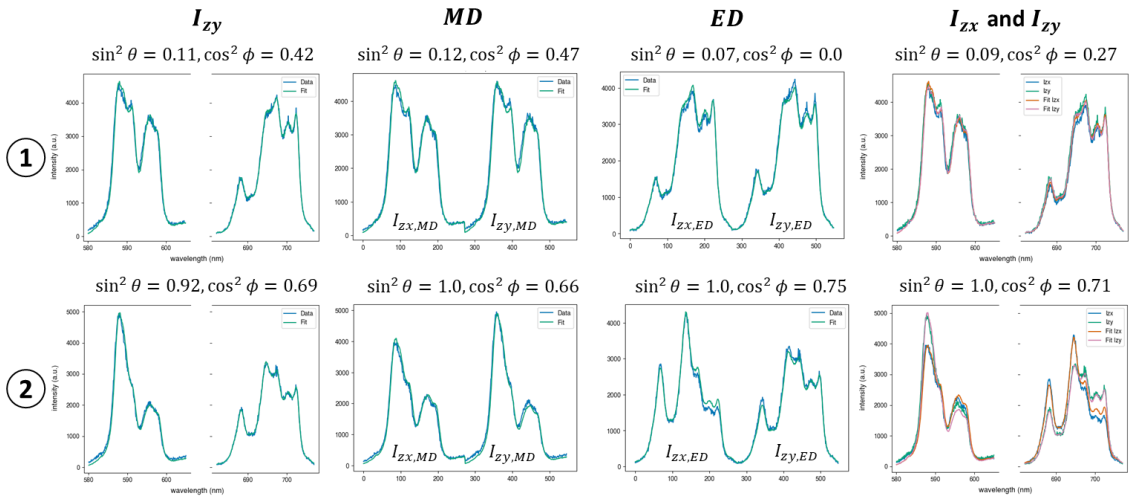

Figure 5.8 Spectral fitting using different combinations of spectra and transitions for positions 1 and 2 as indicated in **Figure 2.30a.**

For the position 1, all methods give very similar results for $\sin^2\theta$ with only a 5° difference between the smallest and largest $|\theta|$ value. It doesn't make much physical sense to compare the azimuthal orientation found, as $\vec{n}$ is close to homeotropic at position 1, indicating that the measured spectra should be independent on ϕ. For position 2, we find quite a large range in the calculated $|\phi|$, ranging from 10° to 30°. From the studies done in nematic reference samples (**Figure 2.27**), we observed that the polarization axis might rotate as much as 5-20° throughout the wavelength domain spanning from 582-702 nm. This means that the effective measured ϕ angle is not the same for the MD and ED transitions. Indeed, we seem to observe this effect if we compare the curve fits performed using only MD or ED transitions as there is a 20° difference in the calculated ϕ angle. This is not only the case at position 2, but all throughout the sample as can be observed in the maps of $|\phi|$ in **Figure 5.9**. Until we solve the origin of this distortion or find a way to correct it, it would therefore be best to use transition peaks which are close together in the spectrum. In principle, the $^5D_0$-$^7F_2$ transition could also be used as the ED, but for rhabdophane the DOP is not sufficiently high. Example spectral fits using this peak shows that although the quality of the fit is good, the values are much less consistent (see annex **Figure 5.39**). However, for monazite samples it should be possible as will be shown in **section 2.4.4**.

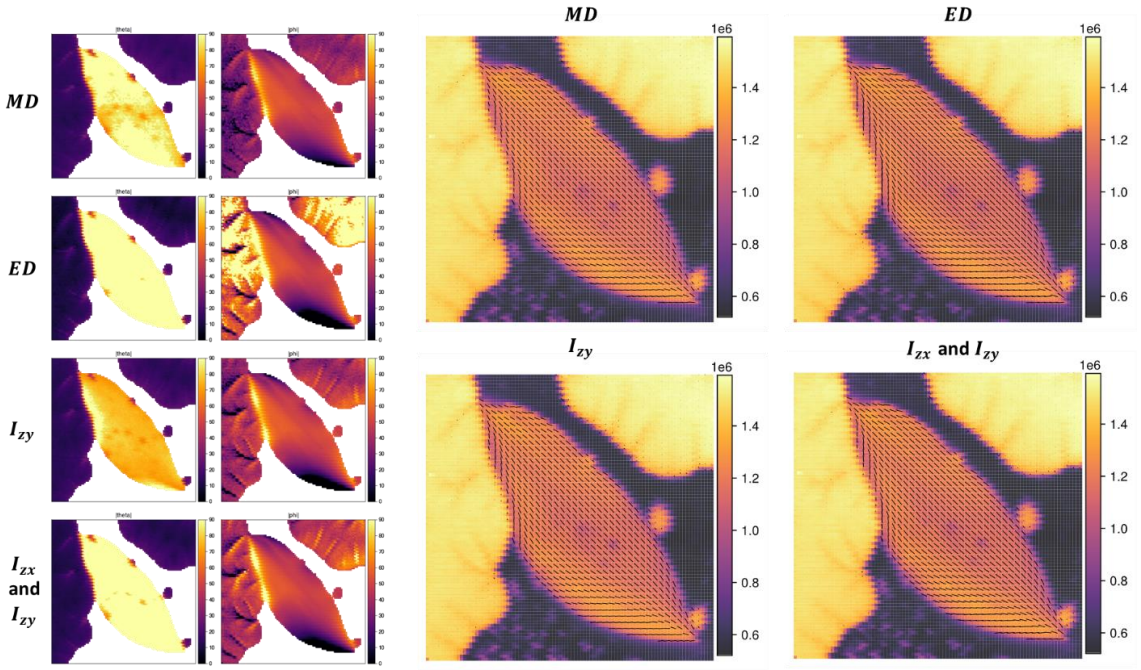

Figure 5.9 Comparison of the orientation found by the different curve fit methods. The first two columns show maps of |θ| and |ϕ| respectively. The large figures show $\vec{n}$ projected onto the observation plane overlaid onto a map of the average PL intensity.

Additionally, we find that all methods except the one using the full I_{zy} spectrum find $\sin^2\theta = 1$ at position 2 (**Figure 5.8**). Fitting only the I_{zy} spectrum results in a value of $|\theta|$ which is ~15° smaller than for the other approaches. We see this effect even more clearly when considering the full maps of $|\theta|$ (**Figure 5.9**).

Choice of subpeak regions for AUC analysis

Previously, subpeaks were separated based on where the I_π and I_σ spectra intersect. However, enlarging the window for integration decreases the associated DOP and thus worsens the sensitivity. We cannot simply consider the peak intensity, as a decreased signal to noise ratio could introduce large error. Instead, a balance between sensitivity and the impact of random noise is achieved by defining the subpeaks based on a minimum normalized intensity difference between the I_π and I_σ. For example, the first subpeaks spans from 586.3-589.5 nm which corresponds to $I_\sigma - I_\pi > 1$. The second MD peak spans 594.38-597.95 nm and the two ED peaks are 687.1-689 nm and 699.5-703.1 nm respectively.

Extended AUC analysis using coordinate system 1

Similar to the equations defined for I_{zx}, we can rearrange the equations for I_{zy} to find

$$y \cdot z = \frac{\left(A_{MD} - k_{zy,MD} \cdot C\right) \cdot (1 + x) + \left(B_{MD} - k_{zy,MD} \cdot D_{MD}\right) \cdot (1 - x)}{(1 - 3x) \cdot \left(-A_{MD} + B_{MD} + k_{zy,MD} \cdot (C_{MD} - D_{MD})\right)} \qquad \textbf{5.18}$$

$$y \cdot (1-z) = \frac{\left(A_{ED} - k_{zy,ED} \cdot C\right) \cdot (1-x) + \left(B_{ED} - k_{zy,ED} \cdot D_{ED}\right) \cdot (1+x)}{(1-3x) \cdot \left(A_{ED} - B_{ED} - k_{zy,ED} \cdot (C_{ED} - D_{ED})\right)} \quad \textbf{5.19}$$

The AUC ratiometry analysis is repeated using all the other possible combinations ($k_{zx,MD}$ and $k_{zy,MD}$, $k_{zx,ED}$ and $k_{zy,ED}$, $k_{zy,ED}$ and $k_{zy,ED}$) as seen in **Figure 5.10,** complementary to **Figure 2.35**. We see similar trends as through the curve fitting analysis. There is a rotation of the value of $|\phi|$ calculated by ED compared to that calculated through the MD k-values (roughly 10-20°). Additionally, $\vec{n}$ is less planar based on the I_{zy} spectrum of MD transition inside the tactoid. This suggests that this is not (only) due to the analysis methodology, but originates in optical distortions of the measurements themselves. Unlike the results of the curve fitting approach, we also observe that using I_{zy} or the ED transition for I_{zy} and I_{zx} results in much higher values for $|\theta|$ inside the flower domain.

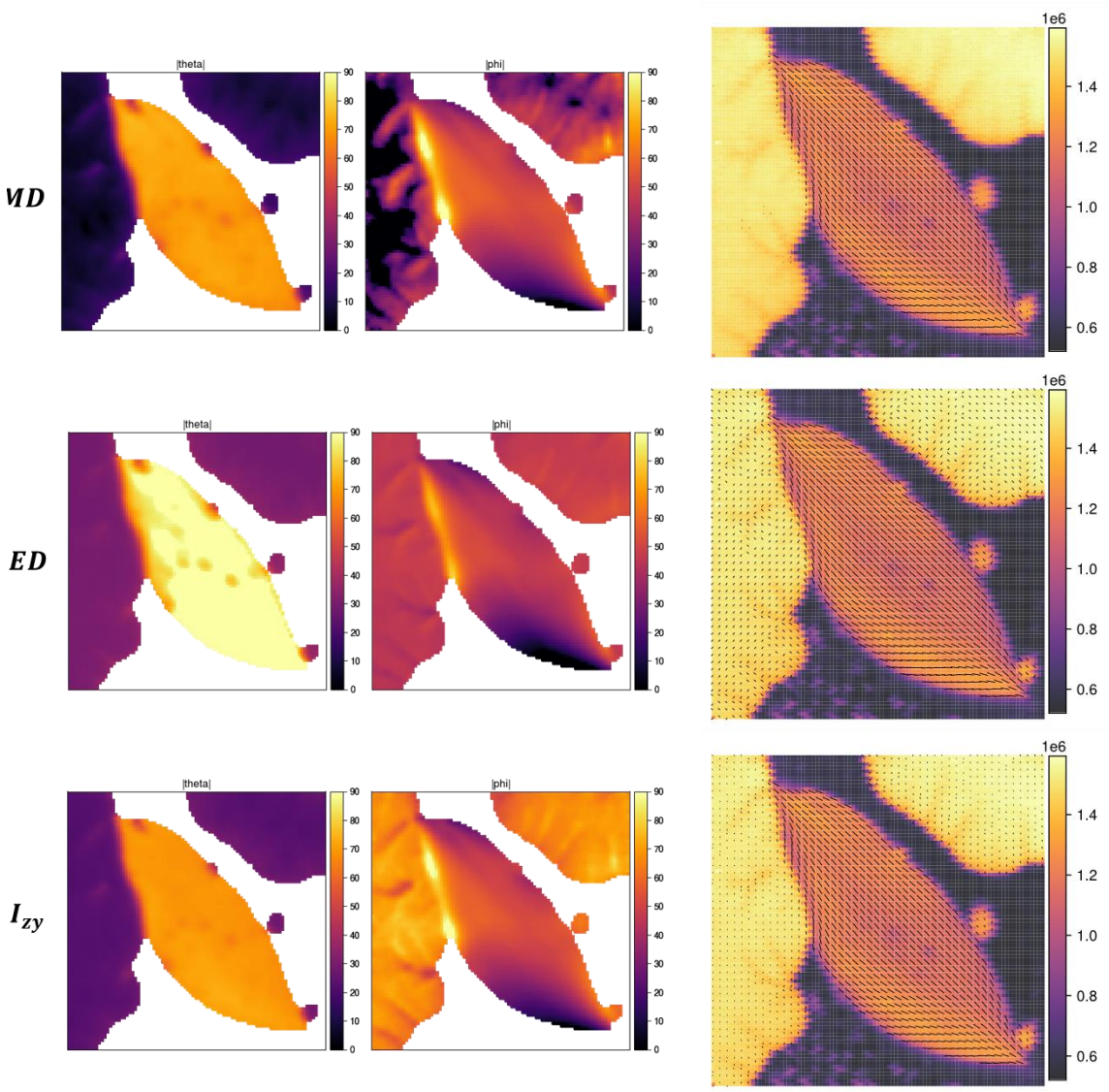

Figure 5.10 Comparison of the orientation found by the AUC approach using different combinations of k-values. The first two columns show maps of |θ| and |ϕ| respectively. The large figures show $\vec{n}$ projected onto the observation plane overlaid onto a map of the average PL intensity.

AUC analysis using coordinate system 2

The analysis can also be performed using expression for the second coordinate system with angles (γ, ψ), found in **annex 5.2**. The value of $u \equiv \sin^2 \gamma$ can be found directly using either $k_{zx,MD}$ or $k_{zy,ED}$ and then $w \equiv \cos^2 \psi$ can be solved for using either $k_{zx,ED}$ or $k_{zy,MD}$. Whereas the expression for $\sin^2 \theta$ depends on two k-values, $\sin^2 \gamma$ can be determined based on only a single k-value. This difference may impact the results, particularly considering the regions where their values saturate to 0 or 1.

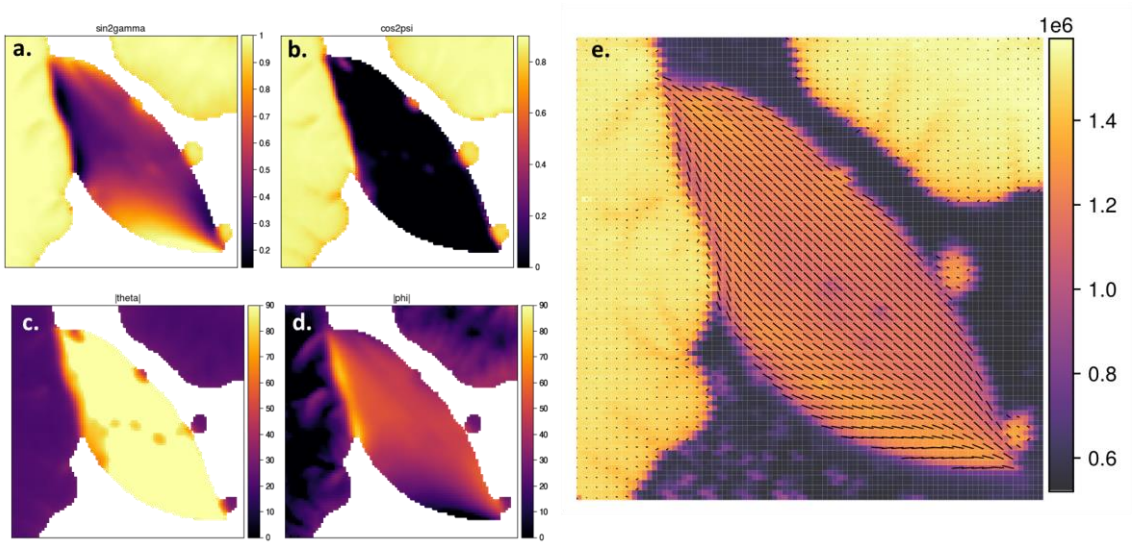

Figure 5.11 Calculated orientation found by AUC analysis using $k_{zx,MD}$ and $k_{zx,ED}$ in the second coordinate system. **a)** $\sin^2\gamma$ and **b)** $\cos^2\psi$. The coordinates are transformed to find absolute angles **c)** $|\theta|$ and **d)** $|\phi|$. **e)** Shows $\vec{n}$ projected onto the xy-plane. The color indicates the average PL intensity.

Figure 5.11a-b, show the values of $\sin^2\gamma$ and $\cos^2\psi$ found using $k_{zx,MD}$ and $k_{zx,ED}$. In this case, both values saturate inside most of the flower domain, and $\cos^2\psi$ saturates in the tactoid. We can then transform the coordinate system using **equation 5.1**-**5.2** and find the resulting maps of $|\theta|$ and $|\phi|$ (**Figure 5.11c-d**). We see only minute differences when comparing to the results obtained using the other coordinate system (**Figure 2.35**). This suggest that the order of computation does not impact the results.

Consistency

For both spectral fitting and AUC ratiometry, we can therefore use four different combinations of $I_{zx,MD}$, $I_{zx,ED}$, $I_{zy,MD}$ and $I_{zy,ED}$to calculate the orientation. **Figure 5.12** shows the mean values of θ, ϕ (top row) comparing all four combinations and their associated standard error (bottom row). This gives an impression to how sensitive each approach is to the polarization dependent distortions in the spectroscopic measurements. Importantly, we notice that the spectral fitting method is better equipped at characterizing the homeotropic domains, as the found value of θ is closer to the expected 0° and the standard error between spectra is much smaller than for the AUC ratiometry.

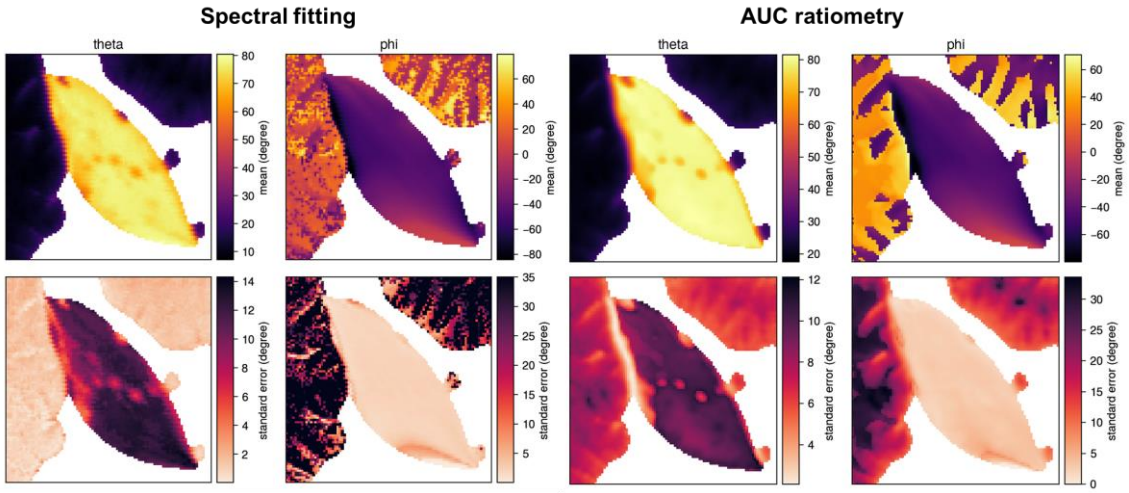

Figure 5.12 The mean and standard error of the calculated orientation θ, ϕ considering the calculated value by analysis of all four possible combinations of $I_{zx,MD}$, $I_{zx,ED}$, $I_{zy,MD}$ and $I_{zy,ED}$

Generally, we therefore see a good agreement between the two approaches in terms of ϕ, but the spectral fitting seems to be more accurate at calculating θ, since we expect to find $\theta \sim 0°$ in the homeotropic and $\theta \sim 80° - 90°$ for the center of the tactoid. Moreover, the spectral fitting approach is expected to be more sensitive as it is considering a wider range of data points and is less sensitive to noise. We therefor expect that the most accurate orientation measurements can be achieved by spectral fitting of the full I_{zx} and I_{zy} spectra simultaneously.

5.3.2 Accuracy of orientation tomography and simulated birefringence

To evaluate the accuracy of the projection of $\vec{n}$, we simulate the birefringence pattern based on the calculated values of ϕ and compare it to the PLM images taken at different polarizer orientations. The theory behind these simulations is discussed in more detail in **section 3.4.3**, but essentially, we can approximate the intensity measured between crossed polarizers as

$$I(\alpha) \propto \sin^2\theta \cdot \sin^2\big(2 \cdot (\phi - \alpha)\big) \qquad \textbf{5.20}$$

where α is the orientation of the crossed polarizers with respect to the x-axis. **Figure 5.13** shows a side by side comparison of the measured and simulated birefringence patterns for the LC sample. Generally, we see the same tendency of a dark fringe appearing at the left side of the tactoid which then moves across it as the polarizers are rotated. There seems to be some discrepancy near the lowest edge of the tactoid, but the rest of the profile looks close to identical for all analyzer angles. As the tactoid has a three-dimensional shape, the fact that the tactoid looks narrower for the simulated results, might indicate that the tomography wasn't performed at the middle height (where it is broadest). Additionally, it is possible that the sample evolved over time, as the PLM images were taken more than a month before the tomographic PL measurements. It should also be noted that this tomographic dataset only considers a

single xy-plane. Because the measurement plane is close to the substrate, θ in the flower domains is close to 0, which may explain why there is almost no birefringence in the simulated flower domains. In **chapter 3.4.3** we show the simulated profiles based on the full volume of a tactoid, which shows the typical birefringence patterns.

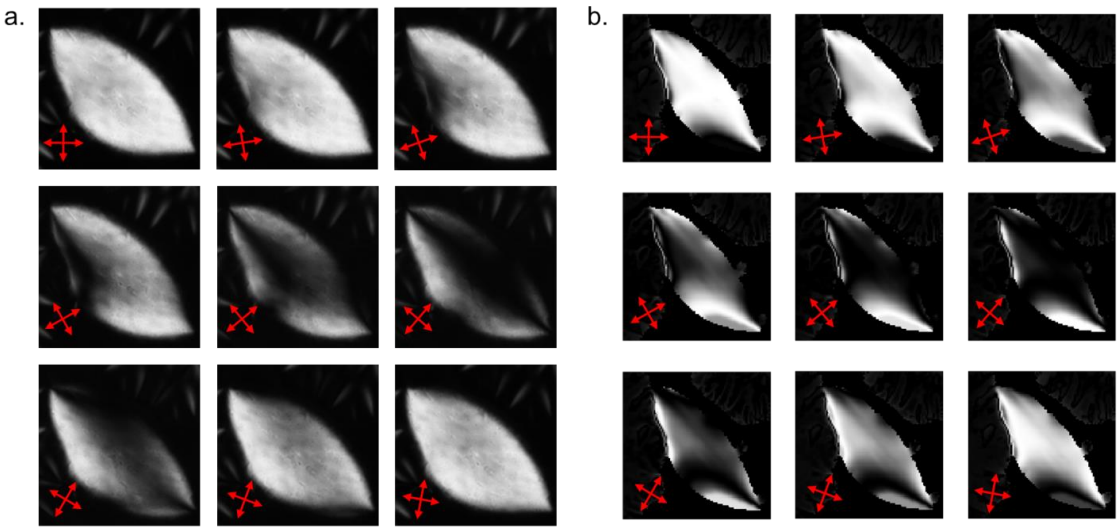

Figure 5.13 a) Measured birefringence pattern using PLM for different orientations of the crossed polarizers (red arrows). **b)** Simulated birefringence patterns based on the orientation found by spectral fitting of I_{zx} and I_{zy}.

In terms of the polar angle, we expect θ to be very close to 90° inside the tactoid as cross sectional views show the tactoid is oriented parallel to the substrate (see annex **Figure 5.42**). Inside the flower domains we expect $\theta \sim 0°$ close to the substrate. The slight discrepancy between the expected and measured values can be partially attributed to the assigned order parameter which may not be correct or uniform. As the expressions for all spectral segments (**equations 2.54-2.57**) depends on $\sin^2\theta \cdot (1 - \langle\cos^2\theta_s\rangle)$, the estimated value of $\langle\cos^2\theta_s\rangle$ directly impacts the value of $\sin^2\theta$ found through the spectral fitting. This in turn affects the value of $\cos^2\phi$. The fact that for some methods $\sin^2\theta$ saturated to 1 inside the tactoid, suggests that the real order parameter may be higher than expected. Additionally, for now we assume that the order parameter is uniform throughout the different nematic domains. This is not physically accurate as a non-uniform gradient of $\vec{n}$ is paired with a non-uniform order parameter distribution. For example, we expect a slightly higher order parameter near the center of the tactoid than near its edges. Moreover, we know that the measurement error is greatest when θ is close to 0° or 90° due to the $\cos^2$ function[26].

5.3.3 Discriminating mirror angle based on the reference

We have previously reported that the mirror angles can be distinguished by comparing the measured k-values to those of the reference spectra[26]. From the reference, we extract values A,B,C,D as defined in

equation 2.58. We can then simulate the k-diagram of a perfectly aligned, planar assembly using the following expression,

$$k_{ref}(\theta_a, \phi) = \frac{A \cdot cos^2(\theta_a - \phi) + B \cdot sin^2(\theta_a - \phi)}{C \cdot cos^2(\theta_a - \phi) + D \cdot sin^2(\theta_a - \phi)} \qquad \textbf{5.21}$$

where θ_a is the orientation of the analyzer with respect to the x-axis and ϕ is the azimuthal orientation of $\vec{n}$. **Figure 5.14** shows such simulated k-diagrams for 3 different orientations, each corresponding to one of the measurement axes for the orientation measurements. The three dumbbells intersect for $|\phi|$ values 22.5° and 67.5°. Considering the difference between two different k-values allows to identify the correct domain of ϕ.

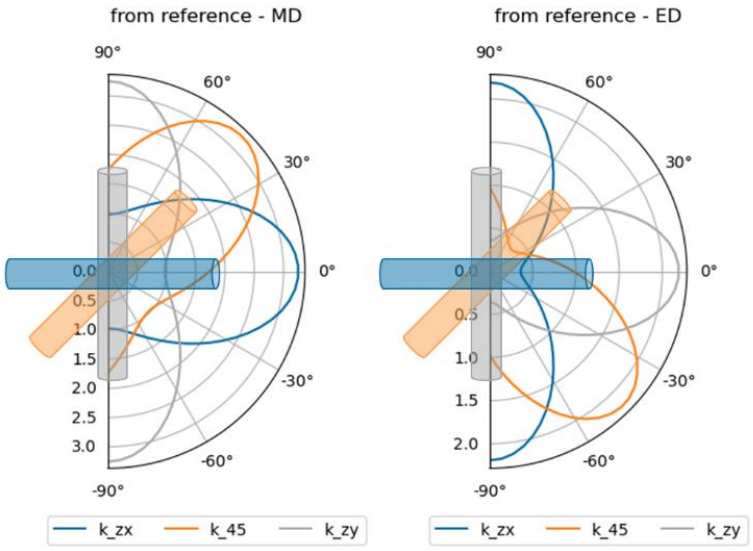

Figure 5.14 Simulated polar diagrams of $\mathrm{k_{MD}}$ and $\mathrm{k_{ED}}$ of perfectly aligned, planar samples with different directors based on the reference.

In principle, it should be possible to distinguish the mirror angle solely based on two spectra, using $I_{z45°}$ and either I_{zx} or I_{zy} using either the MD or ED transition. As an example, the boundary conditions based on I_{zx} and I_{zy} are

For MD transitions

- **0 <|ϕ|<22.5:** if $k_{zx} - k_{45} < k_{ref}(0°, 0°) - k_{ref}(0°, 45°)$ → $\varphi > 0$, otherwise → $\varphi \leq 0$
- **22.5 < |ϕ|< 67.5:** if $k_{45} > k_{zx}$ → $\varphi > 0$, otherwise → $\varphi \leq 0$
- **67.5 < |ϕ|< 90:** if $k_{45} - k_{zx} > k_{ref}(90°, 45°) - k_{ref}(90°, 0°)$ → $\varphi > 0$, otherwise $\varphi \leq 0$

For ED transitions

- **0 <|ϕ|< 22.5:** if $k_{45} - k_{zx} < k_{ref}(0°, 45°) - k_{ref}(0°, 0°)$ → $\varphi > 0$, otherwise $\varphi \leq 0$

- **22.5 < |ϕ|< 67.5:** if $k_{45} < k_{zx}$ → $\varphi > 0$, otherwise $\varphi \leq 0$
- **67.5 < |ϕ|< 90:** if $k_{zx} - k_{45} > k_{ref}(90°, 0°) - k_{ref}(45°, 90°)$→ $\varphi > 0$, otherwise $\varphi \leq 0$

Figure 5.15 shows the resulting mirror angle discrimination based on these boundary conditions for k_{zx} and $k_{z45°}$. For the MD transition, this method seems to work quite well besides some points corresponding to $|\phi| \sim 65° - 70°$. This can be attributed due to the fact that near that angle we expect $k_{zx} \sim k_{z45°}$ which worsens the sensitivity to the boundary condition.

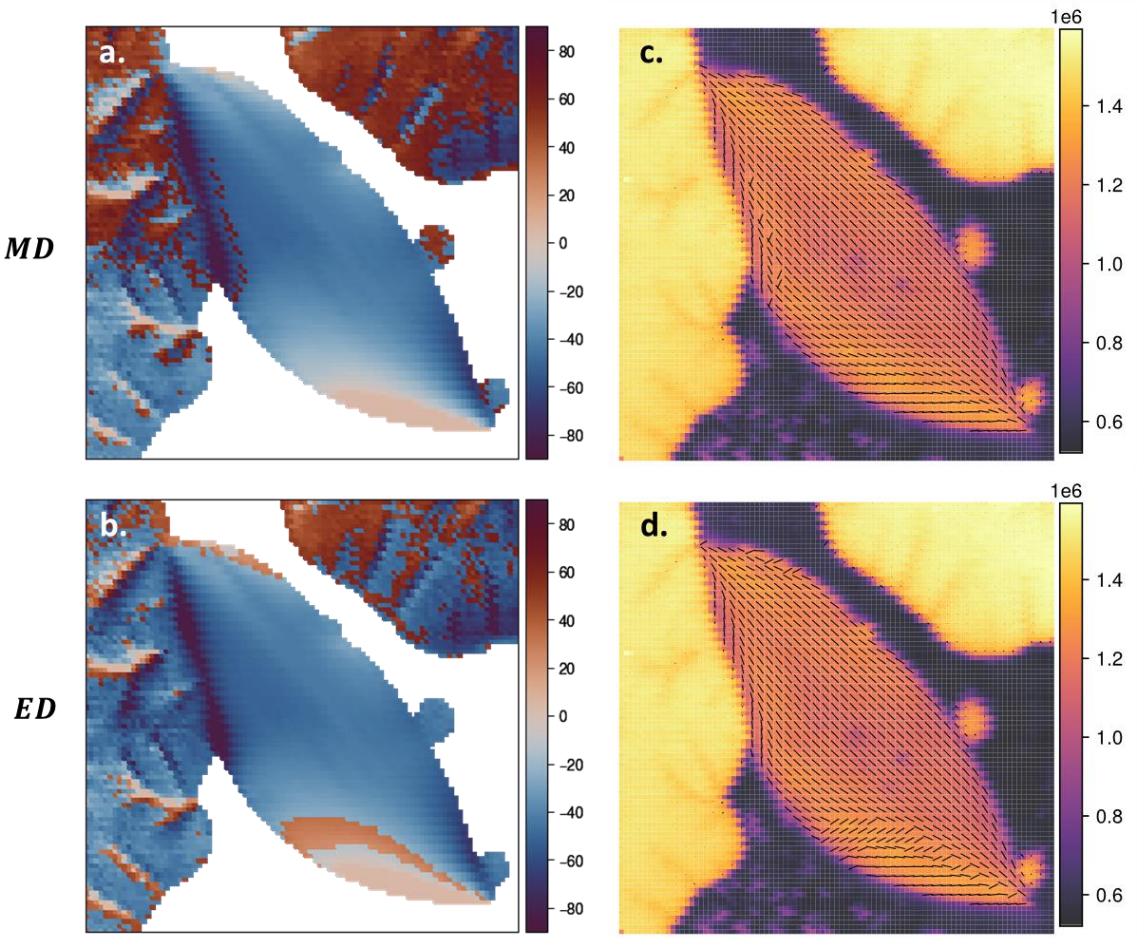

Figure 5.15 Mirror angle elimination based on k_{zx} and $k_{z45°}$. **a-b)** ϕ found based the boundary definitions defined for k-MD or k-ED respectively. |ϕ| was determined through spectral fitting of I_{zx} and I_{zy}. **c-d)** Corresponding $\vec{n}$ projected onto the xy-plane overlaid onto the average PL intensity.

For ED we see a similar boundary condition issue, but at a different position in the tactoid. This difference is most likely due to the fact that k-MD and k-ED may not have orthogonal polar diagrams, due to the wavelength dependent rotation of the polarization axis. Until this issue is fixed, it would therefore be better to consider the MD transition for distinguishing the mirror angles of ϕ.

Although this method doesn't result in a fully continuous director profile due to the discrete nature of the boundary conditions and corresponding domains, it should be possible to fix this issue in the data treatment by enforcing a gradual change in the director. The main advantage of this approach is that it only acquires two spectral measurements. As the spectral fitting and AUC methods for finding $|\phi|$ can also be achieved with two spectra, we could eliminate the third analyzer axis which would significantly decrease the total run time of the acquisition.

5.3.4 Spectral analysis using $^5D_0$-$^7F_2$ as ED transition for planar director

For monazite, the DOP of the $^5D_0$-$^7F_2$ is sufficiently high to perform quantitative orientation analysis. Here, we discuss its accuracy, and compare it to the fitting based on $^5D_0$-$^7F_4$ as demonstrated in the main text (**section 2.4.4**) Even though the quality of the fit using the $^5D_0$-$^7F_2$ transition looks excellent, we find a significant difference between the values calculated through the two different combinations of spectra (**Figure 5.16**), whereas for the $^5D_0$-$^7F_4$ transition the results are more consistent (**Figure 2.38b-c**). This is likely due to the fact that only the final peak of the $^5D_0$-$^7F_2$ transition is strongly polarized, which results in a lowered sensitivity. Even so, the quality of the curve fit seem to be slightly better using $^5D_0$-$^7F_2$. This could be from the fact that the reference spectra didn't have perfectly orthogonal k-diagrams, which means the reference spectrum is more accurate closer to the MD transition.

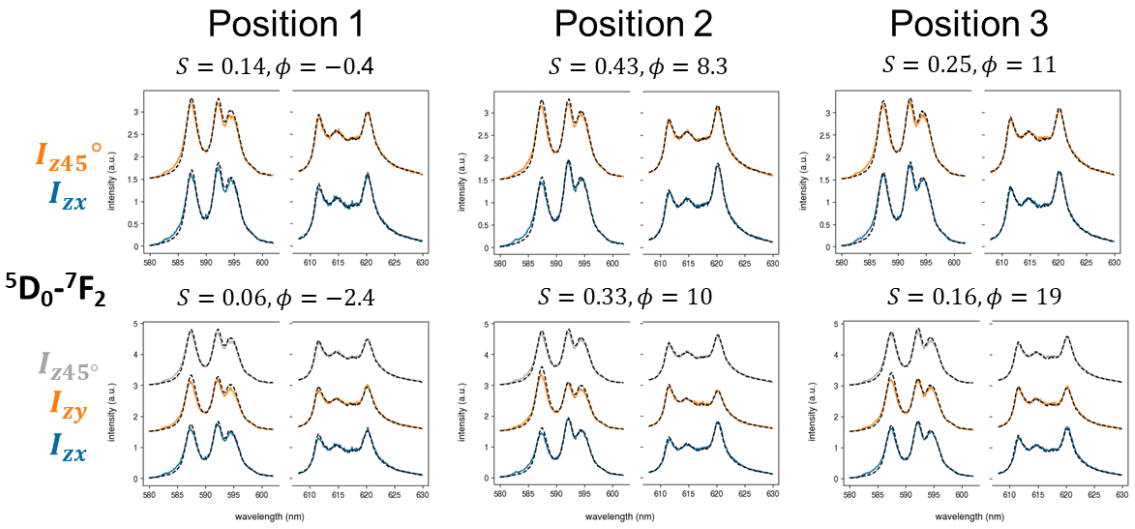

Figure 5.16 Spectral fitting using $^5D_0$-$^7F_2$ as the ED transition, indicated by black dashed lines, at three different positions in the microfluidic channel based on simultaneous fitting of **b)** I_{zx} and $I_{z45°}$ and **c)** I_{zx}, I_{zy} and $I_{z45°}$. The positions match those in **Figure 2.38**

Nonetheless, both can be used to reconstruct the order parameter profile as seen in **Figure 5.17**. When considering I_{zx} and $I_{z45°}$ we see a significant difference in the calculated S depending on which ED transition is used. However, when adding I_{zy} to the fitting, the resulting profiles of S are close to identical, which suggests that spectral fitting with three spectra gives the most consistent results, independent on

which ED transition is used. Finally, the profile seems to be a bit smoother when using $^5D_0$-$^7F_4$. This could be due to the increased DOP, which again enhances the sensitivity making it more consistent.

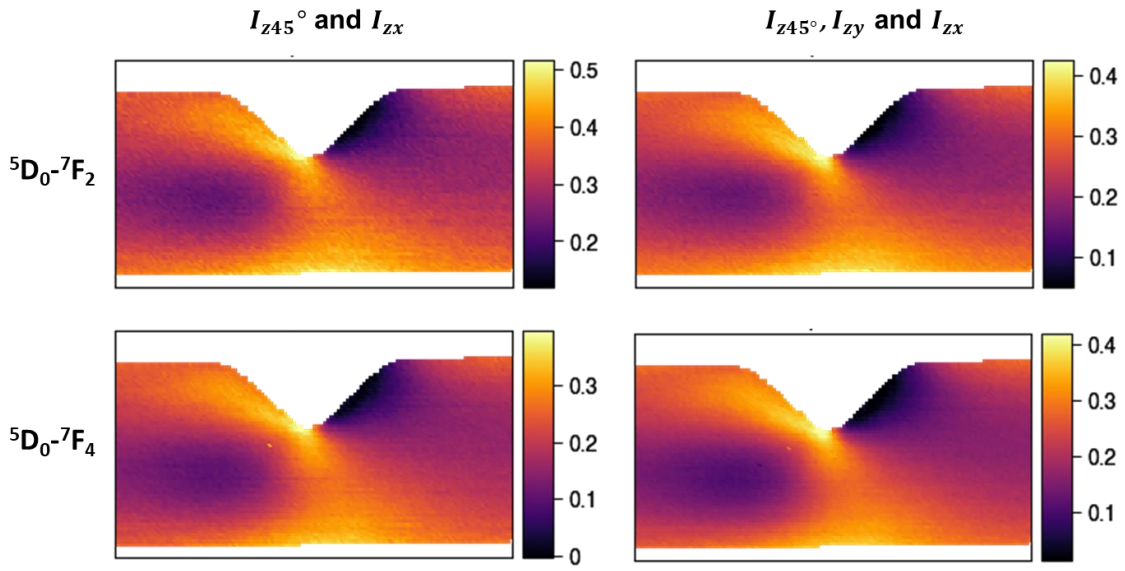

Figure 5.17 Order parameter maps based on the spectral fitting of different combinations of measured spectra, considering either the $^5D_0$-$^7F_2$ or the $^5D_0$-$^7F_4$ transition as the ED transition.

AUC analysis

Analysis based on **equations** using the $^5D_0$-$^7F_2$ as the ED transition yields the maps for S and $\cos^2\phi$ seen in **Figure 5.18**. As expected, the results based on the more polarized $^5D_0$-$^7F_4$ transition (**Figure 2.42**) result in a smoother, more consistent profile of S. The low DOP of the $^5D_0$-$^7F_2$ transition makes it unsuitable for AUC ratiometry, as the difference in k-values is too small, especially for systems with a low value of S.

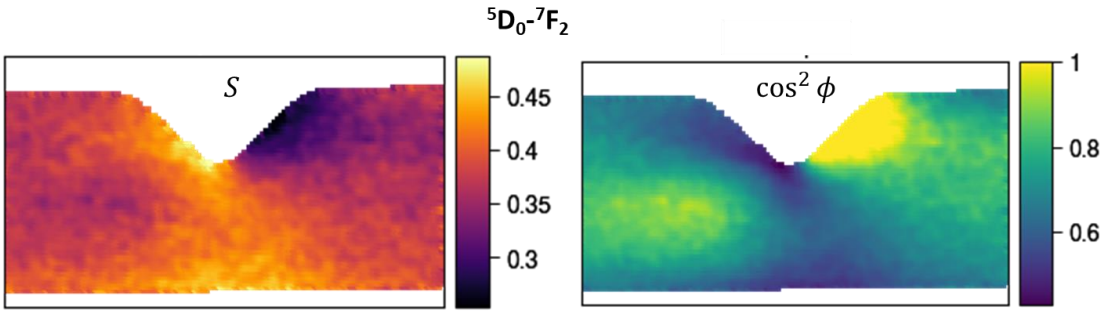

Figure 5.18 Order parameter S and $\cos^2\phi$ maps based on the AUC ratiometry using **equations 2.72-2.73**.

5.3.5 Orientation tomography of flowing rhabdophane suspension

Although the use of the monazite phase is preferential, due to the increased DOP, the rhabdophane phase $LaPO_4$:Eu nanorod suspensions can also be used. In this case, we use nanorods with a higher europium

doping (20%) which increases the signal intensity to be comparable to that of 5% doped monazite rods. For the experiment, the same type of channel with triangular constriction (**Figure 5.2a**) is used, and a suspension of $LaPO_4$:Eu with volume fraction ~0.8% is flowed at a flow rate of 100 nL/min. Due to the difference in rheological properties (discussed in **chapter 4.1.2**), a higher flow rate is required to observe a similar degree of alignment to the monazite suspensions.

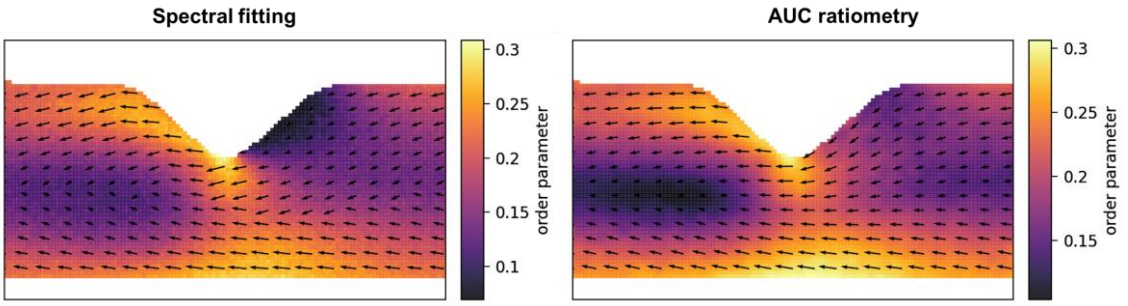

Figure 5.19 Order parameter S and director $\vec{n}$ of a rhabdophane $LaPO_4$:Eu suspension flowing from right to left in a microfluidic channel, found through spectral fitting and AUC ratiometry approach.

We perform the spectral fitting and the AUC ratiometry analysis detailed above. **Figure 5.19** shows a comparison of the two spectral analysis methods. Both give reasonable profiles of S, which match those obtained with the monazite phase. The reference spectra, examples of spectral fits and the k-diagrams needed for AUC ratiometry can be found in the annex **Figure 5.46**-**Figure 5.48**.

5.4 Preliminary results on modeling of the flower structure

The modeling is performed by Prof. Timothy Atherton using the Morpho finite element package.

Using the parameter values obtained from the tactoids (discussed in **section 3.3.2**), we performed simulations of the flower structure, simplifying the geometry to facilitate calculations and using λ=20µm the approximate radius of a single flower domain. The shape optimization problem is posed on a cylindrical geometry, with fixed vertical directors around the edge of the cylinder and on the substrate, reflecting the experimentally observed strong anchoring. The upper surface is initialized as a cone-shaped divot, but remains a free boundary during optimization and moves subject to an overall volume constraint.

Figure 5.20 Simulated flower structure based on a cylindrical geometry.

The resulting optimized structure is displayed in **Figure 5.20** in cross section. Due to the cylindrical geometry, the solution is radially symmetric, and closely resembles the escaped radial structure observed experimentally. The structure is, in effect, complementary to half of a tactoidal solution; the free boundary is deformed to reduce the cost of elastic distortion at the expense of introducing additional surface area while retaining relatively strong planar anchoring. Such a solution is only feasible because the effective surface tension in the colloidal systems is so low; the extrapolation length K/ τ being comparable to the size of the structure. The flower structure has not been previously observed, because thermotropic liquid crystals do not enter this parameter regime, even close to the nematic-smectic transition where spontaneous topography has been previously observed[84].

5.5 Considered configurations for microfluidic channels with incorporated electrodes

In order to replicate the selective ion sweeping in microfluidic systems we considered several different configurations as illustrated in **Figure 5.21**. In principle, the simplest way would be to use two conductive plates and create a space between them to act as a channel (**Figure 5.21a**). This design would result in the maximum surface area for the electrodes, and thus the maximum capacity and sweeping response. In this case, the bottom electrode would have to be transparent and the top electrode non-reflective, otherwise it would not be possible to collect the PL emission of the luminescent probes when measuring the shear. Additionally, the channel should be well sealed, as leaks would cause the delamination of the electrodes. We expected that this would be challenging, especially considering that the height of the channel (and thus the spacer) should be small (<100 μm) to be able to observe significant surface shear under flow. We therefore did not pursue this design.

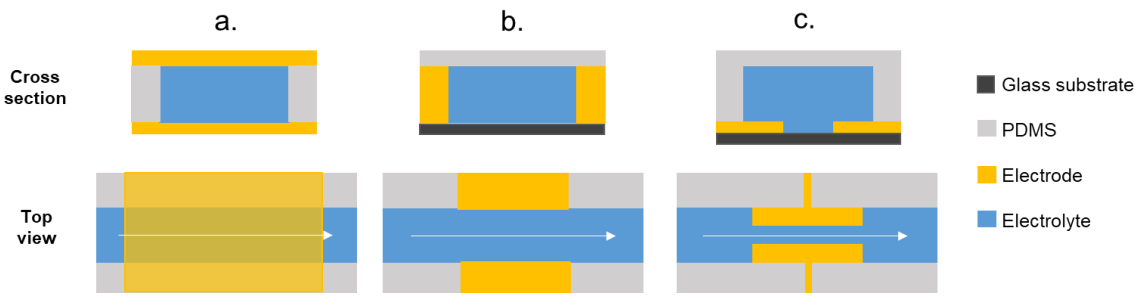

Figure 5.21 Schematic illustration of different ways to incorporate electrodes into a microfluidic channel. **a)** Transparent electrodes forming the top and bottom wall of the channel. **b)** Electrodes incorporated in the channel walls **c)** Planar electrodes patterned on the glass substrate

In terms of the shear measurements, the electrodes would ideally be situated in the side walls of the channel (**Figure 5.21b**), as this would allow us to take advantage of the high lateral resolution, which is 2 times better than the axial resolution of the confocal setup (see **section 2.2.2**). We made some initial trials by trying to inject silver paste into side channels incorporated in the PDMS using the protocol reported in the reference[151], but this didn't yield satisfactory results as the low viscosity made it difficult to control the injection rate and the silver paste always ended up clogging the main channel. Other approaches have been reported, but either don't provide a flat interface or require additional etching steps[152,153].

Finally, we decided to go with planar electrodes which were directly deposited on the glass substrate and simply attach a conventional PDMS channel on top (**Figure 5.21c**). This allowed us to independently optimize the electrode and channel geometries and materials.

5.6 Extended electrochemical characterizations

5.6.1 Flow induced current in straight channel

As discussed in **section 4.4.2**, when flowing electrolyte over two parallel capacitive electrodes (with an applied potential bias between them) in a straight channel a short current peak with the same polarity as the charging current is observed. Increasing the flow rate results in a higher peak current and narrower peak, as seen in **Figure 5.22**. From these I-t plots, the maximum current and peak duration (red dashed lines in **Figure 5.22**) are extracted so a quantitative comparison can be made.

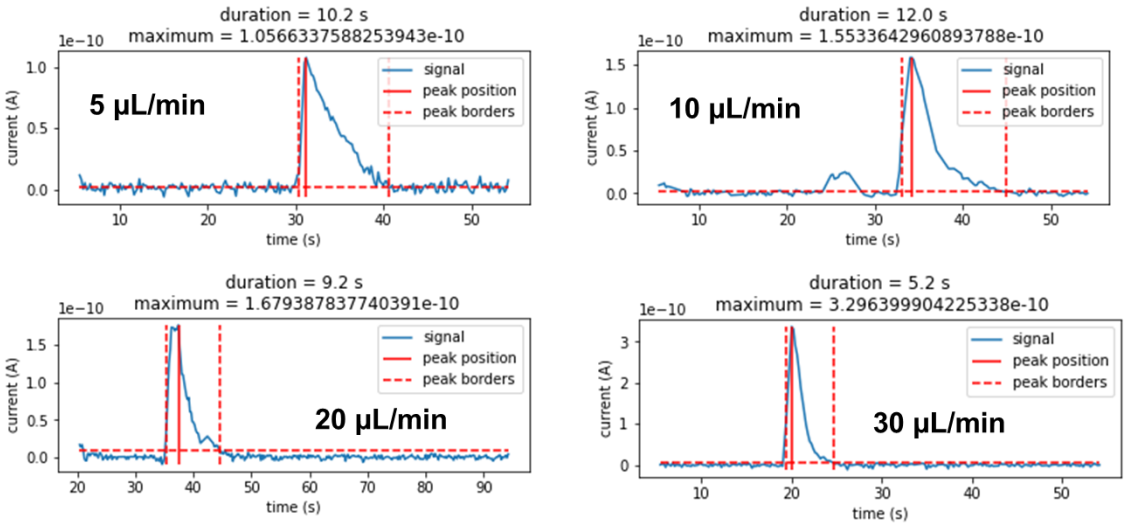

Figure 5.22 Example current peaks for increasing flow rates of 0.1 M $NaNO_3$ solution in a straight channel. A constant baseline current is removed, and the maximum current and peak duration are extracted from the data.

Similar experiments were done with different cations (Li^+, K^+, tetrabutylammonium (TBA^+)), but results were comparable with $NaNO_3$. Again, the peak current is always the same sign as the applied potential and is increasing with the applied flow rate. **Figure 5.23a** shows a comparison of peak current for the different electrolytes, with the error bar representing the standard deviation over 3 to 6 measurements.

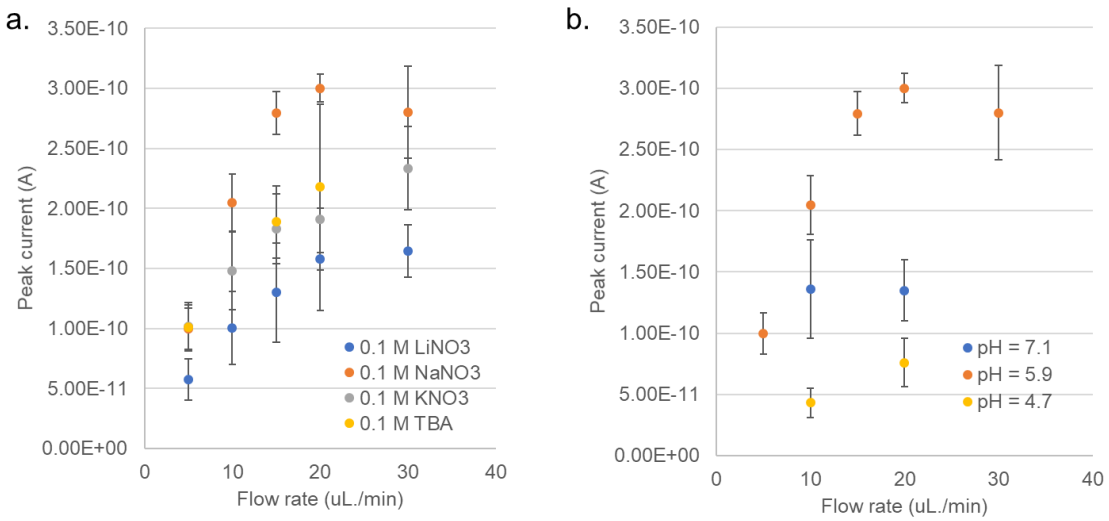

Figure 5.23 Impact of flow rate and electrolyte on the current peak in a straight channel. All electrolytes have a concentration of 0.1M. **a)** Peak current of $LiNO_3$, $NaNO_3$, KNO_3 and tetrabutylammonium (TBA) nitrate and for **b)** $NaNO_3$ at different values of the pH. The error bars represent the standard deviation over 3-5 measurements.

There is a slight difference in the current based on the electrolyte, with $LiNO_3$ giving the lowest current and $NaNO_3$ the highest. Initially, the pH was not controlled, and this may influence the kinetics of the system even more than the species used. Indeed, adjusting the pH of the $NaNO_3$ solution (using NaOH and

HNO_3) caused similar changes to the current, as seen in **Figure 5.23b**. There seems to be an optimal pH, around 6, where the response is strongest. Considering the pH of the different electrolytes, the pH seems to be the dominating factor. The measured pH of both TBA-NO_3 and KNO_3 was 6.0, which may explain why they provide virtually the same datapoints in **Figure 5.23a**, despite the difference in hydrodynamic radii. The lower current observed when using $LiNO_3$ may also simply be attributed to its pH of 5.5.

5.6.2 Current response in anisotropic channel for various flow rates under applied potential

Experiments were done using 0.1 M $NaNO_3$ (pH 6) as the electrolyte on the long electrodes in the channel shown in **Figure 4.25c**, according to the following procedure. First, a potential bias of +0.5V was applied for 5.5 minutes without any flow, such that the current reached zero. A constant flow rate was then applied for 15 seconds followed by another 2 minutes of no flow. The procedure was then repeated using -0.5V. For each flow rate, experiments were repeated 3 times per potential. **Figure 5.24a** shows examples of the observed current response during the flow (highlighted in blue) for both a positive and negative bias.

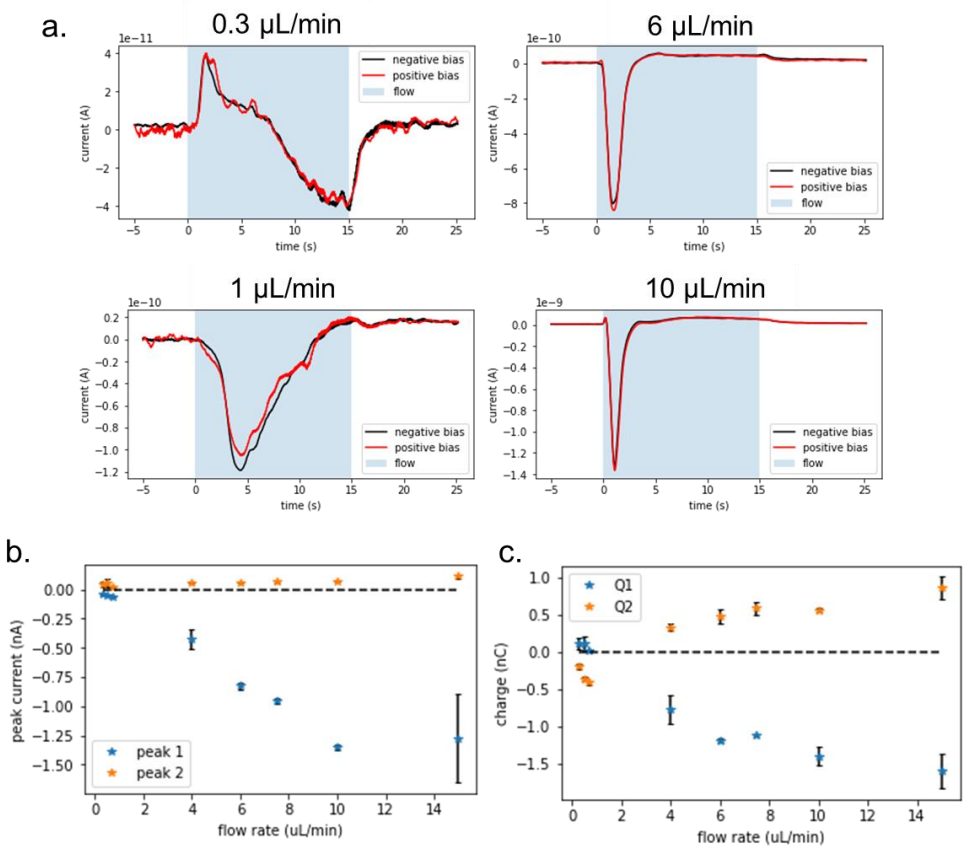

Figure 5.24 Electrochemical response to 15 second flow pulse over the CE in anisotropic channel (geometry of **Figure 4.25c)** using a ±0.5V potential bias. **a)** Current response using 0.1M $NaNO_3$ at different flow rates averaged over three trials while applying a +0.5 V (red) and -0.5 V (black) bias. **b)** Peak current and **c)** total charge (integrated current) for the first major peak (blue) and the second peak (orange) under flow.

For low flow rates (< 1µL/min) the initial current peak is positive followed by a negative peak, but as the flow rate is increased the first peak becomes increasingly negative and the second peak more positive (**Figure 5.24a**). To better understand the flow dependency, we plot the peak current and total charge, found by integrating the current, for the first and second peak observed as a function of the flow rate (**Figure 5.24b-c**). The peak current increases with the flow rate but is much higher for the negative peak. The integrated current (charge) corresponding to each peak seem to be comparable and increase with the flow rate (**Figure 5.24c**).

If the measured charge is related to the initial charge adsorbed to the capacitive electrode, we expect to see a limit to the total charge measured. At 0.5V, there should initially be a charge of 27 nC in the EDL of the electrode, based on a capacitance of 54.4 nF (obtained from the voltammogram in annex **Figure 5.53**). The maximum total charge is ~-1.6 nC (**Figure 5.24c**), which corresponds to around 6% of the charge in the EDL. However, as the charge increases with flow rate but doesn't saturate, it is possible that the flow rate or duration was not sufficiently high yet to remove all charges (**Figure 5.24c**).

5.7 Shear measurement in energy harvesting channel

After establishing the calibration curve, we can now use the nanorods to measure the shear rate $\dot{\gamma}$ in any unknown system. As the goal of this project was to perform such measurements inside the ion sweeping device, we need to confirm that it is possible to do close to/through the ITO electrodes. To validate this, we use simple straight channel with embedded ITO electrodes illustrated in **Figure 5.27**. The channel has a rectangular cross section with a width of 800 µm to accommodate the electrodes which are 300 µm wide each and spaced roughly 50 µm apart. To achieve sufficiently high shear stresses without having to use a large volume of nanorod suspension, the height of the channel is limited to 33 µm. In this section, we will first consider the impact of the ITO layer on the measured PL signal and then perform tomographic mapping of the shear. All experiments were performed using a suspension of monazite phase, 5% doped $LaPO_4$:Eu nanorods in EG.

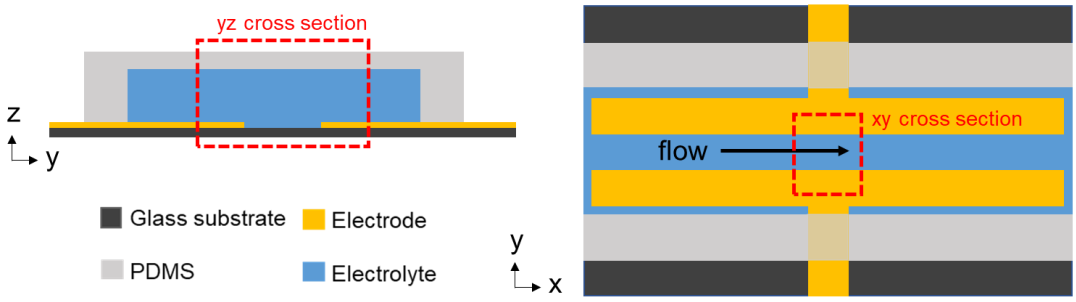

Figure 5.25 Schematic illustration of microfluidic channel with planar electrodes used for optical measurements, showing the yz cross section and xy top view. The rectangular cross section is 33 µm by 800 µm. The electrodes are 300 µm wide and 3mm long each.

Optical measurements through ITO

To investigate the effect of the ITO electrodes on the measured PL intensity and polarization, optical measurements using the confocal microscopy setup were performed in the straight channel with incorporated electrodes filled with a monazite phase $LaPO_4$:Eu suspension. First, emission spectra were collected without any flow, both above the ITO electrodes and in between the gap (without ITO covering the glass), as seen in **Figure 5.26a**. We only see a small (~10%) drop in intensity when comparing the emission collected with and without the additional ITO layer. The APD image (of the PL intensity) of a yz-cross section clearly shows this effect as the ITO casts a shadow throughout the depth of the channel. Additionally, the two electrodes don't seem to have exactly the same thickness, as a larger dark region is observed near the substrate on the left electrode seen in **Figure 5.26b**. Nonetheless, enough of the signal intensity is maintained to clearly reconstruct the top channel wall.

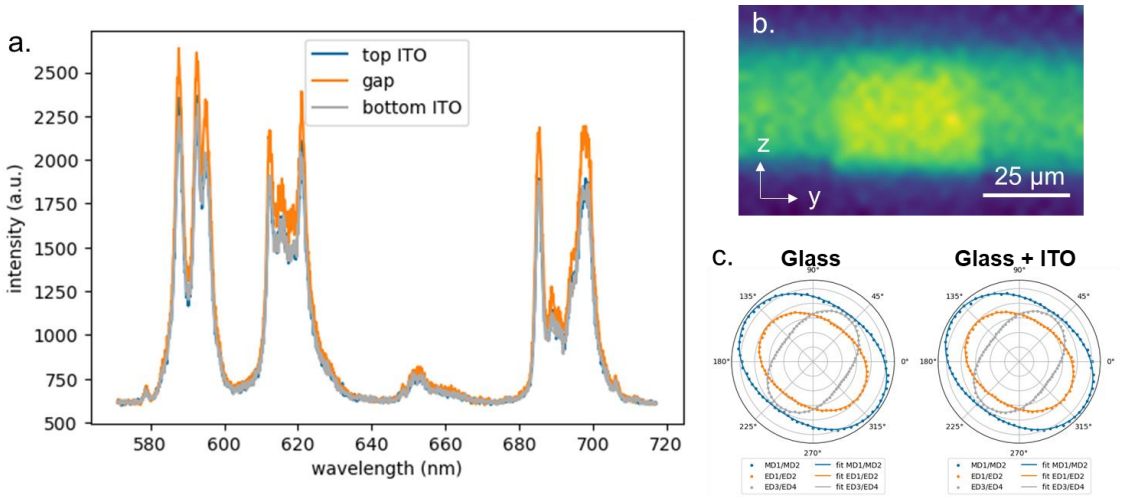

Figure 5.26 a) PL emission collected through the ITO electrodes (blue and grey) and in a region without ITO (orange). **b)** APD image of the PL intensity measured at the yz cross section indicated in **Figure 5.25 c)** Polar diagrams for the k-values of each transition measured through the electrodes or in the gap, matching the spectra found in the annex (**Figure 5.58**).

Additionally, to see if the ITO impacts the measured polarization dependency, we collect emission spectra with the waveplate rotating from 0° to 180° both above the ITO and bare glass whilst flowing the suspension at 200 nL/min (**Figure 5.58**). We then plot the k-values (ratio between the two major peaks) for each transition, seen in **Figure 5.26c**, and find virtually identical polar diagrams. The presence of the ITO therefore does not inhibit or distort the spectral measurement and we should be able to perform *in situ* shear measurements above the ITO electrode surface.

Shear tomography

To see if the presence of the ITO layer impacts the quantitative value of the orientation factor obtained by the spectral analysis, we perform shear tomography in the same channel. First, let's consider the xy-cross section (indicated by the red, dashed box in the right panel of **Figure 5.25**) while flowing the monazite suspension at 200 nL/min. As the ITO layers are very thin and the channel is much wider than it is high, we should expect a uniform distribution of f throughout the whole xy-plane measured. There is a significant difference in the values of f calculated through the spectral fitting or area under the curve (AUC) approach, as seen by **Figure 5.27b-c**. The spectral fitting produces a more uniform f profile than the AUC. The reason for this seems to be the dependency of the AUC analysis on the total PL intensity, as seen in **Figure 5.27d**. For now, it is unclear why the intensity seems to so strongly influence the result of the AUC analysis, and we will therefor only consider the spectral fitting approach for this specific application.

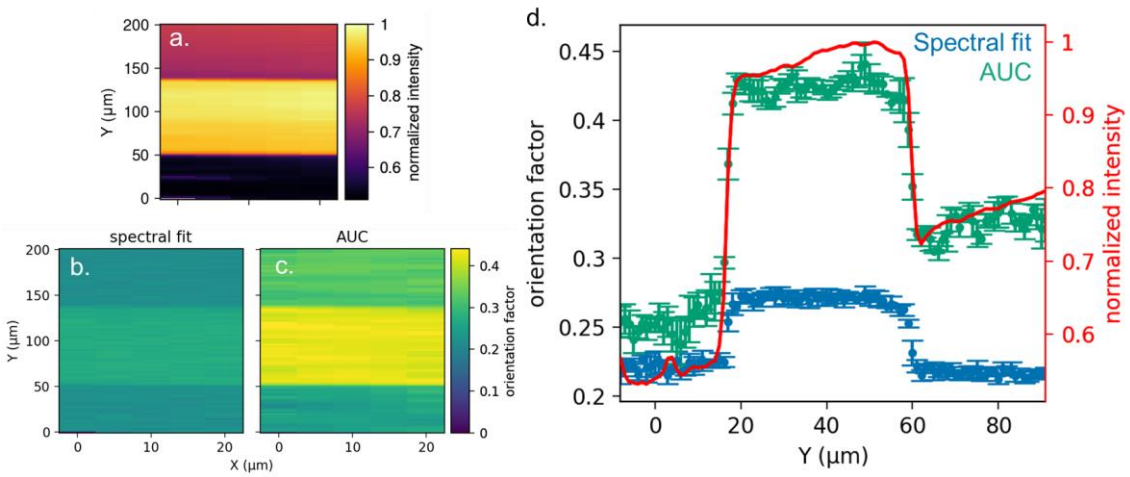

Figure 5.27 Tomographic measurements at the middle height xy-cross section for a flow rate of 200 nL/min. **a)** Normalized PL intensity **b-c)** Orientation factor f calculated from spectral fitting and area under the curve analysis (AUC) respectively. **d)** f along the y-direction. The red line indicates the normalized intensity.

Next, we consider the z-dependency of f and investigate the impact of the ITO layer on the measurements close to its interface. **Figure 5.28** shows f throughout the depth of the channel, both above the ITO and above the center of the gap without ITO, for two different flow rates. The error bars represent the standard deviation based on the measurements from various x-positions. The measurement in the gap gives a more symmetric profile, whereas f is lower far from the ITO surface. Increasing the flow rate seems to decrease this disparity, which suggests that it may be due to a physical difference in flow conditions rather than an optical distortion caused by the ITO layer. This is especially possible as the channel is extremely wide, making it likely that the top wall of the channel is slightly curved, such that the height is lower in the gap than above the electrodes. For the lower half of the channel (near the substrate), the measured f is virtually identical for both positions. This means that the ITO does not inhibit or distort shear measurements close to its interface.

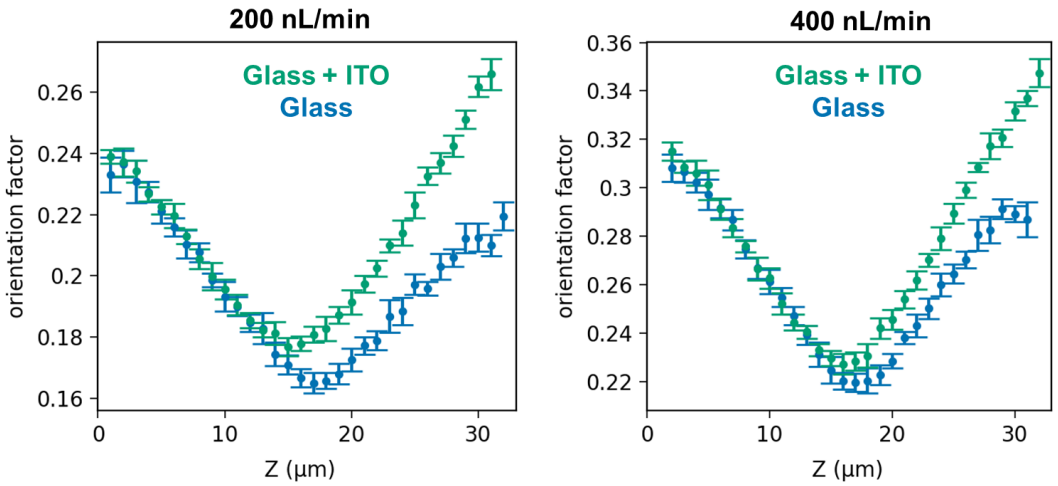

Figure 5.28 Orientation factor f along the depth of the channel at different x,y positions with and without ITO.

5.8 Additional figures

5.8.1 Chapter 2

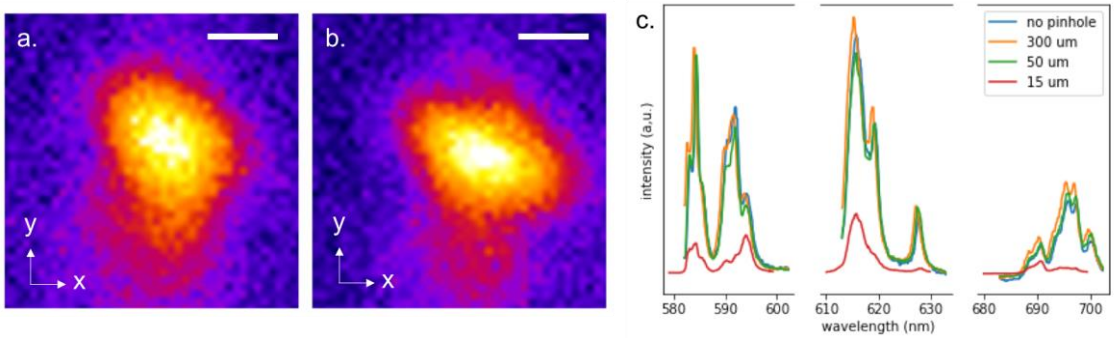

Figure 5.29 Signal intensity loss as a function of pinhole size. **a-b)** PL intensity image of a $NaYF_4$:Eu nanorod using a 300 and 50 µm pinhole respectively. The scale bar corresponds to 1µm. **c)** Emission spectra collected with different pinhole sizes. Note that the spectrum taken with 15 µm pinhole was obtained with a different analyzer angle, hence why the line shape looks different. Figures from M2 internship report.

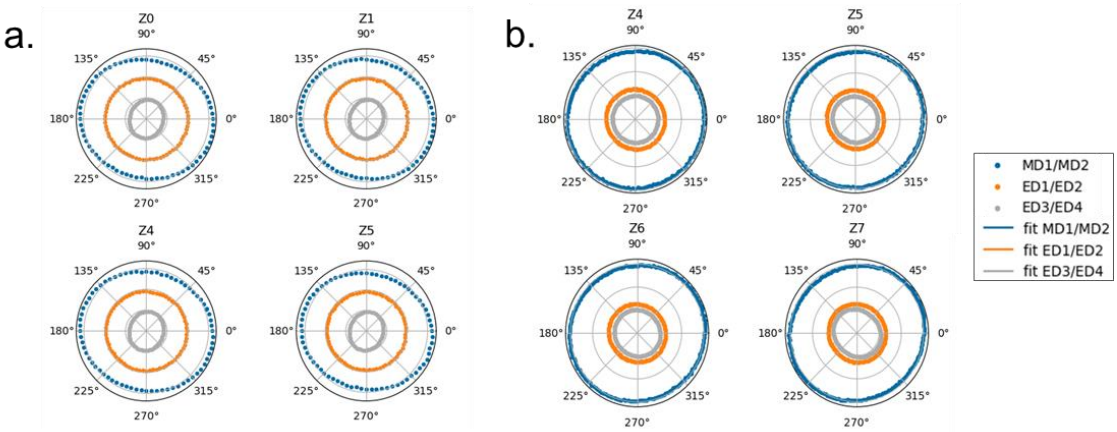

Figure 5.30 Polar diagrams of the ratio between the integrated intensity of the two main peaks of each transition at different depths (spaced by 5 µm) in the sample. The analyzer is parallel to the x-axis when $\theta \sim 48°$. For **a)** diluted isotropic droplet and **b)** the isotropic phase in a phase separated sealed cell, with a nematic phase spanning the substrate surface.

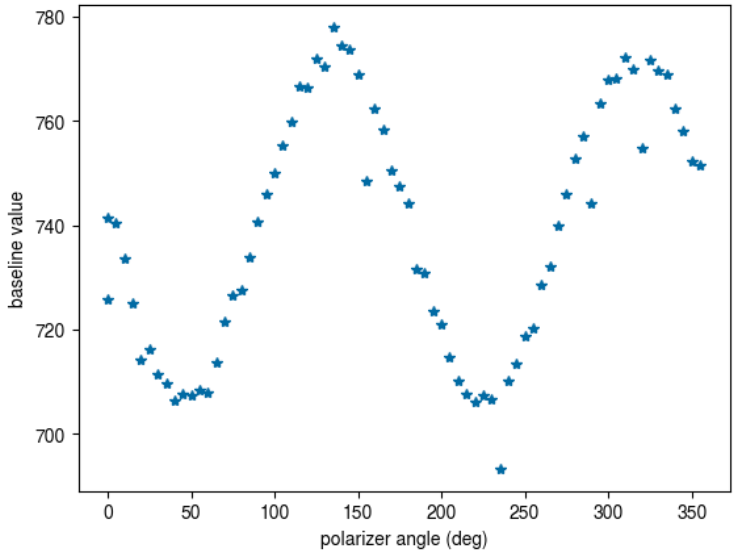

Figure 5.31 Variation of the baseline of collected PL from a nematic $LaPO_4$:Eu domain as a function of the analyzer angle.

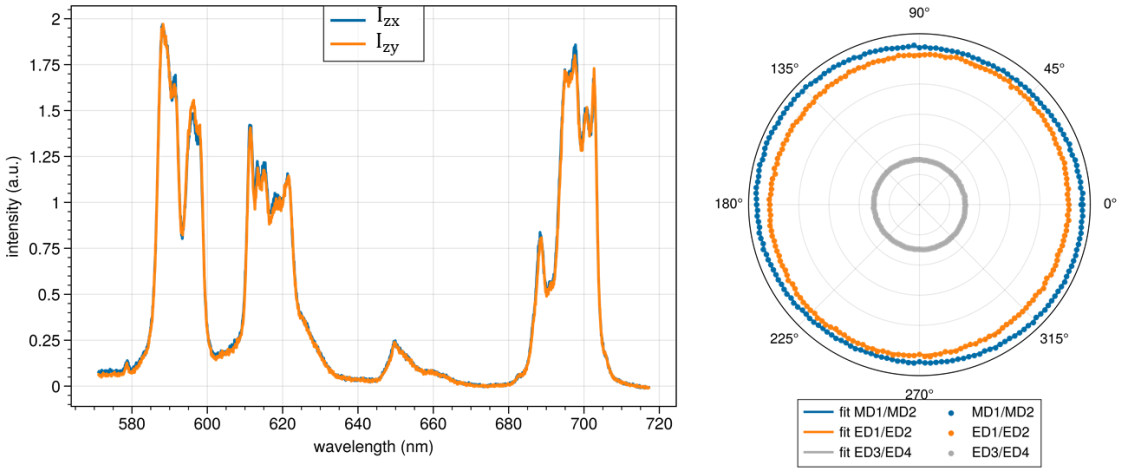

Figure 5.32 Polarized PL homeotropically aligned nematic phase of rhabdophane $LaPO_4$:Eu LC

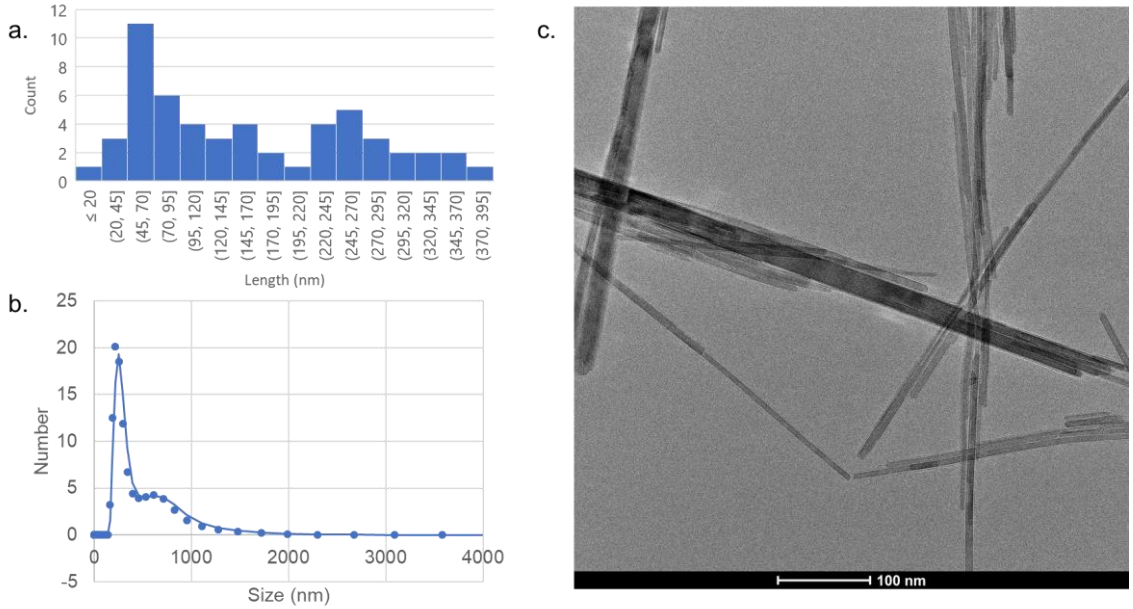

Figure 5.33 Size and aggregation of 20% europium doped monazite $LaPO_4$:Eu. **a)** Length distribution measured by TEM, counting individual rods within the aggregates. **b)** Length distribution found by dynamic light scattering (DLS). **c)** TEM image showing elongated aggregates.

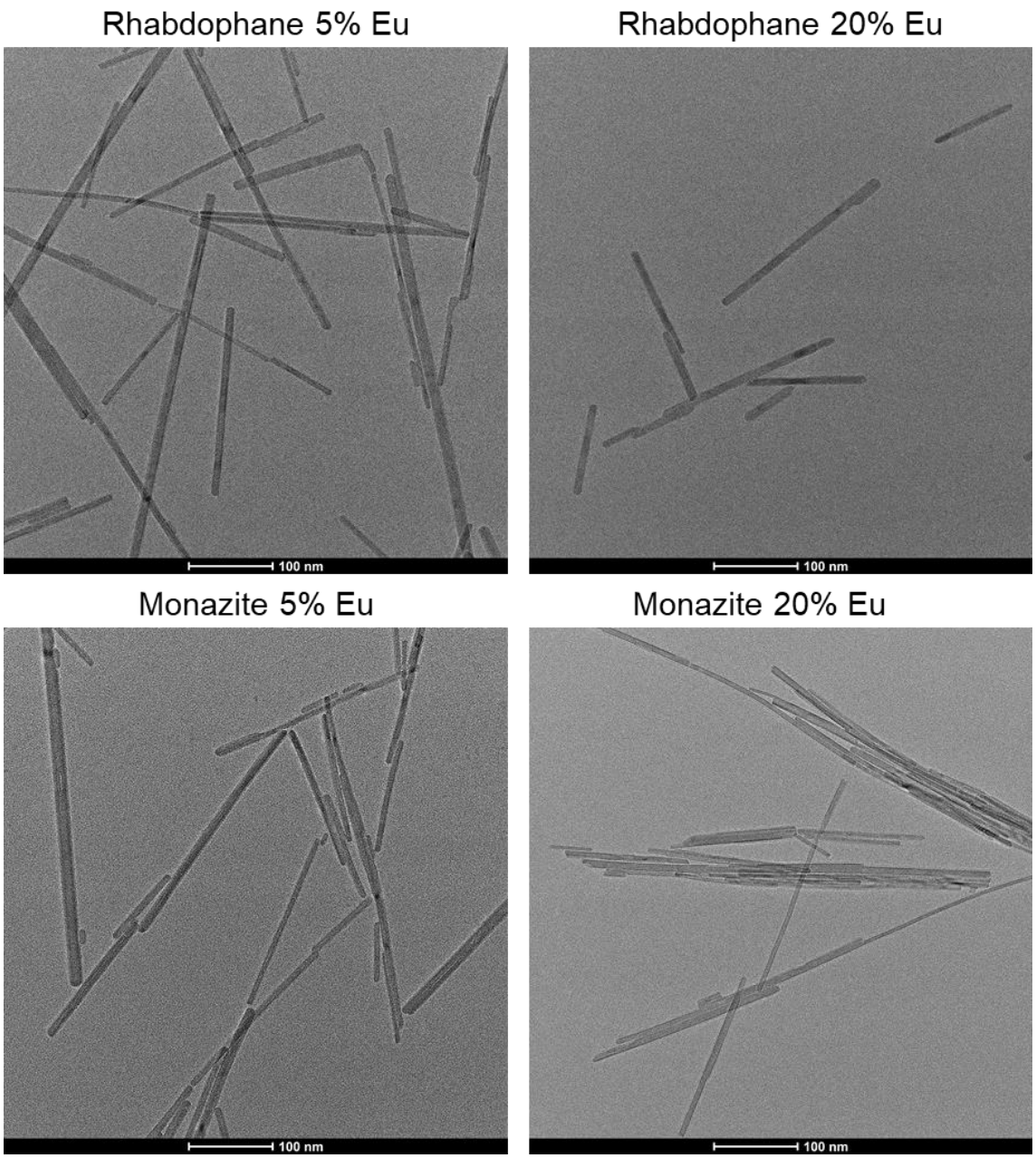

Figure 5.34 TEM images of synthesized $LaPO_4$:Eu nanocrystals in both rhabdophane and monazite phase and 5% and 20% europium doping. The monazite 5% doped sample was synthesized by Marcello Bonetti.

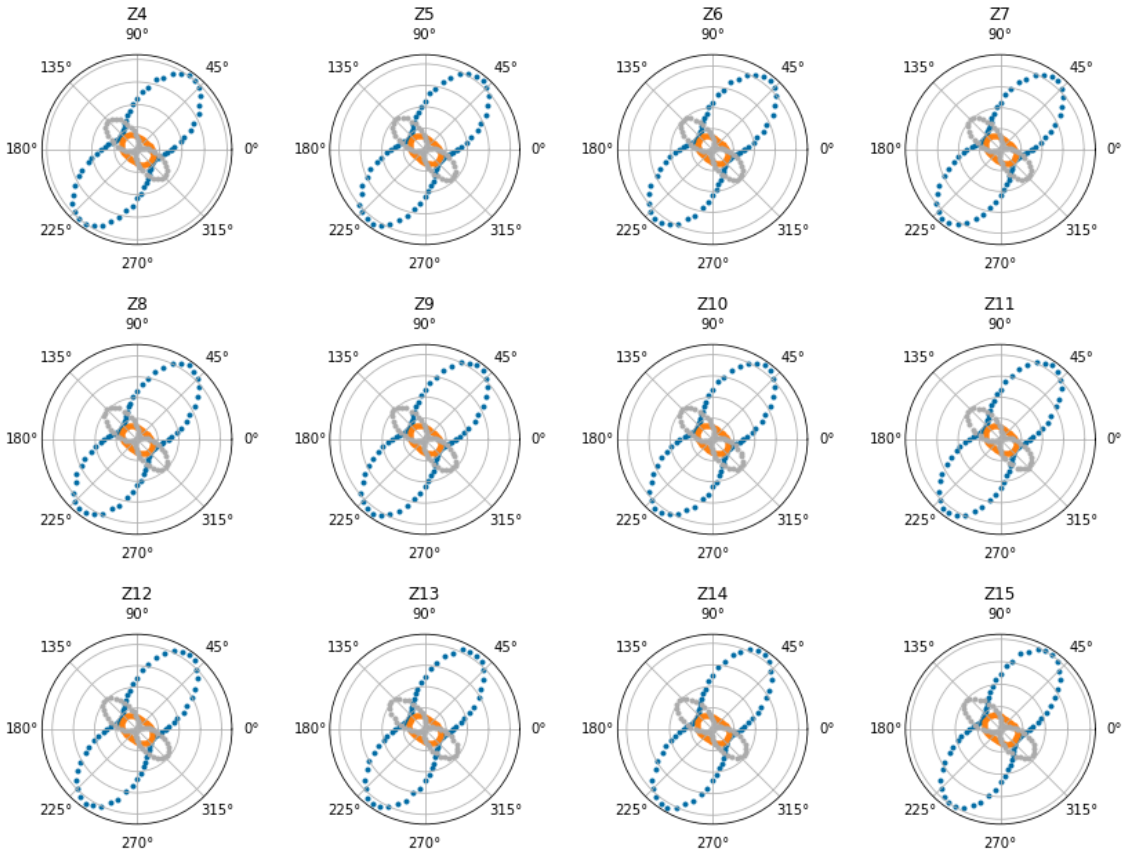

Figure 5.35 k-diagrams obtained in a dense nematic of rhabdophane phase $LaPO_4$:5%Eu at different depths in the sample, spaced by 2.5 µm.

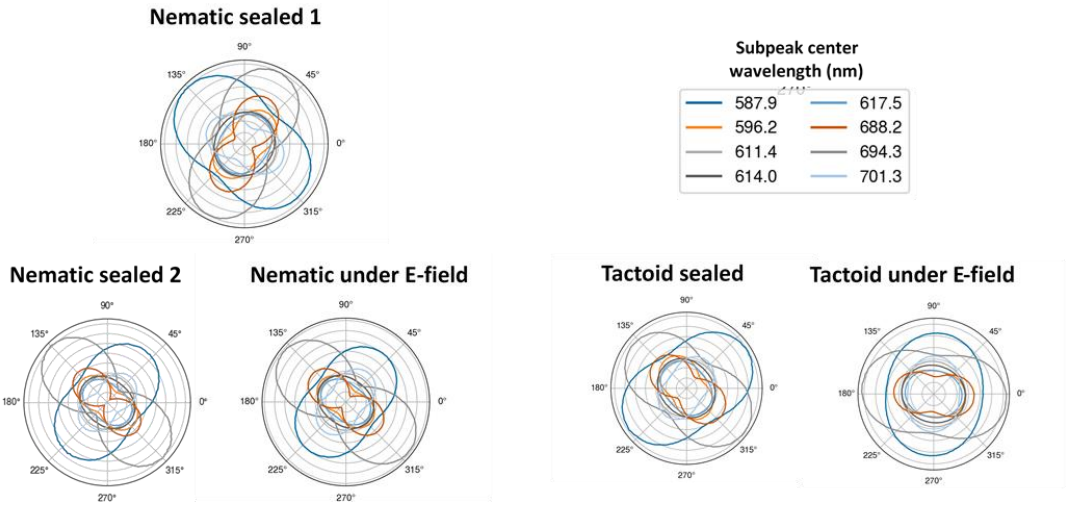

Figure 5.36 Polar diagrams of integrated intensities of the subpeaks highlighted in **Figure 2.26b** for various samples.

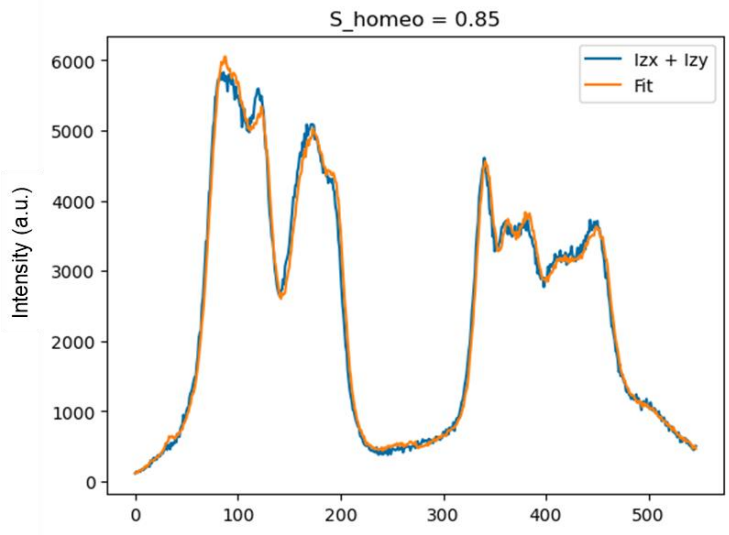

Figure 5.37 Homeotropic order parameter S_{homeo} evaluated close to the substrate in a homeotropic (flower) domain by spectral fitting of $I_z = I_{zx} + I_{zy}$ using **equation 2.19.**

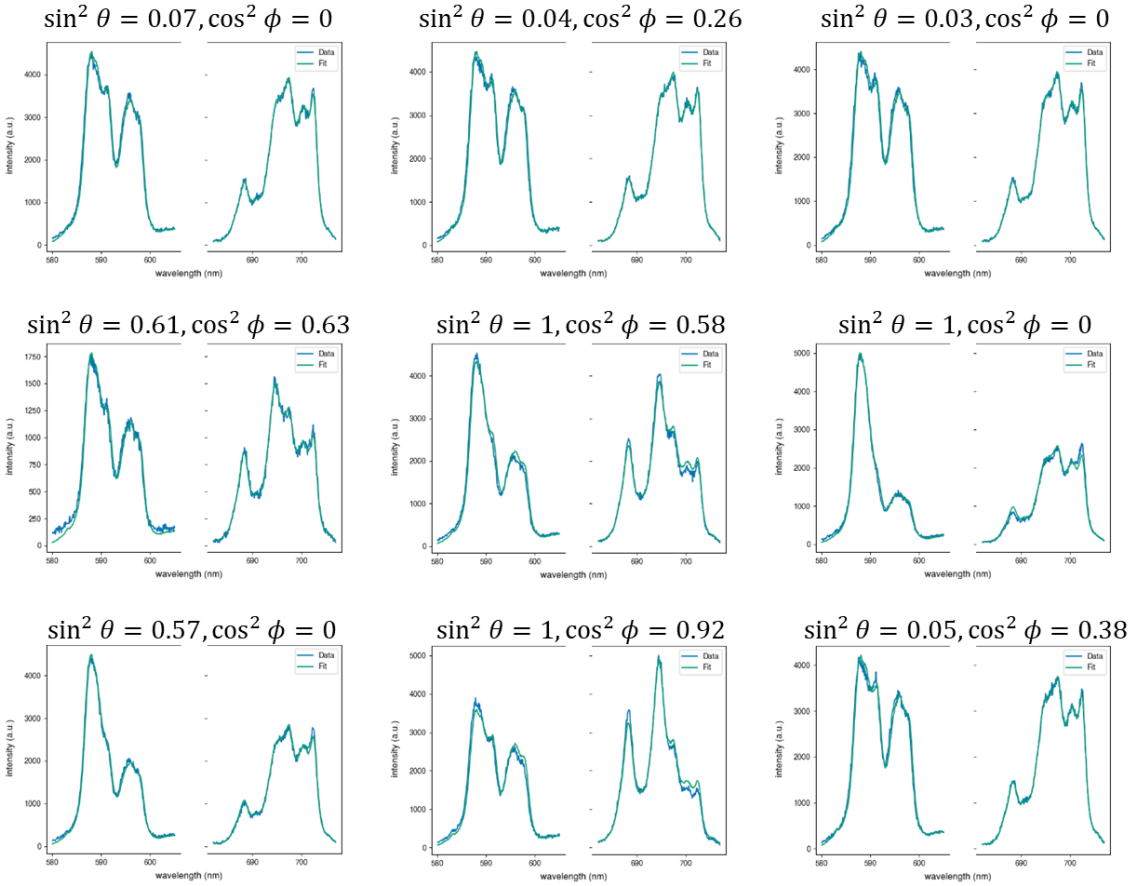

Figure 5.38 Example of spectral fits using I_{zx}

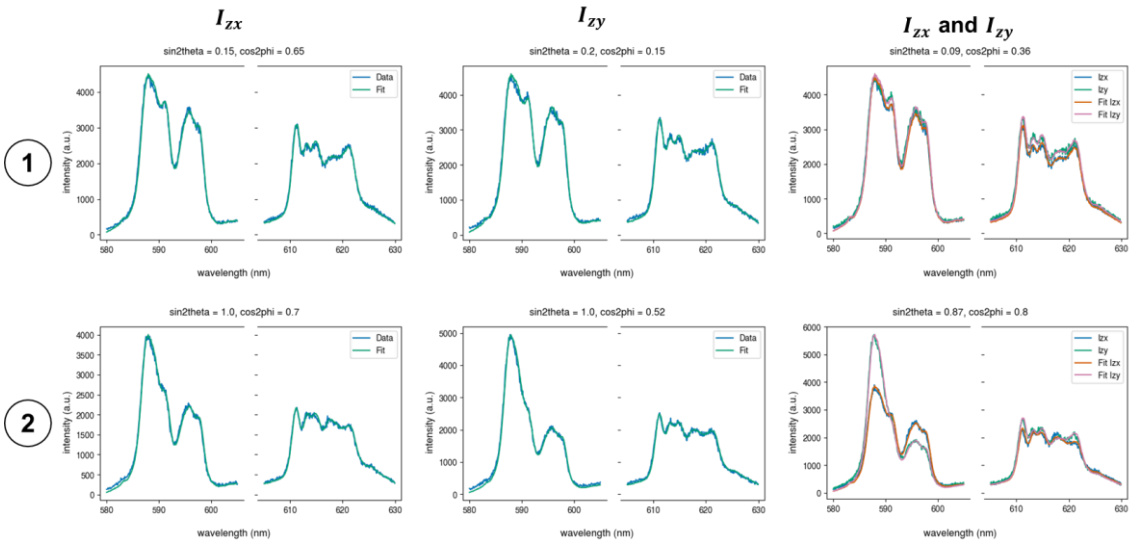

Figure 5.39 Example of spectral fits with $^5D_0$-$^7F_2$ as the ED transition

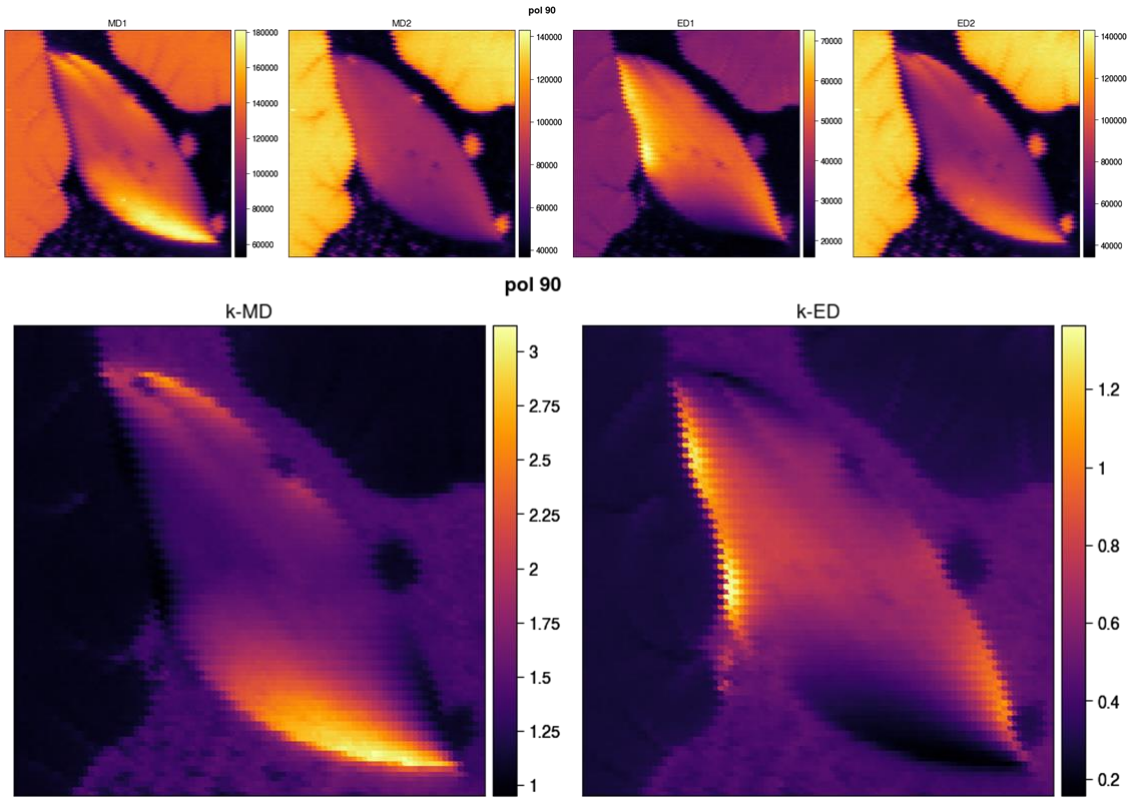

Figure 5.40 AUC for the two subpeaks of the MD and ED transitions and the corresponding k-values such that k-MD = MD1/MD2 and k-ED = ED1/ED2 for I_{zy}

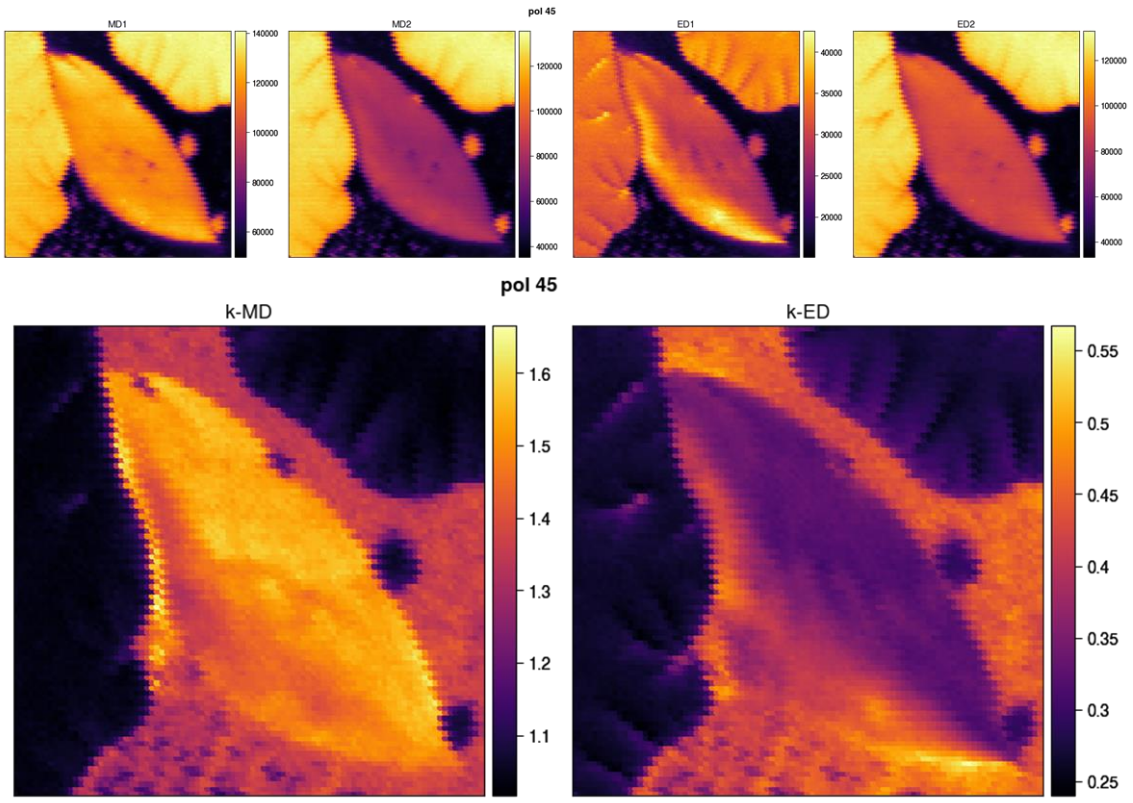

Figure 5.41 AUC for the two subpeaks of the MD and ED transitions and the corresponding k-values such that k-MD = MD1/MD2 and k-ED = ED1/ED2 for $I_{z45°}$

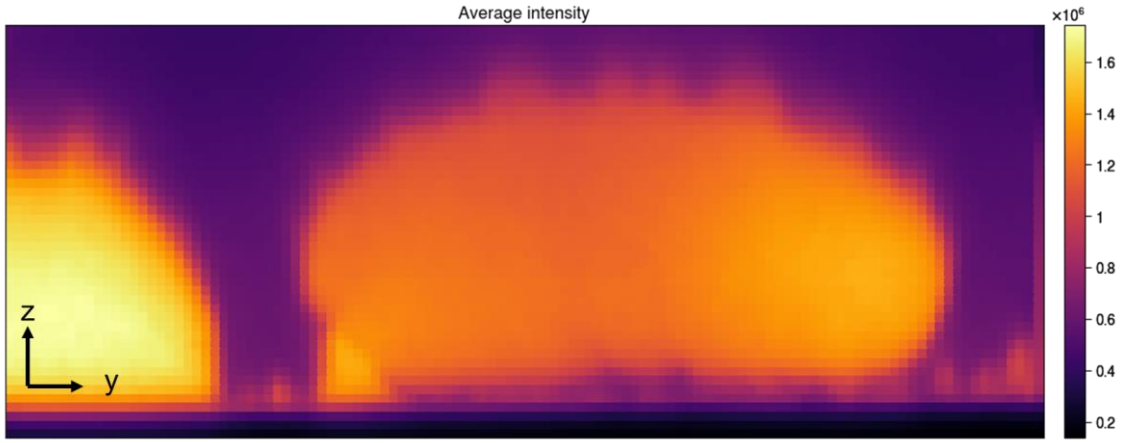

Figure 5.42 Average PL intensity map at the middle yz-cross section of the tactoid and flower domain (seen on left).

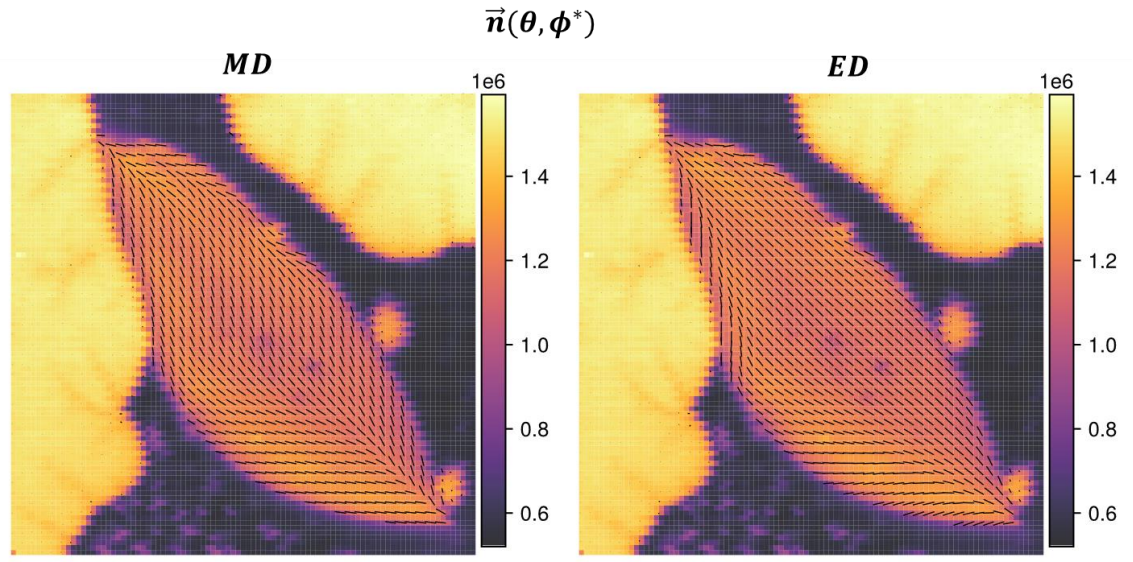

Figure 5.43 Plots of the projected director where the azimuthal angle is found though **equation 2.63**.

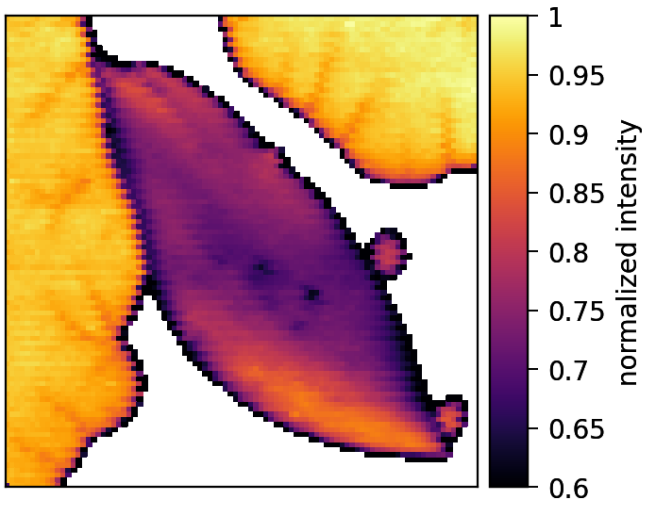

Figure 5.44 Normalized intensity map of the integrated I_{zx} spectra

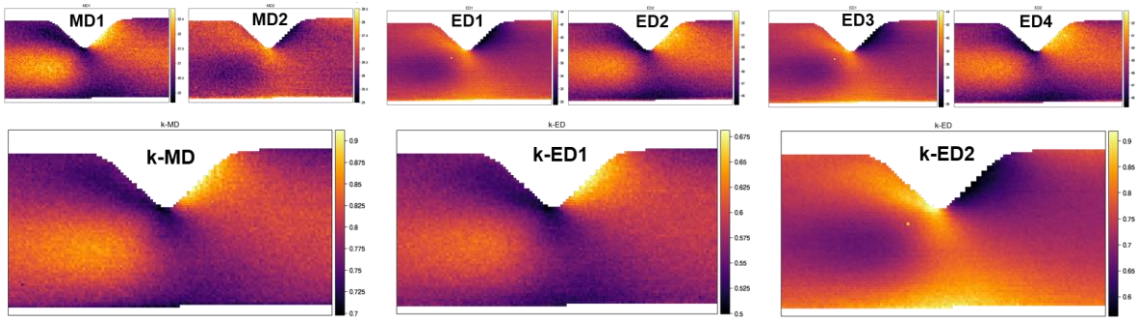

Figure 5.45 AUC for the two subpeaks of the MD and ED transitions based on the I_{zx} spectrum and the corresponding k-values such that $k_{MD} = I_{MD1}/I_{MD2}$, $k_{ED1} = I_{ED1}/I_{ED2}$ and $k_{ED2} = I_{ED3}/I_{ED4}$.

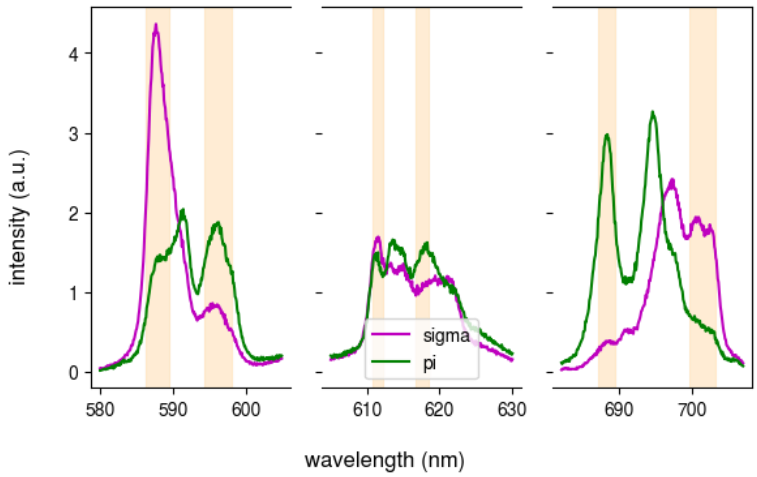

Figure 5.46 Reference spectra of 20% doped $LaPO_4$:Eu obtained from well-aligned nematic LC

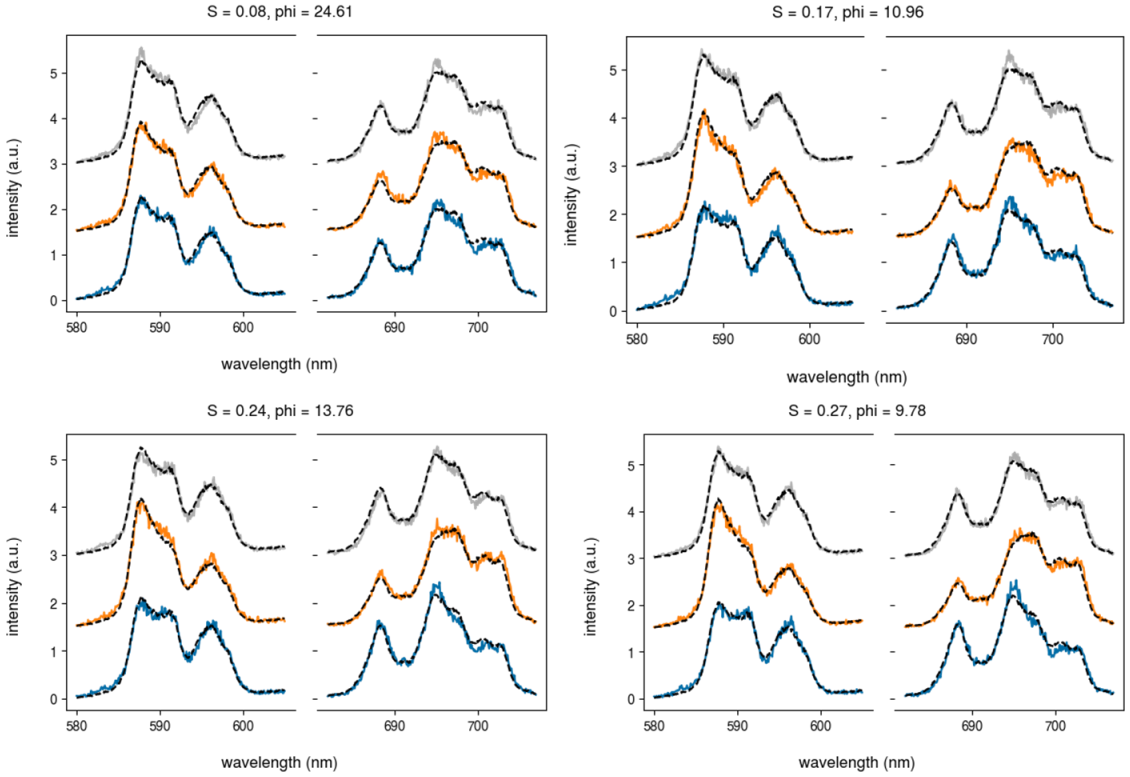

Figure 5.47 Examples of spectral fits in the microfluidic channel using 20% doped $LaPO_4$ nanorods.

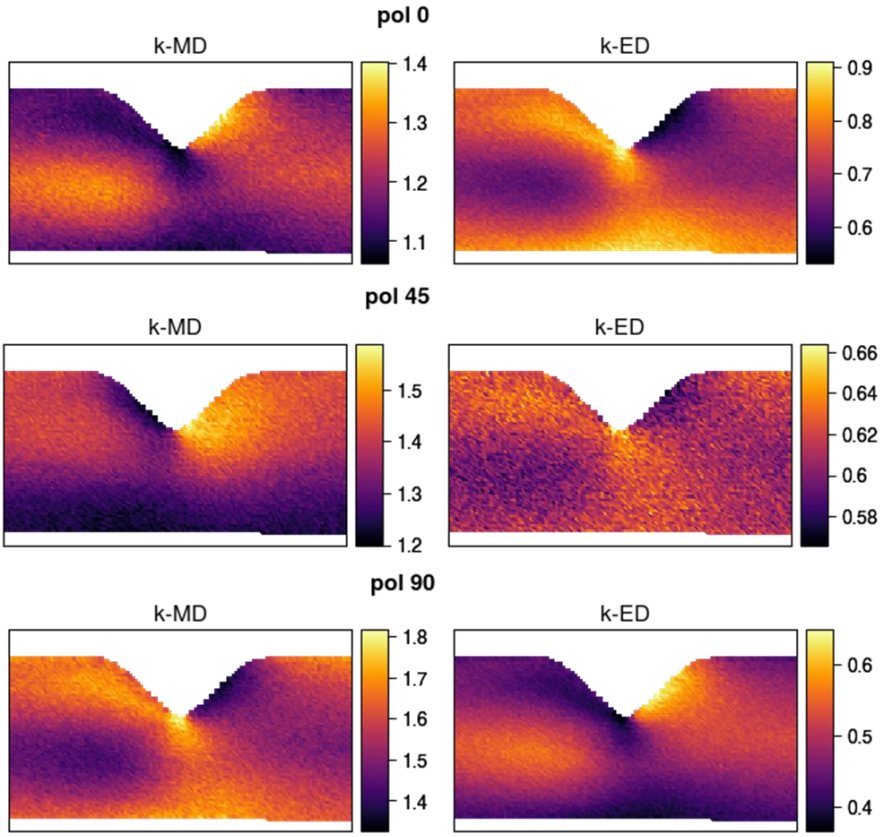

Figure 5.48 K-values of 20% doped rhabdophane phase $LaPO_4$:Eu in microfluidic channel

5.8.2 Chapter 3

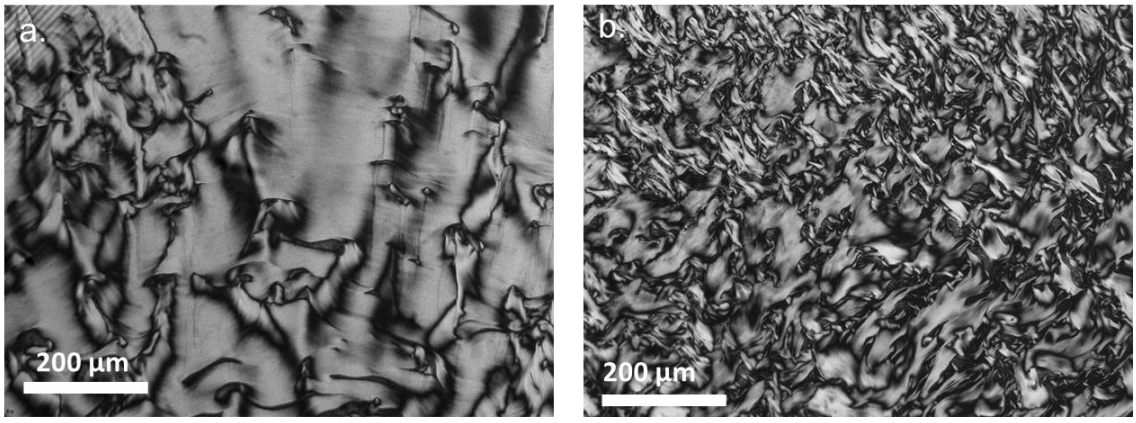

Figure 5.49 PLM images of the **a)** middle and **b)** bottom nematic phase of a triphasic 20% doped $LaPO_4$:Eu LC (**Figure 3.10b**) sandwiched between microscope slide and cover slip**.**

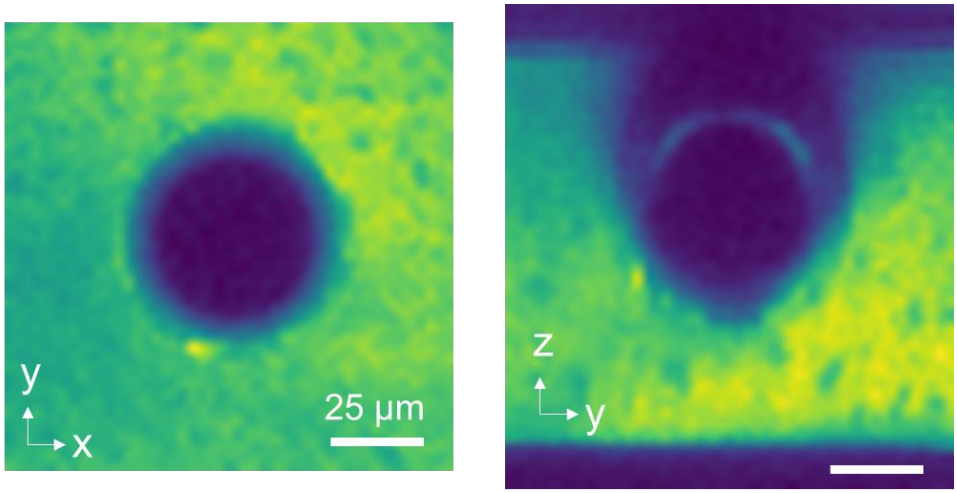

Figure 5.50 APD images of air bubble in nematic sample in a confinement cell. Color represents the normalized intensity. Corresponding to the left dark spot seen in **Figure 3.14b**.

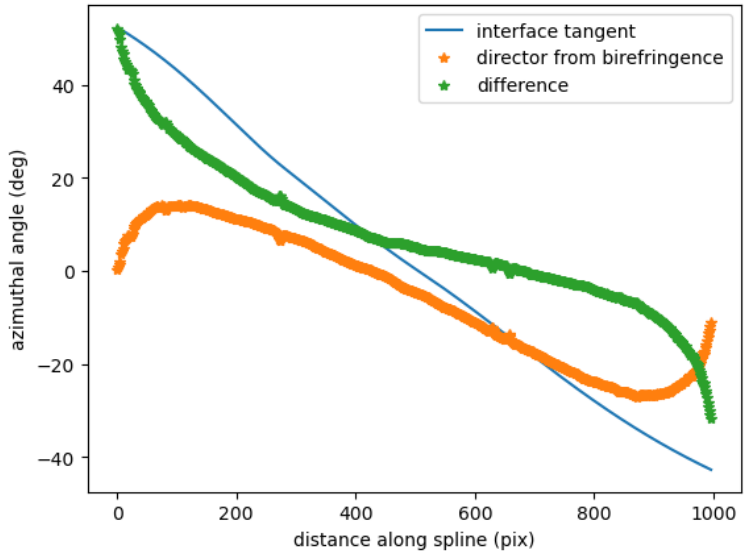

Figure 5.51 Azimuthal angle ϕ of $\vec{n}$ along the spline of a tactoid (orange), the interface tangent $\phi_{interface}$ based on the spline fit (blue line) and the difference between them (green).

5.8.3 Chapter 4

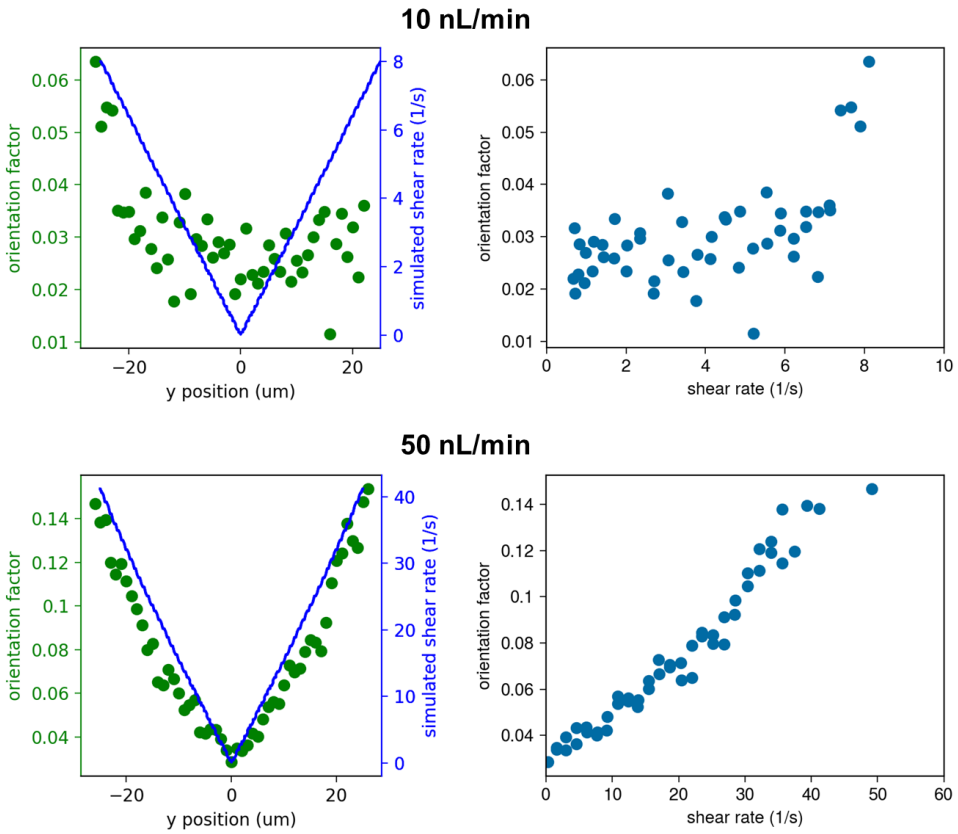

Figure 5.52 Measured orientation factor versus simulated shear rate, for flow rates of 10 and 100 nL/min for rhabdophane $LaPO_4$:Eu in EG.

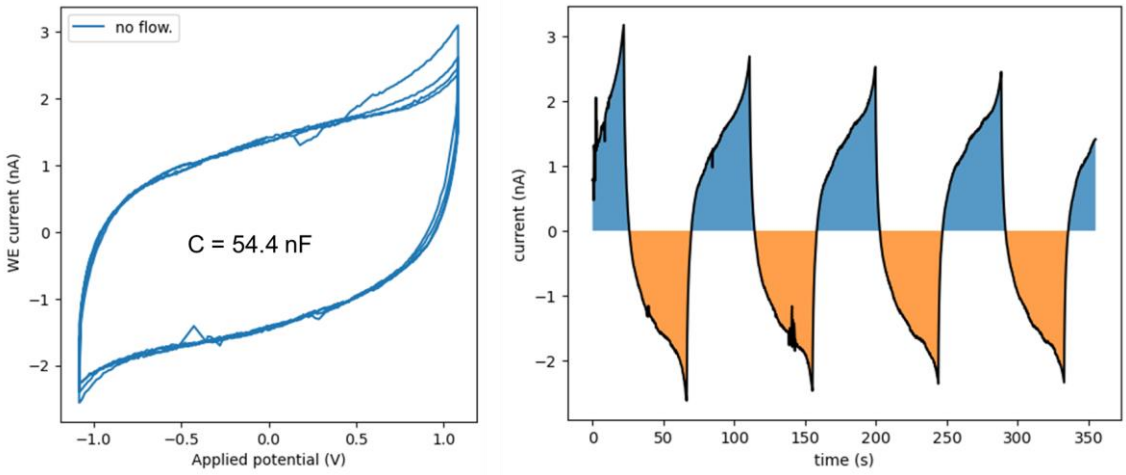

Figure 5.53 Capacitance measurement in anisotropic channel with two ITO electrodes. Electrolyte is 0.1M $NaNO_3$. **a)** Voltammogram **b)** Current as a function of time. The colored regions represent the integrated areas used to determine the capacitance.

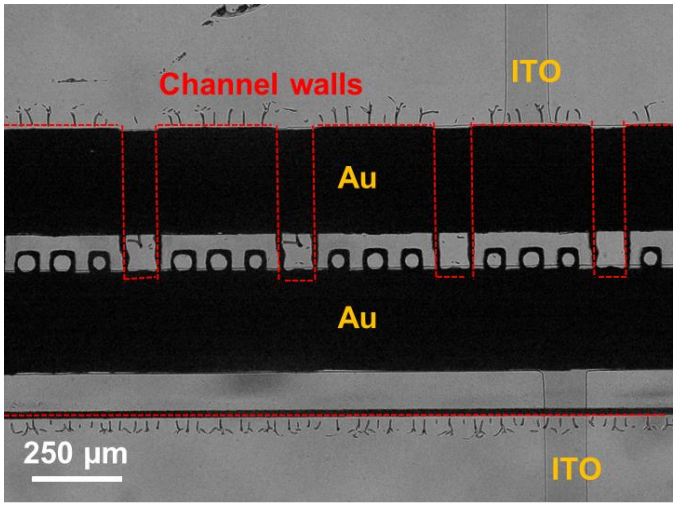

Figure 5.54 Image of the anisotropic channel with integrated gold electrodes. The gold is sputtered onto the ITO only in the regions which are inside the channel.

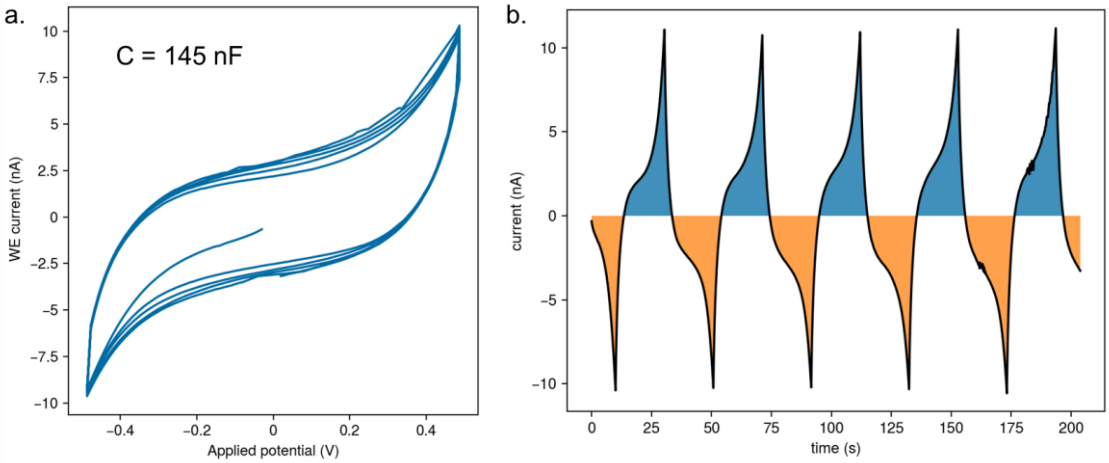

Figure 5.55 Capacitance measurement in anisotropic channel with two gold electrodes. Electrolyte is 0.1M $NaNO_3$. **a)** Voltammogram **b)** Current as a function of time. The colored regions represent the integrated areas used to determine the capacitance.

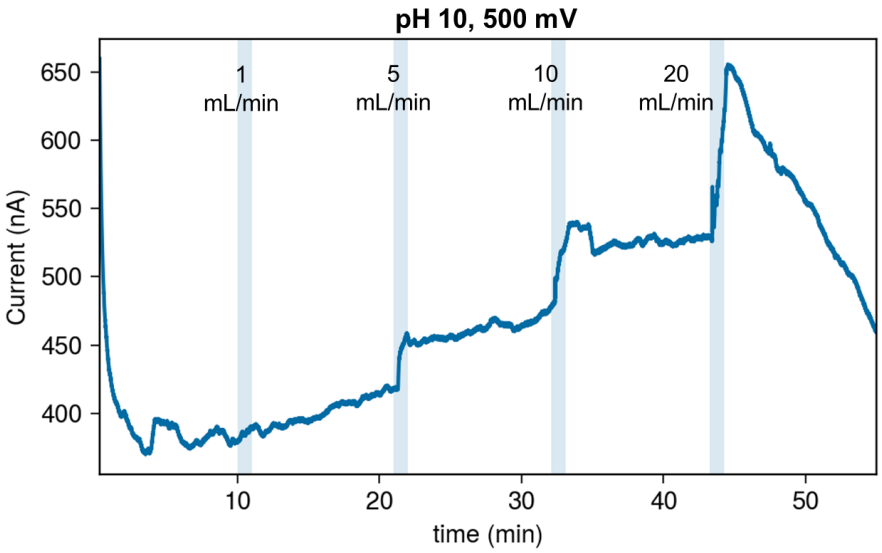

Figure **5.56** Current response for 60 second flow pulses at various flow rates using 1 mM KNO_3 at pH 10 with a 500 mV potential bias.

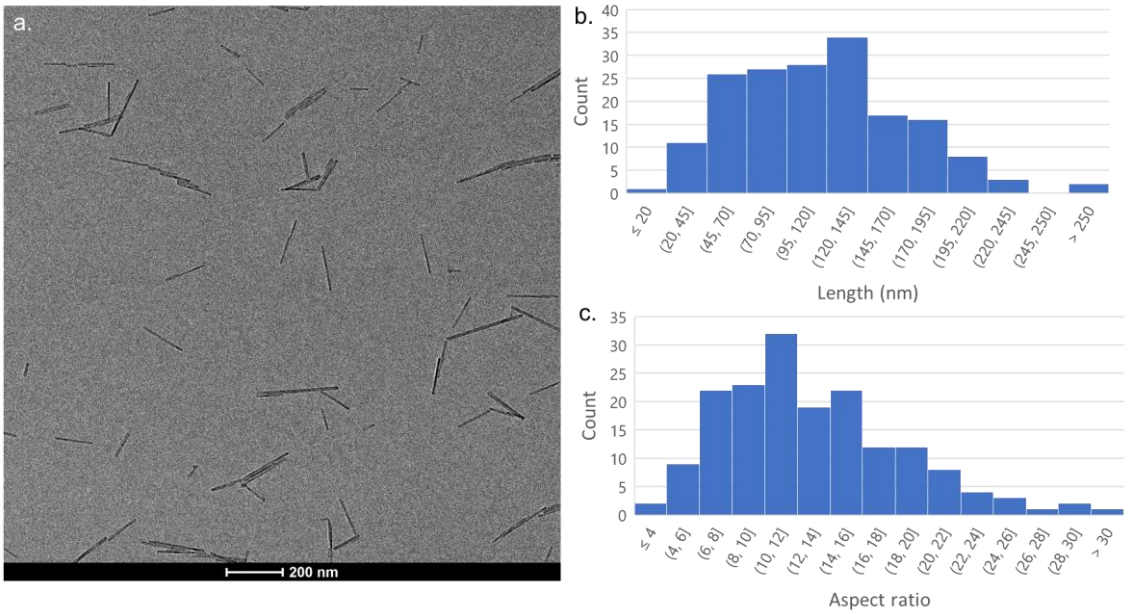

Figure 5.57 Size statistics of rhabdophane $LaPO_4$:Eu nanorods used for the calibration curve. **a)** Representative TEM image **b)** length and **c)** aspect ratio of the nanorods measured from several TEM images.

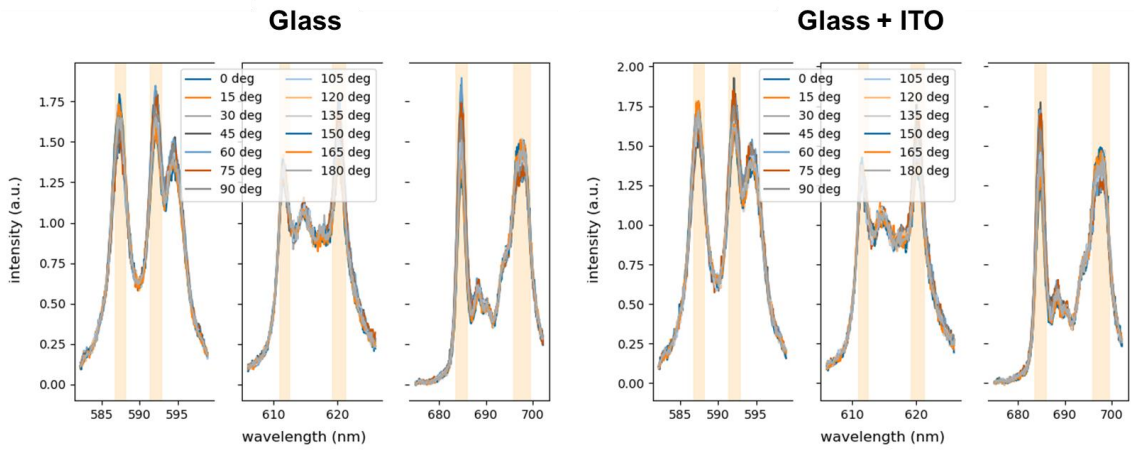

Figure 5.58 Polarized emission spectra of $LaPO_4:Eu^{3+}$ solution flowing at 20 nL/min in a straight channel with incorporated ITO electrodes, measured both above the bare glass and above the ITO coated glass.

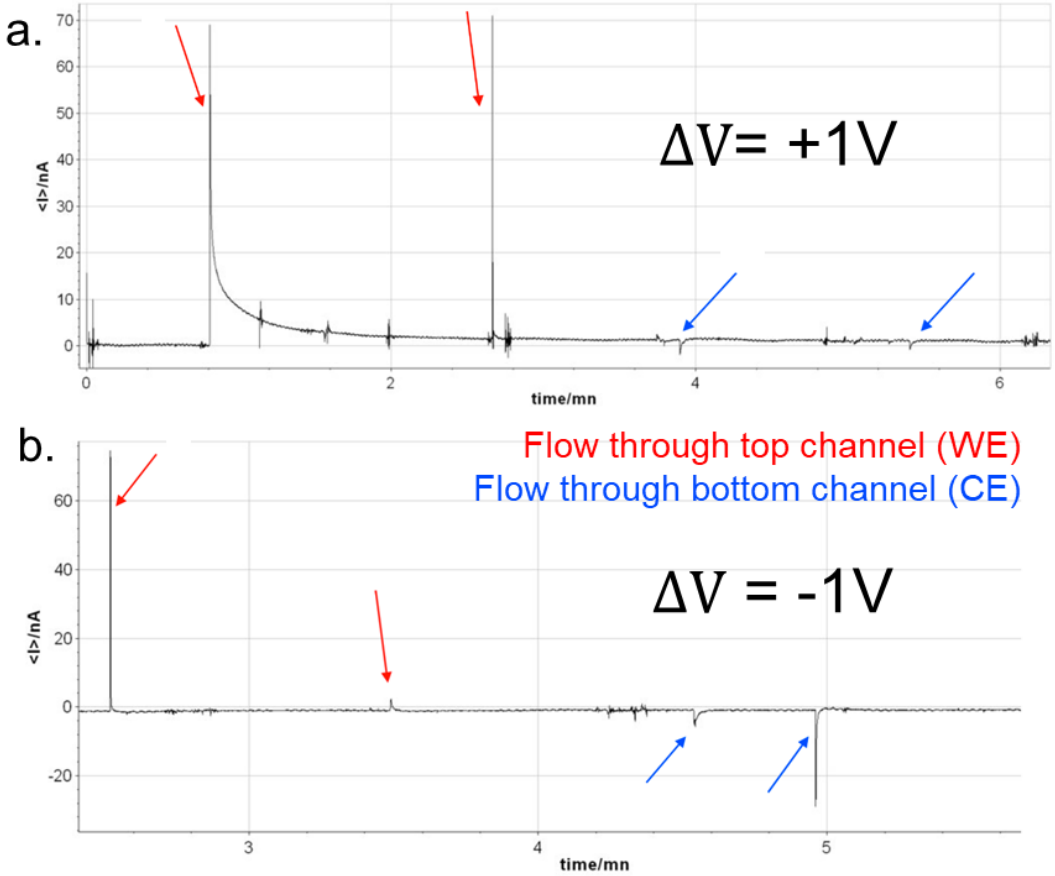

Figure 5.59 Current response for the channel in **Figure 4.38** when applying a short flow pulse (by hand) on the WE (red arrows) or CE (blue arrows) for a **a)** +1V and **b)** -1V potential bias.

5.9 Additional tables

Table 5.1: Pseudo-capacitance calculated from the voltammograms in **Figure 4.32a**. The surface area of each electrode is ~2.7 mm^2

Trial number	1	2	3	4	5	6	7
pH	6.5	10	4.9	8.9	7.2	11.6	10
Capacitance (nF)	71	16	35	54	48	11	22

Table 5.2: Pseudo-capacitance calculated from the voltammograms in **Figure 4.32b**. The surface area of each electrode is ~2.7 mm^2

pH	4.7	7.0	8
Capacitance (nF)	45	52	33

References

1. Kim, J. *et al.* Optimized combination of intrinsic and form birefringence in oriented LaPO4 nanorod assemblies. *Applied Physics Letters* **105**, 061102 (2014).
2. Kim, J. *et al.* $LaPO_4$ Mineral Liquid Crystalline Suspensions with Outstanding Colloidal Stability for Electro-Optical Applications. *Advanced Functional Materials* **22**, 4949–4956 (2012).
3. Wang, Z. *et al.* Monazite LaPO4:Eu3+ nanorods as strongly polarized nano-emitters. *Nanoscale* **13**, 16968–16976 (2021).
4. Onsager, L. The Effects of Shape on the Interaction of Colloidal Particles. *Annals of the New York Academy of Sciences* **51**, 627–659 (1949).
5. Kim, Y.-K., Shiyanovskii, S. V. & Lavrentovich, O. D. Morphogenesis of defects and tactoids during isotropic–nematic phase transition in self-assembled lyotropic chromonic liquid crystals. *Journal of Physics: Condensed Matter* **25**, 404202 (2013).
6. Puech, N., Grelet, E., Poulin, P., Blanc, C. & van der Schoot, P. Nematic droplets in aqueous dispersions of carbon nanotubes. *Physical Review E* **82**, 020702 (2010).
7. Wang, P.-X. & MacLachlan, M. J. Liquid crystalline tactoids: ordered structure, defective coalescence and evolution in confined geometries. *Philosophical Transactions of the Royal Society A: Mathematical, Physical and Engineering Sciences* **376**, 20170042 (2017).
8. Feng, W. *et al.* Static and Dynamic Control of Fingerprint Landscapes of Liquid Crystal Network Coatings. *ACS Applied Materials & Interfaces* **12**, 5265–5273 (2020).
9. Nemitz, I. R. *et al.* Observations of a streak texture in the hybrid-aligned smectic-C phase. *Soft Matter* **14**, 460–469 (2018).
10. Kim, J. Orientation analysis and liquid crystalline behavior of lanthanide-doped nanorods. (Institut Polytechnique de Paris, 2021).
11. Wang, Z. *et al.* Zwitterionic Polymers toward the Development of Orientation-Sensitive Bioprobes. *Langmuir: the ACS journal of surfaces and colloids* **38**, 10512–10519 (2022).
12. Kim, J. *et al.* Monitoring the orientation of rare-earth-doped nanorods for flow shear tomography. *Nature Nanotechnology* **12**, 914–919 (2017).
13. Cotte, A. de la *et al.* Electric field induced birefringence in non-aqueous dispersions of mineral nanorods. *Soft Matter* **11**, 6595–6603 (2015).
14. Werts, M. H. V. Making sense of Lanthanide Luminescence. *Science Progress* **88**, 101–131 (2005).
15. Wang, X.-Z. Synthesis and luminescence of LaPO4:Eu nanoparticles from different phosphate sources. *Journal of Materials Science: Materials in Electronics* **25**, 1264–1268 (2014).
16. Binnemans, K. Interpretation of europium(III) spectra. *Coordination Chemistry Reviews* **295**, 1–45 (2015).

17. Fu, Z. & Bu, W. High efficiency green-luminescent LaPO4:Ce,Tb hierarchical nanostructures: Synthesis, characterization, and luminescence properties. *Solid State Sciences* **10**, 1062–1067 (2008).
18. Chaudan, E. *et al.* Polarized Luminescence of Anisotropic $LaPO_4$:Eu Nanocrystal Polymorphs. *Journal of the American Chemical Society* **140**, 9512–9517 (2018).
19. Tanner, P. A. Some misconceptions concerning the electronic spectra of tri-positive europium and cerium. *Chemical Society Reviews* **42**, 5090 (2013).
20. Murphy, D. B. & Davidson, M. W. *Fundamentals of Light Microscopy and Electronic Imaging*. (Wiley-Blackwell, Hoboken, N.J, 2013).
21. Miller, D. S., Carlton, R. J., Mushenheim, P. C. & Abbott, N. L. Introduction to Optical Methods for Characterizing Liquid Crystals at Interfaces. *Langmuir* **29**, 3154–3169 (2013).
22. Gim, M.-J., Beller, D. A. & Yoon, D. K. Morphogenesis of liquid crystal topological defects during the nematic-smectic A phase transition. *Nature Communications* **8**, 15453 (2017).
23. Scheraga, H. A., Edsall, J. T. & Gadd, J. O. Double Refraction of Flow: Numerical Evaluation of Extinction Angle and Birefringence as a Function of Velocity Gradient. *The Journal of Chemical Physics* **19**, 1101–1108 (1951).
24. Dierking, I. & Archer, P. Imaging liquid crystal defects. *RSC Advances* **3**, 26433–26437 (2013).
25. Gao, M. *et al.* Direct observation of liquid crystals using cryo-TEM: Specimen preparation and low-dose imaging. *Microscopy Research and Technique* **77**, 754–772 (2014).
26. Kim, J. *et al.* Measuring 3D orientation of nanocrystals via polarized luminescence of rare-earth dopants. *Nature Communications* **12**, 1943 (2021).
27. Patra, D., Gregor, I. & Enderlein, J. Image Analysis of Defocused Single-Molecule Images for Three-Dimensional Molecule Orientation Studies. *The Journal of Physical Chemistry A* **108**, 6836–6841 (2004).
28. Böhmer, M. & Enderlein, J. Orientation imaging of single molecules by wide-field epifluorescence microscopy. *JOSA B* **20**, 554–559 (2003).
29. Wu, T., Lu, J. & Lew, M. D. Dipole-spread-function engineering for simultaneously measuring the 3D orientations and 3D positions of fluorescent molecules. *Optica* **9**, 505–511 (2022).
30. Zhang, O., Zhou, W., Lu, J., Wu, T. & Lew, M. D. Resolving the Three-Dimensional Rotational and Translational Dynamics of Single Molecules Using Radially and Azimuthally Polarized Fluorescence. *Nano Letters* **22**, 1024–1031 (2022).
31. Zhang, T. *et al.* Single Bipyramid Plasmonic Antenna Orientation Determined by Direct Photoluminescence Pattern Imaging. *Advanced Optical Materials* **1**, 335–342 (2013).

32. Lethiec, C. *et al.* Polarimetry-based analysis of dipolar transitions of single colloidal CdSe/CdS dot-in-rods. *New Journal of Physics* **16**, 093014 (2014).
33. Smalyukh, I. I., Shiyanovskii, S. V. & Lavrentovich, O. D. Three-dimensional imaging of orientational order by fluorescence confocal polarizing microscopy. *Chemical Physics Letters* **336**, 88–96 (2001).
34. Shin, S. *et al.* Tomographic measurement of dielectric tensors at optical frequency. *Nature Materials* **21**, 317–324 (2022).
35. Li, P. *et al.* Deterministic Relation between Optical Polarization and Lattice Symmetry Revealed in Ion-Doped Single Microcrystals. *ACS Nano* (2022).
36. Kim, J., Lahlil, K., Gacoin, T. & Kim, J. Measuring the order parameter of vertically aligned nanorod assemblies. *Nanoscale* **13**, 7630–7637 (2021).
37. Chaudan, E. Développement de nanoémetteurs polarisés pour leur application comme sondes d'orientation. (Université Paris-Saclay (ComUE), 2018).
38. Wang, Z. *et al.* Shearmetry of Fluids with Tunable Rheology by Polarized Luminescence of Rare Earth-Doped Nanorods. *ACS Nano* (2024).
39. Lee, S. J. & Kim, S. Advanced particle-based velocimetry techniques for microscale flows. *Microfluidics and Nanofluidics* **6**, 577–588 (2009).
40. Lindken, R., Rossi, M., Große, S. & Westerweel, J. Micro-Particle Image Velocimetry (µPIV): Recent developments, applications, and guidelines. *Lab on a Chip* **9**, 2551–2567 (2009).
41. Dabiri, D. & Pecora, C. *Particle Tracking Velocimetry*. (IOP Publishing, 2019).
42. Park, J. S., Choi, C. K. & D. Kihm, K. Optically sliced micro-PIV using confocal laser scanning microscopy (CLSM). *Experiments in Fluids* **37**, 105–119 (2004).
43. Li, H. F. & Yoda, M. Multilayer nano-particle image velocimetry (MnPIV) in microscale Poiseuille flows. *Measurement Science and Technology* **19**, 075402 (2008).
44. Cerf, R. & Scheraga, H. A. Flow Birefringence in Solutions of Macromolecules. *Chemical Reviews* **51**, 185–261 (1952).
45. Gojova, A. & Barakat, A. I. Vascular endothelial wound closure under shear stress: role of membrane fluidity and flow-sensitive ion channels. *Journal of Applied Physiology* **98**, 2355–2362 (2005).
46. Lum, R. M., Wiley, L. M. & Barakat, A. I. Influence of different forms of fluid shear stress on vascular endothelial TGF-beta1 mRNA expression. *International Journal of Molecular Medicine* **5**, 635–676 (2000).
47. Dong, C. & Lei, X. X. Biomechanics of cell rolling: shear flow, cell-surface adhesion, and cell deformability. *Journal of Biomechanics* **33**, 35–43 (2000).

48. Yazdan Parast, F., Gaikwad, A. S., Prabhakar, R., O'Bryan, M. K. & Nosrati, R. The cooperative impact of flow and viscosity on sperm flagellar energetics in biomimetic environments. *Cell Reports Physical Science* **4**, 101646 (2023).
49. Lechtreck, K.-F., Delmotte, P., Robinson, M. L., Sanderson, M. J. & Witman, G. B. Mutations in Hydin impair ciliary motility in mice. *The Journal of Cell Biology* **180**, 633–643 (2008).
50. Jung, I. D. *et al.* Selective Ion Sweeping on Prussian Blue Analogue Nanoparticles and Activated Carbon for Electrochemical Kinetic Energy Harvesting. *Nano Letters* **20**, 1800–1807 (2020).
51. Vetrone, F. *et al.* Temperature Sensing Using Fluorescent Nanothermometers. *ACS Nano* **4**, 3254–3258 (2010).
52. Zhou, S. *et al.* Upconversion luminescence of NaYF4: Yb3+, Er3+ for temperature sensing. *Optics Communications* **291**, 138–142 (2013).
53. Li, Z. Q., Zhang, Y. & Jiang, S. Multicolor Core/Shell-Structured Upconversion Fluorescent Nanoparticles. *Advanced Materials* **21**, (2009).
54. Kaznacheev, A. V., Bogdanov, M. M. & Taraskin, S. A. The nature of prolate shape of tactoids in lyotropic inorganic liquid crystals. *Journal of Experimental and Theoretical Physics* **95**, 57–63 (2002).
55. Almohammadi, H., Khadem, S. A., Bagnani, M., Rey, A. D. & Mezzenga, R. Shape and structural relaxation of colloidal tactoids. *Nature Communications* **13**, 2778 (2022).
56. St. Croix, C. M., Shand, S. H. & Watkins, S. C. Confocal Microscopy: Comparisons, Applications, and Problems. *BioTechniques* **39**, S2–S5 (2005).
57. Kuznetsov, A. V., Hermann, M., Troppmair, J., Margreiter, R. & Hengster, P. Complex patterns of mitochondrial dynamics in human pancreatic cells revealed by fluorescent confocal imaging. *Journal of Cellular and Molecular Medicine* **14**, 417–425 (2010).
58. Guo, S.-M. *et al.* Multiplexed and high-throughput neuronal fluorescence imaging with diffusible probes. *Nature Communications* **10**, 4377 (2019).
59. Lu, P. J. Confocal Scanning Optical Microscopy and Nanotechnology. in *Handbook of Microscopy for Nanotechnology* (eds. Yao, N. & Wang, Z. L.) 3–24 (Springer US, Boston, MA, 2005).
60. Fisher, B. R., Eisler, H.-J., Stott, N. E. & Bawendi, M. G. Emission Intensity Dependence and Single-Exponential Behavior In Single Colloidal Quantum Dot Fluorescence Lifetimes. *The Journal of Physical Chemistry B* **108**, 143–148 (2004).
61. deQuilettes, D. W. *et al.* Tracking Photoexcited Carriers in Hybrid Perovskite Semiconductors: Trap-Dominated Spatial Heterogeneity and Diffusion. *ACS Nano* **11**, 11488–11496 (2017).
62. Cho, C. *et al.* Efficient vertical charge transport in polycrystalline halide perovskites revealed by four-dimensional tracking of charge carriers. *Nature Materials* **21**, 1388–1395 (2022).
63. Smith, C. L. Basic Confocal Microscopy. *Current Protocols in Neuroscience* **56**, (2011).

64. Rayleigh. XXXI. *Investigations in optics, with special reference to the spectroscope*. *The London, Edinburgh, and Dublin Philosophical Magazine and Journal of Science* **8**, 261–274 (1879).
65. Cole, R., Jinadasa, T. & Brown, C. Measuring and interpreting point spread functions to determine confocal microscope resolution and ensure quality control. *Nature protocols* **6**, 1929–41 (2011).
66. Airy, G. B. On the Diffraction of an Object-glass with Circular Aperture. *Transactions of the Cambridge Philosophical Society* **5**, 283 (1835).
67. Luckham, P. F. & Ukeje, M. A. Effect of Particle Size Distribution on the Rheology of Dispersed Systems. *Journal of Colloid and Interface Science* **220**, 347–356 (1999).
68. Arenas-Guerrero, P. *et al.* Determination of the size distribution of non-spherical nanoparticles by electric birefringence-based methods. *Scientific Reports* **8**, 9502 (2018).
69. Kim, J., Peretti, J., Lahlil, K., Boilot, J.-P. & Gacoin, T. Optically Anisotropic Thin Films by Shear-Oriented Assembly of Colloidal Nanorods. *Advanced Materials* **25**, 3295–3300 (2013).
70. Andrienko, D. Introduction to liquid crystals. *Journal of Molecular Liquids* **267**, 520–541 (2018).
71. Swager, T. Handbook of liquid crystals. (4-volume set.) Edited by D. Demus, J. Goodby, G. W. Gray, H. W. Spiess and B. Vill. *Angewandte Chemie, International Edition* **38**, 2279–2281 (1999).
72. Kim, K.-H. & Song, J.-K. Technical evolution of liquid crystal displays. *NPG Asia Materials* **1**, 29–36 (2009).
73. Cunha, M. P. da, G. Debije, M. & J. Schenning, A. P. H. Bioinspired light-driven soft robots based on liquid crystal polymers. *Chemical Society Reviews* **49**, 6568–6578 (2020).
74. Kos, Ž. & Dunkel, J. Nematic bits and universal logic gates. *Science Advances* **8**, eabp8371 (2022).
75. Chuang, I., Durrer, R., Turok, N. & Yurke, B. Cosmology in the Laboratory: Defect Dynamics in Liquid Crystals. *Science* **251**, 1336–1342 (1991).
76. de Gennes, P. G. An analogy between superconductors and smectics A. *Solid State Communications* **10**, 753–756 (1972).
77. Ybert, C. *et al.* Structural study of the liquid-crystal analog of the vortex liquid phase in type-II superconductors. *Europhysics Letters* **63**, 840 (2003).
78. Dierking, I. & Al-Zangana, S. Lyotropic Liquid Crystal Phases from Anisotropic Nanomaterials. *Nanomaterials* **7**, 305 (2017).
79. Oster, G. Two-Phase Formation in Solutions of Tobacco Mosaic Virus and the Problem of Long-Range Forces. *Journal of General Physiology* **33**, 445–473 (1950).
80. Dierking, I. The Nematic and Cholesteric Phases. in *Textures of Liquid Crystals* 51–74 (John Wiley & Sons, Ltd, 2003).
81. Nehring, J. & Saupe, A. On the schlieren texture in nematic and smectic liquid crystals. *Journal of the Chemical Society, Faraday Transactions 2: Molecular and Chemical Physics* **68**, 1–15 (1972).

82. Lavrentovich, O. D. & Nastishin, Yu. A. Defects in Degenerate Hybrid Aligned Nematic Liquid Crystals. *Europhysics Letters* **12**, 135–141 (1990).

83. Link, D. R., Nakata, M., Takanishi, Y., Ishikawa, K. & Takezoe, H. Patterns in Hybrid Nematic Liquid-Crystal Films: Topography and Topology. *Physical Review Letters* **87**, (2001).

84. Ferris, A. J., Rosenblatt, C. & Atherton, T. J. Spontaneous Anchoring-Mediated Topography of an Orientable Fluid. *Physical Review Letters* **126**, 057803 (2021).

85. Chiccoli, C. *et al.* From Point to Filament Defects in Hybrid Nematic Films. *Scientific Reports* **9**, 17941 (2019).

86. Wu, J.-B., Wu, S.-B. & Hu, W. Azimuthal orientation guided topological defect evolution across the nematic-smectic phase transition. *Physical Review B* **108**, 224107 (2023).

87. Kurik, M. V. & Lavrentovich, O. D. Defects in liquid crystals: homotopy theory and experimental studies. *Soviet Physics Uspekhi* **31**, 196 (1988).

88. Lee, S.-D. & Meyer, R. B. Computations of the phase equilibrium, elastic constants, and viscosities of a hard-rod nematic liquid crystal. *The Journal of Chemical Physics* **84**, 3443–3448 (1986).

89. Nemitz, I. R., Ferris, A. J., Lacaze, E. & Rosenblatt, C. Chiral oily streaks in a smectic-A liquid crystal. *Soft Matter* **12**, 6662–6668 (2016).

90. Gharbi, I., Missaoui, A., Demaille, D., Lacaze, E. & Rosenblatt, C. Persistence of Smectic-A Oily Streaks into the Nematic Phase by UV Irradiation of Reactive Mesogens. *Crystals* **7**, 358 (2017).

91. Coursault, D. *et al.* Self-organized arrays of dislocations in thin smectic liquid crystal films. *Soft Matter* **12**, 678–688 (2016).

92. McConney, M. E. *et al.* Topography from Topology: Photoinduced Surface Features Generated in Liquid Crystal Polymer Networks. *Advanced Materials* **25**, 5880–5885 (2013).

93. White, T. J. & Broer, D. J. Programmable and adaptive mechanics with liquid crystal polymer networks and elastomers. *Nature Materials* **14**, 1087–1098 (2015).

94. Serra, F. *et al.* Curvature-Driven, One-Step Assembly of Reconfigurable Smectic Liquid Crystal "Compound Eye" Lenses. *Advanced Optical Materials* **3**, 1287–1292 (2015).

95. Tam-Chang, S.-W. & Huang, L. Chromonic liquid crystals: properties and applications as functional materials. *Chemical Communications* 1957–1967 (2008) doi:10.1039/B714319B.

96. Bowick, M. J., Chandar, L., Schiff, E. A. & Srivastava, A. M. The Cosmological Kibble Mechanism in the Laboratory: String Formation in Liquid Crystals. *Science* **263**, 943–945 (1994).

97. Boltenhagen, P., Kleman, M. & Lavrentovich, O. D. Focal Conics Domains in Smectics. in *Soft Order in Physical Systems* (eds. Rabin, Y. & Bruinsma, R.) 5–32 (Springer US, Boston, MA, 1994). doi:10.1007/978-1-4615-2458-8_2.

98. Zushi, Y. & Takeuchi, K. A. Scaling and spontaneous symmetry restoring of topological defect dynamics in liquid crystal. *Proceedings of the National Academy of Sciences* **119**, (2022).
99. Wang, X. *et al.* Experimental Insights into the Nanostructure of the Cores of Topological Defects in Liquid Crystals. *Physical Review Letters* **116**, 147801 (2016).
100. Zasadzinski, J. A. N. & Meyer, R. B. Molecular imaging of tobacco mosaic virus lyotropic nematic phases. *Physical Review Letters* **56**, 636–638 (1986).
101. Buining, P. A. & Lekkerkerker, H. N. W. Isotropic-nematic phase separation of a dispersion of organophilic boehmite rods. *The Journal of Physical Chemistry* **97**, 11510–11516 (1993).
102. Kimura, F. *et al.* Magnetic Alignment of the Chiral Nematic Phase of a Cellulose Microfibril Suspension. *Langmuir* **21**, 2034–2037 (2005).
103. Vroege, G. J. & Lekkerkerker, H. N. W. Theory of the isotropic-nematic-nematic phase separation for a solution of bidisperse rodlike particles.
104. Wang, P.-X., Hamad, W. Y. & MacLachlan, M. J. Structure and transformation of tactoids in cellulose nanocrystal suspensions. *Nature Communications* **7**, 11515 (2016).
105. Pergamenshchik, V. M., Lelidis, I. & Uzunova, V. A. Stripe domains in a nearly homeotropic nematic liquid crystal: A bend escaped state at a nematic--smectic-A transition. *Physical Review E* **77**, 041703 (2008).
106. Tasaltin, N., Sanli, D., Jonáš, A., Kiraz, A. & Erkey, C. Preparation and characterization of superhydrophobic surfaces based on hexamethyldisilazane-modified nanoporous alumina. *Nanoscale Research Letters* **6**, 487 (2011).
107. Prinsen, P. & van der Schoot, P. Shape and director-field transformation of tactoids. *Physical Review E* **68**, 021701 (2003).
108. Bagnani, M., Azzari, P., Michele, C. D., Arcari, M. & Mezzenga, R. Elastic constants of biological filamentous colloids: estimation and implications on nematic and cholesteric tactoid morphologies. *Soft Matter* **17**, 2158–2169 (2021).
109. Ok, J. M. *et al.* Control of periodic defect arrays of 8CB (4'-n-octyl-4-cyano-biphenyl) liquid crystals by multi-directional rubbing. *Soft Matter* **9**, 10135–10140 (2013).
110. De Gennes, P. G. Short Range Order Effects in the Isotropic Phase of Nematics and Cholesterics. *Molecular Crystals and Liquid Crystals* **12**, 193–214 (1971).
111. Trebin, H.-R. Defects in liquid crystals and cosmology. *Liquid Crystals* **24**, 127–130 (1998).
112. Price, A. D. & Schwartz, D. K. Anchoring of a Nematic Liquid Crystal on a Wettability Gradient. *Langmuir* **22**, 9753–9759 (2006).

113. Peterlin, A. & Stuart, H. A. Uber die Bestimmung der Grobe und Form, sowie der elektrischen, optischen und magnetischen Anisotropie von submikroskopischen Teilchen mit Hilfe der kunstlichen Doppelbrechung und der inneren Reibung. *Physik* **112**, (1939).
114. Perrin, F. Mouvement Brownien d'un Ellipsoide (Ii).Rotation Libre et Dépolarisation des Fluorescences.Translation et Diffusion de Molécules Ellipsoidales. **7**, 1–11 (1936).
115. Datt, C. & Elfring, G. J. Dynamics and rheology of particles in shear-thinning fluids. *Journal of Non-Newtonian Fluid Mechanics* **262**, 107–114 (2018).
116. Bird, R. B., Armstrong, R. C. & Hassager, O. Dynamics of polymeric liquids. Vol. 1, 2nd Ed. : Fluid mechanics. (1987).
117. Papadopoulou, A., Gillissen, J. J., Wilson, H. J., Tiwari, M. K. & Balabani, S. On the shear thinning of non-Brownian suspensions: Friction or adhesion? *Journal of Non-Newtonian Fluid Mechanics* **281**, 104298 (2020).
118. Hu, Z., Gong, S., Chen, J. & Guo, H. Energy harvesting of droplet-based triboelectric nanogenerators: From mechanisms toward performance optimizations. *DeCarbon* **5**, 100053 (2024).
119. Bard, A. J. & Faulkner, L. R. *Electrochemical Methods: Fundamentals and Applications*. vol. 38 (Wiley, New York, 2001).
120. Hu, Y., Liu, H., Ke, Q. & Wang, J. Effects of nitrogen doping on supercapacitor performance of a mesoporous carbon electrode produced by a hydrothermal soft-templating process. *Journal of Materials Chemistry A* **2**, 11753–11758 (2014).
121. Ruiz-Montoya, J. G., Quispe-Garrido, L. V., Gómez, J. C. C., Baena-Moncada, A. M. & Gonçalves, J. M. Recent progress in and prospects for supercapacitor materials based on metal oxide or hydroxide/biomass-derived carbon composites. *Sustainable Energy & Fuels* **5**, 5332–5365 (2021).
122. Zhang, Z. *et al.* Emerging hydrovoltaic technology. *Nature Nanotechnology* **13**, 1109–1119 (2018).
123. Xiao, K., Jiang, L. & Antonietti, M. Ion Transport in Nanofluidic Devices for Energy Harvesting. *Joule* **3**, 2364–2380 (2019).
124. van der Heyden, F. H. J., Stein, D. & Dekker, C. Streaming Currents in a Single Nanofluidic Channel. *Physical Review Letters* **95**, 116104 (2005).
125. Osterle, J. F. Electrokinetic Energy Conversion. *Journal of Applied Mechanics* **31**, 161–164 (1964).
126. Ghosh, M. *et al.* Charge Regulation at a Nanoporous Two-Dimensional Interface. *ACS Omega* **6**, 2487–2493 (2021).
127. Feng, J. *et al.* Single-layer MoS2 nanopores as nanopower generators. *Nature* **536**, 197–200 (2016).
128. Zhang, R. *et al.* A Streaming Potential/Current-Based Microfluidic Direct Current Generator for Self-Powered Nanosystems. *Advanced Materials* **27**, 6482–6487 (2015).

129. Daiguji, H., Yang, P., Szeri, A. J. & Majumdar, A. Electrochemomechanical Energy Conversion in Nanofluidic Channels. *Nano Letters* **4**, 2315–2321 (2004).
130. Iversen, P. & Lacks, D. J. A life of its own: The tenuous connection between Thales of Miletus and the study of electrostatic charging. *Journal of Electrostatics* **70**, 309–311 (2012).
131. Hu, J., Iwamoto, M. & Chen, X. A Review of Contact Electrification at Diversified Interfaces and Related Applications on Triboelectric Nanogenerator. *Nano-Micro Letters* **16**, 7 (2023).
132. Yuan, Z. & Guo, L. Recent advances in solid–liquid triboelectric nanogenerator technologies, affecting factors, and applications. *Scientific Reports* **14**, 10456 (2024).
133. Sun, B., Xu, D., Wang, Z., Zhan, Y. & Zhang, K. Interfacial structure design for triboelectric nanogenerators. *Battery Energy* **1**, 20220001 (2022).
134. Kwon, S.-H. *et al.* An effective energy harvesting method from a natural water motion active transducer. *Energy & Environmental Science* **7**, 3279–3283 (2014).
135. Zhang, X. *et al.* Copper hexacyanoferrate as ultra-high rate host for aqueous ammonium ion storage. *Chemical Engineering Journal* **421**, 127767 (2021).
136. Duffy, D. C., McDonald, J. C., Schueller, O. J. A. & Whitesides, G. M. Rapid Prototyping of Microfluidic Systems in Poly(dimethylsiloxane). *Analytical Chemistry* **70**, 4974–4984 (1998).
137. Casanova-Moreno, J. *et al.* Fabricating devices with improved adhesion between PDMS and gold-patterned glass. *Sensors and Actuators B: Chemical* **246**, 904–909 (2017).
138. Kersey, L., Ebacher, V., Bazargan, V., Wang, R. & Stoeber, B. The effect of adhesion promoter on the adhesion of PDMS to different substrate materials. *Lab on a Chip* **9**, 1002–1004 (2009).
139. Cui, H. & Zheng, Z. Electrically conductive TiO2/indium tin oxide coated glass substrates with high visible light transparency prepared by an electrodeposition method. *Thin Solid Films* **691**, 137612 (2019).
140. Liu, L., Yellinek, S., Valdinger, I., Donval, A. & Mandler, D. Important Implications of the Electrochemical Reduction of ITO. *Electrochimica Acta* **176**, 1374–1381 (2015).
141. Biswas, I. *et al.* Microfluidic Membrane Filtration Systems to Study Biofouling. *Microfluidics and Nanofluidics* (2018).
142. Knijff, L., Jia, M. & Zhang, C. Electric double layer at the metal-oxide/electrolyte interface. in *Reference Module in Chemistry, Molecular Sciences and Chemical Engineering* (Elsevier, 2023).
143. Berns, D. S. & Fuoss, R. M. Electrolyte-Solvent Interaction. IX. Tetra-alkylammonium Tetraphenylborides in Acetonitrile-Carbon Tetrachloride Mixtures at 25°. *Journal of the American Chemical Society* **82**, 5585–5588 (1960).

144. Heyrovska, R. Effective radii of alkali halide ions in aqueous solutions, crystals and in the gas phase and the interpretation of stokes radii. *Chemical Physics Letters - CHEM PHYS LETT* **163**, 207–211 (1989).
145. Irfan, I., Graber, S., So, F. & Gao, Y. Interplay of cleaning and de-doping in oxygen plasma treated high work function indium tin oxide (ITO). *Organic Electronics* **13**, 2028–2034 (2012).
146. Akanda, M. R., Osman, A. M., Nazal, M. K. & Aziz, M. A. Review—Recent Advancements in the Utilization of Indium Tin Oxide (ITO) in Electroanalysis without Surface Modification. *Journal of The Electrochemical Society* **167**, 037534 (2020).
147. Goebbert, C., Nonninger, R., Aegerter, M. A. & Schmidt, H. Wet chemical deposition of ATO and ITO coatings using crystalline nanoparticles redispersable in solutions. *Thin Solid Films* **351**, 79–84 (1999).
148. Ajdnik, U. *et al.* Bioactive Functional Nanolayers of Chitosan-Lysine Surfactant with Single- And Mixed-Protein-Repellent and Antibiofilm Properties for Medical Implants. *ACS applied materials & interfaces* **13**, (2021).
149. Kanai, M. *et al.* PDMS Microfluidic Devices with PTFE Passivated Channels. in (Squaw Valley, Californla USA, 2003).
150. Gökaltun, A., Kang, Y. B. (Abraham), Yarmush, M. L., Usta, O. B. & Asatekin, A. Simple Surface Modification of Poly(dimethylsiloxane) via Surface Segregating Smart Polymers for Biomicrofluidics. *Scientific Reports* **9**, 7377 (2019).
151. Puttaswamy, S. V. *et al.* Versatile microfluidic platform embedded with sidewall three-dimensional electrodes for cell manipulation. *Biomedical Physics & Engineering Express* **5**, 055003 (2019).
152. So, J.-H. & D. Dickey, M. Inherently aligned microfluidic electrodes composed of liquid metal. *Lab on a Chip* **11**, 905–911 (2011).
153. Pavesi, A. *et al.* How to embed three-dimensional flexible electrodes in microfluidic devices for cell culture applications. *Lab on a Chip* **11**, 1593–1595 (2011).

ECOLE DOCTORALE

Titre : Tomographie d'Orientation dans les Cristaux Liquides et Mesures de Cisaillement dans les Systèmes Hydrovoltaïques par Spectroscopie de Luminescence Polarisée des Nanobâtonnets $LaPO_4$:Eu.

Mots clés : spectroscopie de luminescence, terres rares, nanocristaux, cristaux liquides, microfluidique

Résumé : La capacité de mesurer l'orientation d'objets à l'échelle micro- ou nanoscopique a une grande importance pour une large variété de domaines de recherche. Nous avons précédemment démontré que la spectroscopie de l'émission polarisée de nanocristaux dopés aux lanthanides est une méthode efficace pour déterminer leur orientation tridimensionnelle (3D). Dans ce travail, la méthodologie est développée pour être applicable aux assemblages de ces nanobâtonnets. Deux systèmes alignés sont explorés : 1) des assemblages formés spontanément par auto-organisation et 2) des assemblages colloïdaux orientés sous sous écoulement.

Pour le premier système, une suspension colloïdale de cristal liquide (CL) de nanobâtonnets $LaPO_4$:Eu est utilisée. Lorsqu'elle est confinée entre des parois rigides, une telle suspension de CL subit une évolution morphologique remarquable, avec des tactoïdes nematique conventionnels évoluant en motifs semblables à des stries, puis en structures en forme de fleurs jamais observées auparavant. À l'aide de la méthodologie développée dans l'équipe, l'orientation 3D dans ces structures est caractérisée, révélant l'impact relatif des énergies de volume et de surface sur les structure formées.

Comme seconde application, les nanobâtonnets $LaPO_4$:Eu sont utilisés comme sondes de cisaillement en mesurant leur alignement local sous écoulement microfluidique. Une méthode pour obtenir la relation expérimentale entre le degré d'alignement et le cisaillement a été développée. Cette seconde partie du travail vise à appliquer cette approche pour caractériser l'impact du cisaillement de l'écoulement sur la réponse électrochimique d'un système hydrovoltaïque basé sur le balayage sélectif des ions sur des électrodes capacitives.

Title : Orientation Tomography in Liquid Crystals & Shearmetry in Hydrovoltaic Systems by Spectroscopy of Polarized Luminescence of $LaPO_4$:Eu Nanorods

Keywords : luminescence spectroscopy, rare earths, nanocrystals, liquid crystals, microfluidics

Abstract : The ability to measure the orientation of objects at the micro- or nanoscopic scale is of great importance for a wide variety of research fields. We previously demonstrated that spectroscopy of the polarized emission of lanthanide doped nanocrystals is an effective and straightforward way to determine their three-dimensional (3D) orientation. In this work, the methodology is further developed to be applicable to assemblies of such nanorods. Two different aligned systems are explored:
1) Spontaneously formed self-assemblies.
2) Actively aligned ensembles under flow.

To address the first system, a colloidal liquid crystal (LC) of $LaPO_4$:Eu nanorods is used. When confined between rigid walls, such an LC suspension undergoes a remarkable morphogenesis, with conventional nematic tactoids evolving into streak-like patterns and finally never-before-seen flower-like structures. Using the developed spectroscopic analysis, the 3D orientation in these structures is characterized, revealing the relative impact of volume and surface energies.

As a second application, $LaPO_4$:Eu nanorods are used as *shear-probes* by measuring their local alignment under flow. A method for obtaining the experimental relationship between the degree of alignment and the local shear rate is further developed. We aim to apply this approach to characterize the impact of flow shear on the electrochemical response of a hydrovoltaic system based on selective ion sweeping on capacitive electrodes.